Thermal spark formation and plasma-assisted combustion by nanosecond repetitive discharges

Nicolas Minesi

Thèse de doctorat

NNT : 2020UPAST052

université PARIS-SACLAY

Thermal spark formation and plasma-assisted combustion by nanosecond repetitive discharges

Thèse de doctorat de l'université Paris-Saclay

École doctorale n°579 SMEMAG, Sciences Mécaniques et Energétiques, Matériaux et Géosciences
Spécialité de doctorat : Combustion
Unité de recherche : Université Paris-Saclay, CNRS, CentraleSupélec, Laboratoire EM2C, 91190, Gif-sur-Yvette, France
Référent : CentraleSupélec

Thèse présentée et soutenue à Gif sur Yvette, le 16 décembre 2020, par

Nicolas MINESI

Composition du Jury

Armelle Cessou Directrice de recherche, CNRS, CORIA	Présidente
Peter Bruggeman Professeur, University of Minnesota	Rapporteur et Examinateur
Khaled Hassouni Professeur, Université Paris-Nord, LSPM	Rapporteur et Examinateur
David Pai Chargé de recherche, CNRS, PPRIME	Examinateur
Guillaume Pilla Ingénieur de recherche, IFPEN	Examinateur
Svetlana Starikovskaia Directrice de recherche, CNRS, LPP	Examinatrice
Christophe Laux Professeur, CentraleSupélec, Université Paris-Saclay, EM2C	Directeur de thèse
Gabi-Daniel Stancu Professeur, CentraleSupélec, Université Paris-Saclay, EM2C	Co-directeur de thèse
Axel Vincent-Randonnier Ingénieur de recherche, ONERA	Co-encadrant de thèse

université PARIS-SACLAY
ÉCOLE DOCTORALE
Sciences mécaniques et énergétiques, matériaux et géosciences (SMEMAG)

Titre : Formation d'un plasma complétement ionisé et combustion assistée par décharges nanosecondes
Mots clés : plasma, décharges nanosecondes, combustion assistée par plasma, cinétique, spectroscopie

Résumé : Cette thèse porte sur l'étude de la formation et de la recombinaison d'un plasma complétement ionisé généré par une impulsion électrique de quelques nanosecondes. La formation du plasma se décompose en cinq étapes : (i) ionisation partielle de l'espace inter-électrode, (ii) formation d'un filament à la cathode, (iii) formation d'un filament à l'anode, (iv) propagation des filaments et (v) fusion des filaments. Ces derniers sont caractérisés par une émission intense de N^+ et d'un continuum des électrons. Nos mesures montrent que la densité d'électrons augmente de 10^{17} à 10^{19} cm^{-3} en moins de 0.5 ns. Cette augmentation abrupte est due à l'ionisation des états excités de N et O, comme le montre un mécanisme cinétique développé dans cette thèse. Le plasma complétement ionisé est à l'équilibre chimique et thermique.

Après que l'ionisation complète est atteinte, la densité et la température des électrons décroissent en raison d'une expansion isentropique de la colonne de plasma. Les décharges Nanosecondes Répétitives Pulsées (NRP) sont ensuite utilisées en régime hors-équilibre dans deux brûleurs afin de réaliser des études fondamentales et appliquées en combustion assistée par plasma. Dans le brûleur Mini-PAC, près des électrodes, la température du plasma augmente de 1500 K en raison d'une "lente" formation d'un filament. Les décharges NRP accélèrent la réactivité de la flamme comme le montrent l'augmentation de la densité des espèces excitées dans le plasma et l'enrichissement global de la flamme en OH. Dans le brûleur SICCA, les décharges NRP réduisent l'instabilité des flammes oscillantes (méthane, n-heptane et dodécane) et étendent ainsi leur limite d'extinction pauvre.

The Ph.D. defense can be watched following this link: https://youtu.be/TyLPRFxv_Xk

Université Paris-Saclay
Espace Technologique / Immeuble Discovery
Route de l'Orme aux Merisiers RD 128 / 91190 Saint-Aubin, France

Title: Thermal spark formation and plasma-assisted combustion by nanosecond repetitive discharges
Keywords: plasma, thermal spark, nanosecond discharge, plasma-assisted combustion, kinetics, spectroscopy

Abstract: This thesis analyzes the formation and recombination of fully ionized plasmas generated by nanosecond high-voltage pulses: *the thermal sparks*. Their formation occurs in five stages: (i) partial ionization of the plasma channel, (ii) creation of a fully ionized filament at the cathode, (iii) formation of a fully ionized filament at the anode, (iv) propagation of these filaments toward the middle of the interelectrode gap, and (v) merging of the filaments. The filaments are characterized by intense N^+ and continuum emission. We show experimentally that their electron number density increases from 10^{17} to 10^{19} cm^{-3} in less than 0.5 ns. A kinetic mechanism, including the ionization of N and O excited states, successfully describes this 0.5-ns transition. After full ionization is reached, the plasma reaches thermal and chemical equilibrium and the electron number density decreases due to isentropic expansion. Then, Nanosecond Repetitively Pulsed (NRP) discharges in the non-thermal spark regime are applied in two burners for fundamental and practical studies of Plasma-Assisted Combustion (PAC). In the mini-PAC burner, the plasma temperature increases by 1500 K near the electrode due to a "slow" thermal spark formation. The NRP discharges enhance the reactivity of the entire flame, as shown by (i) the growth of the active species in the discharge vicinity and (ii) the increase of the OH number density in the entire flame. In the SICCA burner, NRP discharges reduce the instability of oscillating flames (in methane, heptane, and dodecane), and hence extend their lean blow out limit.

Résumé vulgarisé

Cette thèse est une étude des propriétés physiques de décharges électriques particulières. Pendant quelques milliardièmes de seconde, ou nanosecondes, un fort champ électrique est appliqué entre deux électrodes séparées de quelques millimètres. A cause de ce champ, l'air va « claquer » et un courant électrique va relier les deux électrodes. L'air sera ionisé, c'est-à-dire que certaines molécules seront positives (les ions) et entourées de charges négatives (les électrons), et deviendra un plasma. Habituellement, ces décharges sont si courtes que les électrons n'ont pas le temps de réchauffer les molécules. La chimie est dite « hors-équilibre ». Dans certains cas, assez d'électrons sont formés pour rétablir l'équilibre. La transition hors-équilibre / équilibre est le sujet de la première partie de cette thèse. Dans une deuxième partie, nous utilisons des décharges hors-équilibre pour permettre à des flammes de brûler dans des conditions habituellement interdites. Nos mesures expliquent le mécanisme d'accélération de la combustion par l'augmentation de température des gaz et la génération d'espèces actives connues pour accélérer la combustion.

Université Paris-Saclay
Espace Technologique / Immeuble Discovery
Route de l'Orme aux Merisiers RD 128 / 91190 Saint-Aubin, France

Acknowledgements

First, I would like to thank the jury members who dedicated their scarce time reading this manuscript. Their feedback is very valuable to me and I particularly enjoyed their questions/comments during the defense. I hope that our scientific paths will cross again with more opportunities to discuss plasma physics, and other things.

J'aimerais maintenant mentionner celles et ceux qui j'ai croisé pendant ma thèse. Grâce à eux, je ne regrette aucun jour de cette expérience incroyable.

Tout d'abord merci à toute ma famille qui m'a toujours soutenu depuis ma décision de faire de la recherche. Merci d'avoir été là pour tous mes grands moments. Je remercie mes nombreux colocs (Antoine, Cynthia, Guilhem, Sylvain, Thomas et Victorien) qui ont dû supporter mon caractère, ma liste de course, mes raclettes et mon chat. Je remercie aussi tous mes amis de collège, lycée, prépa et du magistère qui ont régulièrement pris des nouvelles (« alors cette thèse, ça avance ?! »), m'ont forcé à sortir pour profiter de cette vie merveilleuse, alors que tout ce que je voulais c'était faire de la spectroscopie et du Python.

Une mention pour le rugby, ma bouffée d'oxygène lorsque rien n'allait comme prévu. Merci aux arbitres d'Ile de France pour leur accompagnement et leur bonne humeur qui m'ont suivi pendant six ans. Je pense aussi aux arbitres d'Orsay (notamment Brice, Corentin et Gaétan) ainsi qu'à Paul Tremsal et Philippe qui, par leur engagement, nous ont offert un cadre exceptionnel pour progresser. Je ne pouvais pas mieux tomber qu'à Orsay ! Côté jeu, j'aimerais aussi remercier le CRC, grâce à qui, j'ai pu redécouvrir la joie du port de la moustache et le gout si particulier des pommes dauphines. Merci à Louis, qui en dehors du terrain, est courageusement devenu mon coach muscu et œnologie. Merci aussi à Xavier Pujos et Youssef Driss pour m'avoir tant appris, que ce soit de la technique de base de la passe, à la vision d'ensemble de ce sport merveilleux.

J'aimerais maintenant remercier l'ensemble de l'EM2C, des gens formidables dans un laboratoire formidable. Je pense en premier lieu aux ITA qui sont notre socle et sans qui tout serait tellement plus compliqué. Merci à Brigitte, Nathalie et Noï qui ont su, avec beaucoup de gentillesse, me rappeler que j'étais en retard pour à peu près tout (signature de BL, ordre de mission, bon de commande etc.). Merci à Yannick et Erika pour toute votre aide. Même si mes croquis n'étaient pas toujours nickels, même si Yannick ronchonnait un peu, vous avez, à chaque fois, été bien au-delà de ce que j'attendais. Merci à Jérôme qui m'a accompagné lors de mes débuts en plomberie. Grâce à toi, l'armoire du BE a un peu moins de secret pour moi. Merci aussi à tous les autres ITA d'avoir toujours été là, même dans l'urgence, quand j'en avais besoin. J'aimerais

aussi mentionner toute l'équipe du CDL avec qui j'ai pu comprendre ce qui se passe dans l'envers du décor. En particulier, merci à Sébastien Ducruix qui a toujours mis en priorité le bien-être des doctorants lors de chacune de ses décisions. Merci à Aymeric pour toutes ces discussions que nous avons eu, des plus sérieuses à d'autres moins essentielles, comme la gestion de la machine à café. Merci à Philippe Rivière, pour le temps qu'il a passé à m'expliquer ses travaux sur les élargissements de raies atomiques. Merci à Anouar Soufiani et Emmanuel Odic qui m'ont prêté du matériel essentiel pour mes mesures. Je remercie toute l'équipe SICCA avec qui j'ai beaucoup appris et avec qui j'aurais aimé faire encore plus.

En dehors du laboratoire, j'aimerais remercier Cécile Oriot qui a accepté de mettre en images nos décharges et notre équipe. Aussi, je remercie Divya d'avoir passé du temps sur l'anglais de ma thèse et ma présentation GEC. J'ai largement fait de la pub pour le Learning Center et j'espère que tu n'as pas trop de travail maintenant !

Merci aussi à tous les doctorants du laboratoire. J'ai une pensée toute particulière pour mes co-bureaux. Les plus anciens d'abord : Marek et Mélo qui auront connu les joies de Chatenay et les visites de Kevin à la recherche des derniers potins, mais aussi Adrien qui a toujours trouvé les mots justes et l'humour pour commenter les petits aléas de la thèse et Aurélien qui était toujours là pour écouter quand les simus ne fonctionnaient pas. Les petits derniers maintenant : Luc et Valentin, vous êtes maintenant les garants de la bonne humeur du bureau EB.202. Laissez tomber la cantine de l'ONERA et du CEA et revenez à temps plein !! Also, I'd like to thank Agnes, who has been so kind even when I did not deserve it. Enfin, j'aimerais remercier Arthur, Erwan et Roxane. Il y a beaucoup de choses que je retiendrai : la recherche de formations adum, l'optimisation du H factor, les soirées chez Erwan, le débat hebdomadaire sur le lundi végétarien, le couple secret du labo (🤫 shhhhut !), la naissance de Spark/RADIS/PrintempsÉcologique, les e-mails incroyables de cs.tous, le Chablis, les raclettes et bien d'autres choses que la décence m'empêche de mentionner. Du fond du cœur, merci d'avoir été là et de rester mes amis.

J'aimerais aussi remercier les nombreux doctorants et post-docs de l'axe plasma. Plus particulièrement, j'aimerais mentionner Sergey, qui m'a rapidement mis au travail expérimental sans négliger la bibliographie (« allez badaud, on lit un article par jour ! »). J'ai apprécié sa vision si pragmatique de la recherche et je n'oublierai jamais son soutien honnête sur le plan personnel. Enfin, j'aimerais saluer son courage pour avoir été le premier correcteur de mes écrits en anglais ! J'aimerais remercier Augustin, avec qui j'ai fait mes premiers pas en politique au prestigieux conseil du labo. Je garderai en tête son organisation incroyable, que ce soit sur le plan scientifique ou festif (on n'aura jamais vu un BBQ du labo aussi bien réussi que celui de 2018). Il me tarde d'avoir à affronter tes questions sur les tubes à choc en conférence. Beaucoup d'aspects de ma thèse ne seraient pas aussi avancés sans le travail d'Erwan, qui a préparé tant de choses dont j'avais

besoin. Je pense par exemple à la mesure d'énergie, au câblage pour les NRP, à ZDPlasKin, la rédaction sur Word, et j'en oublie sûrement. Merci d'avoir été là, toutes ces fins de journées à Chatenay pour me transmettre tout ce que tu savais. La partie simulation de ma thèse doit aussi beaucoup à Pierre, qui a passé tant de temps sur les cross-sections, le Stark broadening et la recombinaison. Enfin, cela aura été une joie pour moi d'apprendre Python aux côtés d'Augustin, Erwan et Pierre. J'aurais été l'heureux testeur stupide de PySpecair, (encore) un autre outil sans lequel une partie de mes analyses auraient été beaucoup plus difficiles à mettre en place. Il ne nous reste plus qu'à convaincre Christophe que Python survivra encore quelques années (et que tout n'est pas perdu !! !! !!). Merci à Sean, que j'ai vu passer du statut de jeune post-doc à l'accent sexy à un (moins) jeune maitre de conférences, marié et père de famille. Les pauses-cafés que nous prenions me manquerons beaucoup ! Je pars en te faisant une dernière petite blague : quelque chose s'est caché dans ton bureau… J'aimerais aussi remercier Victorien, qui a courageusement pris en main la combustion assistée par plasma. Pendant les longues heures passées avec toi sur Mini-PAC, tu m'as démontré que tu avais bien mieux compris la combustion assistée par plasma que moi. Faire une colocation avec un thésard qui bosse sur le même sujet et avec le même directeur était un pari risqué, qui s'est révélé être l'une de mes meilleures décisions (malgré tes goûts originaux en termes de radio, pesto et toutes ces heures de violon que tu m'as fait subir). Il nous reste maintenant à suivre les progrès de Jean-Baptiste qui nous volera certainement les meilleurs postes de chercheurs ! Je remercie aussi tous les autres membres de l'équipe plasma : Arnaud (nouvel organisateur des J-RED), Arthur (co-leader de la pause-café avec Sergey), Ciprian (now a successful scientist in Romania), Corentin (spécialiste rangement, nutrition et photofeeler), Fabien (qui doit soutenir bientôt !), Jean Maillard (génie du saxophone), Moises (nouveau pilier de Spark), Ulysse (qui prend la relève pour l'organisation des confs – courage !) et Valentin (le collectionneur de livres).

J'aimerais adresser mes remerciements les plus sincères à Axel, Gabi et Christophe, qui ont rempli leur rôle bien au-delà d'un simple travail d'encadrement. J'ai commencé ma thèse avec trois directeurs, et je la termine avec trois amis. Merci à Axel, tout d'abord pour avoir pris de son précieux temps pour permettre nos expériences à l'ONERA. Au cours de ces deux campagnes à tes côtés, j'ai eu la chance de découvrir tes systèmes (la caméra rapide maison ou l'injecteur plasma) et ta connaissance si transverse et complète de la combustion et des plasmas. Tellement verrous ont été levés grâce à toi et d'autres succès nous attendent, j'en suis sûr. Merci à Gabi, d'avoir été là pour poser toutes ces questions dérangeantes qu'on ne veut pas entendre. Grâce à toi, j'ai eu à cœur d'aller chercher tout ce qui se trouvait derrière le Stark et la LIF pour te prouver solidement que mes mesures avaient du sens. Merci, enfin, à Christophe sans qui les succès de cette thèse n'auraient jamais eu lieu. Je ne compte plus les soirées, les vacances et les week-ends que tu as consacré à mon projet (à commencer par l'écriture du sujet de thèse un dimanche après-midi). Tu aurais pu t'énerver des dizaines de fois quand je refusais de faire ce que tu me demandais. Au lieu de cela, tu as patiemment répété que « ça serait bien si tu … », jusqu'à ce que je réalise enfin que tu avais encore eu une

bonne idée. Ta porte était toujours ouverte pour écouter ce que tes doctorants ont à dire, et je crois que j'ai abusé de ce privilège. Tu étais là pour tous les moments difficiles (quand j'ai cru que la combustion assistée par plasma ça ne marcherait jamais) et aussi pour les célébrations (cet incroyable raclette-gala de GEC). Je crois que si j'ai été aussi heureux et insouciant pendant ma thèse c'est parce que je savais que tu serais là pour m'épauler au moindre problème. Tu ne comptes pas tes heures avec tout tes doctorants sans exception, tout simplement parce que tu souhaites le meilleur pour nous. Après avoir été si bien encadré, il me reste à construire sur tout ce que tu m'as appris et, je l'espère, suivre tes pas.

Finalement, j'aimerais remercier Manon pour tout son soutien, si essentiel pour moi, et la patience dont elle a fait preuve lorsque je ne pensais qu'à travailler. De nouveaux défis s'offrent à nous maintenant, et j'espère qu'il y en aura beaucoup d'autres.

Table of Content

Introduction

Motivation

The temperature, pressure, and composition of a gas at rest are determined by thermodynamics and chemistry. In an electromagnetic field, the state of this gas will also be subject to plasma physics. Such a field can be applied continuously (AC, DC) or transiently. Among transient sources of electric fields, nanosecond discharges stand out. Applied at frequencies in the range 1 – 100 kHz for voltages of several kilovolts, their average electrical power remains low (1 – 100 W). This advantage triggered the application of Nanosecond Repetitively Pulsed (NRP) discharges in many research areas: flow control, medicine, agriculture, nanotechnologies, combustion. Indeed, a branch of the combustion community is interested in extending the flammability of combustible mixtures under challenging conditions, such as ultra-lean mixtures, oscillating flames (thermo-acoustic instabilities), or during fast variations of the equivalence ratio. NRP discharges offer the possibility to (i) produce chemically active species, (ii) increase the temperature, and (iii) generate hydrodynamic perturbations. These three effects can sharply enhance the traditional flame chain-initiation reactions and hence accelerate combustion.

Plasma-Assisted Combustion (PAC) by NRP discharges is the principal motivation of this work. However, the use of nanosecond discharges raises fundamental questions that were unanswered at the beginning of this thesis. A few measurements in the literature (Shcherbanev *et al.*, 2016; Lo *et al.*, 2017; Sainct *et al.*, 2020) reported that nanosecond discharges could abruptly generate fully ionized plasma at tens of thousand kelvin, which are called *thermal sparks* in this thesis. Such measurements implied that the nanosecond plasmas are in thermal and chemical equilibrium. In contrast, other works at Stanford University and EM2C laboratory demonstrated the existence of nonequilibrium nanosecond sparks (Packan, 2004; Pai, 2008; Rusterholtz, 2012; Xu, 2013). In most potential applications, we aim to use NRP discharges to generated non-equilibrium plasmas. Consequently, the formation of thermal sparks is a critical issue that needs to be addressed. Therefore, we conducted a fundamental study of nanosecond discharges in ambient air in order to:

- characterize the parameters responsible for the formation of the thermal spark
- describe the formation and recombination of the thermal spark.

The fundamentals of nanosecond discharges initially represented a small fraction of this Ph.D. thesis but grew considerably with the author's interest. In parallel to the experimental characterization of the thermal spark, a chemical kinetic mechanism was developed and two more challenging objectives were pursued:

- explain the increase of temperature during the full ionization in nanosecond discharges
- identify the key mechanisms responsible for the full ionization of thermal sparks

The principal subject of this thesis, PAC, was investigated following the results obtained by Galley, Pilla, Xu, and co-authors (Galley *et al.*, 2005; Pilla *et al.*, 2006; Pilla, 2008; Xu, 2013). In their works, NRP discharges were applied in propane-air mixtures across a 5-mm gap in the recirculation zone of a bluff-body burner called Mini-PAC. Using Optical Emission Spectroscopy (OES), Pilla measured a significant increase of the temperature and atomic oxygen number density in the center of 10-ns discharges applied at 30 kHz. These effects allowed for stabilizing the Mini-PAC flame at leaner conditions. Later, Xu performed a pulse-by-pulse study of the transition from a non-assisted to a plasma-assisted flame. He demonstrated that the stabilization of the lean flames is strongly coupled with the advection of OH radicals. To pursue these encouraging results, the PASTEC[1] ANR-project aims to describe the full interaction of NRP discharges with lean methane-air flames. For that purpose, in this thesis, we extend the measurements of Pilla and Xu to achieve the following objectives:

- identify the regime of the NRP spark applied in the mini-PAC burner: non-thermal or thermal?
- understand the critical mechanisms of heating and cooling in a methane-air flame stabilized by NRP discharges
- describe the process of stabilization related to the active species formation
- guide the numerical simulations of PAC, also conducted in the PASTEC project

The PASTEC project is devoted to studying methane-air flames, but some industrial applications of PAC require more complex fuels. Therefore, we also aim to extend the lean blow-out limit in the SICCA-spray facility to:

- demonstrate the scalability of PAC with heavier fuels

[1] PASTEC is the acronym of Plasma AssiSTEd Combustion.

Scope of this thesis

This manuscript has been divided into three parts to answer the foregoing objectives.

Part I, entitled *Fundamental and practical aspects of nanosecond discharges*, summarizes the theoretical and practical aspects at the roots of the two following parts. Experienced or hurried researchers can probably skip certain portions.

- Chapter 1 introduces, in an academic format, the distribution of rotational, vibrational, and electronic levels and the concept of partition functions. Then, temperature measurements by Optical Emission Spectroscopy are described, and followed by an extensive study of atomic line broadening. Finally, a simplified 2-level model of Laser-Induced Fluorescence is provided.
- Chapter 2 compares two different methods for voltage, current, and energy measurements of nanosecond discharge.

Part II, dedicated to the *thermal spark*, attempts to give a structure to the nascent literature on fully ionized plasmas generated by nanosecond pulses, including the experimental and numerical results obtained in this work.

- Chapter 3 provides a short review of previous work on the formation of partially and fully ionized plasmas by nanosecond discharges.
- Chapter 4 is an experimental work on the thermal spark formation and recombination. Our measurements are analyzed and then compared to other works in the literature.
- Chapter 5 presents a new 0-D kinetic mechanism to describe the thermal spark formation. The mechanism is tested at thermal equilibrium and in two-temperature plasmas.
- Finally, in Chapter 6, the thermal spark formation is simulated using the kinetic mechanism of Chapter 5. First, this simulation is run on an academic example. Then, the electron number density measured in our thermal spark setup is compared with the simulation results.

Part III describes the *Application of NRP discharges to plasma-assisted combustion* and is organized in three chapters.

- Chapter 7 gives a short overview of the plasma-assisted combustion field, with an emphasis on large-scale, high-power experiments.
- Chapter 8 focuses on the thermal and chemical effects of NRP discharges on a methane-air flame in a bluff-body configuration: Mini-PAC. The evolution of the temperature and excited species

densities is measured by Optical Emission Spectroscopy in the plasma, whereas Laser-Induced Fluorescence and chemiluminescence are used to monitor the dynamic flame response.

- In Chapter 9, the lean blow-out limit of methane, n-heptane, and dodecane flames are extended by NRP discharges in the SICCA burner.

Three appendices follow:

- Appendix A is a technical description of the two pulse generators used in this thesis.
- Appendix B describes the calibration procedure of an Optical Emission Spectroscopy setup.
- Appendix C presents a comparison of the available cross-sections for N_2 excitation, dissociation, and ionization by electron impact. The choices of cross-sections used in the kinetic mechanism are discussed.

Part I: Fundamental and practical aspects of nanosecond discharges

Chapter 1

Optical Emission Spectroscopy, Line-Broadening diagnostics, and Laser-Induced Fluorescence

In this chapter, we describe basic physical concepts underlying much of the work presented in this thesis, as well as the principles of diagnostics based on Optical Emission Spectroscopy (OES), Rayleigh scattering, and Laser-Induced Fluorescence. Particular attention is given to the description of the electronic structure of atoms and molecules in Section 1.1. The determination of the translational temperature by OES is detailed in Section 1.2, followed by a short description of the Rayleigh scattering technique in Section 1.2.4. Section 1.3 is dedicated to the spectral broadening of atomic lines. Finally, the theoretical background of Laser-Induced Fluorescence is given in Section 1.4.

1.1 Distribution of internal energy level populations in atoms and molecules

Optical Emission Spectroscopy diagnostics require knowledge of atomic and molecular spectroscopic properties, described in this section. The fundamental description of atoms and molecules is freely inspired from the "Atomic, Molecular, and Radiation Physics" course[1]. This section can be referred to by Master's students following the same course and supplemented by (Vincenti and Kruger, 1965; Alberty and Silbey, 1992).

[1] Laux, C. O. (2015) *Atomic, Molecular, and Radiation Physics - TC07*. Université Paris-Saclay - Master Physique des Plasmas et de la Fusion

1.1.1 Excited populations of atomic and molecular states in plasma

According to Boltzmann's theory, when equilibrium is reached at temperature *T*, the entropy, *S*, can be calculated using Eq. 1.1, where E_i is the energy level of state *i*, g_i the state degeneracy, k_b the Boltzmann constant, *N* the total number of particles, *E* the total energy and $\beta = k_bT$. This formulation is valid if the thermal de Broglie wavelength, Λ, is negligible compared to the volume of the considered plasma as given in Eq. 1.2, where *m* is the mass of the particle and *h* the Planck constant.

$$S = Nk_b\left[\ln\left(\frac{1}{N}\sum_i g_i \exp(-\beta E_i)\right)+1\right]+\frac{E}{T} \quad \text{Eq. 1.1}$$

$$\frac{V}{\Lambda^3} = V\left(\frac{2\pi m k_b T}{h^2}\right)^{\frac{3}{2}} \gg 1 \quad \text{Eq. 1.2}$$

The partition function Z of a particle is defined as:

$$Z = \sum_i g_i \exp(-\beta E_i) \quad \text{Eq. 1.3}$$

Hence, then entropy can be written

$$S = Nk_b\left[\ln\left(\frac{\mathrm{Z}}{N}\right)+1\right]+\frac{E}{T} \quad \text{Eq. 1.4}$$

We define the Gibbs free energy in Eq. 1.5.

$$F = E - TS \quad \text{Eq. 1.5}$$

Thus, $S = -\partial F/\partial T$ and F is related to the partition function:

$$F = -Nk_BT\left[\ln\left(\frac{Z}{N}\right)+1\right] \quad \text{Eq. 1.6}$$

Using Eq. 1.5, the average energy can be calculated as:

$$E = -\mathrm{T}^2\frac{\partial\left(\frac{F}{T}\right)}{\partial T} = Nk_bT^2\frac{\partial \ln(Z)}{\partial T} \quad \text{Eq. 1.7}$$

The pressure, the chemical potential per molecule, and the thermal capacity are determined in Eq. 1.8, Eq. 1.9 and Eq. 6.16, respectively.

$$P = -\frac{\partial F}{\partial V} \quad \text{Eq. 1.8}$$

$$\hat{\mu} = \frac{\partial F}{\partial N} \quad \text{Eq. 1.9}$$

$$c_v = \frac{1}{N}\frac{\partial \mathrm{E}}{\partial T} \qquad \text{Eq. 1.10}$$

The relations in Eq. 1.8 and Eq. 1.9, are implicitly included in Eq. 1.11.

$$\mathrm{d}F = -P\mathrm{d}V - S\mathrm{d}T + \hat{\mu}\mathrm{d}N \qquad \text{Eq. 1.11}$$

Therefore, the thermodynamic properties of plasmas (entropy, pressure, energy …) are determined by the gas partition functions. In the following paragraph, we will derive the expression of the translational, rotational, vibrational, and electronic partition functions, assuming they are independent. The thermodynamic properties of plasma will be calculated, in parallel.

1.1.2 Translational partition function

The translational energy of a particle in a cubic box of dimension L is equal to E in Eq. 1.12, where n_1, n_2, n_3, are the quantum numbers in the three directions in the phase volume.

$$E(n_1, n_2, n_3) = \frac{h^2}{8m}\frac{n_1^2 + n_2^2 + n_3^2}{L} \qquad \text{Eq. 1.12}$$

Thus, the translational partition function can be written using Eq. 1.3 as:

$$Z_{trans} = \sum_{n_1,n_2,n_3} \exp\left[-\frac{h^2}{8mk_bT}\frac{n_1^2 + n_2^2 + n_3^2}{L}\right] \qquad \text{Eq. 1.13}$$

The expression of Eq. 1.13 can be simplified into three sums. Also, the sum increments, n_i, being sufficiently small, Eq. 1.13 can be approximated by its integral equivalent. Therefore, the translation partition function is equal to:

$$Z_{trans} = \frac{V}{\Lambda^3} = V\left(\frac{2\pi m k_b T}{h^2}\right)^{\frac{3}{2}} \qquad \text{Eq. 1.14}$$

For now, the temperature T_{trans} will be used to characterize the heavy particles (kinetic) temperature[1] and T_e for the electrons (kinetic) temperature. Therefore, using Eq. 1.8 and Eq. 1.7, we obtain the theorem of equipartition, the ideal gas law, and the thermal capacity of a monoatomic gas:

$$E_{trans} = \frac{3}{2}Nk_bT \qquad \text{Eq. 1.15}$$

[1] Depending on the context, "T_{trans}" can also be denominated "T_{gas}".

$$P = \frac{N}{V} k_b T \quad \text{Eq. 1.16}$$

$$c_{v,trans} = \frac{3}{2} k_b \quad \text{Eq. 1.17}$$

The thermal capacity of a monoatomic gas is constant, but this is not the case at high temperatures due to the inclusion of the electronically excited states in the derivation (Colonna, D'Angola and Capitelli, 2012).

1.1.3 Electronic partition function

According to quantum mechanics, the electrons bound to an atom can occupy specific states of a given energy. The occupation of the electronic shell is commonly represented by an energy diagram, such as shown in Figure 1.1 for atomic nitrogen. The degeneracy of each level, g_i, and its energy, E_i can be found on the NIST website[1] (Kramida *et al.*, 2018). The spectroscopic notation of a level is written $^{2S+1}L_J$. The L term is the orbital angular momentum equal to 0, 1, 2, 3, etc. whose symbol are S, P, D, F, etc. for atoms. For molecules, the Greek alphabet is used ($\Lambda = \Sigma, \Pi, \Delta, \Phi, \ldots$). J is the total angular momentum defined by J = L + S, where S is the spin. The degeneracy of each state is given by $g_i = 2J + 1$. If the number of electrons in odd orbitals is odd, the total state parity is odd and a "0" can be added to the spectroscopic notation, such as for N($^2D^0$).

[1] See https://physics.nist.gov/PhysRefData/ASD/lines_form.html

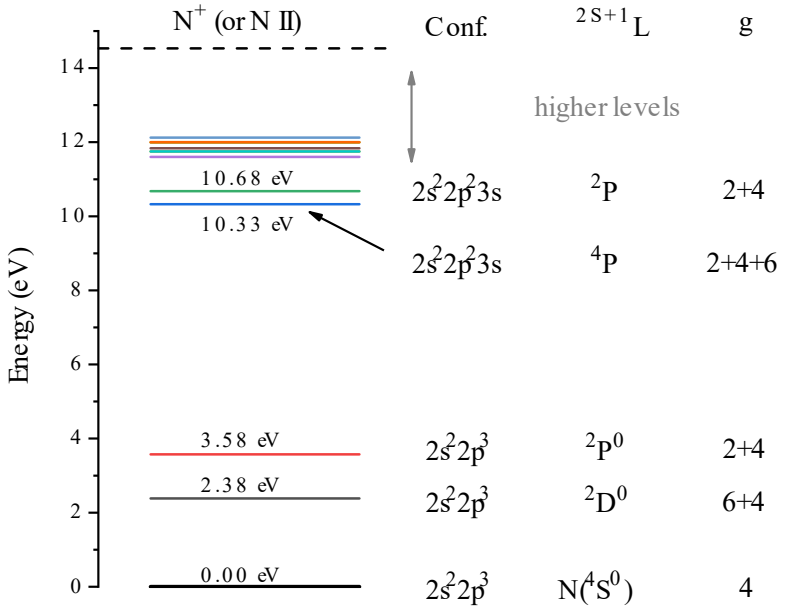

Figure 1.1 Energy diagram of atomic nitrogen. The energy, configuration, term, and degeneracy of the five first levels are also given. In the case of spin separation, the degeneracy of each internal level is given (e.g. the degeneracy of N($^2D^0$) is equal to 6+4=10).

In the case of atomic nitrogen, the partition function is equal to:

$$Z_{elec}(N) = \sum_i g_i \exp\left(-\frac{\varepsilon_i}{k_b T_{elec}}\right) = 4 + 10 \times e^{-\frac{27\,666\mathrm{K}}{T_{elec}}} + 0(e^{-\frac{41{,}493\mathrm{K}}{T_{elec}}}) \qquad \text{Eq. 1.18}$$

The first term in Eq. 1.18 is the degeneracy of the ground state. The $^2D^0$ state composed of the states $^2D^0_{5/2}$ and $^2D^0_{3/2}$ (of degeneracy 6 and 4, respectively) is grouped in one unique state of energy E_1 = 2.384 eV = 27,666 K. It is usually not necessary to include the next terms because atomic nitrogen is usually ionized above 30,000 K.

For molecules, the same calculation can be performed. The first excited state of N_2 is $N_2(A^3\Sigma_u^+)$ separated from the ground state $N_2(X^1\Sigma_g^+)$ by T_e = 6.22 eV = 72,183 K (Laux, 1993). Therefore, the electronic partition function of N_2 can be written:

$$Z_{elec}(N_2) = 1 + 3 \times e^{-\frac{72\,183\,\mathrm{K}}{T_{elec}}} + 0(e^{-\frac{85\,782\,K}{T_{elec}}}) \qquad \text{Eq. 1.19}$$

An existing program from Zare (Zare, 1964) is used to calculate rotationless Rydberg-Klein-Rees potentials based on Dunham expansion coefficients Y_{ij}, available in Laux's thesis (Laux, 1993). The result of the calculation is shown in Figure 1.2 where the potentials of $N_2(X)$, $N_2(A)$, $N_2(B)$, and $N_2(C)$ are plotted.

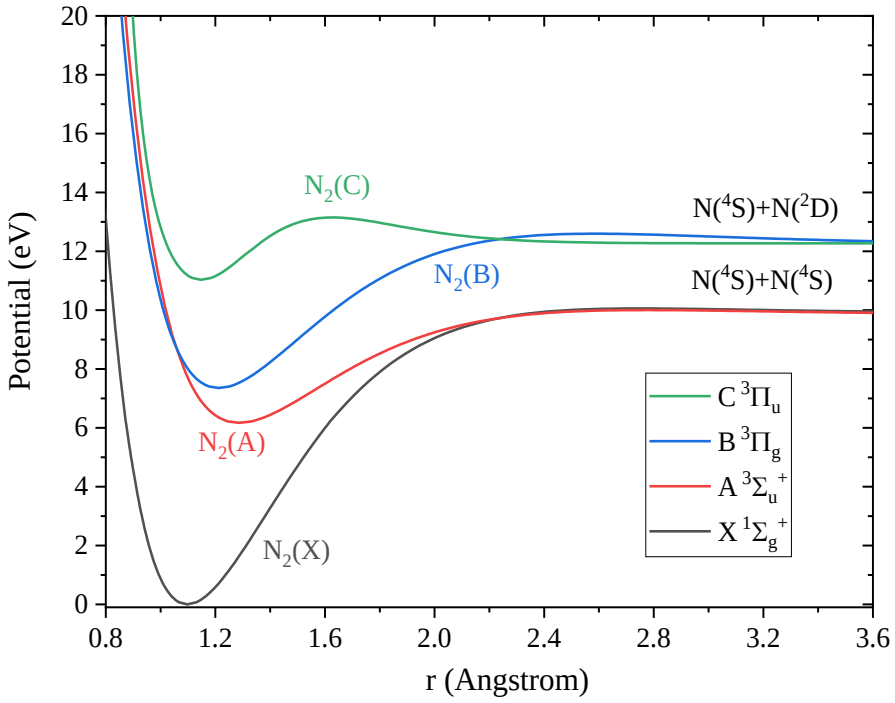

Figure 1.2 Potential curves of N_2(X, A, B, C) as a function of the radius between the two nuclei, calculated using the theory described in the work of Zare (Zare, 1964).

The separation between electronic levels is typically a few eV (1 eV = 11,605 K). This is much greater than the average translational energy of particles at 300 K. Therefore, at room temperature, only the ground state is occupied. The electronic thermal capacity, $c_{v,elec}$, is characterized by sharp increases when the temperature overcomes the energy of excited states, because $c_{v,elec}$ is a derivative of E_{elec} (see Eq. 1.17). An example considering only N_2(X) and N_2(A) is shown in Eq. 1.20.

$$c_{v,elec}(N_2) = k_b \left(\frac{72\,183\ \mathrm{K}}{T_{elec}}\right)^2 \frac{g_1}{g_0} \frac{e^{-\frac{72\,183\ \mathrm{K}}{T_{elec}}}}{\left(1 + \frac{g_1}{g_0} e^{-\frac{72\,183\ \mathrm{K}}{T_{elec}}}\right)^2} \qquad \text{Eq. 1.20}$$

1.1.4 Rotational partition function

Assuming a diatomic molecule[1] to be a rigid rotor of moment of inertia[2], I, the energy and the degeneracy of a rotational level are defined by Eq. 1.21 and Eq. 1.22:

$$\varepsilon_{rot}(J) = J(J+1)\frac{h^2}{8\pi^2 I} = J(J+1)k_b\Theta_{rot} \quad \text{Eq. 1.21}$$

$$g_{rot}(J) = 2J+1 \quad \text{Eq. 1.22}$$

The spacing between rotational levels[3] ($\Theta_{rot} = 1-10$ K) is well below the typical rotational temperatures of the plasmas produced by discharges. Therefore, ε_{rot} is a function that varies slowly with J and an integral expression can replace the sum in Eq. 1.23.

$$Z_{rot} = \sum_J (2J+1)e^{-J(J+1)\frac{\Theta_{rot}}{T_{rot}}} \approx \int e^{-J(J+1)\frac{\Theta_{rot}}{T_{rot}}}\, d[J(J+1)] = \frac{T_{rot}}{\sigma\Theta_{rot}} \quad \text{Eq. 1.23}$$

If the molecule is homonuclear, $\sigma = 2$ to account for indistinguishable states and $\sigma = 1$ for heteronuclear molecules (Alberty and Silbey, 1992).

In Figure 1.3, the distribution of the rotational populations is given for the OH molecule in the ground state. The increase of the rotational temperature flattens the population peak and shifts it to the higher rotational numbers.

---

[1] Triatomic molecules (and higher polyatomic molecules) are beyond the scope of this thesis.

[2] In classical mechanics, for two masses, m_1 and m_2, at a distance r_1 and r_2 of their center of mass, the moment of inertia is $I^{(classical)} = m_1 r_1^2 + m_2 r_2^2$.

[3] For OH, $\Theta_{rot,OH}$ = 18.91 cm^{-1} = 27 K, while N_2 is heavier and Θ_{rot,N_2} = 2.00 cm^{-1} = 2.9 K (Huber and Herzberg, 1979)

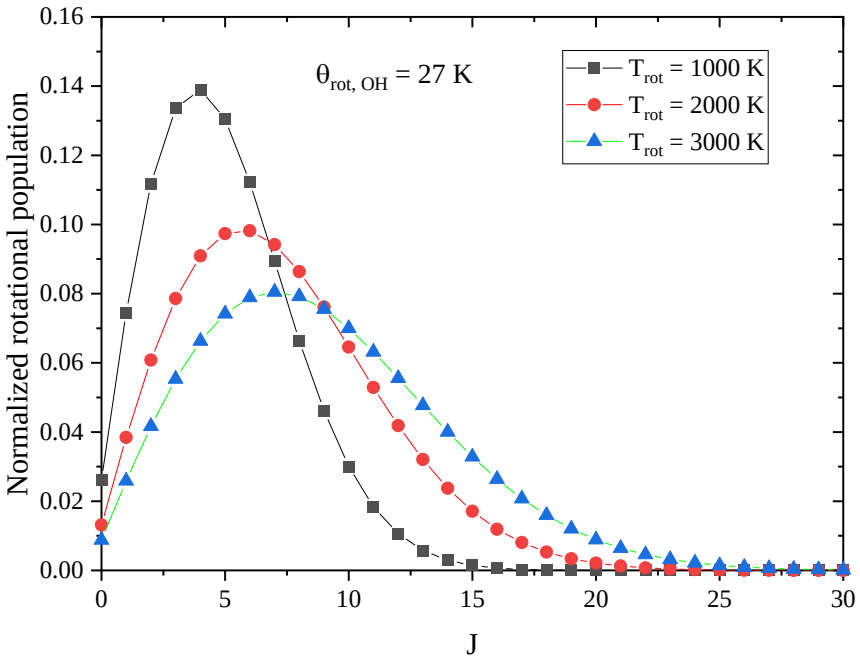

Figure 1.3 Distribution of the rotational population in the OH(X, v=0) state at T_{rot} = 1000 K, 2000 K, and 3000 K. The sum of the rotational states' population is equal to 1.

Using Eq. 1.7 and Eq. 1.23, we obtain:

$$E_{rot} = N k_b T_{rot} \qquad \text{Eq. 1.24}$$

$$\hat{c}_{v,rot} = \frac{1}{N}\frac{\partial E_{rot}}{\partial T} = \frac{2}{2}k_b \qquad \text{Eq. 1.25}$$

1.1.5 Vibrational partition function

Assuming the molecule vibration to be described by a harmonic oscillator, the energy[1] of the vibrational levels is provided in Eq. 1.26, where v is the vibrational quantum number and $h\nu = k_b\Theta_{vib}$ the energy spacing between two consecutive vibrational levels.

[1] The energy reference $E = 0$ is taken at the bottom of the electronic potential well. It is sometimes taken at the first vibrational level $v = 0$. The energy would therefore be $E_{vib}(v) = h\nu v$. Nevertheless, changing the energy reference does not change the calculation of c_v(!).

$$\varepsilon_{vib}(v) = \left(v + \frac{1}{2}\right) h\nu = \left(v + \frac{1}{2}\right) k_b \Theta_{vib} \quad \text{Eq. 1.26}$$

The degeneracy of each level is equal to 1 for a diatomic molecule. The typical energy spacing between vibrational levels is in the range $\Theta_{vib} = 3000 - 4000$ K. Thus, at room temperature, most molecules are in their ground vibrational level. The vibrational partition function is calculated in Eq. 1.27.

$$Z_{vib} = \sum_{v} \exp\left(-(v + \frac{1}{2})\frac{\Theta_{vib}}{T_{vib}}\right) \approx \frac{\exp\left(-\frac{1}{2}\frac{\Theta_{vib}}{T_{vib}}\right)}{1 - \exp\left(-\frac{\Theta_{vib}}{T_{vib}}\right)} \quad \text{Eq. 1.27}$$

It can be noted that $N_2(C)$ has only five bound vibrational levels. Thus, in the specific case of $N_2(C)$, the sum in Eq. 1.27 must be calculated up to v'=4. The vibrational levels of N_2 in multiple excited electronic states are reported in Figure 1.4.

Using Eq. 1.7, for $T_{vib} \gg \Theta_{vib,}$ we obtain:

$$E_{vib} = N k_b T_{vib} \quad \text{Eq. 1.28}$$

and we get using Eq. 1.25:

$$\hat{c}_{v,\text{vib}} = \frac{1}{N}\left|\frac{\partial E_{vib}}{\partial T}\right|_V = \frac{2}{2} k_b \quad \text{Eq. 1.29}$$

In non-equilibrium plasma discharges, the following ordering[1] is usually observed:

$$T_{trans} \leq T_{rot} \leq T_{vib} \leq T_{elec} \leq T_e \quad \text{Eq. 1.30}$$

For instance, in preheated air at 1500 K, the temperatures of NRP discharges applied at 30 kHz are T_{rot} = T_{trans} = 1500 – 3000 K and T_{vib} = 4000 K (Rusterholtz *et al.*, 2013). The electron temperature T_e is approximately 17,000 K (1.5 eV) for a voltage difference of 5 kV applied across a 4 mm gap at atmospheric pressure (Raizer, 1991). These values are typical in non-thermal nanosecond spark discharges.

[1] We emphasize the difference between T_e, the electron translational temperature, and T_{elec}, the excitation temperature of the bound electrons.

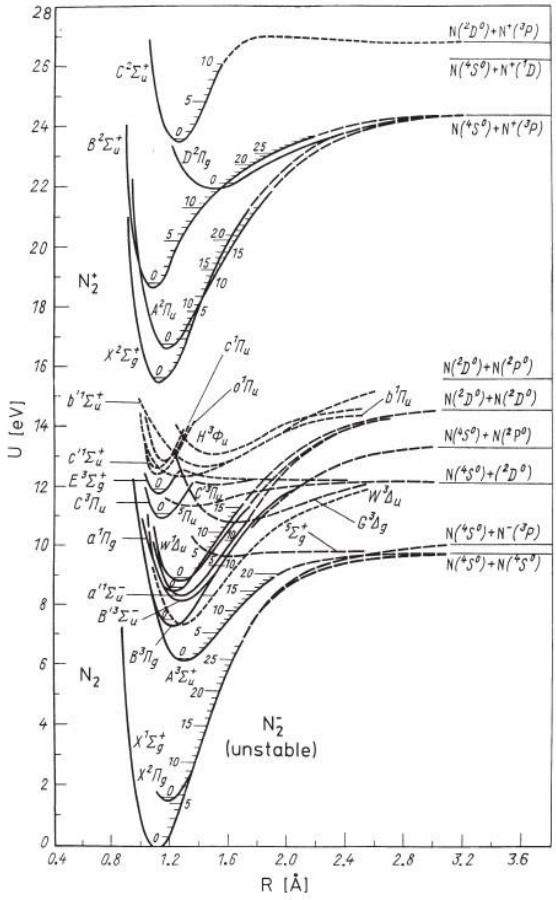

Figure 1.4 Energy diagram (Gilmore, 1965; Radzig and Smirnov, 1985, p. 370) of N_2, N_2^-, and N_2^+, including the vibrational structure of each electronic state.

1.1.6 Theorem of equipartition

According to the theorem of equipartition of energy, each quadratic term in the Hamiltonian contributes $1/2\ k_b$ to the heat capacity. In the following equations, the translational, rotational, and vibrational energies are written according to classical mechanics, where *k* is the spring stiffness, ω, the angular speed of rotation, and *I*, the moment of inertia.

$$E_{trans}^{(classical)} = \frac{1}{2}m(\dot{x}^2 + \dot{y}^2 + \dot{z}^2)$$

$$E_{vib}^{(classical)} = \frac{1}{2}m\dot{x}^2 + \frac{1}{2}kx^2$$

$$E_{rot}^{(classical)} = \frac{1}{2} I\left(\omega_x^2 + \omega_y^2\right)$$

The translational mode is always activated and contributes to $3 \times \frac{1}{2} k_b$. The heat capacity of a monoatomic gas is therefore $\frac{3}{2} k_b$. Rotation is activated above a few K and counts as $2 \times \frac{1}{2} k_b$. The heat capacity of a diatomic gas is therefore $\frac{5}{2} k_b$ for temperatures below about 2000 K. Above this threshold, vibration is activated, and the heat capacity of the gas is equal to $\frac{7}{2} k_b$.

1.1.7 Measurements of plasma temperatures: T_{rot}, T_{vib} and T_{elec}

For atoms, the population of any internal energy state *i* is given by the Boltzmann distribution relation:

$$\frac{n_i}{N} = \frac{g_i \exp\left(-\frac{\varepsilon_i}{k_b T_{elec}}\right)}{Z_{elec}} \qquad \text{Eq. 1.31}$$

For diatomic molecules, assuming $T = T_{el} = T_{vib} = T_{rot}$, the population distribution is given by Eq. 1.32 assuming $T = T_{el} = T_{vib} = T_{rot}$.

$$\frac{n_{e,v,J}}{N} = \frac{g_e(2\mathrm{J}+1) \exp\left(-\frac{\varepsilon_e + \varepsilon_{vib}(v) + \varepsilon_{rot}(J)}{k_b T}\right)}{Z_{elec} Z_{vib} Z_{rot}} \qquad \text{Eq. 1.32}$$

The intensity of spontaneous emission from an emitting *upper* level u to a *lower* level l is given in Eq. 1.33, where n_u [cm^{-3}] is the density of the upper state, A_{ul} [s^{-1}], the Einstein coefficient for spontaneous emission of the upper state, ΔE_{ul} [J], the difference of energy between the upper and lower states, Δl [cm], the length of the plasma layer, and $\phi(\lambda)$ [nm^{-1}], the normalized transition lineshape defined in Eq. 1.34.

$$I_{ul}[\mathrm{W.cm^{-2}.sr^{-1}.nm^{-1}}] = n_u \frac{A_{ul}}{4\pi} \Delta E_{ul} \phi(\lambda) \Delta \mathrm{l} \qquad \text{Eq. 1.33}$$

$$\int \phi(\lambda) \mathrm{d}\lambda = 1 \qquad \text{Eq. 1.34}$$

We assumed in Eq. 1.33 that the plasma layer is optically thin. Considering an atomic species, we take the logarithm of Eq. 1.33 and inject Eq. 1.31. We obtain Eq. 1.35 for a state *u* radiating to *l*:

$$ln\frac{I_{ul}}{g_u A_{ul}\Delta E_{ul}} = const + ln\frac{n_u}{g_u} = const - \frac{E_u}{k_b T_{elec}} \quad \text{Eq. 1.35}$$

The slope of the curve $ln\frac{I_{ul}}{g_u A_u \Delta E_{ul}}$ *versus* E_u, obtained from the intensities of several atomic lines, gives the electronic temperature. The spectroscopic parameters are available from the NIST database (Kramida *et al.*, 2018) and the line intensity I_{ul} can be precisely measured if different lines emitted by different states do not overlap. This is the case for N emitting at 740 and 742 nm for instance. In the case of N^+, the emission lines are mixed in the visible emission spectrum. The most intense lines of N^+ at 500 nm are reported in Table 1.1. Eight different lines, from three different levels, overlap in a 2 nm spectral range. At electron number densities above 10^{16} cm^{-3}, the Stark broadening (see Section 1.3) of these lines enhances the mixing effect. Therefore, in this work, the method of the Boltzmann plot will not be used to determine T_e, despite previous attempts having been made (Orriere, Moreau and Pai, 2018). Here, we will assume that the electronic level populations of any atom follow a Boltzmann distribution. The Specair code (Laux, 2002; Laux *et al.*, 2003) will be used to calculate the population of each state, and the corresponding emission intensity.

The Boltzmann plot method can also be performed for rotational and vibrational levels, see for example (Bruggeman *et al.*, 2014). However, the method of spectral fitting was preferred in this thesis because it better accounts for overlapping lines. The spectral fitting can be used as well to get the radiating species density if the spectrum intensity is absolutely calibrated.

Table 1.1 Principal lines of N^+ (NII) from the NIST database (Kramida *et al.*, 2018). The typical spacing between these intense lines is below 1 nm. Other lines between 499.4360 and 502.5659 nm are listed in the NIST database but are weaker.

λ (nm)	A (s^{-1})	E_l (eV)	E_u (eV)	Configuration, Term
499.4360	2.62e+07	25.497873	27.979665	$2s2p^2(4P)3p\ ^5P^0$
500.1474	1.04e+08	20.653591	23.131853	$2s^22p3d\ 3F°$
500.2703	8.33e+06	18.462312	20.939965	$2s^22p3p\ 3S$
500.5150	1.14e+08	20.665517	23.141959	$2s^22p3d\ 3F°$
500.7328	7.43e+07	20.939965	23.415329	$2s^22p3d\ 3P°$
501.0621	2.10e+07	18.466227	20.939965	$2s^22p3p\ 3S$
501.6381	1.59e+07	20.653591	23.124489	$2s^22p3d\ 3F°$
502.5659	1.04e+07	20.665517	23.131853	$2s^22p3d\ 3F°$

1.2 Measurements of the plasma translational temperature: T_{trans}

The results of this section are used notably in Section 8.5.

The translational temperature of a plasma can be measured by OES via Doppler broadening. The Doppler broadening of atomic lines will be described in Section 1.3. This broadening is typically much smaller than the instrumental broadening for the conditions of this thesis and, thus, cannot be used to measure T_{trans}. In LTE plasmas, the electronic, vibrational, and rotational distributions follow distributions at the translational temperature. In non-equilibrium plasmas, this is not the case. The rotational temperature is usually the closest to the translational temperature, Eq. 1.30. The objective of this section is to determine the conditions under which $T_{trans} = T_{rot}$, following the recommendations of (Bruggeman *et al.*, 2014). We start by discussing rotational-translational (RT) relaxation, which drives the equilibration between the rotational and translational modes. Then, we examine the rates of the main reactions populating and depopulating the N_2 excited states in air and CH_4/air mixtures. Finally, we compare the RT and populating/depleting rates to infer the conditions under which the measured OES rotational temperatures are representative of the gas temperature.

1.2.1 Thermalization of the rotational distribution: models

How long will it take for a set of given molecules initially in a given rotational distribution to thermalize with the translational distribution? To answer this question, Parker introduced the rotational-translational relaxation time τ_{RT} (Parker, 1959) which is expressed in Eq. 1.36,

$$\tau_{RT} = Z_{RT}\tau_0 \qquad \text{Eq. 1.36}$$

where Z_{RT}, the number of collisions needed for thermalization, is a function of T_{trans} and the gas composition, and τ_0, the average time between collisions defined in (Laux, 1993).

$$\tau_0[\mathrm{s}] = \frac{\sqrt{T[K]/300}}{10^{10}P[atm]}. \qquad \text{Eq. 1.37}$$

In his model, Parker assumed that no energy is initially stored in the rotational mode (T_{rot}^0 = 0 K) and that the molecules are in a thermostat (i.e. $T_{trans} = const$). Z_{RT} is found to increase with the temperature of the translational thermostat, T_{trans}, and this result is in agreement with experimental data gathered in (Brau and Jonkman, 1970; Capitelli *et al.*, 2017), see Figure 1.5.

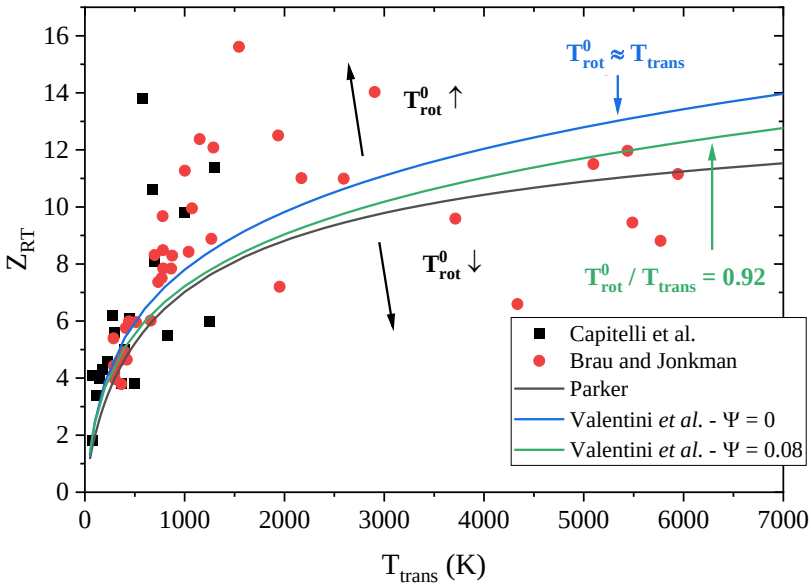

Figure 1.5 Number of collisions needed for a nitrogen molecule to equilibrate its translational and rotational temperatures. The theory of Parker (grey solid line) agrees with the data gathered by Capitelli *et al.* or Bran and Jonkman. The theory of Valentini *et al.* is shown for Ψ = 0 (blue solid line). A calculation is also shown for the nascent rotational distribution of N_2(C) after electron impact, which corresponds to Ψ = 0.08 (green solid line).

Valentini *et al.* calculated the translation-rotational relaxation time of nitrogen with Molecular Dynamics (MD) simulations and Direct Simulation Monte Carlo (DSMC) (Valentini *et al.*, 2014). The initial translation and rotational states are distributed at given initial temperatures. In this case, the translational temperature is also constant (translational thermostat). Parker already showed that Z_{RT} increases with T_{trans} (Parker, 1959). Valentini *et al.* demonstrated that Z_{RT} is also a function of the initial rotational temperature, T_{rot}, via the Ψ function defined in Eq. 1.38.

$$\Psi = 1 - \frac{T_{rot}(t=0)}{T_{trans}} \qquad \text{Eq. 1.38}$$

It was shown by Valentini and co-authors that the relaxation time is longer for Ψ < 0 than for Ψ > 0, i.e. the relaxation time is longer for higher $T_{rot}(0)$ as illustrated in Figure 1.5. At Ψ ≈ 0 (i.e. $T_{rot}(0) \approx T_{trans}$), the calculation shows good agreement with the experimental data. In typical nanosecond discharge experiments (Pai, Lacoste and Laux, 2010b; Rusterholtz *et al.*, 2013), N_2(C) is populated by electron-impact excitation of N_2(X) and the nascent rotational temperature of N_2(C) is equal to $T^0_{rot} = 0.92\, T_{trans}$ (see Section 1.2.3).

At $\Psi = 0.08$, $Z_{RT}(\Psi = 0.08)$ is between $Z_{RT}(\Psi \approx 0)$ and the result of Parker[1]. We calculate the corresponding relaxation times by applying Eq. 1.37 and we compare them to experimental references in Figure 1.6. We also show, for comparison, the relaxation time calculated by Panesi *et al.* for temperatures above 5000 K (Panesi *et al.*, 2013). All the RT relaxation times are close in Figure 1.6. Therefore, both theories of Parker and Valentini *et al.* can be used in this work.

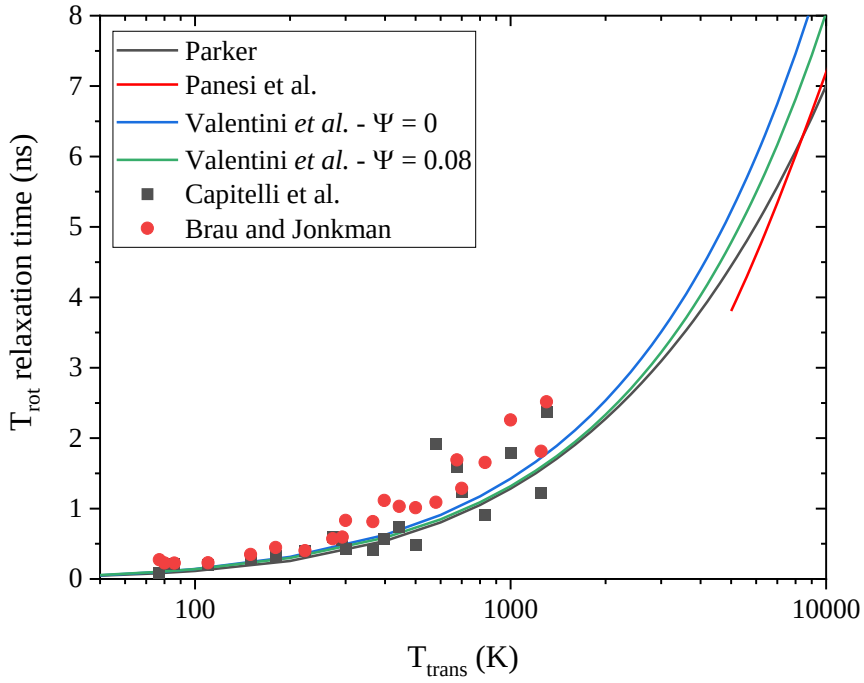

Figure 1.6 Variation of the rotational - translational relaxation time. The Z_{RT} of Figure 1.5 values are converted using Eq. 1.37. The theoretical calculations of Panesi *et al.* are also shown (red solid line).

1.2.2 Effective lifetime

If the effective lifetime of the emitting species is shorter than the relaxation time, $\tau_{eff} < \tau_{RT}$, the rotational distribution will not thermalize with the translational distribution before the probed species is depleted. For instance, it was shown that the rotational temperature of $N_2^+(B)$ was not representative of the gas temperature

[1] We compared a simulation at $\Psi = 1$, which corresponds to $T_{rot}(0) = 0$. This calculation does not match the result of Parker, although it corresponds to Parker's initial condition (Parker, 1959). The origin of this difference is unknown and beyond the scope of this thesis.

in a recombining plasma at the exit of a 15-cm long recombination tube (Tibère-inglesse, 2019, chap. 4). In this specific case, $\tau_{eff} \approx 2$ ns was below $\tau_{RT} \approx 3$ ns (Parker model).

Eq. 1.39 gives the net rate of formation of the radiating molecule, where N_{rad} is the density of the radiating molecule, N_i the density of the colliders, K_i the source terms of N_{rad}, A_i the total[1] Einstein coefficient of N_{rad} (inverse of the lifetime in vacuum) and, k_{Qi} the quenching rate of N_{rad}.

$$\frac{d}{dt}N_{rad} = \sum K_i - A_i N_{rad} - \sum k_{Qi} N_i N_{rad} \qquad \text{Eq. 1.39}$$

The effective lifetime of the radiating species, Eq. 1.40, corresponds to the characteristic time of an exponential decay were the production pathways to be suddenly terminated.

$$\tau_{eff} = \frac{1}{A_i + \sum k_{Qi} N_i} = \frac{1}{1/\tau_{rad} + 1/\tau_{quen}} \qquad \text{Eq. 1.40}$$

In nanosecond discharges, the rotational temperatures of N_2(C) and N_2(B) are typically used to determine T_{trans}. The radiative lifetimes of N_2(C) and N_2(B) are 39.3 ns (Valk *et al.*, 2010) and 4 – 8 µs, respectively (Bruggeman *et al.*, 2014). At atmospheric pressure, τ_{eff} is usually dominated by the quenching term. The N_2(C) and N_2(B) rates of collisional quenching in air and combustible mixtures are discussed below and summarized in Table 1.2.

The quenching rate coefficients of N_2(C) by N_2, O_2, CO_2, and H_2O were measured by Albugues *et al.* (Albugues *et al.*, 1974), who gave values for the (0,0) and (0,1) vibrational bands that differ at most by 10%. Only the values of the (0,0) band are shown in Table 1.2. The quenching of four vibrational levels of N_2(C) by N_2, O_2, H_2O, and H_2 was also investigated[2] in (Pancheshnyi, Starikovskaia and Starikovskii, 2000) and compares well with the work of Albugues *et al.* However, in (Morozov *et al.*, 2005), the rate coefficient of

[1] This effective Einstein coefficient is summed on all the allowed transitions.

[2] This study, performed in 2000, follows a study conducted in 1998 by the same authors (Pancheshnyi, Starikovskaia and Starikovskii, 1998). We took the most recent values of Pancheshnyi *et al.* Note however that the quenching rate coefficients of N_2^+(B) can be found in (Pancheshnyi, Starikovskaia and Starikovskii, 1998).

$N_2(C)$ quenching by H_2O is twice higher than the rate coefficient measured by Albugues *et al.* and Pancheshnyi *et al.* According to Morozov *et al.*, the difference is due to the uncertainty on the H_2O concentration in the experiments of Albugues *et al.* and Pancheshnyi *et al.*

The quenching rate coefficient of $N_2(C)$ by N_2 is reported in the work of Dilecce *et al.* (Dilecce, Ambrico and De Benedictis, 2007). Valk *et al.* (Valk *et al.*, 2010) averaged the quenching rate coefficients of $N_2(C)$ by N_2 from 17 references, including their own measurements. They found a value identical to that of Dilecce *et al.* The quenching rate coefficient of $N_2(C)$ by O_2 measured by Valk *et al.* coincides with the average values of other references. It was shown (Rusterholtz *et al.*, 2013) that the quenching rate coefficient of $N_2(C)$ by O_2 varies with $T_{gas}^{0.3}$ in the range 300-2000 K. For H_2O, the value reported in (Albugues *et al.*, 1974) will be used since they obtain the same O_2 quenching rate as Valk *et al.*

For atomic oxygen, (Shkurenkov *et al.*, 2014) successfully described the formation of NO following a nanosecond discharge by the quenching of N_2 excited states, using a gas-kinetic[1] rate $k_{kin} = 3.0\times10^{-10}$ cm^3s^{-1} for Reac. 1.1.

$$N_2\left(B^3\Pi_g, C^3\Pi_u\right) + O(^3\mathrm{P}) \rightleftharpoons \mathrm{NO}(\mathrm{X}^2\Pi_\mathrm{r}) + \mathrm{N}(^4S) \qquad \text{Reac. 1.1}$$

This result is surprising because $N_2(A)$ is known to react with $O(^3P)$ according to Reac. 1.2 with a rate 10 times lower, 3.0×10^{-11} cm^3s^{-1} (Piper, 1982; Thomas and Kaufman, 1996).

$$N_2(A^3\Sigma_u^+\ v \leq 2\ ) + O(^3\mathrm{P}) \rightleftharpoons \mathrm{O}(^1\mathrm{S}) + \mathrm{N}_2(X^1\Sigma_g^+) \qquad \text{Reac. 1.2}$$

[1] The k_{kin} rate is the kinetic rate of collision between two particles assuming they are hard spheres. It can be easily obtained using the following equation, with r_A and r_B the radius of the colliding particles, μ_{AB} the reduced mass of the colliders, k_b the Boltzmann constant, and T the temperature.

$$k_{kin} = \pi(r_A + r_B)^2 \sqrt{\frac{8k_bT}{\pi\mu_{AB}}}$$

If each collision between quenchers and excited particles is effective, then the quenching rate coefficient should be equal to k_{kin}. The kinetic rate is considered as an upper bound of the quenching rate coefficient, which is reached by many quenchers (Piper, 1987) and is sometimes overreached (see Table 1.2).

However, for $N_2(A, v > 2)$, more than 60% of the $N_2(A)$ quenching by $O(^3P)$ will form NO molecules (Thomas and Kaufman, 1996). The quenching of $N_2(B)$ and $N_2(C)$ by atomic oxygen was not considered in the early mechanism of Popov (Popov, 2001, 2011a). After inclusion of Reac. 1.2 in his latest mechanism, Popov obtained better agreement with the experimental temperature increase obtained after a nanosecond pulse in preheated air (Rusterholtz *et al.*, 2013; Popov, 2016a, fig. 13).

The quenching rate of $N_2(B)$ by N_2 used by Popov (Popov, 2009a) is taken from other numerical investigations. The rate of $N_2(B)$ quenching by N_2 used by Kossyi *et al.* is higher, 5.0×10^{-11} $cm^3.s^{-1}$, than the other values reported in Table 1.2. The quenching rate coefficient of $N_2(B)$ by N_2 and O_2 was measured in (Young, Black and Slanger, 1969). The quenching rate coefficient of $N_2(B)$ by O_2 was found to be constant in the range 300 – 2200 K (Rusterholtz *et al.*, 2013). More recently, Piper (Piper, 1992) measured the quenching rates of $N_2(B)$ by CO_2, CH_4, N_2, and O_2. Piper's values correspond to those of Young (N_2 and O_2) and will be selected in the following calculations, because they cover the broadest range of molecules. The quenching of $N_2(B)$ by CO_2 was also measured by (Campbell and Thrush, 1966) at 196 K. They suggested that this quenching induces the dissociation of CO_2 as in Reac. 1.3.

$$N_2(B) + CO_2 \rightleftharpoons N_2 + CO + O \qquad \text{Reac. 1.3}$$

Using the bold values of Table 1.2, we compare τ_{eff} and τ_{RT} in Table 1.3. To our knowledge, the quenching rate of $N_2(B)$ by H_2O is unknown (missing in Table 1.2). For this application, we assume it to be equal to 4×10^{-10} cm^3s^{-1}, the quenching coefficient rate of $N_2(C)$. The variation of the quenching rates with the temperature is neglected, except for $N_2(C)$ quenched by O_2. The following three cases are studied:

- Air: N_2 (79%) / O_2 (21%)
- Stoichiometric methane-air flame before ignition: N_2 (71.5%) / O_2 (19%) / CH_4 (9.5%)
- Stoichiometric methane-air flame after complete combustion: N_2 (71.5%) / H_2O (19%) / CO_2 (9.5%)

Table 1.2 Collisional quenching rate coefficients of $N_2(B)$ and $N_2(C)$, at 300 K if not specified. Values reported in (Valk *et al.*, 2010) are averaged on several references, removing outliers. The bold values are used later in the calculations of the effective lifetime. When they are differentiated in the references, only the value of $N_2(C, v=0)$ band is reported.

Quencher	$N_2(B)$		$N_2(C)$	
	Rate coef. ($cm^3 \cdot s^{-1}$)	Reference	Rate coef. ($cm^3 \cdot s^{-1}$)	Reference
N_2	**3×10^{-11}**	(Piper, 1992)	**1.1×10^{-11}**	(Dilecce, Ambrico and De Benedictis, 2007; Valk *et al.*, 2010)
	2.7×10^{-11}	(Young, Black and Slanger, 1969)		
	5.0×10^{-11}	(Kossyi *et al.*, 1992)		
	1.0×10^{-11}	(Popov, 2009a, 2016a)		
O_2	2.7×10^{-10}	(Rusterholtz *et al.*, 2013) at 2200 K	3.0×10^{-10}	(Pancheshnyi, Starikovskaia and Starikovskii, 2000)
	1.1×10^{-10}	(Young, Black and Slanger, 1969)	2.7×10^{-10}	(Albugues *et al.*, 1974; Valk *et al.*, 2010)
	3.0×10^{-10}	(Kossyi *et al.*, 1992; Popov, 2009a)	5.8×10^{-10}	(Rusterholtz *et al.*, 2013) at 2200 K
	2×10^{-10}	(Piper, 1992)		
H_2O			3.9×10^{-10}	(Pancheshnyi, Starikovskaia and Starikovskii, 2000)
			4.2×10^{-10}	(Albugues *et al.*, 1974)
			7.1×10^{-10}	(Morozov *et al.*, 2005)
H_2	2.5×10^{-11}	(Popov, 2008)	3.3×10^{-10}	(Pancheshnyi, Starikovskaia and Starikovskii, 2000)
	5×10^{-11}	(Piper, 1992)		
CO_2	**2×10^{-10}**	(Piper, 1992)	**3.5×10^{-10}**	(Albugues *et al.*, 1974)
	8.5×10^{-11}	(Campbell and Thrush, 1966) at 196 K		
	1.5×10^{-10}	(Young, Black and Slanger, 1969)		
CH_4	**3×10^{-10}**	(Piper, 1992)	**5.7×10^{-10}**	(Albugues *et al.*, 1974)
Ar			3.0×10^{-13}	(Bruggeman *et al.*, 2014)
O	3.0×10^{-10}	(Shkurenkov *et al.*, 2014)	3.0×10^{-10}	(Shkurenkov *et al.*, 2014)
CO	8.5×10^{-11}	(Young, Black and Slanger, 1969)		

Table 1.3 Comparison of the rotational-translational relaxation time and the effective lifetime of N_2(B) and N_2(C). The quenching rates are assumed to be constant with temperature, except the quenching of N_2(C) by O_2, which varies with $T^{0.3}$. The rotational-translational relaxation time is taken from (Valentini *et al.*, 2014).

Gas mixture (1 atm)	N_2(B)			N_2(C)			
	τ_{rad}	τ_{quen}	τ_{eff}	τ_{rad}	τ_{quen}	τ_{eff}	τ_{RT}
Air 300 K	4 – 8 μs	0.6 ns	0.6 ns	39.3 ns	0.6 ns	0.6 ns	0.5 ns
Air 3000 K	4 – 8 μs	6.2 ns	6.2 ns	39.3 ns	3.1 ns	2.8 ns	3.5 ns
CH_4 / O_2 / N_2 2000 K - ϕ = 1	4 – 8 μs	3.1 ns	3.1 ns	39.3 ns	1.7 ns	1.6 ns	2.6 ns
CO_2 / H_2O / N_2 2000 K - ϕ = 1	4 – 8 μs	2.3 ns	2.3 ns	39.3 ns	2.3 ns	2.2 ns	2.6 ns

In pure air, the effective lifetime of N_2(B) is below the RT time calculated by Valentini *et al.* at high temperature. Otherwise, the effective lifetimes of N_2(B) and N_2(C) are similar or below the RT time. Therefore, at this point in the analysis, it should be expected that $T_{trans} \neq T_{rot}$.

The variations of τ_{eff} and τ_{RT} with temperature are shown in Figure 1.7. The assumptions of the calculations performed in Figure 1.7 are summarized here:

- The air composition is assumed to be constant up to 3000 K. It was shown that for constant pressure or constant volume processes, the NO and O mole fractions were below 10% (Sher, Ben-Ya'ish and Kravchik, 1992).
- The quenching rate of N_2(B) by H_2O is assumed to be equal to that of N_2(C): 4×10^{-10} $cm^{-3}.s^{-1}$. This assumption is justified considering the relative values of N_2(C) and N_2(B) quenching by CO_2, CH_4, N_2 and O_2
- We neglect the impact of electron quenching, known to affect N_2(C) effective lifetime in recombining plasmas (Lepikhin *et al.*, 2016), because this effect strongly depends on the Electron Energy Distribution Function, which in turn is related to the gas composition. The rate coefficient of electron quenching derived by Lepikhin *et al.* is therefore not supposed to apply here.
- The rotational-translational relaxation rate, τ_{RT} is calculated for N_2(X) colliding with N_2(X). We assume that τ_{RT} is identical for N_2 excited states.

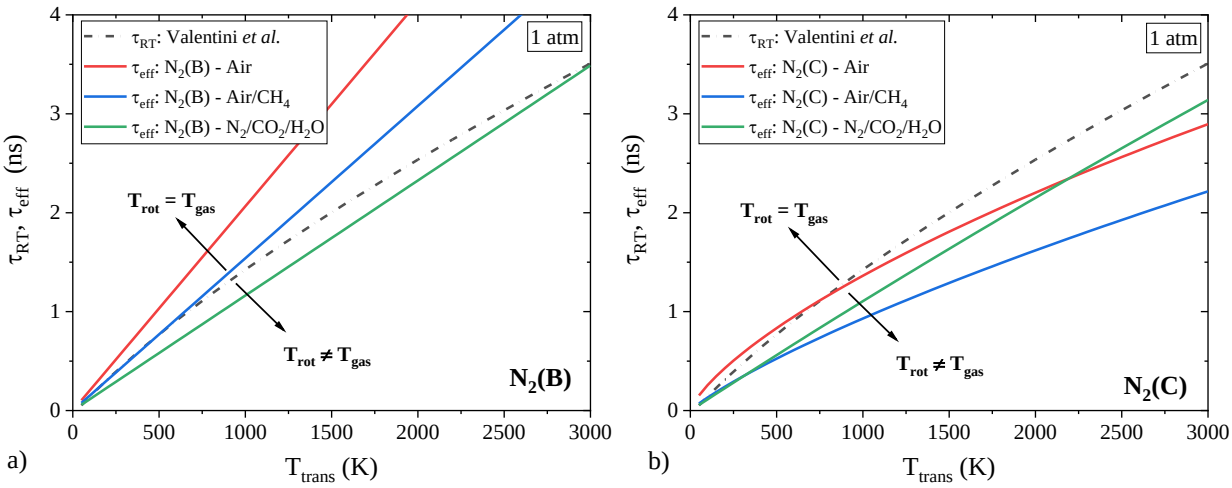

Figure 1.7 Comparison between RT relaxation time and effective lifetime at atmospheric pressure of (a) N_2(B), and (b) N_2(C) in air, in a stochiometric air-CH_4 mixture, and in a stochiometric air-CO_2-H_2O mixture.

For N_2(B) in pure air, we have $\tau_{eff} > 2\ \tau_{RT}$, see Figure 1.7a). With the approximations of these estimations, the rotational distribution of N_2(B) can thus be expected to be representative of the gas temperature in air and burnt mixtures. For a CH_4 – air unburned mixture, RT relaxation may not be achieved. N_2(C) emission is usually more intense than N_2(B), hence more accessible for OES. However, for N_2(C), RT relaxation is not achieved in the three mixtures (Figure 1.7 b) and *a priori* $T_{rot} \neq T_{trans}$.

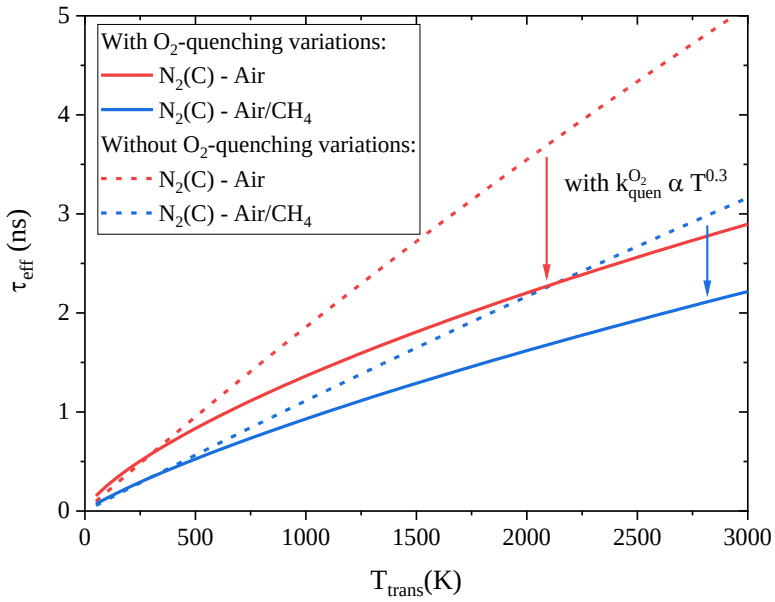

Figure 1.8 Variation of the effective lifetime in air (red curves) and stoichiometric CH_4/air mixtures (blue curve). The dashed lines are the calculations with the O_2 quenching rate assumed constant $k = 3.0 \times 10^{10} cm^{-3} s^{-1}$ whereas the full solid lines take the $T^{0.3}$ variation into account.

It should be noted that the presence of oxygen drastically reduces the τ_{eff} of $N_2(C)$ below τ_{RT}. If the temperature variation of $N_2(C)$ quenching by O_2 is not taken into account, τ_{eff} will be underestimated by a factor of 2 in air and 1.5 in air/CH_4, see Figure 1.8.

1.2.3 Population mechanism

If the rotational distribution is not relaxed under the experimental conditions, it is still possible to relate T_{rot} and T_{trans} under certain assumptions. In a reduced field E/N > 80 – 100 Td, $N_2(C)$ is principally populated by electron impact of $N_2(X)$ as in Reac. 1.4 (Popov, 2011b).

$$N_2(X) + e \rightarrow N_2(C) + e \qquad \text{Reac. 1.4}$$

The $N_2(X)$ rotational distribution is thermalized with the gas temperature. Reac. 1.4 maps the rotational distribution of $N_2(X)$ into $N_2(C)$ (Rusterholtz *et al.*, 2013; Bruggeman *et al.*, 2014). The two rotational temperatures are then related by the relation in Eq. 1.41, where Θ_{rot} is the characteristic temperature of the rotational distribution (Rusterholtz *et al.*, 2013):

$$\frac{T_{rot}^{C}}{T_{rot}^{X}} = \frac{\Theta_{rot}^{C}}{\Theta_{rot}^{X}} \qquad \text{Eq. 1.41}$$

The values of Θ_{rot} are calculated in Table 1.4 for a few states of N_2. The rotational constants are taken from (Huber and Herzberg, 1979; Laux, 1993). The correction factors for electronic transitions between five states are also calculated. For E/N in the 20 – 100 Td range, Popov (Popov, 2011b) estimated the primary production mechanism of N_2(C) as being caused by electronic excitation of N_2(B) via Reac. 1.6.

$$N_2(X) + e \rightarrow N_2(B) + e \qquad \text{Reac. 1.5}$$

$$N_2(B) + e \rightarrow N_2(C) + e \qquad \text{Reac. 1.6}$$

If N_2(C) is produced by Reac. 1.5 and Reac. 1.6, and because the rotational distribution of N_2(B) is frozen during the process, the gas temperature can be obtained as in Eq. 1.41 since Θ_{rot}^{B} cancels out:

$$T_{gas} = T_{rot}^{X} = \frac{\Theta_{rot}^{X}}{\Theta_{rot}^{B}} \frac{\Theta_{rot}^{B}}{\Theta_{rot}^{C}} T_{rot}^{C} \qquad \text{Eq. 1.42}$$

It was shown by Popov that the electron excitation of N_2(a') does not contribute significantly to the population of N_2(C) due to a small cross-section compared to that of Reac. 1.6.

Table 1.4 T_0 is the classical notation for the term energy of v=0, B_e is the rotational constant, and Θ_{rot}^{el} the characteristic temperatures of N_2(X,A,B,C,a'). Note that Θ_{rot}^{el} is proportional to B_e. The B_e values are taken from (Huber and Herzberg, 1979) but can also be found on the NIST website.

State	T_0 (cm^{-1})	T_0 (eV)	B_e (cm^{-1})	Θ_{rot}^{el} (K)	$\Theta_{rot}^{X}/\Theta_{rot}^{el}$	$\Theta_{rot}^{A}/\Theta_{rot}^{el}$	$\Theta_{rot}^{B}/\Theta_{rot}^{el}$
$N_2(X\ ^1\Sigma_g^+)$	0	0	1.998 24	2.9	1	-	-
$N_2(A\ ^3\Sigma_u^+)$	50 203.66	6.22	1.454 6	2.1	1.37	1	-
$N_2(B\ ^3\Pi_g)$	59 619.09	7.39	1.637 4	2.4	1.22	0.89	1
$N_2(a'\ ^1\Sigma_u^-)$	68 152.56	8.45	1.479 9	2.1	1.35	0.98	1.11
$N_2(C\ ^3\Pi_u)$	89 136.88	11.05	1.824 7	2.6	1.10	0.80	0.90

For E/N < 20 Td, N_2(C) is principally produced by metastable excitation (Popov, 2011b; Bruggeman *et al.*, 2014), Reac. 1.7.

$$N_2(A) + N_2(A) \rightarrow N_2(C) + N_2(X) \qquad \text{Reac. 1.7}$$

In this case, the nascent rotational temperature will be far from T_{trans}, and it is necessary to have strong RT relaxation to determine the gas temperature by N_2 OES.

In the following section, OES of the second positive system of N_2 is used to determine the temperature of ambient air at the exit of a heater. The results are compared with the measurements of a thermocouple and Rayleigh scattering.

1.2.4 Rayleigh scattering

We briefly present the Rayleigh scattering technique. This laser diagnostic is only used in this thesis to assess the results obtained by OES. Such a comparison was already performed in (Verreycken *et al.*, 2011) in a DC glow discharge above a water electrode. Verreycken *et al.* showed that the rotational temperature of $N_2(C)$ was close (± 10%) to the gas temperature, whereas the OH(A) rotational temperature was significantly higher.

The Rayleigh elastic scattering intensity, $I_{Rayleigh}$, is proportional to the intensity of the laser beam, I_{Laser}, the gas density, n_{tot}, and the total cross-section of the gas, σ_R:

$$\mathrm{I_{Rayleigh}} \propto \mathrm{I_{Laser} n_{tot} \sigma_R} \qquad \text{Eq. 1.43}$$

The total Rayleigh cross-section of the gas depends on the cross-section of each gas component, $\sigma_{R,i}$, and its mole fraction, x_i. The evaluation of the total cross-section is particularly challenging in combustible mixtures because the gas composition is usually not known with accuracy. The dimensionless cross-section and the Rayleigh scattering intensity are calculated in Eq. 1.44 and Eq. 1.45, respectively:

$$\hat{\sigma} = \frac{\sigma_R}{\sigma_0} = \frac{\sum x_i \sigma_{R,i}}{\left(\sum x_i \sigma_{R,i}\right)_0} \qquad \text{Eq. 1.44}$$

$$\hat{I} = \frac{\hat{\sigma}}{\hat{T}} \qquad \text{Eq. 1.45}$$

Assuming uniform pressure, $\hat{I}$ directly depends on the dimensionless temperature $\hat{T} = T/300\ K$. The cross-section of air or combustion gases varies by less than 8% from 300 to 1500 K and is independent on the wavelength except in the UV (Sutton and Driscoll, 2004).

We applied this technique to measure the temperature 1 cm above the outlet of an air heater (temperature ranging from room temperature to 1000 K). The x-axis of Figure 1.9 is the temperature measured with a thermocouple placed 1 cm before the exit of the air heater, and used as a reference. In Figure 1.9, the temperature from Rayleigh scattering is compared with the temperature of a thermocouple placed at the same location. No significant difference is observed.

A third technique, based on the use of NRP-corona (Pai, Lacoste and Laux, 2010b) generated at the same position, is used to measure the rotational temperature of $N_2(C)$ using the N_2 second positive system. The NRP-corona is chosen since this discharge is known to not increase the gas temperature (Pai *et al.*, 2009). The rotational temperature of $N_2(C)$ agrees with the gas temperature with an offset of +50 K. This offset is relatively constant in the studied range, albeit small in relative to the error bars.

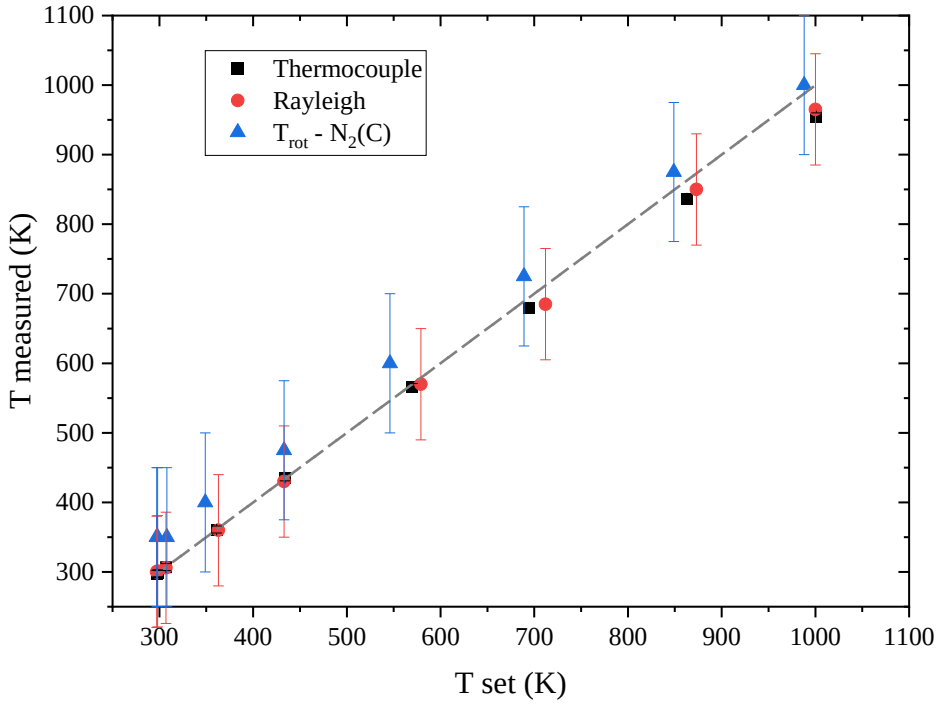

Figure 1.9 Comparison of three temperature measurement[1] techniques in preheated air from 300 to 1000 K. The temperature from Rayleigh scattering and the thermocouple are consistent. The temperatures obtained with the rotational structure of $N_2(C)$ agree with the other measurements with an offset of 50 K (inside the fitting error bar of 100 K).

In this OES measurement, $\tau_{RT} \approx \tau_{eff}$ and it is not clear if RT thermalization happened. If we consider that RT thermalization is not reached, the rotational temperature of $N_2(C)$ must be multiplied by the ratio of the $N_2(C)$ and $N_2(X)$ rotational constants, as described in Section 1.2. The systematic difference would be of

[1] These data were obtained with the assistance of Julien Lambert (visiting Ph.D. student from McGill University) during his stay at EM2C laboratory.

+100 K, but the gas temperature measurements by OES would remain inside the error bars. These results validate the use of OES spectroscopy for temperature measurements throughout this thesis.

1.2.5 Conclusion on gas temperature measurements

The rotational distribution of an excited species depends on two processes: (i) the rotational-translational relaxation and (ii) the population/depletion mechanism. For $N_2(C)$ and $N_2(B)$ in air and methane-air mixtures, the RT relaxation time is close to their effective lifetime. Thus, we cannot rigorously state whether the rotational-translational equilibrium is reached. However, in nanosecond discharges, the reduced field is typically well above 20 Td and N_2 excited states are primarily populated by electron impact of $N_2(X)$. This process maps the rotational population of $N_2(X)$. Thus, the gas temperature can be determined from the rotational temperature of these excited states. For $N_2(C)$, if we consider a partial RT relaxation, the inequality $T_{rot} < T_{gas} < 1.1\ T_{rot}$ gives a reasonable estimate of the gas temperature.

1.3 Atomic line broadening

The results of this section are used notably in Sections 4.3, 6.2.1, and 8.4

In OES, the lineshape of the observed atomic or ionic lines is due to natural, Van der Waals, Stark, resonant (Lorentzian profile) and Doppler (Gaussian profile) broadening mechanisms. The instrumental function of the spectrometer must also be considered. In this thesis, self-absorption is negligible and has no impact on the linewidth. In Sections 4.3, the Stark broadening widths of O^+ (at 490 nm), N^+ (at 500 nm) and H_α will be used to determine the electron number density. Therefore, it is essential to discuss the broadening mechanisms of these various lines. The broadening widths of H_α, O^+, and N^+ lines are calculated following the methods of (Griem, 1964; Laux *et al.*, 2003). We also performed these calculations for H_β, O (at 777nm), and N (at 746 nm). **The term "width" will refer to the Half-Width at Half-Maximum (HWHM).** In the following, the expressions and data necessary to determine the broadening widths are presented. Most of the calculations presented in this section were presented in (Minesi, Stepanyan, *et al.*, 2020).

1.3.1 Natural broadening

Natural broadening is due to the uncertainty on the energy of the two states of the transition and can be calculated using Eq. 1.46 where λ_{ul} is the transition wavelength, A_{un} and A_{ln} the Einstein coefficients of

the transition from level *u* and *l*, respectively, and *c* the light speed. This broadening is negligible and is not considered further here.

$$\Delta\lambda_{Natural} = \frac{{\lambda_{ul}}^2}{4\pi c}\left(\sum_{n<u} A_{un} + \sum_{n<l} A_{ln}\right) \qquad \text{Eq. 1.46}$$

1.3.2 Doppler broadening

Doppler broadening is due to the velocity distribution of emitters and can be obtained from Eq. 1.47 (Griem, 1964), where T_{gas} is the translational temperature and *M* the molar mass of the emitter:

$$\Delta\lambda_{Doppler}[\text{nm}] = 3.58 \times 10^{-7}\, \lambda_{ul}[\text{nm}] \sqrt{\frac{T_{gas}\,[K]}{M\,[g.mol^{-1}]}} \qquad \text{Eq. 1.47}$$

1.3.3 Van der Waals broadening

Van der Waals broadening is due to collisions between the emitter and other gas particles[1] (Griem, 1964, 1997; Laux *et al.*, 2003). The Van der Waals broadening HWHM can be calculated using Eq. 1.48 (Griem, 1964):

$$\Delta\lambda_{Van\ der\ Waals} = 0.98\, \frac{\lambda_{ul}^2}{2c} \left(\frac{9\pi\hbar^5\overline{R^2}}{16 m_e^3}\right)^{\frac{2}{5}} \left(\frac{8kT_{gas}}{\pi}\right)^{\frac{3}{10}} \sum_{perturbers} \left[\frac{N_{perturbers}}{E_p^{\frac{4}{5}} m_{rp}^{\frac{3}{10}}}\right] \qquad \text{Eq. 1.48}$$

where m_e is the electron mass, *k* the Boltzmann constant, $\hbar$ the Planck constant divided by 2π, and $N_{perturbers}$ the number density of the perturbers. The values of $E_p^{0.8} m_{rp}^{0.3}$ for the main perturbers (O, N, O^+, N^+ in the present work) are given in Table 1.5, m_{rp} being the reduced mass of the perturber-emitter system and E_p the energy of the perturbing transition (the first allowed to the ground state). The sum on the right-hand side of Eq. 1.48 requires knowledge of the gas composition. $\overline{R^2}$ is given in the following equation:

[1] A contribution from identical particles in states not radiatively linked to the radiating transition can also be considered (Griem, 1997). This contribution is negligible in the present conditions and, therefore, will be neglected in our calculations.

$$\overline{R^2} = \overline{R_{up}^2} - \overline{R_{low}^2} \qquad \text{Eq. 1.49}$$

$\overline{R_\alpha^2}$ is the mean square distance (in Bohr units) of the electron in orbital l_α and can be calculated with Eq. 1.50:

$$\overline{R_\alpha^2} \approx \frac{1}{2}\frac{E_H}{E_\infty - E_\alpha}\left[5\frac{z^2 E_H}{E_\infty - E_\alpha} + 1 - 3l_\alpha(l_\alpha + 1)\right] \qquad \text{Eq. 1.50}$$

where E_H = 13.6 eV, E_∞ is the energy of ionization of the considered atom (13.6 eV for H and O, 35.1 eV for O^+, 14.5 eV for N and 29.6 eV for N^+), E_α the energy of state α, l_α the orbital quantum number of state α (see Table 1.6), and z the number of effective charges (z = 1 for H or N, z = 2 for N^+ or O^+). Taking the difference between the upper and lower state of the transition we obtain $\overline{R^2}$ in Eq. 1.49. Eq. 1.50 is exact only for hydrogen (Kelleher, 1981; Allard and Kielkopf, 1982). The term $\overline{R_{low}^2}$ is neglected in the work of Griem (Griem, 1964, 1997). If taken into account, it represents a difference of 11% and 3% for H_α and H_β in the Van der Waals calculation. The difference reaches 39% for the oxygen line at 777 nm, which explains why our results differ slightly from the work of (Laux, 1993). In Table 1.6, $\langle\overline{R^2}\rangle$ is obtained by averaging the contribution of each l_α with their respective emission weight (i.e. Einstein coefficient times degeneracy, obtained from the NIST database). Finally, we did not follow one of Griem's recommendation from reference (Griem, 1997). The author suggested multiplying the Van der Waals broadening by $N_e^{2/5}$, where N_e is the number of valence electrons of the perturbers. However, this statement was not referenced, nor quoted or justified later.

Table 1.5 Contribution of various perturbers (N, O, O^+, N^+, N_2, O_2, NO, and H_2) to the Van der Waals broadening of H, N, N^+, O, and O^+. The contributions of N_2, O_2, and NO can be found in (Laux *et al.*, 2003). Data for H_2 are taken from (Field, Somerville and Dressler, 1966).

Perturber			Radiating atom									
			m_{rp} g mol^{-1}					$E_p^{-\frac{4}{5}} m_{rp}^{-\frac{3}{10}}$ eV$^{-0.8}$(g mol^{-1})$^{-0.3}$				
	Allowed transition ground state	E_p (eV)	H	N^+	N	O^+	O	H	N^+	N	O^+	O
N^+	$^3D \rightarrow {}^3P$	11.4	0.93	-	7	7.4	7.4	0.15	-	0.08	0.08	0.08
N	$^4P \rightarrow {}^4S^0$	10.3	0.93	7	-	7.4	7.4	0.16	0.09	-	0.08	0.08
O^+	$^4P \rightarrow {}^4S$	14.9	0.94	7.47	7.47	-	8	0.12	0.07	0.06	-	0.06
O	$^3S^0 \rightarrow {}^3P$	9.5	0.94	7.47	7.47	8	-	0.17	0.09	0.09	0.09	-
O_2	$B^3\Sigma_u^- \rightarrow X^3\Sigma_g^-$	6.2	0.97	9.74	9.74	10.7	10.7	0.23	0.12	0.12	0.11	0.11
N_2	$b^1\Pi_u \rightarrow X^1\Sigma_g^+$	12.6	0.97	9.33	9.33	10.2	10.2	0.13	0.07	0.07	0.07	0.07
NO	$A^2\Sigma^+ \rightarrow X^2\Pi$	5.5	0.97	9.55	9.55	10.4	10.4	0.26	0.13	0.13	0.13	0.13
H_2	$B^1\Sigma_u^+ \rightarrow X^1\Sigma_g^+$	11.2	0.67	1.75	1.75	1.78	1.78	0.16	0.12	0.12	0.12	0.12

An equivalent formulation to Eq. 1.48, using the perturbing atom polarizability, can also be used (Kelleher, 1981; Allard and Kielkopf, 1982; Djurovi'c and Konjevi'c, 2009). For comparison, we consider the N transition at 742 nm, in a gas composed of N_2 at 1 bar and 300 K. Applying the formulation of (Kelleher, 1981; Allard and Kielkopf, 1982; Djurovi'c and Konjevi'c, 2009), with a polarizability of 1.77×10^{-30} m^3 (McQuarrie and Simon, 2014), we obtain a Van der Waals HWHM of 0.021 nm. If we apply the formulation of van der Horst (van der Horst *et al.*, 2012), based on (Djurovi'c and Konjevi'c, 2009), we get an HWHM of 0.018 nm. In the present work, with Eq. 1.48 and $\gamma_{N_2 \rightarrow O}$ = 1.26 (see later in Table 1.10), we get 0.013 nm. This value is slightly lower (about 28 %) because the polarizability is implicitly simplified in Eq. 1.48, but remains, however, within the accuracy of the calculation.

Table 1.6 Constants used for the calculation of R^2. The N^+ and O^+ lines (at 500 nm and 470 nm, respectively) comprise 15 and 12 transitions, respectively, and only major lines are shown (Kramida et al., 2018)

Transition	Upper State		Lower State		$\overline{R^2}$	Weight (%)	$\langle\overline{R^2}\rangle^{2/5}$
	E_{low} (eV)	Conf. - l_{low}	E_{up} (eV)	Conf. - l_{up}			
H_α	12.09	3s – 0	10.20	2p - 1	177	2%	
		3p – 1		2s - 0	138	17%	6.4
		3d – 2		2p - 1	96	81%	
H_β	12.75	4s – 0	10.20	2p – 1	618	2%	
		4p – 1		2s - 0	558	21%	12.0
		4d – 2		2p – 1	474	77%	
N (742.37 nm)	11.996	3p – 1	12.325	3s - 0	31	12%	
N (744.23 nm)			12.330			25%	3.9
N (746.83 nm)			12.335			63%	
N^+ (500.52 nm)	23.14	3d – 2	20.67	3p – 1	7.1	25%	
N^+ (500.15 nm)	23.13		20.65		7.0	18%	7.3
N^+ (500.11 nm)	23.13		20.65		7.0	12%	
…	…	…	…	…	…	…	
O (777.19 nm)	10.74	3p – 1	9.15	3s - 0	19	47 %	
O (777.42 nm)						33 %	3.3
O (777.54 nm)						20 %	
O^+ (470.54 nm)	28.88	3d - 2	26.25	3p - 1	9.33	17%	
O^+ (469.90 nm)	31.15		28.51		51	15%	
O^+ (469.92 nm)	28.86		26.23		9.2	14%	4.4
O^+ (470.12 nm)	31.47		28.83		65	14%	
O^+ (470.32 nm)	31.15		28.51		51	14%	
…	…	…	…	…	…	…	

1.3.4 Resonant broadening

Resonant broadening is due to the interaction of the radiating atom with other like-atoms in states radiatively linked to the upper (u) or lower (l) level of the transition. In (Laux *et al.*, 2003), the theory of resonant broadening was based on the book of Griem published in 1964 (Griem, 1964, p. 97). The authors took into account the contributions of three states of the perturbing atom radiatively linked to the radiating atom: (i) g → u, (ii) g → l, and (iii) l →u, where *g* is the ground state.

Later, Ali and Griem (Ali and Griem, 1965b, 1965a) published improvements and corrections which are used in (Griem, 1997; Drake, 2006; Djurovi'c and Konjevi'c, 2009; Castera, 2015). The correction of Ali and Griem leads to resonant broadening widths 1.6 times higher than with the non-corrected formula of (Laux *et al.*, 2003). The corrected expression is given in Eq. 1.51:

$$\Delta\lambda_{Res} = \frac{8{,}61 \times 10^{-28}}{2}\,\lambda_{ul}^2 \left[\lambda_{ug} f_{gu}\sqrt{\frac{g_g}{g_u}}n_g + \lambda_{lg} f_{gl}\sqrt{\frac{g_g}{g_l}}n_g + \lambda_{ul} f_{lu}\sqrt{\frac{g_l}{g_u}}n_l + \cdots\right] \qquad \text{Eq. 1.51}$$

where λ_{ab} is the wavelength (in nm) of the transition between *a* and *b* states, f_{ab} the (absorption) oscillator strength, g_i the degeneracy, and n_i population (in cm^{-3}) of the perturbing state *i*. Also, we note that (Laux *et al.*, 2003) considered the perturbation of $l \rightarrow u$. The population of state *l* is usually very low (less than 1% of the states at 10,000 K in the case of H_α), that its contribution is often neglected by other authors. However, at higher temperatures higher than 10,000 K, the state *l* can be significantly populated. Thus, in this work, we considered other resonant states of the perturber with energies below a certain threshold, given in Table 1.7. H_α and H_β, all the resonant levels below the upper level of the transition are included in the calculation. This means for H_β that we calculated the resonance of n = 1→ n = 4, n = 1→ n = 2, n = 2→ n = 4 and n = 3→ n = 4. The effect of these additional resonant states has an important impact on the calculation for H_β and O^+ with a maximal increase of 50% and 97% in the 1000 – 50,000 K range, compared to the calculation with only the ground state. For other atoms and ions, the effect is negligible.

Table 1.7 Coefficient β tabulated from 1000 to 50,000 K. All states under the specified threshold energy are considered in the calculation.

T_e (K)	H_α 656 nm	H_β 495 nm	N 746.831 nm	N^+ 500 nm	O 777 nm	O^+ 470 nm
1000	0.52	7.1x10^{-2}	8.3x10^{-2}	5.1x10^{-4}	3.9x10^{-7}	6.0x10^{-6}
10,000	0.51	7.0x10^{-2}	7.0x10^{-2}	4.9x10^{-5}	8.6x10^{-6}	2.1x10^{-5}
20,000	5.5x10^{-2}	1.0x10^{-2}	4.2x10^{-2}	4.6x10^{-5}	1.4x10^{-3}	8.4x10^{-5}
30,000	4.1x10^{-3}	2.3x10^{-3}	2.2x10^{-2}	4.8x10^{-5}	4.3x10^{-3}	1.2x10^{-4}
40,000	1.7x10^{-3}	2.0x10^{-3}	1.2x10^{-2}	6.3x10^{-5}	4.5x10^{-3}	1.4x10^{-4}
50,000	1.0x10^{-3}	1.9x10^{-3}	7.2x10^{-3}	9.1x10^{-5}	3.7x10^{-3}	1.5x10^{-4}
Threshold (eV)	12.1	12.8	3.6	13.6	4.2	5.1

A simplified formula of the resonant broadening is given later in Eq. 1.57. For O, the resonant broadening of the three lines is averaged with their respective emission weight in a similar way than what is shown in Table 1.6. The same procedure is applied for N^+ and O^+. For N emission at 744.229 and 742.364 nm, the results of N emission at 746.831 nm can be taken within a maximal difference of a factor of two.

A "unified theory" of resonant broadening for the H_α line (including higher-order interaction potentials) was developed in (Allard *et al.*, 2008). We use this theory for comparison with the present estimates. From

(Allard *et al.*, 2008, Table 2), a density of atomic hydrogen $n_H = 10^{17}$ cm^{-3} at a temperature $T = 12{,}000$ K leads to a resonant HWHM of H_α of 8.4×10^{-4} nm; when using (Ali and Griem, 1965b, 1965a; Djurovi'c and Konjevi'c, 2009) (Griem corrected) we obtain 16.0×10^{-4} nm and using (Griem, 1964; Laux *et al.*, 2003) (Griem non-corrected) we have 10.0×10^{-4} nm. The difference being small, the corrected formula taken from (Ali and Griem, 1965b, 1965a; Djurovi'c and Konjevi'c, 2009) is used in the present work.

1.3.5 Stark broadening

Stark broadening is directly related to the electron number density: the relation is in a first approximation linear for all emitting species, except hydrogen. Therefore, using the database of (Konjević *et al.*, 2002) or the calculated coefficient of Griem in (Griem, 1974, p. 370) (updated and different from his previous book (Griem, 1964)), one can convert a Stark width to an electron number density. The Stark broadening of hydrogen is accurately calculated by Gigosos *et al.* (Gigosos *et al.*, 1996; Gigosos, González and Cardeñoso, 2003). In their papers, Gigosos *et al.* recommend using the Full Width at Half Area (FWHA) instead of the classical FWHM to characterize the Stark broadening since the FWHA is less dependent on the ion temperature. However, in the case of H_α, the Stark profile of the line is close to a Lorentzian and it can be assumed that FWHA = FWHM (Konjević, Ivković and Sakan, 2012). Therefore, the H_α line is fitted by a Lorentzian profile convolved with the instrumental broadening function, and the electron number density is obtained using Eq. 1.52 after subtraction of the other Lorentzian broadenings:

$$\Delta\lambda_{HWHM,\mathrm{H}\alpha}[nm] = 0.549 \times \left(\frac{n_e}{10^{23} m^{-3}}\right)^{0.67965} \qquad \text{Eq. 1.52}$$

It was pointed out in (Konjević, Ivković and Sakan, 2012) that what was called FWHM by Gigosos *et al.* in (Gigosos, González and Cardeñoso, 2003) is, in fact, the HWHM.

The Stark shift of H_α can be related to its Stark broadening width, according to Eq. 1.53:

$$H_\alpha{:}\ \Delta\lambda_{Stark}[nm] = \frac{1}{2}\left(\frac{s_{Stark}[nm]}{0.056}\right)^{2/3} \qquad \text{Eq. 1.53}$$

The relation is non-linear and can be discriminated from the Van der Waals shift, Eq. 1.54.

$$\Delta\lambda_{Van\ der\ Waals}[nm] = \frac{3}{2} s_{Van\ der\ Waals}[nm] \qquad \text{Eq. 1.54}$$

In Figure 1.10, the measured shifts and widths of H_α taken from (Minesi, Stepanyan, *et al.*, 2020) are reported and compared to the theoretical relations of Eq. 1.53 and Eq. 1.54. These measurements clearly show

that the main broadening effect is due to the Stark effect. This approach was already used by Sainct *et al.* (Sainct *et al.*, 2020) to confirm that the measured H_α broadening widths were due to the Stark effect.

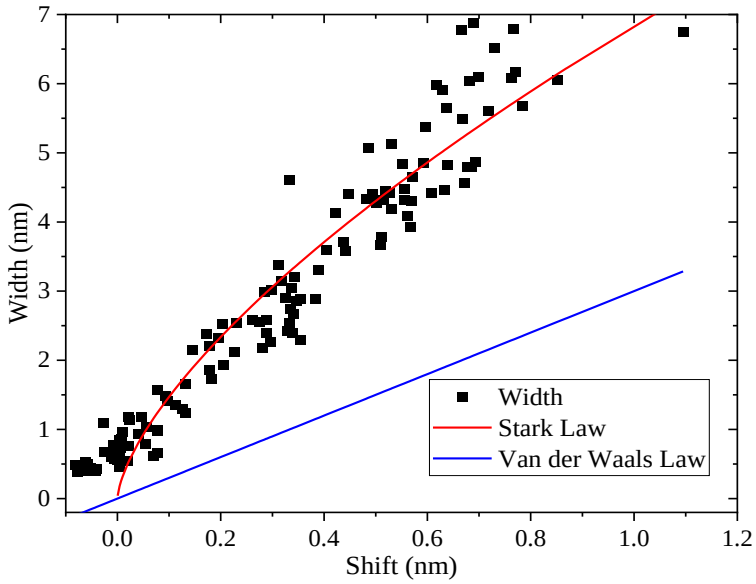

Figure 1.10 Fitted widths as a function of the corresponding shifts. The measurements correspond to the data obtained in (Minesi, Stepanyan, *et al.*, 2020)**.**

The Stark coefficients of N^+ and O^+ are implemented in an in-house development of Specair[1] (Laux *et al.*, 2003) using the coefficients calculated by Griem (Griem, 1974, p. 366). The tables of Griem give the reference coefficients, $\omega_{Stark,ref}$, at $n_e = 10^{17}$ cm^{-3} and the Stark broadening at a given n_e is obtained using Eq. 1.55. Since Stark broadening of O, O^+, N, and N^+ by ions is negligible, the effect of positive ions is not considered in our in-house extension of Specair.

$$\omega_{Stark} = \frac{n_e}{10^{17} cm^{-3}} \omega_{Stark,ref} \qquad \text{Eq. 1.55}$$

Stark broadening coefficients for the N^+ transitions at 519 nm are not given in the book of Griem. Based on our measurements (Minesi, Stepanyan, *et al.*, 2020), we find that the lines at 519 nm are well fitted using Eq. 1.55 by a coefficient $\omega_{Stark,519\,nm} = 0.015$ nm. This coefficient is consistent with the values measured

[1] www.spectralfit.com

by Mar et al. (Mar *et al.*, 2000) and calculated by Riviere (Rivière, 2002) as shown in Table 1.8. The agreement is illustrated in Figure 1.11 where the data of Table 1.8 are reported with the corresponding error bars (Mar *et al.*, 2000; Konjević *et al.*, 2002; Rivière, 2002). The uncertainty on the x-axis corresponds to the range of temperatures measured in (Minesi, Stepanyan, *et al.*, 2020). The uncertainty on the value itself is the sum of (i) the uncertainty of the n_e measurement (± 10%) and (ii) the variation of the coefficient on the temperature range supposed, in a first approximation, to vary with $T_e^{-0.5}$ (± 20%). Such a variation is typical of Stark broadening coefficient of ionic lines (Rivière, 2002). The three lines (519.038, 518.20, and 518.621 nm) composing the emission at 519 nm could not be resolved because of their broad Stark widths. Thus, the coefficients of the ^{5}D and ^{5}P transitions are assumed to be equal.

Table 1.8 Empirical Stark coefficients of N^+ used in this article for the determination of the Stark HWHM. For comparison, other values are extracted from the review of (Konjević *et al.*, 2002) at $n_e = 10^{17}$ cm^{-3} and $T_e = 28$ kK (original experimental work of (Mar *et al.*, 2000)). Calculated values based on the method of (Griem, 1964) are from (Rivière, 2002).

Lower Conf. Lower Term	Upper Conf. Upper Term	λ (nm)	ω_{Stark} (HWHM - nm) at $n_e = 10^{17}$ cm^{-3}		
			(Rivière, 2002) T_e = 25 kK	(Mar *et al.*, 2000) T_e = 28 kK	(Minesi, Stepanyan, *et al.*, 2020) Te = 30 – 50 kK
2s.2p2.3d ^{5}F	2s.2p2.3p ^{5}D^0	519.038	0.0273	0.0219	0.015
2s.2p2.3d ^{5}D	2s.2p2.3p ^{5}P^0	518.20 518.621	0.0296 0.0297	0.0241 0.02445	0.015

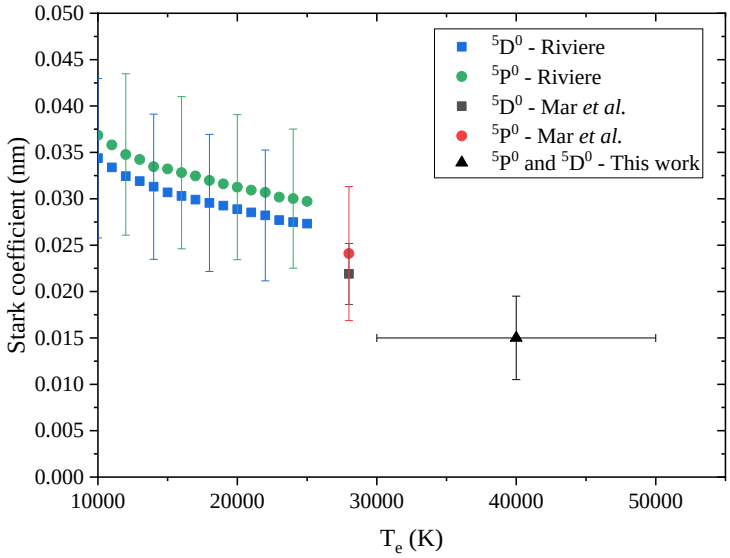

Figure 1.11 Comparison of the Stark coefficients for the N^+ lines at 519 nm from (Rivière, 2002), (Mar *et al.*, 2000), and our work (Minesi, Stepanyan, *et al.*, 2020)

1.3.6 Conclusions and simplified formulas

The broadening HWHM formulas for H_α, H_β, O, O^+, N, and N^+ are simplified in Eq. 1.56 - Eq. 1.58. The coefficients α, β, and γ are given in Table 1.9. The reference density of 2.7×10^{19} cm^{-3} is the total gas density at 273 K, 1 atm (Loschmidt constant). The resonant broadening is expressed as a function of the emitter number density, $n_{emitter}$.

$$\Delta\lambda_{Doppler}[nm] = \alpha\sqrt{\frac{T}{273\ K}} \qquad \text{Eq. 1.56}$$

$$\Delta\lambda_{resonance}[nm] = \beta\frac{n_{emitter}}{2.7\times10^{19}\ cm^{-3}} \qquad \text{Eq. 1.57}$$

$$\Delta\lambda_{Van\ der\ Waals}[nm] = \sum_{pert}\frac{\gamma_{pert}}{100}\times\frac{n_{pert}}{2.7\times10^{19}\ cm^{-3}}\left(\frac{T_{gas}}{273\ K}\right)^{0.3} \qquad \text{Eq. 1.58}$$

We can also rewrite Eq. 1.58 using the molar fraction, x_{pert}, and the pressure, p, as sometimes done in the literature (Laux *et al.*, 2003; van der Horst *et al.*, 2012):

$$\Delta\lambda[nm] = \frac{n_{total}}{}\left(\frac{T_{gas}}{}\right)^{0.3}\sum\left(\frac{\gamma_{pert}}{}\times \right) \qquad \text{Eq. 1.59}$$

$$= \frac{p}{1\ atm}\left(\frac{273\ K}{T_{gas}}\right)^{0.7} \sum_{pert}\left(\frac{\gamma_{pert}}{100} x_{pert}\right)$$

Table 1.9 Summary of the simplified formulas for HWHM determination and tabulated coefficients α, β, and γ. The broadening expressions derived in this work are given in Eq. 1.56 - Eq. 1.58. The α coefficient is exact. The β coefficient is calculated at T_e = 30,000 K and can be found for other temperatures in Table 1.7.

Transition	$\Delta\lambda_{Doppler}[nm]$	$\Delta\lambda_{res}[nm]$	$\Delta\lambda_{Van\ der\ Waals}[nm]$			
	$\alpha\ [nm]$	$\beta\ [nm]$	$\gamma\ [nm]$			
			N^+	N	O	O^+
H_α (656 nm)	$\alpha_{H_\alpha} = 3.87 \times 10^{-3}$	$\beta_{H_\alpha} = 4.1 \times 10^{-3}$	$\gamma_{N^+\to H_\alpha} = 3.4$	$\gamma_{N\to H_\alpha} = 3.6$	$\gamma_{O\to H_\alpha} = 3.8$	$\gamma_{O^+\to H_\alpha} = 2.7$
H_β (486 nm)	$\alpha_{H_\beta} = 2.87 \times 10^{-3}$	$\beta_{H_\beta} = 2.3 \times 10^{-3}$	$\gamma_{N^+\to H_\beta} = 3.5$	$\gamma_{N\to H_\beta} = 3.7$	$\gamma_{O\to H_\beta} = 3.9$	$\gamma_{O^+\to H_\beta} = 2.7$
N^+ (500 nm)	$\alpha_{N^+} = 0.78 \times 10^{-3}$	$\beta_{N^+} = 4.8 \times 10^{-5}$	--	$\gamma_{N\to N^+} = 1.3$	$\gamma_{O\to N^+} = 1.4$	$\gamma_{O^+\to N^+} = 0.95$
N (746 nm)	$\alpha_N = 1.18 \times 10^{-3}$	$\beta_N = 2.2 \times 10^{-2}$	$\gamma_{N^+\to N} = 1.4$	--	$\gamma_{O\to N} = 1.6$	$\gamma_{O^+\to N} = 1.1$
O (777 nm)	$\alpha_O = 1.15 \times 10^{-3}$	$\beta_O = 4.3 \times 10^{-3}$	$\gamma_{N^+\to O} = 1.3$	$\gamma_{N\to O} = 1.4$	--	$\gamma_{O^+\to O} = 0.99$
O^+ (470 nm)	$\alpha_{O^+} = 0.69 \times 10^{-3}$	$\beta_{O^+} = 1.2 \times 10^{-4}$	$\gamma_{N^+\to O^+} = 0.62$	$\gamma_{N\to O^+} = 0.67$	$\gamma_{O\to O^+} = 0.70$	--

Complementary Van der Waals coefficients, γ, are given in Table 1.10 for the following collision partners: N_2, O_2, NO, CO, CO_2, CH_4, H_2O, H_2, and Ar. The γ coefficient being proportional to the collider polarizability, α_C, we multiplied γ_{N_2} by $\left(\alpha_C/\alpha_{N_2}\right)^{2/5}$ to get the γ_C coefficients of C = CO, CO_2, CH_4, H_2O, and Ar (McQuarrie and Simon, 2014, p. 668). For instance, we obtain $\gamma_{CO_2\to H_\alpha} = 3.43$ using the polarizability ratio of N_2 and CO_2. The same result can be obtained, knowing that the first excited state of CO_2 radiatively linked to the ground state is $^1\Pi_g$ at 8.9 eV (Pannier, 2019, Table 4.1), giving a factor $E_p^{-0.8} m_{rp}^{-0.3} = 0.20\ \mathrm{eV}^{-0.8}\left(\mathrm{g.mol}^{-1}\right)^{-0.3}$, which results in $\gamma_{CO_2\to H_\alpha} = 4.51$.

Table 1.10 Coefficient γ tabulated for Van der Waals broadening by the following colliders: N_2, O_2, NO, CO_2, CO, CH_4, H_2O, H_2, and Ar.

Emitting	Perturbing								
	N_2	O_2	NO	H_2	CO_2	CO	H_2O	CH_4	Ar
H_α (656 nm)	2.9	5.2	5.9	3.6	3.4	3.1	2.7	3.4	2.8
H_β (486 nm)	3.0	5.3	6.0	3.7	3.5	3.2	2.8	3.5	2.9
N^+ (500 nm)	1.0	1.8	2.0	1.8	1.2	1.1	1.0	1.2	1.0
N (746 nm)	1.3	2.2	2.3	2.2	1.5	1.3	1.2	1.5	1.2
O (777 nm)	1.1	1.8	2.1	1.9	1.3	1.2	1.1	1.3	1.1
O^+ (470 nm)	0.6	0.9	1.0	1.0	0.7	0.6	0.5	0.7	0.5

As a final remark, note that most of the previous formulas were developed in the book of Griem (Griem, 1964) published in 1964 (improved and corrected in (Ali and Griem, 1965a, 1965b)). Griem later stated (1974) that his formulas for the resonant and Van der Waals broadening widths were “very approximate” (Griem, 1974, p. 169) and therefore should be used only for estimation.

1.4 Laser-Induced Fluorescence

The results of this section are used notably in Section 8.2.

The OES technique provides information about excited states in plasmas. Usually, most of the plasma species are in the ground state and are not accessible by OES. The Laser-Induced Fluorescence (LIF) diagnostic allows reliable measurements of the ground state species densities (Croonenbroek, 1996; Demtröder, 2008).

1.4.1 Two-level model

We introduce the LIF diagnostic with a simplified 2-level model of molecules. Let us define N_1 and N_2 as the densities of OH(X) and OH(A). Transitions between these two levels occur due to:

- Spontaneous emission
- Absorption
- Stimulated emission
- Quenching.

Assuming that the total population of OH is conserved, i.e. $N_1(t) + N_2(t) = N_1(t=0) = N_1^0$, the variation of the two states's population is dictated by Eq. 1.60, where W_{12} and W_{21} are the rates of absorption and stimulated emission, A_{21} the Einstein coefficient of the transition, and Q_{21} the quenching rate of OH(A) by other molecules.

$$\frac{dN_1}{dt} = -\frac{dN_2}{dt} = -N_1 W_{12} + N_2(W_{21} + A_{21} + Q_{21}) \quad \text{Eq. 1.60}$$

The rates of absorption and stimulated emission are given by Eq. 1.61,

$$W_{ij} = B_{ij} I_{Laser} = B_{ij} \rho f(\nu) \quad \text{Eq. 1.61}$$

where ρ [J cm^{-3}] is the photon density, $f(\nu)$ [s] the linewidth, and B_{ij} and B_{ji} [cm^{3}J^{-1}s^{-2}] the second Einstein coefficients related by the states's degeneracy in Eq. 1.62.

$$g_1 B_{12} = g_2 B_{21} \quad \text{Eq. 1.62}$$

This model is summarized in Figure 1.12.

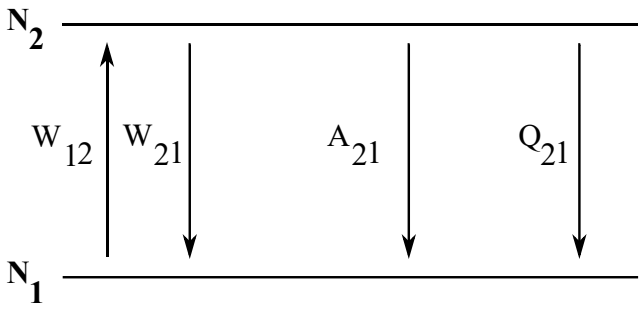

Figure 1.12 Schematic of the 2-level LIF model.

We define τ the characteristic time of the system in Eq. 1.63:

$$\tau = \frac{1}{W_{12} + W_{21} + A_{21} + Q_{21}} \quad \text{Eq. 1.63}$$

Solving Eq. 1.60, the population of N_2 is obtained

$$N_2(t) = N_1^0 W_{12} \tau (1 - e^{-\frac{t}{\tau}}) \quad \text{Eq. 1.64}$$

and can be rewritten as:

$$N_2(t) = N_1^0 \frac{I_{Laser} B_{12}}{I_{Laser} B_{12} \left(1 + \frac{g_2}{g_1}\right) + A_{21} + Q_{21}} (1 - e^{-\frac{t}{\tau}}) \qquad \text{Eq. 1.65}$$

We now estimate the characteristic time of this system, Eq. 1.63, to guide our following discussions. In air at 2000 K, the quenching time of OH(A) is equal to 5 ns using the values of Table 5 in (Bruggeman *et al.*, 2014). This value drops to 3 ns in a stoichiometric premixed CH_4 – air mixture. Thus, we consider that $Q_{21} \sim 10^9$ Hz. The value of A_{21} can be found in the LIFBASE software (Luque and Crosley, 1998) and is below $A_{21} < 10^6$ Hz for all OH transitions. Finally, the rate of laser excitation, W_{12}, can be calculated using Eq. 1.61. The typical laser linewidth is 0.1 $cm^{-1} = 3\times10^9$ Hz, whereas the Doppler broadening is equal to 2 pm $= 6\times10^9$ Hz at 2000 K. We therefore assume the OH absorption linewidth to be equal to 10^{10} Hz. The second Einstein coefficients of OH range from 10^{21} to 10^{23} $cm^3J^{-1}s^{-2}$. In the present work, the $Q_2(3)$ line at 282.937 nm is used, with $B_{12} = 2.390\times10^{23}$ $cm^3J^{-1}s^{-2}$ (Luque and Crosley, 1998). The photon density, ρ, can be calculated by dividing the laser fluence, F, in W cm^{-2} by the speed of light, $\rho = F/c$. We obtain $W_{12} = 10^{10}$ Hz for $F = 10^7$ W cm^{-2}. Therefore, for F > 10 MW cm^{-2}, the characteristic time of the system, in Eq. 1.63, will be dominated by laser absorption and laser induced stimulation. The distinction between the two regimes is detailed in Section 1.4.2 and 1.4.3.

We showed that, due to the quenching, the characteristic time of the 2-level system is below τ < 1 ns. The laser pulse being 10-ns long, the coefficient $(1 - e^{-\frac{t}{\tau}})$ in Eq. 1.65 is close to one. Note that the laser intensity is assumed to be a Heaviside function and spatially uniform, which implies that the absorption and stimulated emission rates are constant and uniform in this model.

1.4.2 Linear LIF

If the relation $I_{Laser} B_{12} \ll A_{21} + Q_{21}$ is satisfied[1], the LIF regime is said to be linear. In this case, the population of the ground state remains practically unchanged. Simplifying Eq. 1.65, the LIF radiation from OH(A) is proportional to the laser intensity and the ground state density. In the case of OH, $A_{21} \sim 700$ ns^{-1} (Bruggeman *et al.*, 2014), which is usually negligible compared to the quenching rate.

[1] The transition occurring at F = 1 – 10 $MWcm^{-2}$, we practically assume that the laser fluence is below 1 $MWcm^{-2}$.

$$I_{LIF} \propto N_2 \propto \frac{I_{Laser} B_{12}}{A_{21} + Q_{21}} N_1^0 \approx \frac{I_{Laser} B_{12}}{Q_{21}} N_1^0 \qquad \text{Eq. 1.66}$$

The difficulty in interpreting this regime is related to the uncertainty on the quenching rate, Q_{21}, which depends on the nature, density, and temperature of the colliders. We investigate NRP-discharges in the recirculation zone of a premixed CH_4 – air flame, where the flame composition is unknown and sharply varies with time and position.

Moreover, additional losses via vibrational and rotational relaxation must be considered in the ground and excited states. For instance, Verreycken *et al.* took rotational and vibrational relaxation into account in a mixture of He and 0.84% of H_2O (Verreycken *et al.*, 2012). UV absorption of OH was also performed, confirming their results within the experimental uncertainties. We estimate the typical time of RET, using the coefficients of OH(A) obtained in (Kienle, Jörg and Kohse-Höinghaus, 1993, Table 4), and those of OH(X) in (Kliner and Farrow, 1999). We assume the gas is composed of N_2 : H_2O (90 % : 10 %) at p = 1 atm and T = 3000 K for comparison purpose and obtain a RET time of τ_{RET}^{A} = 1.1 ns for OH(A) and τ_{RET}^{X} = 0.5 ns for OH(X). The model of Verreycken *et al.* cannot be directly applied here because the gas composition is different and, thus, we operate instead in the saturated regime of LIF, described in the next section.

1.4.3 Saturated LIF

Increasing the laser intensity until $I_{Laser} B_{12} \gg A_{21} + Q_{21}$, the LIF regime is said to be saturated[1]. In this condition, Eq. 1.65 simplifies to Eq. 1.67 and the LIF intensity is proportional to the unperturbed ground-state density, N_1^0.

$$I_{LIF} \propto N_2 = \left(1 + \frac{g_2}{g_1}\right)^{-1} N_1^0 \qquad \text{Eq. 1.67}$$

Therefore, for a steady laser intensity in the saturated regime, the LIF signal will depend practically only on the variation of the OH density. In Section 8.2, we monitor the LIF signal for:

- Spatial comparison of the OH density along the laser beam, and,

[1] Practically if the laser fluence is above 10 $MWcm^{-2}$.

- Temporal comparison of the OH density using phase-locked experiments.

Several methods, including laser absorption (Croonenbroek, 1996), Rayleigh scattering (Salmon and Laurendeau, 1985) or OH absorption (Verreycken *et al.*, 2013) have been applied successfully to calibrate saturated LIF but are not used in this work. In the next section, we discuss another LIF regime which could potentially be used for future work.

1.4.4 Laser-induced pre-dissociative fluorescence (LIPF)

In this section, we discuss the Laser-induced pre-dissociative fluorescence (LIPF) technique, that corresponds to when OH(X) is pumped to the pre-dissociated excited-state OH(A, v' = 3). The key point of this method is that the quenching rate of OH(A, v' = 3) is at least one order of magnitude lower than its predissociation rate, Q^P (Croonenbroek, 1996). Eq. 1.66 can thus be rewritten:

$$I_{LIF} \approx \frac{I_{Laser} B_{12}}{Q^P} N_1^0 \qquad \text{Eq. 1.68}$$

In the case of linear LIPF, because the rate Q^P is well determined and independent of the environment, the LIF signal variation can be related to the ground state OH density.

This technique has been successfully applied by Koch *et al.* in a combustible mixture (Koch, Chryssostomou, *et al.*, 1993; Koch, Voges, *et al.*, 1993). LIPF was also recently performed in an H_2 flame ignited by a nanosecond discharge (Ono and Oda, 2008). The sources of uncertainty (such as RET, VET, spatial homogeneity) were carefully taken into account in the calibration of the LIPF signal. However, it could be argued that the excitation of OH(A, v' = 3) requires a laser beam at 248 nm. This UV laser beam also induces O_3 photodissociation, resulting in additional OH production (Verreycken *et al.*, 2012). Further investigations are therefore needed before LIPF can be used for 2D imaging of OH absolute density.

1.4.5 Conclusion on Laser Induced Fluorescence

In this section, we shortly detailed the theoretical bases of Laser-Induced Fluorescence and discussed three regimes:

- Linear
- Saturated

- Predissociative

The LIF signal of the linear regime cannot be easily calibrated, mostly due to the large uncertainty on the quenching at atmospheric pressure. The pre-dissociative and saturated regimes can be used at atmospheric pressure to determine the OH number density. The use of UV laser radiation at 248 nm is, however, suspected to be intrusive due to potential ozone production. Therefore, in Section 8.2, we will perform saturated LIF in the Mini-PAC experiment to directly measure the spatial and temporal variations of the OH number density.

1.5 Conclusions

In Section 1.1, we academically derived the expression of the partition atomic and molecular functions. Based on these grounds and literature review on rotational-translational relaxation and quenching, we showed in Section 1.2 that the $N_2(C)$ and $N_2(B)$ rotational temperatures are close within 10% to the gas temperature. In Section 1.3, we determined explicit general formulation of natural, resonant, Doppler, Van der Waals, and Stark broadening for H_α, H_β, N^+ (at 500 nm), O^+ (at 490 nm), O (at 777nm), and N (at 746 nm). Finally, in Section 1.4, we justified the use of saturated LIF in our experiments based on the derivation of a 2-level LIF model.

Chapter 2

Electrical diagnostics of nanosecond discharges

The results of this chapter are used notably in Section 8.2.

Rigorous determination of the discharge electrical characteristics is mandatory for the reproducibility of the experiments. For instance, three different regimes of NRP discharges (corona, glow, non-thermal spark) can be reached by only varying the voltage (Pai, Lacoste and Laux, 2010b). The voltage and current of the discharge can be measured by attaching probes directly on the high voltage electrodes. This *direct configuration* was used in previous work at the EM2C laboratory and gave satisfactory results (Pilla *et al.*, 2006; Pai, Lacoste and Laux, 2010b; Xu *et al.*, 2011; Rusterholtz *et al.*, 2013; Sainct *et al.*, 2014). However, the probes occupy a significant volume around the discharge, which is not always compatible with optical diagnostics. Also, for practical applications in combustion, NRP discharges will be used in aggressive environments that typical probes cannot resist (high temperatures, high pressures, corrosive gas mixtures …). Therefore, in this thesis, the voltage and current probes are plugged halfway in the coaxial cable delivering the NRP discharges, as already performed in (Dumitrache *et al.*, 2019; Minesi *et al.*, 2019; Stepanyan *et al.*, 2019; Minesi, Stepanyan, *et al.*, 2020). This *remote configuration* solves the practical problems mentioned above and is found to provide additional information for plasma monitoring.

In this chapter, we describe the measurement of the electrical energy deposited by the nanosecond discharges in the remote configuration. We focus on the technic, while the interpretation of the results will be discussed in other chapters. In Section 2.1, the fundamental aspects of the transmission line physics are reminded, and the typical experimental setup is given. In Section 2.2, we detail the measurement of the energy deposition of a single pulse. A comparison with the direct configuration is also presented. In Section 2.3, we provide some examples of practical interest of the remote configuration.

2.1 Nanosecond high-voltage pulse propagation

The generic electrical setup employed in this work is shown in Figure 2.1. Two FID generators are used in this thesis:

- FPG 30-100MC4K (pulser #2)
- FID 10-30NM10 (pulser #4).

The technical aspects concerning pulser #2 and pulser #4 are given in Appendix A. In this thesis, the output of the pulser is connected to a plasma reactor by a coaxial cable (Alphawire 9011a, 75 Ω). In the middle of the coaxial cable, we connect a voltage probe (typically, LeCroy PPE 20 kV) and a current transformer (typically, Pearson 6585).

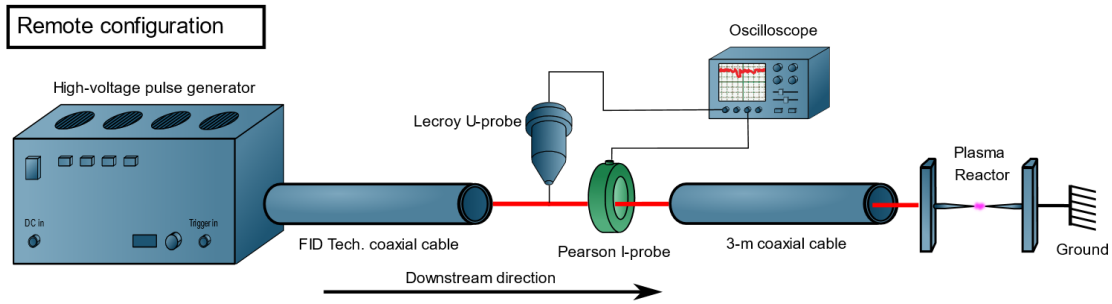

Figure 2.1 Default electrical setup of this work: remote configuration. The core of the coaxial cables is represented in red and link the pulser to the plasma reactor. The impedance mismatch between the cables (75 Ω) and the plasma induces reflections going in the upstream direction.

Let us assume a pulse wave of amplitude $U_{incident}$, propagating along a transmission line of impedance Z_0, terminated by a load. The load is, in our case, a pair of electrodes:

- insulated by air, or
- connected by plasma.

If the load is a short circuit, Z_{load} = 0 Ω, the incident pulse will be balanced by a negative pulse of amplitude -$U_{incident}$ to satisfy U_{load} = 0. In the case of an open circuit, $Z_{load} \gg Z_0$, the incident pulse will be reflected, which will fulfill $U_{load} = 2 \times U_{incident}$. These statements can be summarized (Pai, 2008, chap. 3) by the following equation, which is valid for any load impedance:

$$U_{reflected} = \left(1 + \frac{Z_{load} - Z_0}{Z_{load} + Z_0}\right) U_{incident} = \frac{2\,Z_{load}}{Z_{load} + Z_0} U_{incident} \qquad \text{Eq. 2.1}$$

Additional theoretical aspects of transmission lines can be found in (Martin and Martin, 2018). Thus, the shape of the reflected pulse provides information about the plasma impedance. If the amplitude of the reflected pulse is equal to the incident one, no breakdown occurred (the air in the gap is a perfect insulator in this case). If the reflected amplitude is opposite to the incident one, the impedance of the plasma is close to zero. We note that if the load/plasma impedance, Z_{load}, is identical to the transmission line impedance (Z_0 = 75 Ω), no reflection will arise.

In the coaxial cables used, the pulses propagate at $c_{coax} = 2.0\times10^8$ m.s^{-1}. Therefore, a 10-ns pulse spreads over a length of 2 m. The voltage and current probes are typically connected 3 m away from the plasma reactor, making it possible to separate the incident pulse from the reflected pulse in the measurements. Following the scheme in Figure 2.1 from left to right (defined as the downstream direction), the high-voltage pulse is generated by the pulser and propagates through a coaxial cable. Then the pulse travels through the voltage and the current probes. This order (current probe downstream of the voltage probe) is essential to properly measure a potential current leak in the voltage probe (Pannier, 2019, App. D). Finally, the pulse reaches the plasma reactor, is reflected in the upstream direction according to Eq. 2.1 and is measured again by the probes.

2.2 Energy deposition by a single pulse

2.2.1 Probes halfway of a 6-m coaxial cable

We now illustrate the procedure of energy measurements using the data of Section 8.3.1. The setup corresponds to Figure 2.1. The energy deposited by the discharge is measured using a voltage probe (Lecroy PPE 20kV, 100 MHz) and a current probe (Pearson Coil Model 2877, 200 MHz, rise time 1.5 ns) connected to an oscilloscope (Lecroy HDO 6104, 1 GHz). We assume the probes are accurately calibrated[1]. We use pulser #4 at a repetition frequency of 20 kHz and set an output amplitude of the incident pulse of 3.5 kV, i.e. a gap voltage of about 7 kV at the electrodes before breakdown. The plasma is initiated in a gap of 5 mm in a lean mixture of CH_4-air (Φ = 0.8).

[1] Pannier showed that incorrect compensation in the voltage probe internal impedance could lead to a two-fold increase/decrease of the measured energy (Pannier, 2019, App. D).

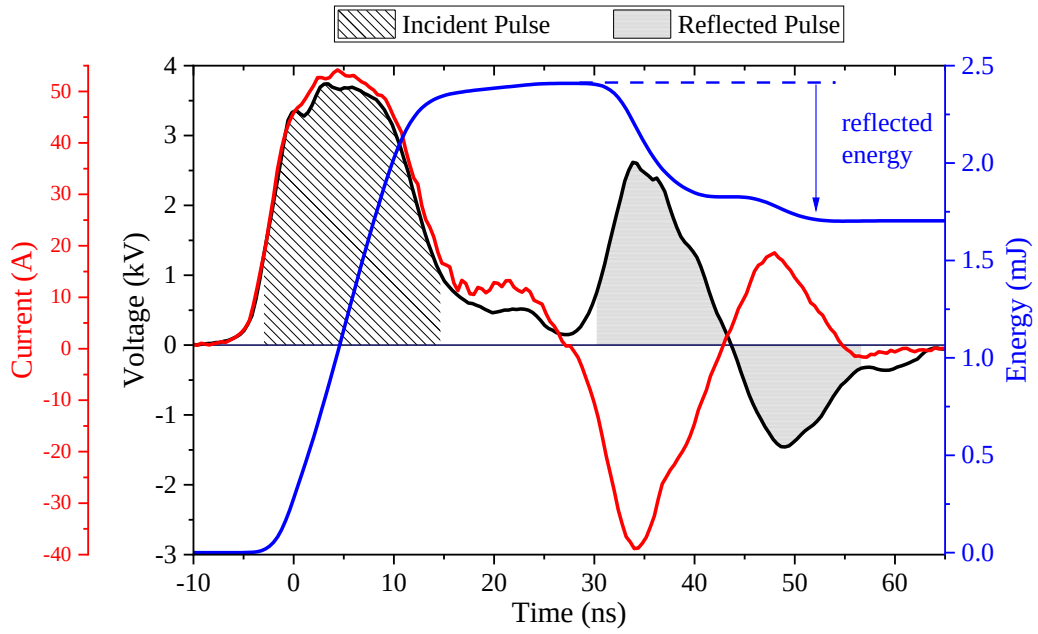

Figure 2.2 Typical energy measurement in a gap of 5 mm in a lean mixture of CH_4-air (Φ = 0.8) using the remote configuration. The cumulated energy (blue) is the time integral of the product of the voltage (black) and current (red) signals. Dashed and dotted areas represent the incident and reflected pulses, respectively.

First, the electric signal of the current and voltage probes must be synchronized within a nanosecond scale. In the remote configuration, the measurements are performed in the middle of a coaxial cable, acting as a purely resistive impedance[1]. Hence, in this configuration, the current is proportional to the voltage. In Figure 2.2, typical electrical outputs of the probes are shown and were synchronized by shifting the current.

Note that this synchronization account for the length of the two different wirings between the oscilloscope and the probes. We assume that the current and voltage measurements are performed at the same location on the coaxial cable. A measurement in two different locations would generate a delay between the two probes that cannot be compensated with synchronization (Pannier, 2019, App. D). For illustration, let us assume that the current probe is located at L = 1 m downstream the voltage probe. The incident pulse current would be measured with a delay of 5 ns (L/c_{coax}). However, the reflected pulse current would be measured

[1] In previous work at the EM2C laboratory (Pai, 2008; Pilla, 2008; Xu *et al.*, 2011; Rusterholtz *et al.*, 2013; Sainct *et al.*, 2014), the synchronization is performed at the electrode without plasma formation and the impedance is purely capacitive. See discussion in Section 2.2.2 or detailed in (Rusterholtz, 2012, chap. 4; Rusterholtz *et al.*, 2013).

in advance by 5 ns. Practically, a distance of L = 2 cm is respected in this work. The measurements in Figure 2.2 demonstrate that the incident and reflected signals are synchronized accurately.

We arbitrarily set the time origin so that the incident pulse is measured between t = 0 ns and t = 15 ns, see the dashed area in Figure 2.2. The front of the reflected pulse is measured at t ~ 30 ns, see the dotted area in Figure 2.2. This timing is coherent, considering the distance traveled by the pulse divided by the speed of propagation in a coaxial cable (6 m / 2.0×10^8 m·s^{-1} = 30 ns).

The total (or cumulated) energy deposited downstream, *E(t)*, is obtained by integrating in time the product of voltage, *U(t)*, and current, *I(t)*, assuming no energy is deposited before t_0 = -10 ns.

$$E(t) = \int_{t_0}^{t} I(t)U(t)dt \qquad \text{Eq. 2.2}$$

The averaged[1] cumulated energy is represented in Figure 2.2. If the voltage and the current are of the same sign, then energy is transported downstream. Otherwise, energy is reflected upstream (to the pulser). Taking the value of *E(t)* at t = 25 ns, we obtain that pulser #4 generates pulses of 2.4 mJ in this configuration. The current and voltages of the reflected pulses being opposite, the cumulated energy decreases by 0.7 mJ between 35 and 50 ns. Considering there is no loss of energy in the cables (see later), the total deposited energy in the plasma is, therefore, equal to 1.7 mJ.

2.2.2 Probes at the electrodes

In previous works at the EM2C laboratory (Pai, 2008; Pilla, 2008; Xu *et al.*, 2011; Rusterholtz *et al.*, 2013; Sainct *et al.*, 2014), the voltage and current probes were placed close to the electrodes. This direct configuration is reproduced in Figure 2.3; one coaxial cable is removed compared to Figure 2.1.

[1] It is worth mentioning that $\langle \int I(t)U(t)dt \rangle \neq \int \langle I(t) \rangle \langle U(t) \rangle dt$.

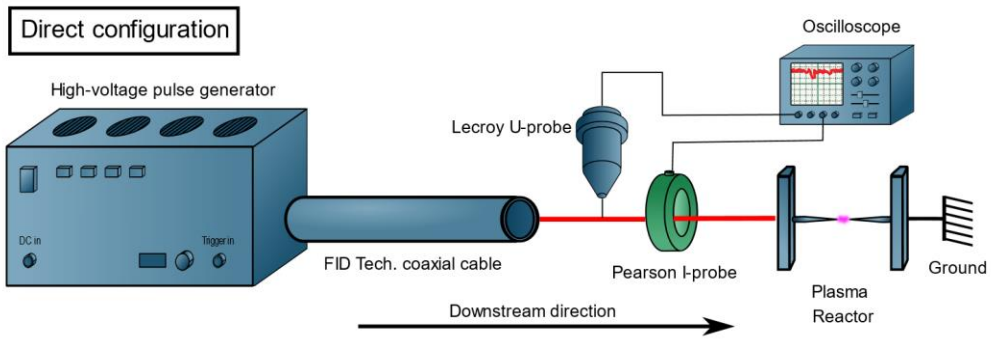

Figure 2.3 Electrical setup with a coaxial cable removed: direct configuration. This configuration is usually not used in this work.

The synchronization of the current and voltage measurements cannot be performed as above since the voltage is not proportional to the current anymore. At low voltage, no breakdown occurs; the electrodes act as a capacitor. Thus, the current is proportional to the voltage derivative; see Eq. 2.3, where *C* is the electrode system capacity.

$$I(t) = C\frac{d}{dt}U(t) \qquad \text{Eq. 2.3}$$

The synchronization is therefore performed with the current and the voltage derivative. This procedure is extensively detailed in (Rusterholtz, 2012, chap. 4; Rusterholtz *et al.*, 2013).

If the probes are plugged to the electrodes, it is impossible to distinguish the incident pulse from its reflection. Nevertheless, Eq. 2.2 remains valid. For comparison of the two setups, the measurements of Figure 2.2 are reproduced with the setup of Figure 2.3. In Figure 2.4, the current, voltage, and energy measured at the anode are showed. The maximum voltage measured at the anode is 6 kV for an incident pulse of 4.5 kV. During the first nanosecond, the plasma is not formed. The impedance of the load is significatively higher than the cable impedance. Therefore, the positive incident pulse is reflected, and the reflected pulse is positive. At the breakdown, the measured voltage at the electrodes is consequently twice the incident voltage, Eq. 2.1. Then, the plasma forms and the impedance of the load decreases, inducing an increase of the current and a fall of the applied voltage.

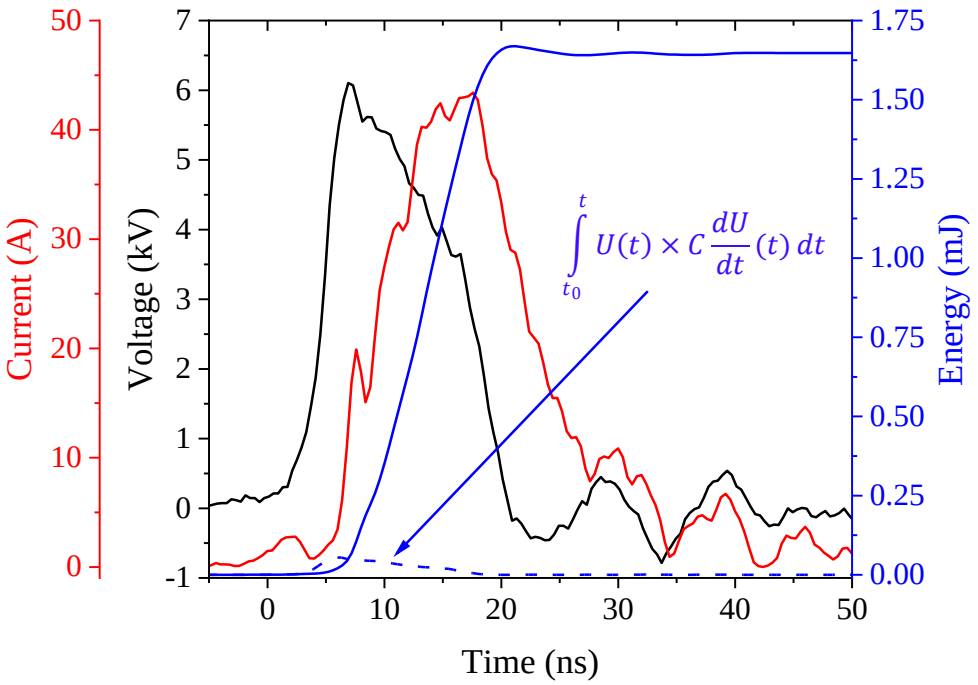

Figure 2.4 Voltage (black solid line), current (red solid line), and energy (blue solid line) measured with the direct configuration, see Figure 2.3. The conditions are identical to the measurement of Figure 2.2, except for the location of the probe. The energy stored in the capacitance, *C* = 2 pF, is also given (dashed blue line).

In the literature, to get the energy deposition, the displacement current is sometimes subtracted to the measured current. We will demonstrate that this procedure is unnecessary to measure the deposited energy. The energy calculated after subtraction of the capacitive current is given in Eq. 2.4 where $C \approx 2$ pF is the typical capacitance of the electrodes.

$$E(t) = \int_{t_0}^{t} \left(I(t) - C \frac{d}{dt} U(t) \right) U(t) dt \qquad \text{Eq. 2.4}$$

After separation and integration, we obtain:

$$E(t) = \int_{-10}^{t} I(t)U(t)dt - C \left[\frac{U^2(t)}{2} \right]_{t_0}^{t} \qquad \text{Eq. 2.5}$$

The second term in Eq. 2.5 is the energy cumulated in the capacity of the electrodes, $E_C(t) = C \left[\frac{U^2(t)}{2} \right]_{t_0}^{t}$.

We are usually interested in the total energy deposited by the pulse. Thus, the integration is often performed up to *t* significantly longer than the temporal width of the pulse. Therefore, E_c is null and the formulations

in Eq. 2.2 and Eq. 2.4 are equivalent[1], as demonstrated in Figure 2.3, where the energy stored in the equivalent capacitance is given. The maximum of E_c is reached at t = 5 ns and then decay down to negligible values.

In the direct configuration (probes are plugged at the electrodes), the applied voltage is directly accessible and (for instance) ready to use in simulations to calculate the electric field. In the remote configuration, Figure 2.1, the applied gap voltage can be reconstructed[2]. In Figure 2.5, the measured voltage at the electrode (from Figure 2.4) is compared to the sum of the incident and reflected pulse (Figure 2.2). The comparison agrees within ± 500 V.

[1] The voltage induced by the parasite cable inductance, $V_{ind} = L\ dI(t)/dt$, can also be subtracted. In Orriere's work, the cable inductance induced a difference of 400 V, between the plasma and the measured voltage (Orriere, 2018; Orriere, Moreau and Pai, 2018). However, as for the displacement current, the total energy stored in the inductance is necessarily null at the end of the pulse. Therefore, it is not necessary to include this feature for energy calculations.

[2] Such a reconstruction is easier with longer cables.

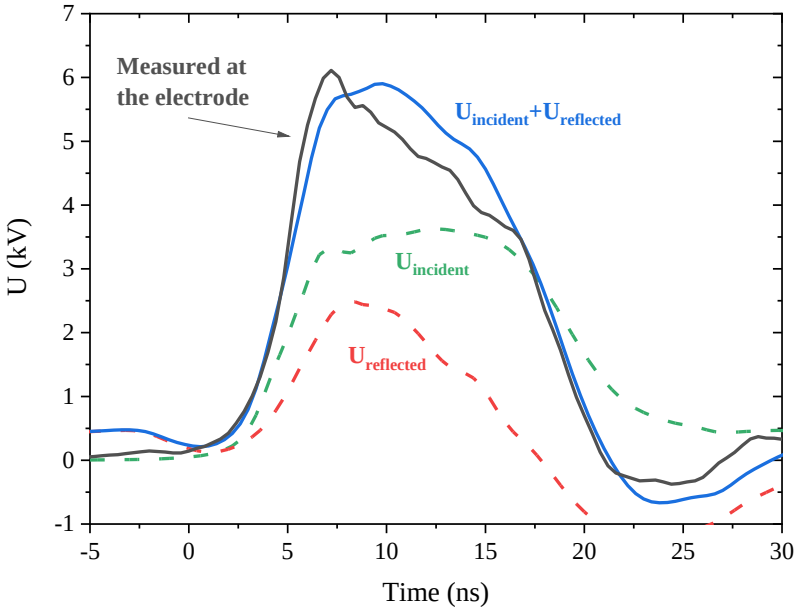

Figure 2.5 Comparison of the measured voltage at the electrode, in grey, and the reconstructed voltage from the incident and reflected pulses, in blue. The incident and reflected pulses are shown in green and red, respectively. The reflected pulse was shifted by -33 ns for synchronization with the incident one.

2.3 Examples of application

2.3.1 Plasma-assisted combustion: energy deposition

The reflected pulse is also subject to an additional reflection when it reaches the generator. A new pulse is therefore sent downstream. Its energy is at most equal to the energy of the first upstream reflection. After several reflections, the pulse energy is entirely absorbed by plasma, the pulser internal circuits, and the cable[1]. In Figure 2.6, the deposited energy is measured with both setups, and we report a difference of 0.06 mJ at t = 50 ns, and 0.04 mJ at t = 300 ns. This systematic error being small, the user is free to place the probes anywhere along the wire linking the electrode to the pulser (the result does not depend on the measurement position).

[1] We will show in Section 2.3.3 that the cable losses are negligible.

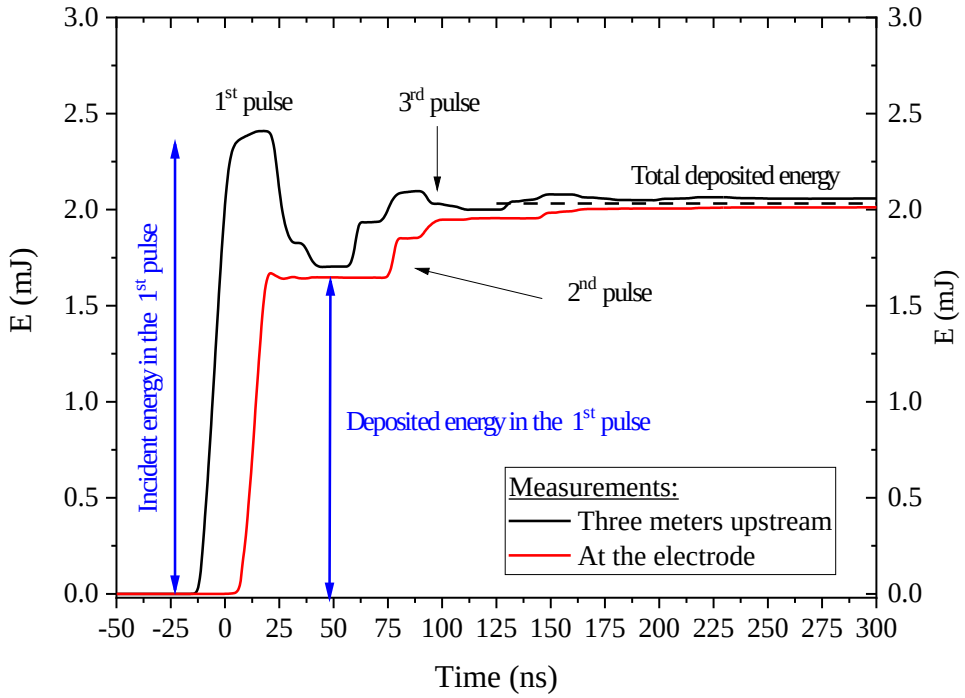

Figure 2.6 Comparison of the energy measurements when the probes are placed three meters away from the electrodes (black curve) or at the electrodes (red curve).

As in Section 2.2, the incident energy is equal to 2.4 mJ. Approximately 0.7 mJ is reflected in the upstream direction. Between 70 and 85 ns, approximately 0.2 mJ is deposited by the 2nd and 3rd pulses. At t = 140 ns, 0.1 mJ is deposited in a 4th pulse. It is worth mentioning that the energy sent by the pulser (2.4 mJ) is independent of the load connected to the wire end. Thus, it is possible to know the maximal deposited energy that can be deposited per pulse. For a pulse of constant voltage, it would be E_{max} defined in Eq. 6.16 where V is the maximum voltage in the coaxial cable, Δt the pulse duration, and Z_{line} the coaxial cable impedance.

$$E_{max} = \frac{V^2 \Delta t}{Z_{line}} \qquad \text{Eq. 2.6}$$

The setup of Figure 2.1 also permits to monitor the electrical stability of the pulser and the plasma, respectively, by a statistical study of the generated and reflected pulses. This study is impossible if the probes are plugged at the electrodes.

2.3.2 Plasma-assisted combustion: electron number density of non-thermal sparks

The results of this section are used notably in Section 8.4.

The plasma impedance can be used to measure the electron number density produced by nanosecond discharges, see (Pai, 2008; Orriere, Moreau and Pai, 2018). Assuming the plasma to be a homogeneous cylinder between two pins, the impedance of the plasma can be written (Raizer, 1991) as:

$$Z_{plasma} = \frac{L}{S\sigma_{plasma}} \quad \text{Eq. 2.7}$$

$$\sigma_{plasma} = \frac{n_e e^2}{m_e \nu_c} \quad \text{Eq. 2.8}$$

where L is the length of the plasma between the two electrodes, S the section of the plasma, n_e the electron number density, ν_c the electron-heavy collision frequency, m_e the electron mass, and e the electron charge. Assuming a plasma to be weakly ionized, we get Eq. 6.16 where, N is the total gas density, σ_n the cross-section of electron-neutral collision and v the average thermal speed of the electrons:

$$\nu_c = N\sigma_n v \quad \text{Eq. 2.9}$$

The speed of the electrons can be simplified in Eq. 6.16 where T_e is the electron temperature.

$$v = \sqrt{\frac{8k_b T_e}{\pi m_e}} = \frac{T_e[\text{eV}]}{1.24} \times 10^7 \text{ cm.s}^{-1} \quad \text{Eq. 2.10}$$

Finally, the ionization fraction of weakly ionized plasma is equal to

$$\frac{n_e}{N} = 2.85 \times 10^{10} \frac{T_e[\text{eV}]}{Z_{plasma}[\Omega]} \frac{L}{S}[\text{cm}]\, \sigma_n[\text{cm}^2] \quad \text{Eq. 2.11}$$

In the remote configuration, the plasma impedance is calculated from Eq. 2.1. In the direct configuration, Z_{plasma} is obtained by dividing the plasma voltage by the conduction current, Eq. 2.12, neglecting its imaginary part.

$$Z_{plasma} = \frac{U_{plasma}}{I_{conduction}} \quad \text{Eq. 2.12}$$

The use of this technic requires that the plasma is homogenous and the knowledge of the plasma section.

2.3.3 Thermal spark: loss in the cables and the generator

In the case of no breakdown, assuming no losses in the cables, the energy reflected in the upstream direction must be equal to the energy initially transported in the downstream direction. A comparison between two cases, with and without discharge, is performed in Figure 2.7. In this case, a 3.5-kV incident pulse is sent to the electrode by pulser #2 in a 2-mm gap in air. The electrodes are placed inside of a sealed cell with pressure

control. At atmospheric pressure, breakdown occurs; the current, voltage, and energy waveforms follow the description given previously. Approximately 2.5 mJ is deposited (black curve in Figure 2.7). At four bars, the breakdown does not occur (dashed gray curve in Figure 2.7). The value of the energy close to zero at t = 40 ns, t = 130 ns, and t = 220 ns shows that no energy is lost in the cables during the reflections. However, during the reflections on the pulser, from the 3.3 mJ contained in the incident pulse, only 1.6 mJ remains in the second pulse, and finally 1.2 mJ in the third one. This measurement demonstrates that, when the pulse is reflected on the generator, a fraction of the pulse energy is absorbed by the generator.

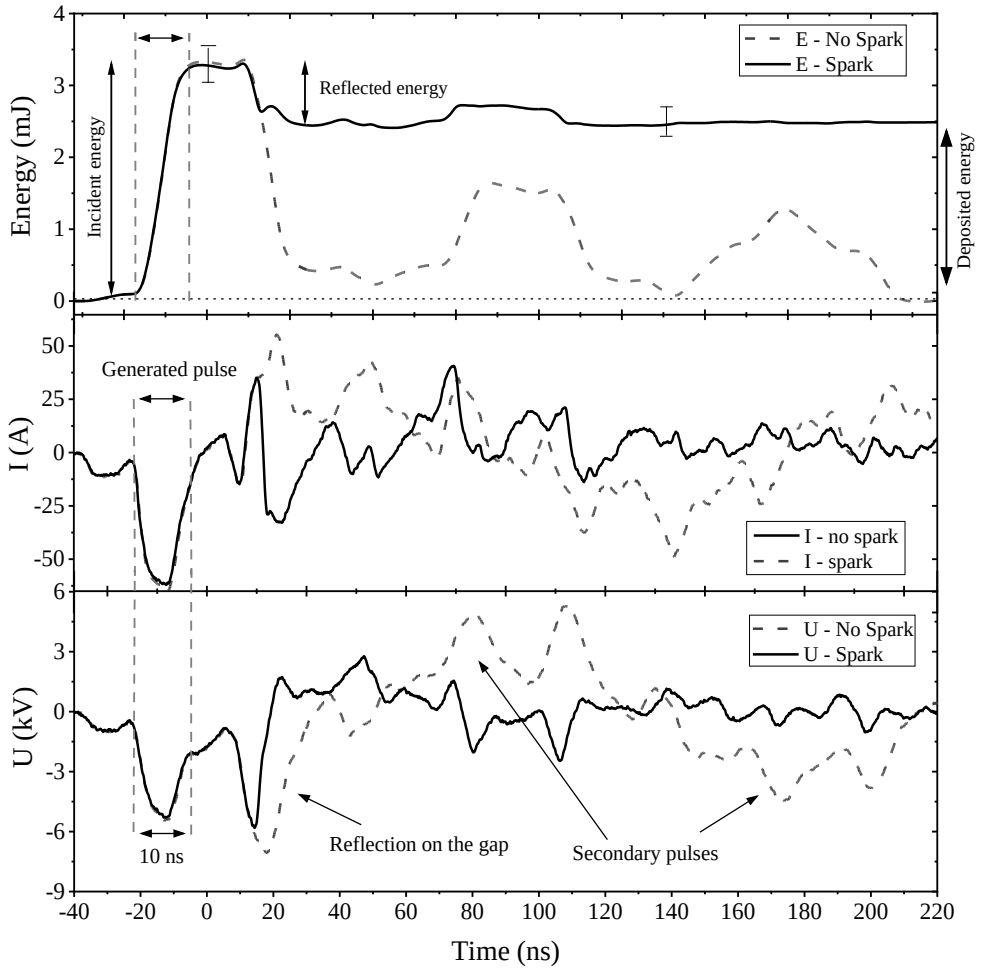

Figure 2.7 Comparison of energy (top), current (middle), and voltage (bottom) with breakdown (solid) and without breakdown (dash).

2.4 Conclusions

In this thesis, the probes are always placed three meters away from the electrodes. The advantages of such a configuration are listed below:

- ✓ Incident pulse monitoring (maximum energy available, stability of the pulser)
- ✓ Secondary pluses monitoring
- ✓ Direct synchronization (the voltage is proportional to the current)
- ✓ Plasma impedance directly available from the reflected voltage
- ✓ Applied voltage on the electrode available after post-processing

Part II: The thermal spark

Chapter 3

The thermal spark in the literature

Nanosecond discharges are often assumed to be non-equilibrium because of their short duration. However, under certain conditions, high electron number densities (10^{18} – 10^{19} cm^{-3}) and temperatures (30,000 K to 50,000 K) are obtained. These conditions are sufficient to reach Local Thermal Equilibrium (LTE) thanks to Coulomb collisions (Barreto, Jurenka and Reynolds, 1977; Stritzke, Sander and Raether, 1977; Almazova *et al.*, 2020). The state of this equilibrium plasma initiated by nanosecond pulses has various denominations in the literature: "spark" in (Stritzke, Sander and Raether, 1977; Shao *et al.*, 2011, 2012; Lo *et al.*, 2017), "filament" in (Stepanyan *et al.*, 2014; Shcherbanev *et al.*, 2016), "constricted/filamentary" in (Shao *et al.*, 2011, 2012; Houpt and Leonov, 2016). In this thesis, we will call "thermal spark" the transient fully ionized plasma generated by a nanosecond pulse in order to emphasize the equilibrium state of the plasma (thermal), and be consistent with the literature of spark transient discharges (Raizer, 1991) (spark).

3.1 Experimental studies of non-thermal and thermal sparks

As shown in (Pai, Lacoste and Laux, 2010b), three regimes of Nanosecond Repetitively Pulsed (NRP) discharges can be distinguished in air: (i) NRP-corona, (ii) NRP-glow, and (iii) NRP-spark. Typical emission spectra of these NRP-corona, glow and spark discharges in air are dominated by $N_2(B)$ and $N_2(C)$ emission. Emission of O atoms and $N_2^+(B)$ is also present in the glow and spark regimes. Criteria for the corona-glow and glow-spark transitions were proposed in (Pai, Lacoste and Laux, 2010b). The corona and glow discharges are characterized by high voltages, low conduction currents (< 1 A), and low deposited energies (less than 100 μJ per pulse) (Pai, Lacoste and Laux, 2010b). These two nonequilibrium discharges produce moderate gas heating (less than 200 K) and relatively low electron number densities (less than 10^{13} cm^{-3} in air at atmospheric pressure) (Pai *et al.*, 2009). Corona discharges are confined near the electrodes, whereas the glow and the spark fill the entire interelectrode space (Figure 3.1). The NRP-spark is characterized by a much higher current (> tens of A) and higher energy deposition (> 1 mJ per mm per pulse) (Pai, Lacoste and Laux, 2010b, 2010a; Stepanyan *et al.*, 2019). The gas temperature in the nanosecond spark was found to increase by a few thousand kelvins in a few tens of nanoseconds due to the ultrafast heating mechanism (Pai, 2008; Pai, Lacoste and Laux, 2010a; Popov, 2011a, 2016b; Rusterholtz *et al.*, 2013). Although the

electron number density reaches 10^{15}-10^{16} cm^{-3} in the nanosecond non-thermal spark (Rusterholtz et al., 2013), the plasma does not reach equilibrium.

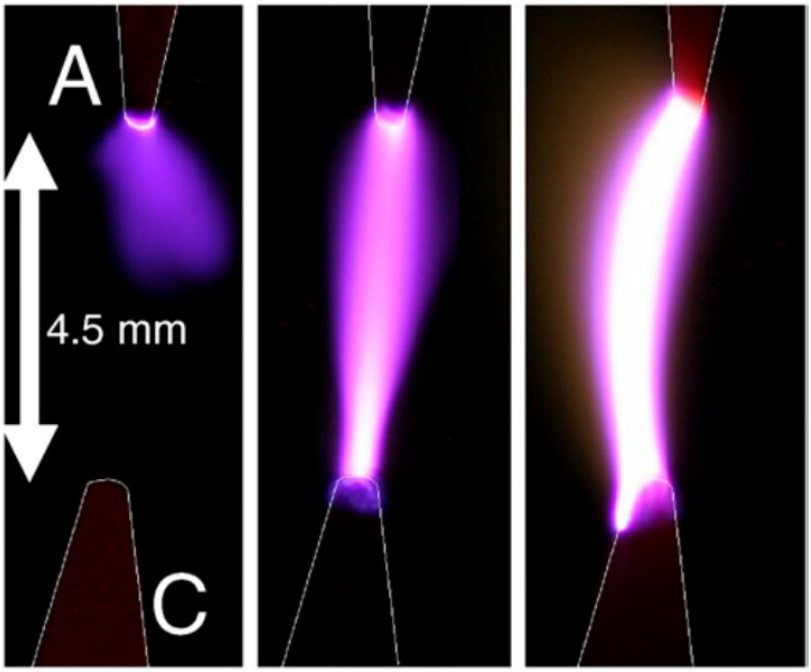

Figure 3.1 Three non-equilibrium nanosecond discharges in the NRP-corona, NRP-glow, and NRP-spark regimes (Pai, Lacoste and Laux, 2008).

In a recent study of single microsecond pulses in ambient air, (Lo *et al.*, 2017) observed a complete ionization of the gas with high electron number densities (10^{18} – 10^{19} cm^{-3}) that do not correspond to any of the discharge regimes described above. The electron number density was measured from the Stark broadening of N^+ lines. The transition from the partially to fully ionized plasma, called "streamer-to-arc" was shorter than 5 ns. The emission spectrum observed in (Lo *et al.*, 2017) is first dominated by $N_2(C \rightarrow B)$ emission (as in the case of the NRP-spark) and then by continuum emission and lines of N^+. This abrupt change of spectrum corresponds to the transition from a partially to a fully ionized plasma. The gas temperature before the transition was measured from $N_2(C \rightarrow B)$ rotational lines and after the transition using a Boltzmann plot of the N^+ lines. These measurements showed a dramatic rise of the gas temperature, from 1200 K to 36,000 K in less than 5 ns. In the afterglow, the slow decay of the electron number density and temperature was explained by isentropic expansion. However, in (Orriere, Moreau and Pai, 2018), this decay was shown to be due to three-body recombination of N^+. Observations of fully ionized plasmas under nanosecond discharges were also reported in water vapor (Sainct, 2014; Sainct *et al.*, 2020) and in air (van der Horst *et al.*,

2012). A similar transition, called "streamer-to-filament", was observed for a 20-ns Surface Dielectric Barrier Discharge (SDBD) (Stepanyan *et al.*, 2014; Shcherbanev *et al.*, 2016). Shcherbanev *et al.* observed a transition from molecular emission to a continuum-dominated spectrum accompanied by an "enormously large" broadening of H_α (20-30 nm) and O_{777nm} (5 nm) lines. No emission of N^+ was recorded at these conditions. The same authors recently measured electron number densities $n_e = 10^{18} – 10^{19}$ cm^{-3} in a similar configuration (Shcherbanev *et al.*, 2019). Their observations are reproduced in Figure 3.2. Similar results were obtained in (Houpt and Leonov, 2016) for a 50-µs SDBD in ambient air. Houpt and Leonov showed that the "contraction" of the discharge channel is associated with the appearance of a continuum spectrum and lines of N^+, N, O, and H_α.

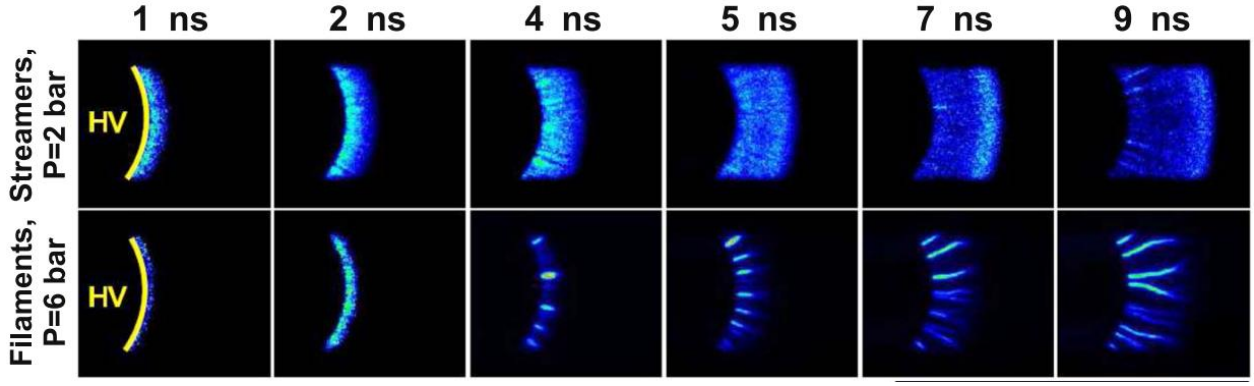

Figure 3.2 Formation of a SDBD streamer by a nanosecond discharge (top). The increase of pressure induced the formation of filaments (bottom). Reproduced with permission from (Shcherbanev *et al.*, 2019)

In 1977, (Stritzke, Sander and Raether, 1977) measured, in a pin-to-pin configuration, the distribution of the electron number density before and during the transition from a discharge dominated by N_2 emission to a discharge dominated by N^+ emission. The map of the electron temperature during and after the transition was measured using lines of N^+, N^{++}, N^{+++}, and N^{++++}. For the conditions of Stritzke *et al.*, the emission of N^+ appeared at electron number densities above 10^{16} cm^{-3}, and the electron temperature reached 50,000 K after the transition. In 1977 also, (Albrecht *et al.*, 1977) measured with Stark broadening the electron number density in a 1-mm discharge generated in N_2 at 1 bar. The spatially resolved emission spectra of N_2 and N^+ were used to obtain the gas and electron temperatures, respectively. In addition, the hydrodynamic effects of the discharge were measured by laser interferometry. Observations of N^+ emission for nanosecond discharges in pin-to-pin configuration were also presented in (Shao *et al.*, 2011, 2012). These authors showed that the "constriction" was accompanied by the emission of spots at the electrodes. A picture and a spectrum of these spots is given in Figure 3.3. It can be noted that lines of the cathode material (Fe) are present along with N^+ and O^+ lines on top of an intense continuum emission.

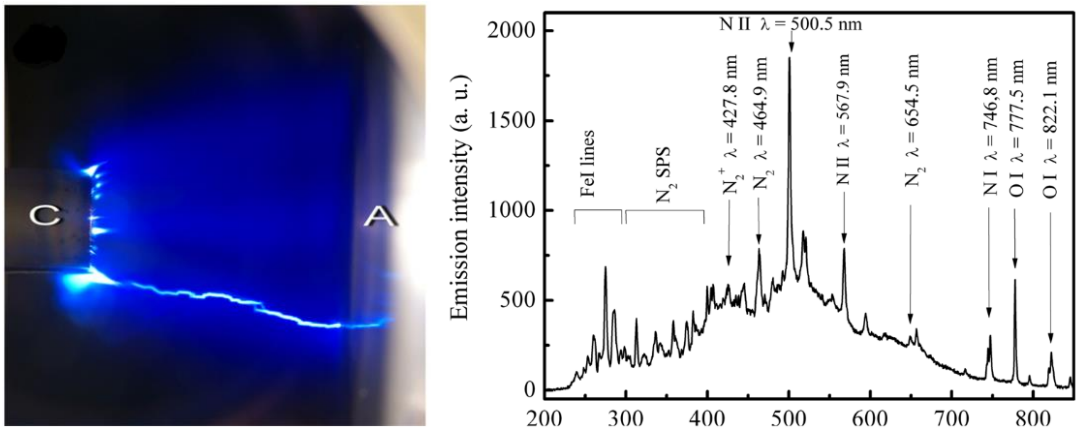

Figure 3.3 (left, picture) Image of the spark emission in air at 1.5 atm with impurities of CH_4. (right, plot) Spectrum of cathode spots recorded in air at atmospheric pressure. (Shao *et al.*, 2012)

Finally, Parkevich *et al.* recently presented laser interferometry measurements of fully ionized nanosecond discharges (Parkevich, Khirianova, *et al.*, 2018; Parkevich, Medvedev, *et al.*, 2018; Parkevich *et al.*, 2019). In their latest work, Parkevich *et al.* (Parkevich *et al.*, 2019) improved the resolution of their system with low astigmatism lenses and showed that the discharge propagates in the form of more than ten fully ionized filaments, 10-50 μm in diameter, whereas the discharge looks homogeneous if conventional lenses are used.

3.2 Numerical studies of non-thermal and thermal sparks

3.2.1 Non-thermal sparks

We begin by a short and non-extensive review of numerical simulations of nonequilibrium discharges (non-thermal sparks) in N_2-O_2 mixtures. Most of them are based on kinetic mechanisms such as those proposed by (Kossyi *et al.*, 1992), which lists 445 reactions including nitrogen and oxygen electronic and vibronic states excitation, or (Capitelli *et al.*, 2000). For the simulation of re-entry plasmas and the interpretation of shock tube experiments, the work of Park is often the reference (Park, 1989, 1990, 1993). Reaction rates for low-temperature plasmas have also been recommended by Herron *et al.* in nitrogen (Herron, 1999) and in humid air (Herron and Green, 2001). These rates are of primary importance for predicting radiation during reentry to Titan's atmosphere (Dutuit *et al.*, 2013).

Simulations of non-thermal sparks in air have been extensively conducted by Popov (Popov, 2001, 2009a, 2009b, 2011a, 2011b, 2013, 2016b), primarily based on the kinetic mechanism of Kossyi *et al*. Vibrational excitation is included, and Popov's simulations are usually resolved along the plasma radius (1D).

In a recent review, Popov (Popov, 2016b) compared his simulations of spark discharges with a series of experimental results.

The first example is a comparison with experiments performed with NRP discharges in a pin-to-pin configuration in preheated air at the EM2C laboratory. In (Stancu, Kaddouri, *et al.*, 2010), the O number density of a reference case was measured by TALIF, whereas in (Stancu, Janda, *et al.*, 2010), the N_2(A) number density was measured by CRDS. The N_2(B) and N_2(C) number densities measured by OES in (Stancu, Kaddouri, *et al.*, 2010) are extended in (Rusterholtz *et al.*, 2013). For the same conditions, Rusterholtz *et al.* also measured the electron number density and the increase of the gas temperature by OES. The experimental results obtained by Stancu *et al.* and Rusterholtz *et al.* are summarized in Figure 24 of (Rusterholtz *et al.*, 2013). In the experiments, the gas temperature increased by 900 K and the O_2 molecules were almost entirely dissociated in about 20 ns. Indeed, the O number density reached 10^{18} cm^{-3} by the end of the pulse, which corresponds to about 50% dissociation of molecular oxygen. Popov numerically reproduced these results, showing that 63% of the atomic oxygen was produced by N_2^* quenching and only 37% by electron-impact dissociation of O_2 (Popov, 2016b). The evolution of the N_2(C) number density was within a factor of five[1] of the experimental value (Popov, 2013). The energy spent on O_2 dissociation was found to be relatively low, 6-7 eV/atom, while the bond dissociation energy of O_2 is around 5.15 eV. It can be noted that the N_2^* quenching by atomic O was initially neglected in the work of Popov (Popov, 2001). After the inclusion of this mechanism (Popov, 2016b), the numerical simulations accurately followed the experimental results of (Rusterholtz *et al.*, 2013), see 'curve 1.' in Figure 3.4.

[1] This rescaling is presented in Figure 5 of (Popov, 2013). The results presented in (Popov, 2016b) are very similar to those in (Popov, 2013) but the comparison between the measured and simulated N_2(B, C) number density are not provided.

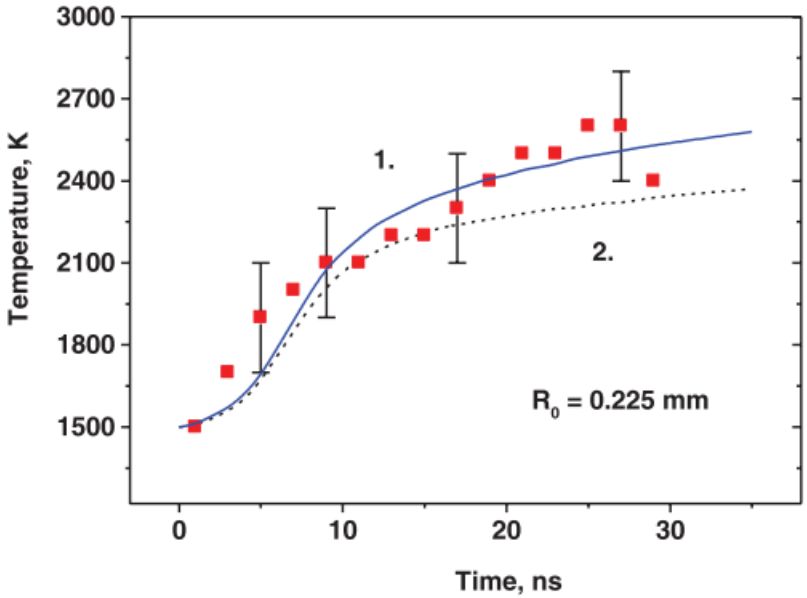

Figure 3.4 Comparison of the temperature measurements of (Rusterholtz *et al.*, 2013) and the simulations of Popov with (solid line) and without (dotted line) inclusion of the N_2* quenching by atomic oxygen. (Popov, 2016b).

In (Popov, 2016b), a second comparison is presented with experiments performed at the CORIA laboratory, using nanosecond discharges applied at 10 Hz in a pin-to-plane configuration (Lo *et al.*, 2014; Lo, Cessou and Vervisch, 2014). Vibrational populations of N_2 and O_2 ground state were measured by spontaneous Raman scattering, and the rotational temperature was obtained by Optical Emission Spectroscopy (OES). The simulation of Popov compares well with the experimental data of Lo *et al.* (Popov, 2016b). Remarkably, the degree of oxygen dissociation and the spatial profiles of temperatures are accurately matched.

Flitti and Pancheshnyi also conducted simulations of spark discharges, mostly based on the reaction set of Capitelli *et al.* and Popov (Flitti and Pancheshnyi, 2009). They studied the mechanism of ultrafast heating in an N_2-O_2 mixture under reduced fields ranging from 50 to 400 Td. Flitti and Pancheshnyi used ZDPlasKin and BOLSIG in their simulation, and made their code freely available[1] (Hagelaar and Pitchford, 2005; Pancheshnyi *et al.*, 2008).

[1] http://www.zdplaskin.laplace.univ-tlse.fr/author/sergey-pancheshnyi/index.html

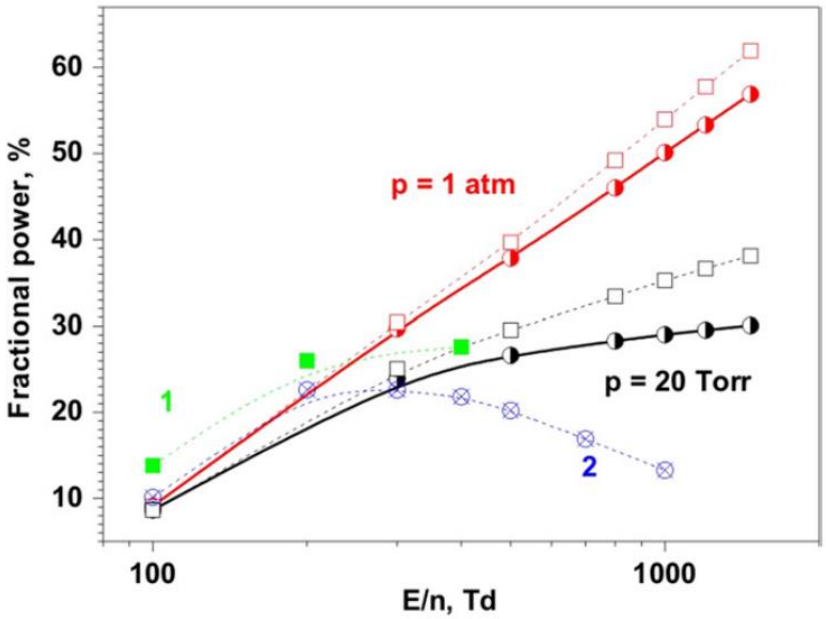

Figure 3.5 Fraction of electron power transferred into heat in dry air at 20 Torr and 1 atm according to the calculation in (Aleksandrov *et al.*, 2010). Their results are compared to the mechanism developed in (Flitti and Pancheshnyi, 2009), green squares of curve 1, and (Popov, 2001), blue circles of curve 2. Reproduced from (Aleksandrov *et al.*, 2010).

For the reduced fields up to 1000 Td, Aleksandrov *et al.* extended Popov's kinetic mechanism (Aleksandrov *et al.*, 2010). Notably, the excitation of N_2 excited states above 13.5 eV and the ion-ion recombination were included. At E/N = 1000 Td, the heating due to these two processes is, at least, of the same importance as the quenching of N_2 excited states. Aleksandrov *et al.* showed that their extension of Popov's mechanism was necessary at E/N > 300 Td where a significant fraction of the electron energy is spent on ionization. Indeed, Figure 3.5 demonstrates that, at 1 atm and for E/N > 300 Td, the fraction of energy transferred to heat in 1 µs is at least doubled compared to Popov's mechanism (Popov, 2001).

The simulation of ultra-fast heating has also been conducted by the team of IST in Lisbon University. A topical review (Guerra *et al.*, 2019) extends the validation of the IST-Lisbon LXCat database (Alves, 2014) and describes, among various results, the heating of 5-ms discharges in air at 1 Torr. The temperature measurements were performed by absorption spectroscopy in (Hübner *et al.*, 2012) and demonstrated a 200-K increase in their conditions. Guerra *et al.* showed that ultrafast-heating is responsible for a 150-K increase in less than 1 ms. The increase of temperature is improved compared to their previous work by adjusting the heat conduction to the wall, whereas the effect of VT relaxation is relatively minor.

Bak and Cappelli published a mechanism for nanosecond discharges in the glow and non-thermal spark regimes (Bak and Cappelli, 2015). They initially implemented the complete mechanism of Kossyi *et al.* and

reduced its size by discarding the unimportant reactions. Practically, they authorized a tolerance of 1% in terms of production and heating rate between the reduced and complete mechanisms. They found that the NRP-glow regime can be accurately simulated with a reduced mechanism of 20 species and 49 reactions, while 19 species and 48 reactions are sufficient to simulate the NRP-spark.

Finally, Laux et al. (Laux *et al.*, 1999) proposed a kinetic mechanism mainly based on (Park, 1993) to describe two-temperature discharges at T_{gas} = 2000 K and 8000 K < T_e < 18,000 K. This reaction set will be used as a baseline mechanism in this work and is be detailed later.

3.2.2 Thermal sparks

Numerical simulations of the thermal spark formation are scarce in the literature. However, this domain is evolving rapidly (Popov, Babaeva and Naidis, 2019). In (Shcherbanev *et al.*, 2019), kinetic simulations were performed in an attempt to explain the fast increase of n_e up to values of about 10^{19} cm^{-3}, following a nano-second discharge in nitrogen at 6 bar, with an initial reduced field of 230 Td. The initial electron number density was assumed to be 10^{15} cm^{-3}.

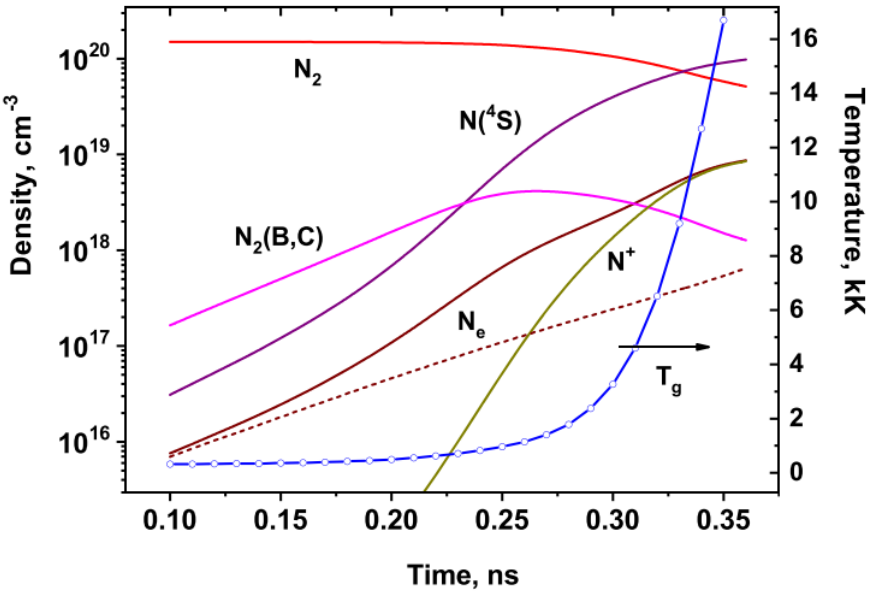

Figure 3.6 Calculated density of main species and gas temperature in discharge in nitrogen at P = 6 bar, $T_{gas,0}$ = 300 K, $(E/N)_0$ = 230 Td and $n_{e,0}$ = 10^{15} cm^{-3}. The dashed line is n_e calculated without the N_2^* ionization. Reproduced from (Shcherbanev *et al.*, 2019).

Figure 3.6 shows the evolution of the dominant species calculated in (Shcherbanev *et al.*, 2019). From t = 0.1 ns to t = 0.35 ns, the electron number density increases by three decades, which corresponds to the abrupt formation of filaments measured in their work. The formation of $N_2(B)$ and $N_2(C)$ molecules plays a key role as it accelerates the ionization process. Indeed, if this process is not included, the ionization is slower (see the dashed curve in Figure 3.6). Shcherbanev *et al.* calculated the heat released by the recombination of electrons with O_2^+ and N_2^+ at $n_e \sim 10^{18}$ cm^{-3} and showed that a temperature increase of 14,000 to 22,000 K could be obtained in about 1 ns. The authors concluded that the plasma approaches[1] LTE, and hence full ionization, in less than 1 ns. The authors also showed that the SDBD filamentation is not the result of magnetic compression of the plasma channel. Finally, they noted that the question of the filament's origin remains open.

3.3 Objectives of this study

Most investigations on the thermal spark remained experimental and isolated. Some studies were more focused on the formation or the recombination of the fully ionized plasma. In this part, we aim to:

- Rigorously describe the stages of formation of the thermal spark.
- Discriminate the typical features of the thermal spark for easier identification in other conditions.
- Explain the slow recombination of the electrons in the thermal spark afterglow.

The conclusions derived from these three tasks must be coherent with the literature on the thermal spark. The mechanism of the thermal spark formation also needs to be determined. For that purpose, a kinetic mechanism was developed, keeping in mind two objectives:

- Identify the critical reactions responsible for the fast full ionization of nanosecond discharges.
- Explain the fast increase of temperature during the thermal spark formation.

This kinetic study is among the first ones. Hence, our objectives must be meticulously completed, as our conclusions will lay grounds for future investigations.

[1] The relative impact of ion recombination on the heating is challenged in Section 6.1.3, where the impact of electron-ion elastic collisions is quantified.

In Chapters 4 to 6, we characterize experimentally and numerically the thermal spark formation and recombination. In Chapter 4, the influence of air pressure in the range 50 – 1000 mbar is investigated experimentally at 300 K. The transition from a non-thermal to a thermal spark is decomposed in five steps. Then, the evolution of n_e and T_e is studied in the plasma afterglow. We show that the decay of n_e is due to the isentropic expansion of the plasma in chemical equilibrium. Most of the experimental results presented in Chapter 4 were published in (Minesi, Stepanyan, *et al.*, 2020).

In Chapter 5 the mechanism of air ionization by a single nanosecond discharge under atmospheric conditions is provided and tested. In Chapter 6, the mechanism of the thermal spark formation is studied for an initial reduced field of 240 Td, which is close to the experimental conditions studied in Chapter 4. We will see that the excitation and ionization of atomic species (N and O) play a key role on the thermal spark formation. Also, the importance of heating by electron-ion collisions is demonstrated. Finally, we will compare the experimental and numerical evolution of n_e during the thermal spark formation at ambient pressure.

Chapter 4

Experimental characterization of the thermal spark

4.1 Experimental setup

An overview of the experimental setup is shown in Figure 4.1. The experiments presented in Chapters 4-6 are performed with nanosecond discharges initiated by single high-voltage pulses between pin tungsten electrodes. The radius of curvature of the electrodes is approximately 300 μm, and the inter-electrode distance is 0.9 or 2 mm. The discharges are initiated by a generator (FID FPG 30-100MC4K) producing pulses of 10-ns duration, amplitudes up to 30 kV and Pulse Repetition Frequencies (PRF) up to 100 kHz. For the experiments at various pressures presented in Section 4.2, a positive voltage pulse is sent to the anode and a negative voltage pulse to the cathode. For the experiments presented in Section 4.3, practical reasons dictated the use of only a negative pulse at the cathode and a grounded anode. A summary of these two experimental configurations is presented in Table 4.1. Low PRFs of 10 and 50 Hz are used to reproduce the conditions of single-pulse experiments.

The electrical characteristics of the discharges are monitored by two high voltage probes (LeCroy PPE20kV) and two current probes (Pearson 6585) connected to an oscilloscope (Lecroy HDO 6104 or Lecroy Wavepro 7100A). The high-voltage generator and the camera are synchronized with a gate-and-delay generator (BNC Model 575). The electrodes are placed inside a sealed cell in order to control the pressure (50 – 1000 mbar) and gas composition (pure air or a mixture of air with 1.6% of hydrogen).

The current and voltage measurements are performed about midway of a 7-m coaxial cable, as described in Section 2.2. Figure 4.2 presents typical voltage and current waveforms for a 5.5-kV high voltage pulse sent to a 2-mm interelectrode gap (setup #2 in Table 4.1). The cable length induces a delay of 20 ns between the electrical and the OES measurements. This delay was taken into account for the synchronization of the voltage and emission signals. The energy displayed at the top of Figure 4.2 is the integral over time of the product of voltage and current. In the case of breakdown (black solid curves), the generated pulse measured by the probes begins at t = - 20 ns and carries approximately 3.5 mJ. About 1 mJ of this energy is reflected

to the generator, as shown by the energy decay in Figure 4.2 at t = 20 ns. *Therefore, about 2.5 mJ are deposited in the plasma.* Further reflections of the pulse between the electrodes and the generator do not change the energy deposited in the plasma by more than 10%. If a positive pulse and a negative pulse are sent to the anode and the cathode, respectively, the energy is measured in both cables and summed. The applied voltage at the cathode is the sum of the incident and reflected pulses and results in a maximum voltage of U_{max} = – 10 kV. We also confirmed that there are no significant losses in the electrical circuit if breakdown does not occur. The gray dashed curve in Figure 4.2 presents the waveforms for the case when breakdown is prevented by increasing the pressure to 4 atm. In this case, the incident energy (3.5 mJ) is sent to the electrode (t = -20 ns) and is completely reflected to the pulser (t = 20 ns). The estimated relative error on the deposited energy is 20% (Pannier, 2019, Appendix D). Finally, in Figure 4.2, it should be noted that the 1-kV at $t \approx 30$ ns is due to a peculiarity of the pulser.

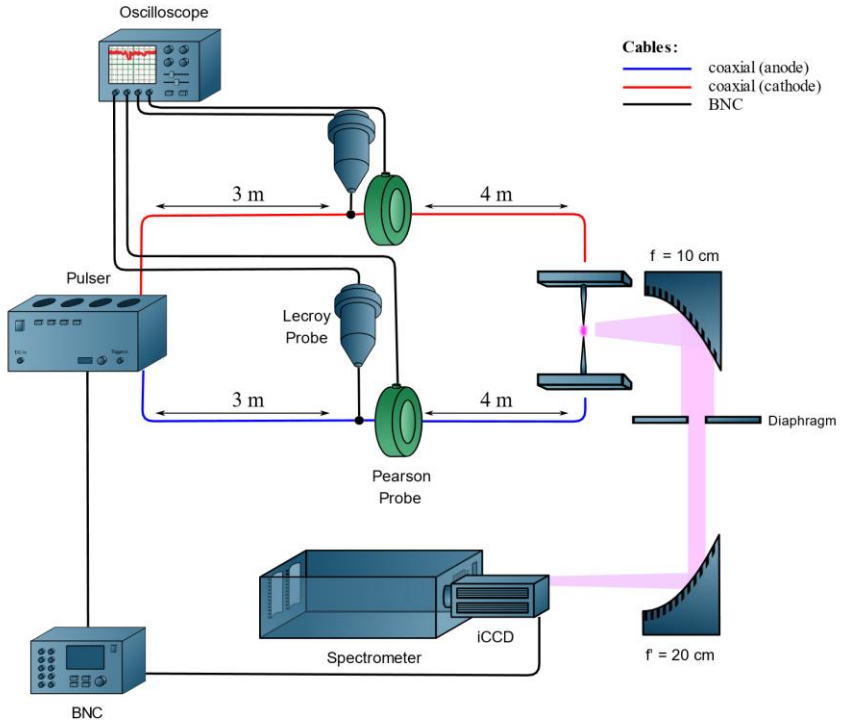

Figure 4.1 Experimental setup for the cathode-anode configuration. In the cathode-ground configuration, only the red coaxial cable is used, and the other electrode is grounded.

Optical Emission Spectroscopy (OES) is used to measure electron number densities and electron temperatures. The discharge is placed at the focal point of an off-axis parabolic mirror (f = 10 cm), as shown in Figure 4.1. The collimated light from the plasma is then refocused by a second parabolic mirror (f = 20 cm) onto the monochromator (Acton 500i) entrance slit. The monochromator is equipped with two gratings of

300 and 1800 gr/mm, both blazed at 500 nm. An ICCD camera (Pi-MAX4) coupled to the monochromator is used to record the spectra with a minimum gate of 450 ps. The pitch of the pixels on the ICCD is 13 μm. A HeNe laser (Thorlabs at 632.8 nm) is used to determine the instrumental broadening of the OES system. The discharge spatial and temporal reproducibility is sufficient to perform phase-locked acquisitions for imaging and OES experiments because the temporal jitter of the pulse is below 0.5 ns and the displacement of the axis of the plasma channel is about ±50 μm from shot to shot. The discharge imaging is performed using the zeroth order of diffraction of the monochromator grating. A 150-μm slit, aligned with the interelectrode axis, is used to capture the entire emission of the discharge. The width of the slit is sufficient to capture the discharge, even with its fluctuations in position. The overall optical system has a spatial resolution of about 8 μm per pixel.

Table 4.1 Summary of the two configurations used in this work.

Configuration	Setup #1	Setup #2
Electrode polarities	Cathode-Anode	Cathode-Ground
Interelectrode gap	0.9 mm	2 mm
Deposited energy	2.5 - 3.5 mJ per pulse	2.5 mJ per pulse
Amplitude of incident pulse	Cathode: -5 kV Anode: +3.5 kV	Cathode: -5.5 kV
Pressure	58 mbar – 1 bar	1 bar
Gas	Ambient air	Ambient air + 1.6% of H_2
Data used in:	Section 4.2	Section 4.3
Study of:	Effect of pressure	Electron number density evolution

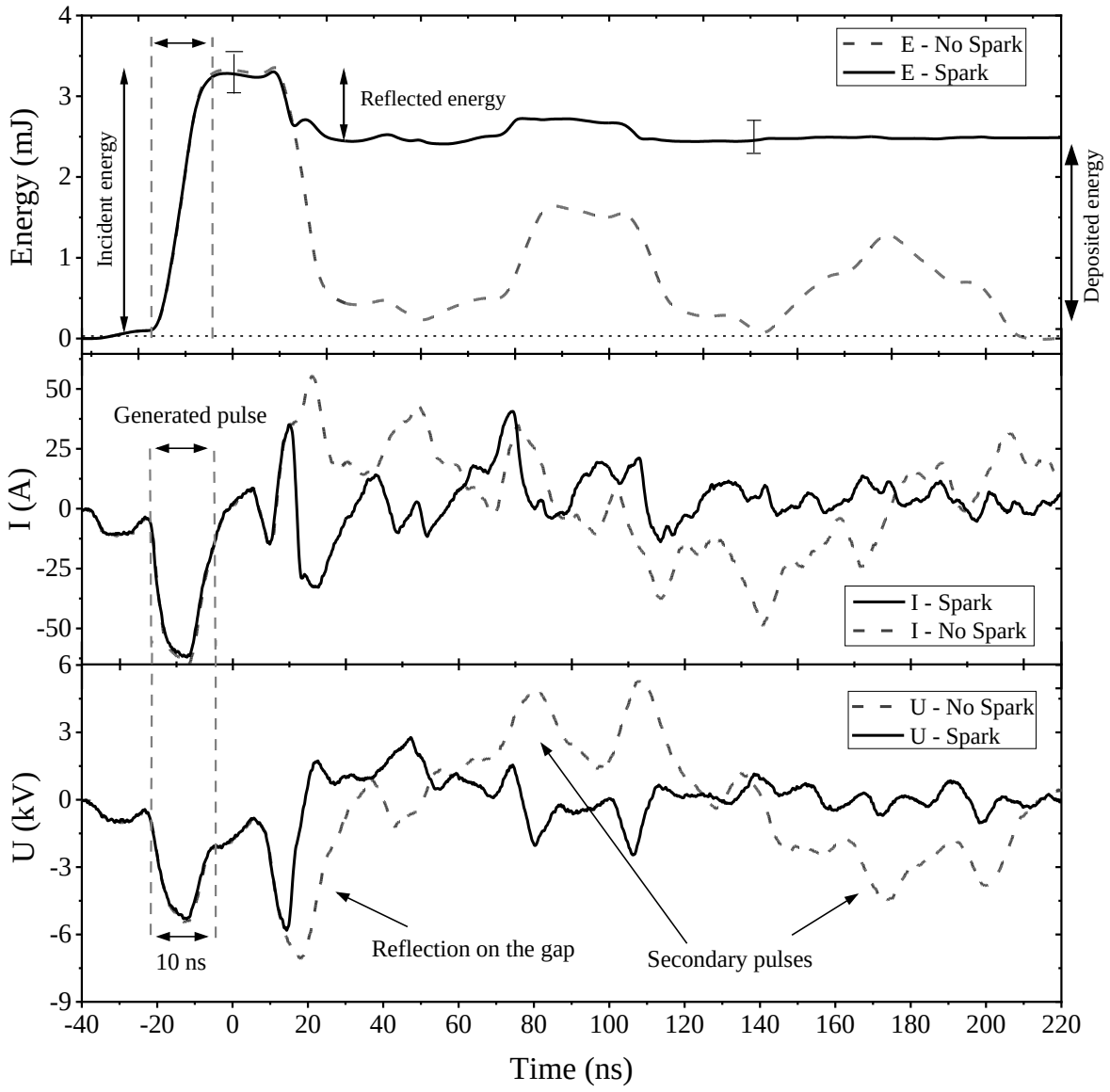

Figure 4.2 Voltage, current and energy waveforms for the cathode-ground configuration in air in a 2-mm gap (setup #2). A thermal spark is obtained at atmospheric pressure (solid black lines). At 4 atm, the breakdown is prevented (dashed gray lines). Note that this figure is reproduced from Figure 2 of (Minesi, Stepanyan, *et al.*, 2020) where the "No Spark" and "Spark" currents were erroneously swapped.

4.2 Influence of pressure on the thermal spark formation

This section presents observations of the thermal spark produced by a single nanosecond discharge in the cathode-anode configuration (setup #1). The images of total emission, shown in Figure 4.3, are obtained with a Canon 5D Mrk II digital camera. The exposure time of the camera is 100 milliseconds, which is longer than the discharge duration and its afterglow. At low pressure (50 and 80 mbar), the discharge forms a bright channel between the pins and a corona covering mostly the cathode (top electrode in Figure 4.3). The emission radius (Half Width at Half Maximum, noted HWHM) of the channel is 250 µm at 50 mbar. The bright cathode and anode spots have a typical radius between 50 and 150 µm. When the pressure increases to one atmosphere, the visible channel radius reduces to 140 µm, the spots and the corona disappear, and the color of the discharge changes from purple to white. These spots were already reported by (Shao *et al.*, 2012; Parkevich, Medvedev, *et al.*, 2018).

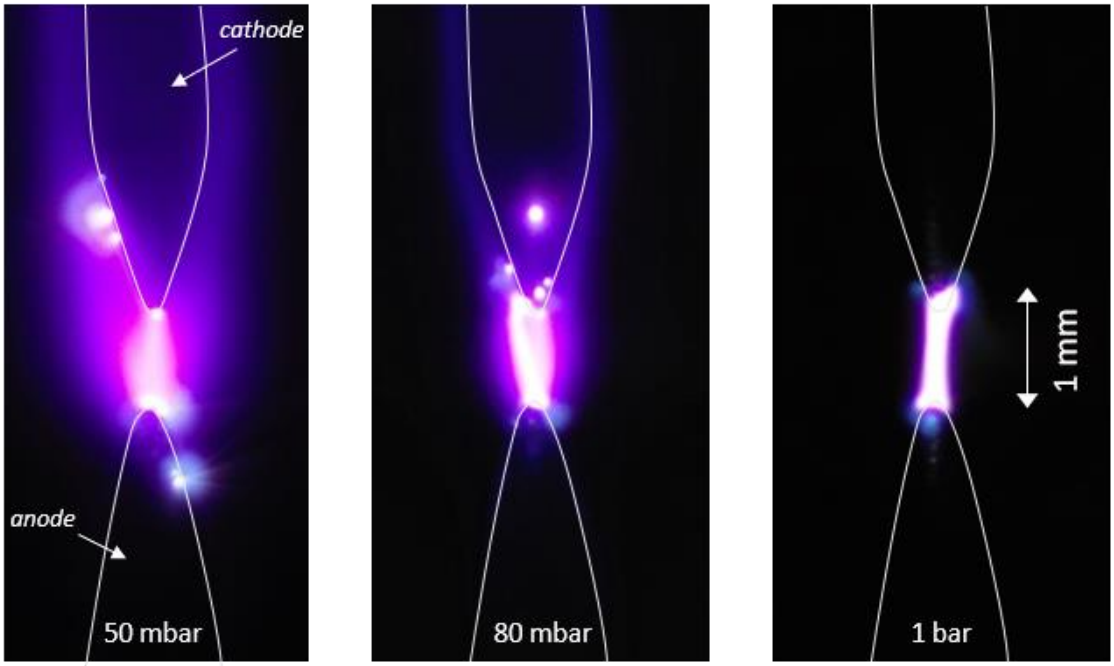

Figure 4.3 Photographs of single ns-discharges in real colors (Canon 5D Mrk II) at 50 mbar, 80 mbar and 1 bar. The electrode contours are represented by the white lines. In this case only, the distance between the electrodes (top: cathode, bottom: anode) is 1 mm. The intensity scale is adjusted in each picture. Cathode spots are visible at 50 mbar and 80 mbar. An anode spot is visible at 50 mbar.

To observe the evolution of the plasma during the applied pulse at different pressures, ICCD imaging and OES are performed with a temporal resolution of 480 ps. The discharge emission is recorded from 0 to 100

ns in steps of 0.5 ns. Figure 4.4 shows the map of total emission obtained for a single pulse nanosecond discharge initiated in ambient air at 58, 240, 600 and 1000 mbar. The distance between the electrodes is 0.9 mm. The intensity scale is logarithmic and identical for all images.

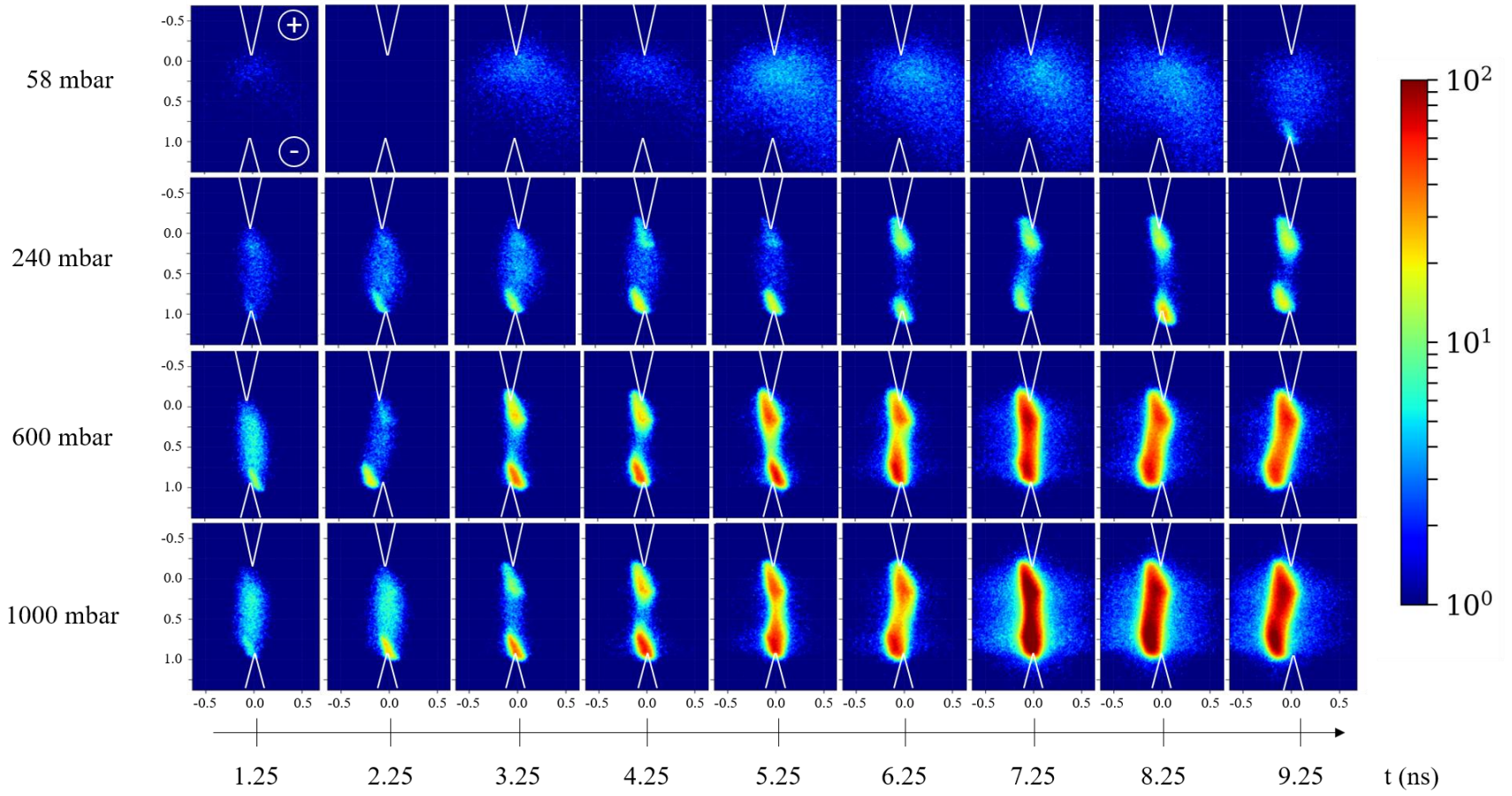

Figure 4.4 Phase-locked evolution of the total recorded intensity in a logarithmic scale of a nanosecond discharge (setup #1, inter-electrode gap of 0.9 mm) at 58, 240, 600, and 1000 mbar. The distance is shown on all pictures in mm units and the position of the electrodes is represented by white lines. The time step is 1 ns with camera gates of 0.48 ns (for example, the measurement at 4.25 ns is recorded from 4 to 4.5 ns). The cathode and the anode are respectively marked by – and + signs in the top left corner. These images are all single-shot and are not Abel-inverted.

At 58 mbar, a streamer propagates from the anode to the cathode. No sharp increase in the emission is recorded during the propagation phase. At the end of the pulse (9 – 10 ns), a bright filament appears at the cathode.

At 240 mbar, the streamer propagation is faster and cannot be resolved with the present camera gate (i.e. the interelectrode gap is filled within 0.5 ns). A cathode filament appears at about t = 2.25 ns and an anode filament at about t = 4.25 ns. These 250-µm long filaments form within less than 0.5 ns. Therefore, their formation cannot be resolved with the camera. This means that either the filaments are created simultaneously in the entire volume or that they propagate from the electrode surface toward the middle of the gap at a speed above 5×10^5 m/s (0.5 mm/ns).

At pressures below 450 mbar, the filaments do not propagate toward the middle of the gap after they are formed. Above 600 mbar, however, the filaments start to propagate toward each other and rapidly merge (in less than 2 ns) in the middle of the gap. The length and diameter of the filaments are independent of the pressure in the studied conditions. Figure 4.5 presents the propagation speed of the filaments *versus* pressure. One can see that the cathode filament is typically faster than the anode one (~ 5×10^4 m/s *versus* ~ 2.5×10^4 m/s).

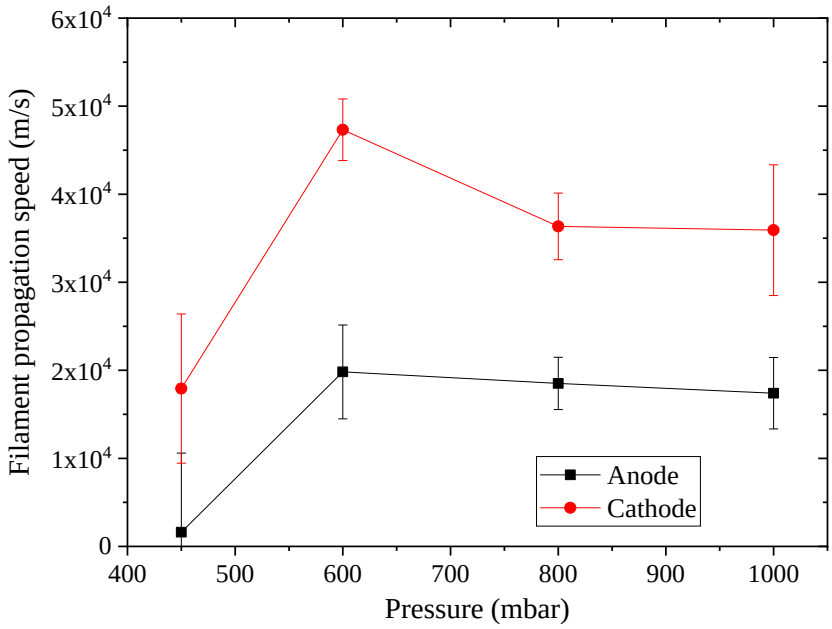

Figure 4.5 Propagation speed of the filaments from 400 mbar to 1 bar. At the anode, the speed is relatively constant ≈ 20 µm·ns^{-1}. The speed of propagation of the cathode filament is of the same order of magnitude, with a peak at 5×10^4 m·s^{-1} = 50 µm·ns^{-1}.

The discharge spectra integrated over the pulse duration and plasma volume are shown in Figure 4.6. The streamer emission (i.e. not the filaments) at low pressure is mainly due to the N_2(C→B) and N_2^+(B→X) transitions. The filaments that appear at higher pressure are characterized by a continuum

emission. Several intense emission lines around 500 nm can also be identified, corresponding to transitions from $N^+(^3S, ^3P^0, ^3F^0)$ (Kramida *et al.*, 2018). Shcherbanev *et al.* (Shcherbanev *et al.*, 2019) also showed that the constriction of an SDBD is accompanied by a transition from a broad (~ 40 µm) channel with N_2 emission to a thin channel (~ 18 µm) with N^+ emission.

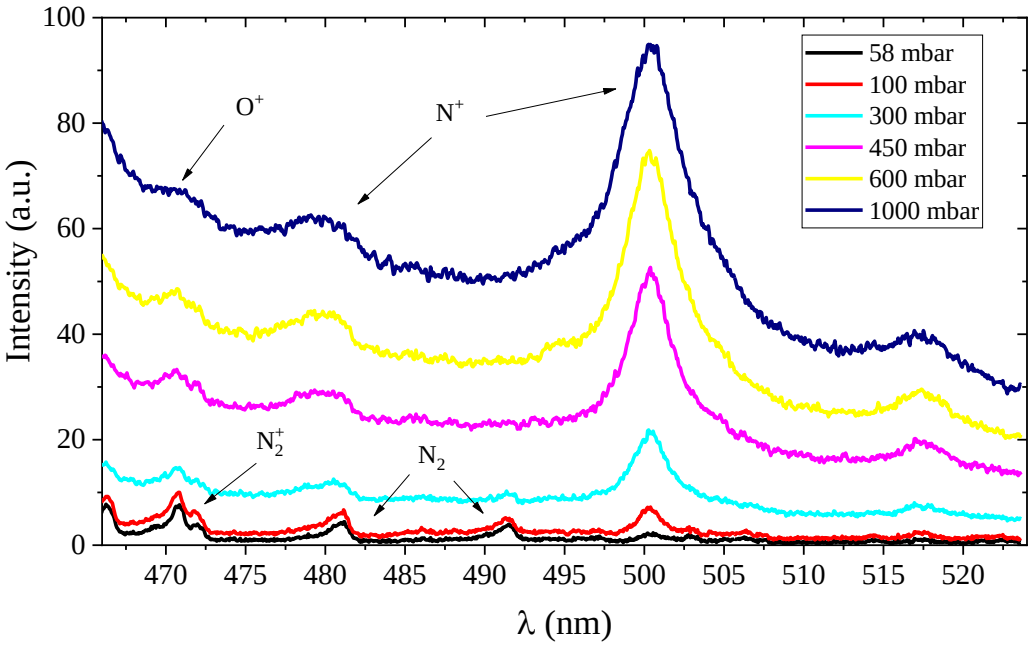

Figure 4.6 Measured emission spectra (middle of the gap) integrated from t = 0 to 10 ns at several pressures. The interelectrode gap is 0.9 mm (setup #1). For the sake of clarity, only six spectra are displayed.

The data presented in Figure 4.4 and Figure 4.6 show that the thermal spark formation comprises the followings steps: (i) formation of a preionized channel between the electrodes; (ii) creation of a 250-µm long filament at the cathode characterized by N^+ emission; (iii) 1 – 2 nanoseconds later, creation of a 250-µm filament at the anode; (iv) the filaments start propagating to the middle of the gap at a speed ~ 10^4 m/s; (v) filaments merge at the gap center (i.e. the thermal spark is formed). These steps of formation were also reported in the work of Orriere (Orriere, 2018, p.82). The filaments were observed in a 200-µm and 1-mm gap and their formation could also not be resolved with a 3-ns gate (Orriere, 2018, p.82).

The molecular emission at low pressure (58 mbar) and the atomic/continuum emission at high pressure (1 bar) show that the plasma composition varies significantly in the considered pressure range. The dependence of the deposited energy as a function of the pressure is presented in Figure 4.7. The energy does not vary significantly in the studied pressure range, even though the spectra show a drastic change in the plasma (N^+ and continuum emissions *versus* N_2 band emission). This indicates that there is *no significant change in the total deposited energy at the transition from a non-thermal to a thermal spark*.

Thus, the energy appears to be deposited in a smaller volume for the thermal spark, which is consistent with the observation of Shcherbanev *et al.* (Shcherbanev *et al.*, 2019).

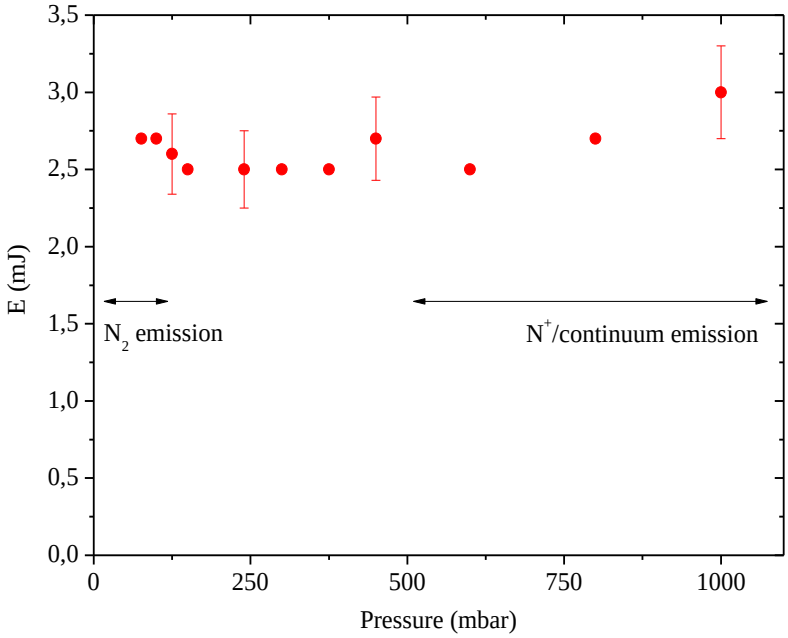

Figure 4.7 Deposited energy as a function of pressure for a gap of 0.9 mm between the electrodes (setup #1). The ranges dominated by the emission of N_2 or N^+ are shown by the arrows.

4.3 Evolution of the electron number density at 1 atm

In this section, the objective is to study the evolution of the electron number density, n_e, and of the electron temperature, T_e, in the post-discharge of the thermal spark at 1 atm. The gap is 2 mm, the anode is grounded, and the total deposited energy is equal to 2.5 mJ (Table 4.1). Single-shot images of the discharge development sequence for this case are shown in Figure 4.8. As described in Section 4.2, the thermal spark develops according to the following sequence: (i) a homogeneous plasma is formed between the electrodes; (ii & iii) the filaments appear at the cathode and the anode; (iv) the filaments propagate; and (v) merge at the end of the pulse. With setup #1, the filaments had a constant length of 250 µm. With setup #2, the filaments are twice as long (500 µm). The filament length is therefore field-dependent. This aspect is not investigated any further.

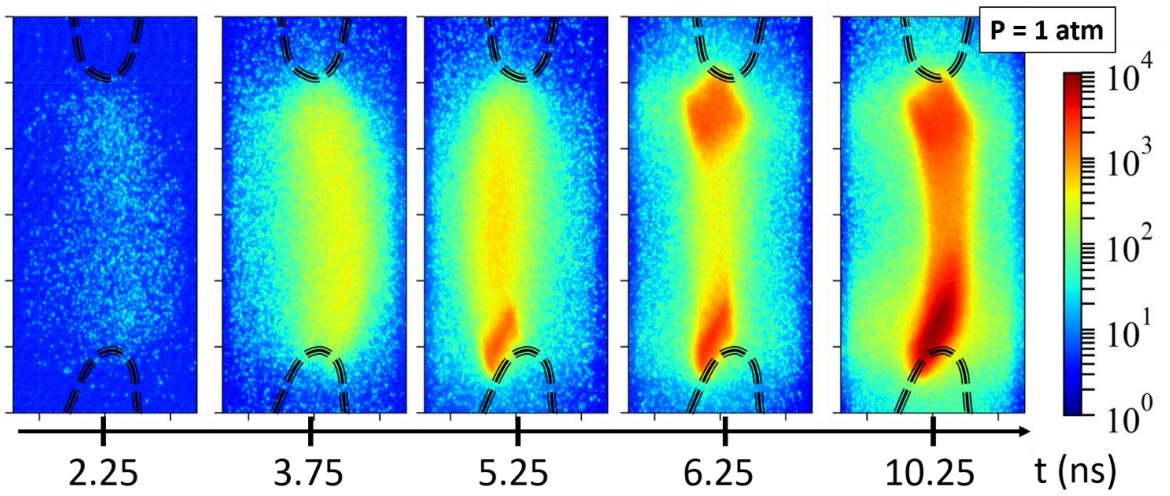

Figure 4.8 Phase-locked images with gates of 0.48 ns of a single nanosecond discharge applied across a 2-mm gap (setup #2). The images are single shot and are not Abel-inverted. The cathode is at the bottom.

The electron number density, n_e, is measured from the Stark broadening of N^+ lines with a temporal resolution of 0.5 ns. The electron temperature, T_e, is assumed equal to the excitation temperature and obtained from the relative emission intensity of the three major groups of N^+ lines shown in Figure 4.9. The excited states of N^+ are assumed to follow a Saha-Boltzmann distribution in equilibrium with the free electrons, as considered in previous studies (Albrecht *et al.*, 1977; van der Horst *et al.*, 2012; Lo *et al.*, 2017; Orriere, Moreau and Pai, 2018).

The following procedure is applied to obtain n_e. A spectrum is generated by an in-house extension of the Specair code[1] (Laux *et al.*, 2003). The lines are convolved with the instrumental broadening line-shape (fixed) and a Lorentzian (line-dependent). The width of the Lorentzian component and the electron temperature are varied until good agreement between the measured and simulated spectra is reached. The electron temperature is used to determine the Van der Waals and resonant broadening widths using the constants and formulas given in Section 1.3. The Stark width is obtained by subtracting the Van der Waals and resonant widths from the total Lorentzian width of each line. The Stark width is then converted to n_e using the work of Griem (Griem, 1974). The Doppler broadening is negligible. A typical fit of the thermal spark emission spectrum is shown in Figure 4.9. The estimated errors on the electron number density and temperature measurements are ±15% and ±10%, respectively, based on the maximal uncertainty of the fit and the uncertainty in the Van der Waals width. The values of n_e and T_e extracted from this spectrum are $1.4 \pm 0.2 \times 10^{19}$ cm^{-3} and 39,300 ± 3900 K.

[1] www.spectralfit.com

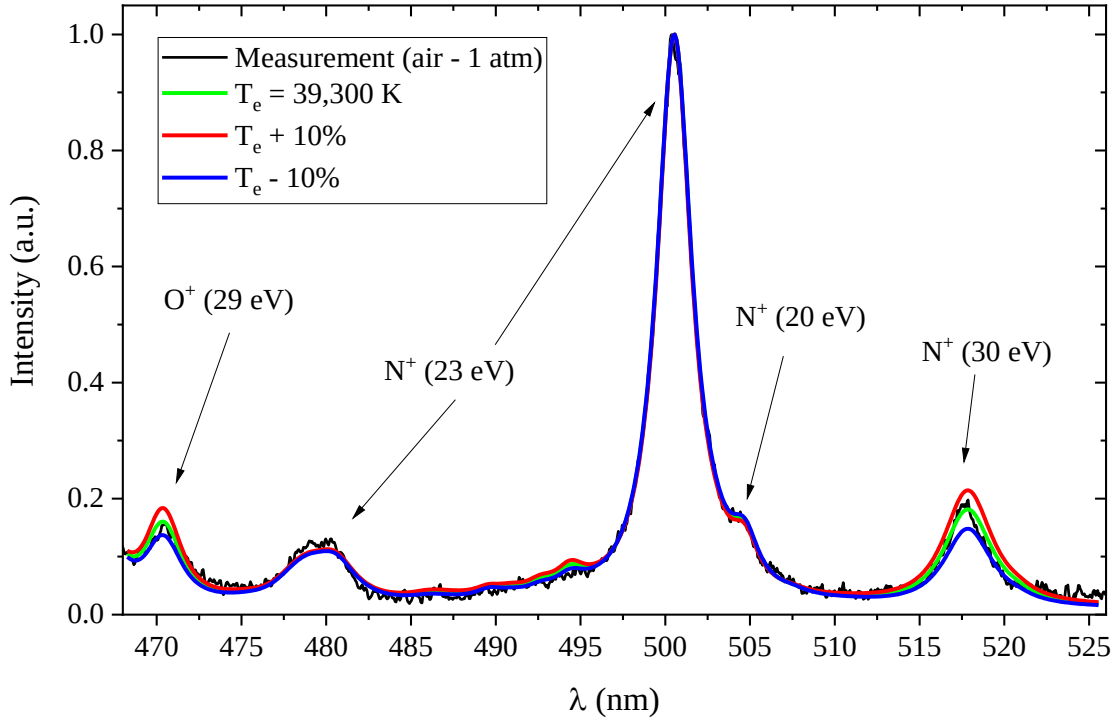

Figure 4.9 Measurements (black) and best fit (green) of the N^+ and O^+ lines emitted by the discharge at t = 19.5 - 20 ns in the setup #2 (1 bar) near the cathode. Continuum emission (assumed to be linear) is subtracted. Best fit results: $n_e = 1.4\times10^{19}$ cm^{-3}, T_e = 39,300 K. The experimental spectrum is obtained with 100 on-CCD accumulations. The energies of the dominant emitting levels, relative to the ground state of the corresponding ions, are indicated for reference.

The evolutions of n_e and T_e in the discharge afterglow are presented in Figure 4.10 and Figure 4.11. The entrance slit of the spectrometer is aligned parallel to the inter-electrode axis to perform measurements along the inter-electrode gap. Electron number densities are measured at four positions along the interelectrode gap, with the spatial binning indicated in Figure 4.10. From t = 6 ns to t = 10 ns, the emission of N^+ is visible only at the electrodes (i.e. only inside the filaments shown in Figure 4.8). The N^+ Stark broadening measurements show that, after t = 10 ns, the electron number densities are approximately uniform across the entire interelectrode space. The electron number density approaches 4×10^{19} cm^{-3} at t = 6 ns for T_e = 45,000 K. The total gas density at 300 K, 1 atm, is 2.5×10^{19} cm^{-3}. According to the Figure 2 in (Sher, Ben-Ya'ish and Kravchik, 1992), after isochoric heating to temperatures around 45,000 K the main species are N^+, O^+, and electrons (the N^{++} mole fraction is below 8% at 45,000 K and the O^{++} mole fraction is less than 1%). Therefore, the total gas density at the end of the pulse should be around four times the initial density because, for each initial diatomic molecule, two atoms are formed, which in turn transform into two atomic ions and electrons. Thus, full ionization at the end of the pulse would correspond to about 5×10^{19} heavy particles/cm^3 and the same density for free electrons, assuming each atom is ionized once. Therefore, the measured electron number density of about 4×10^{19} cm^{-3} is consistent with full ionization and dissociation at the end of the pulse. The spatial distribution of the electron temperature is also found to be uniform across the gap. The temporal evolution of the spatially

averaged T_e is shown in Figure 4.11. The maximal electron temperature right after the discharge is 48,000 ± 5,000 K, then decays to about 30,000 K within 90 ns.

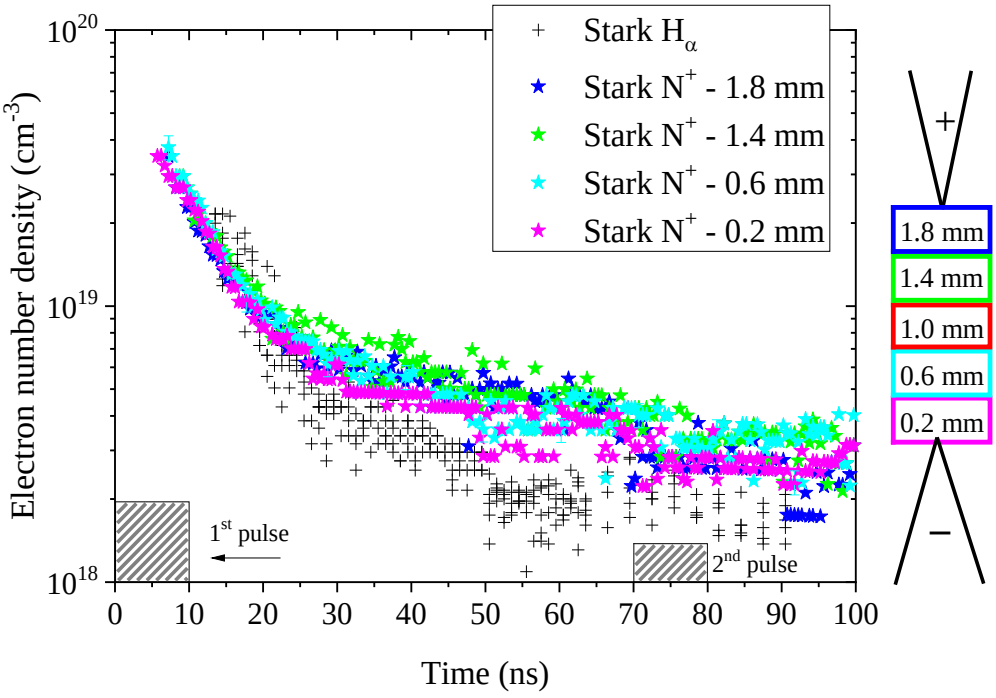

Figure 4.10 Temporal evolution of the measured electron number density at various positions along the 2-mm interelectrode gap (setup #2), determined from the Stark width of N+ lines (colored stars) and Hα (black crosses). The distance from the cathode is shown in mm. The nanosecond pulses are represented by the dashed areas.

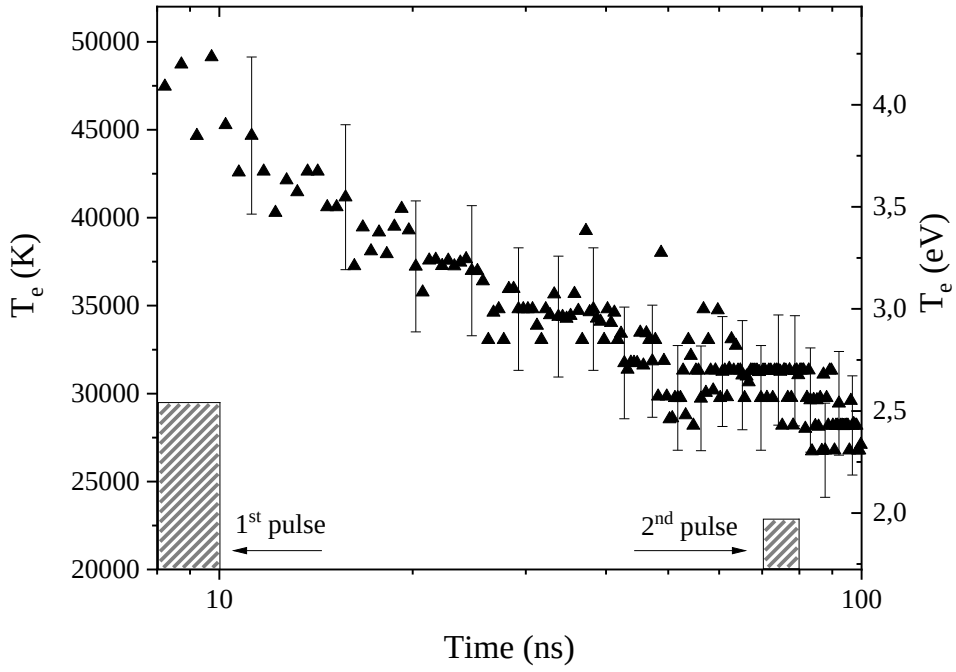

Figure 4.11 Decay of the measured electron temperature. The measurements are spatially averaged along the gap.

An additional measurement of the electron number density is obtained from the Stark broadening of H_α (recall that for these experiments with setup #2, 1.6% of hydrogen is added to air). Figure 4.12 shows two measurements and two fits of the Stark-broadened H_α line at t = 60 and 1000 ns. The instrumental broadening width is always less than the measured linewidth over this entire time interval, although it becomes comparable with the Stark width at 1000 ns. We apply the same fitting procedure as for N^+: a Lorentzian convolved with the instrumental broadening lineshape is fitted to the experimental spectrum. The electron number density is obtained after subtraction of the Van der Waals and resonant broadening widths from the total Lorentzian width. The Doppler width is still negligible. The electron number densities inferred from the Stark broadening of the N^+ and H_α lines are compared in Figure 4.10. The data from H_α broadening are also spatially resolved, and we find a homogeneous distribution of the electrons along the gap. This homogeneity was also reported in a similar discharge (Lo *et al.*, 2017). The results obtained with the H_α line are only shown for $t > 12$ ns, i.e. after the electron number density has decayed to 2×10^{19} cm^{-3}. This is because the Stark-broadened H_α line is much wider than the spectral measurement window at electron number densities higher than 2×10^{19} cm^{-3}. For example, according to (Gigosos, González and Cardeñoso, 2003), an electron number density of 10^{19} cm^{-3} leads to an H_α FWHM of 25 nm. The results obtained from the Stark-broadened H_α line after 12 ns are in good agreement with those of the N^+ line given that the experimental (Konjević *et al.*, 2002) and theoretical (Griem, 1974) N^+ Stark coefficients can differ by up to a factor of two in the literature[1].

Spatially averaged measurements of n_e from H_α broadening are shown in Figure 4.13 up to t = 1 µs. At $t \approx 70$ ns, a reflected pulse reaches the electrodes[2]. The deposited energy is lower than for the first pulse (≈ 0.1 mJ *versus* 2.5 mJ) but is sufficient to induce a small amount of additional ionization. For $t > 100$ ns, the temperature is not known. The uncertainty on the Van der Waals calculation is therefore increased. The lower limit of the error bars in Figure 4.13 indicates the values that would be obtained if a constant value of T_{gas} = 28,000 K were chosen in the Van der Waals width calculation. Our measurements are compared in Figure 4.13 with those reported for other thermal sparks in the literature (van der Horst *et al.*, 2012; Lo *et al.*, 2017; Orriere, Moreau and Pai, 2018). They are found to agree in first approximation, and a detailed comparison is given in Section 4.4.

[1] Note that the variation of the N^+ Stark coefficient with T_e is also not known accurately.

[2] This timing corresponds to the speed of propagation of the electrical signal, 20 cm/ns, and the length of the cables, 7 m. The same phenomenon was seen in Ref. (Babický *et al.*, 2018).

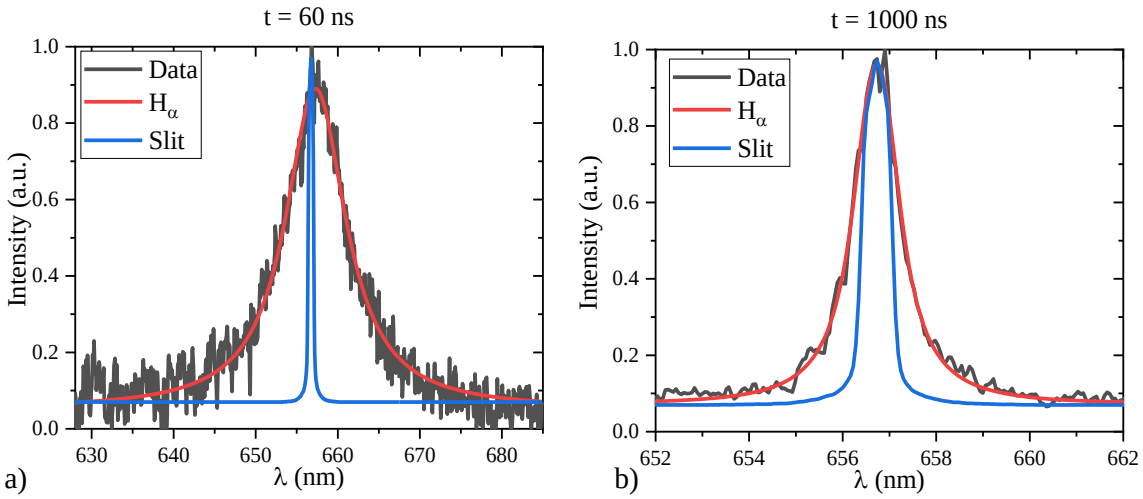

Figure 4.12 Spatially averaged emission of the H_α line in black recorded at (a) t = 60 ns and (b) t = 1000 ns. The instrumental broadening lineshape is displayed in blue and the fit including Stark broadening in red. The line at t = 1000 ns corresponds to the narrowest H_α line measured in this work (Stark FWHM of 0.81 nm).

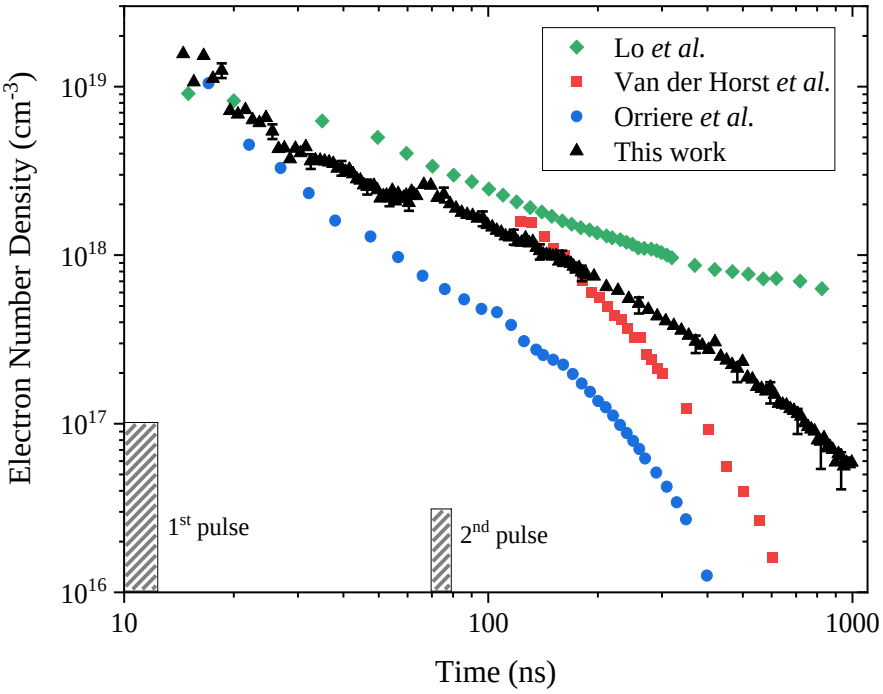

Figure 4.13 Decay of the electron number density, measured from the Stark broadening of H_α (black triangles). The increase of n_e at t ≈ 70 ns is caused by the reflected pulse. The measurements performed by (van der Horst *et al.*, 2012) in N_2 + 0.9% H_2O (red squares), (Orriere, Moreau and Pai, 2018) in air (blue circles), and (Lo *et al.*, 2017) in air (green diamonds) are shown for comparison.

Van der Horst *et al.* (van der Horst *et al.*, 2012) measured the gas temperature in the first few nanoseconds of a similar discharge by fitting the rotational structures of N_2(C-B), and 1 μs after the discharge

by Rayleigh scattering. The authors also measured n_e, shown in Figure 4.13, and estimated the dominant electron loss process to be three-body recombination via Reac. 4.1.

$$N^+ + e^- + e^- \rightarrow N + e^- \qquad \text{Reac. 4.1}$$

Van der Horst *et al.* assumed the rate coefficient of Reac. 4.1 to be $k_{3,rec} = 7 \times 10^{-20}(300/T_e)^{4.5}$ cm^6/s (taken from (Capitelli *et al.*, 2000)), and deduced from a fit of the n_e decay that the electron temperature (not measured in their work) should be around 2.3 eV, a value they deemed too high for a recombining plasma. Instead, they concluded that additional electrons were produced via Penning ionization.

If we apply the approach of van der Horst *et al.*, we also find that our experimental decay rate of electrons is much slower than the rate of Reac. 4.1 (Capitelli *et al.*, 2000). In our conditions, a fit of the n_e decay within 10 – 20 ns would require a temperature of 70,000 K, which is almost twice the measured value. In this section, we propose an explanation for our observed electron decay.

The importance of volume expansion in the decay of n_e was shown in (Lo *et al.*, 2017). The speed of sound is equal to $c_s = \sqrt{\gamma R T_{gas}/M}$, where $\gamma = 1.25$ is the ratio of specific heats (Colonna, D'Angola and Capitelli, 2012), R the perfect gas constant, T_{gas} the gas temperature, and M the molar mass. In a gas composed of electrons (50%), nitrogen ions (40%), and oxygen ions (10%), the molar mass is 7.2 g·mol^{-1}, and the speed of sound ranges between 6500 and 7500 m·s^{-1} for T_e in the range 30,000 – 50,000 K. Thus, the hydrodynamic timescale for a plasma with a radius r = 100 µm is $r/c_s \approx 14$ ns. Therefore, the pressure is homogeneous in the plasma channel and the volume expansion already begins by the end of the pulse. We therefore expect the volume expansion to induce a decrease in the electron number density. Lo *et al.* showed that the decay of n_e, reproduced in Figure 4.13, was due to an isentropic volume expansion up to t = 150 ns (Lo *et al.*, 2017). The relation between T_e and n_e during an isentropic expansion is given by Eq. 4.1 (Lo *et al.*, 2017).

$$\frac{n_e^{\gamma-1}}{T_e} = cst \qquad \text{Eq. 4.1}$$

Figure 4.14 shows our measurements of n_e *versus* T_e, fitted by $T_e = a(n_e)^b$. The fit gives $\gamma = 1.24$, which is close to:

- 1.2 – 1.3, the value measured in (Lo *et al.*, 2017), and
- 1.2 – 1.25, the value calculated in (Colonna, D'Angola and Capitelli, 2012) for air at 100 bar between 30,000 and 50,000 K.

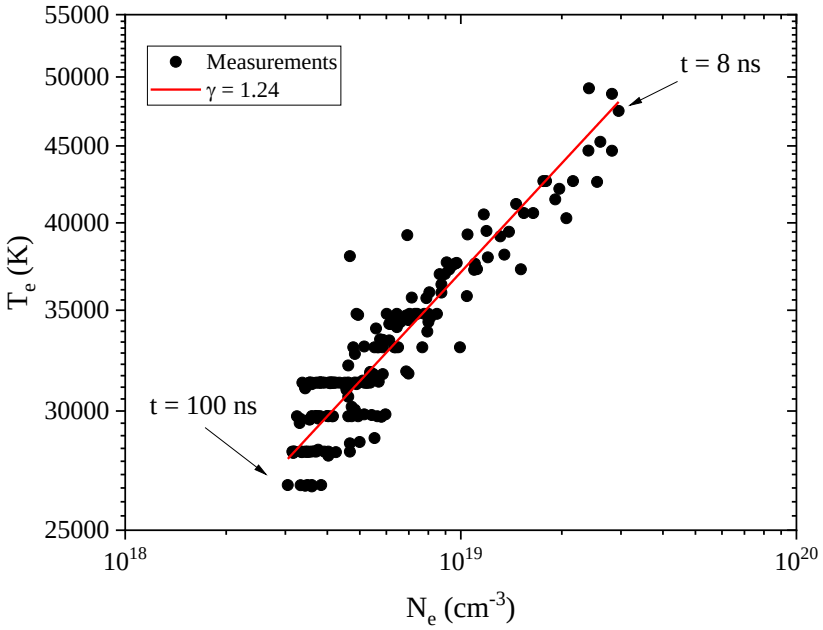

Figure 4.14 T_e versus n_e from 8 to 100 ns in a logarithm scale. Spatially averaged values are displayed. The measurements are fitted by a law in $T_e = a \times n_e^{0.24}$ which corresponds to $\gamma = 1.24 \pm 0.01$ in Eq. 4.1.

It is interesting to determine when heat conduction starts cooling the plasma. The characteristic time of cooling by heat conduction can be estimated as $\tau_{cond} = \rho c_p r^2/\lambda$ (Raizer, 1991, p. 199). The thermophysical quantities[1], taken at 133 bar and 20,000 K (the average temperature of the plasma and of ambient air), are ρ = 0.9 kg·m^{-3}, c_p = 10 kJ·kg^{-1}·K^{-1} and λ = 7.8 W·m^{-1}·K^{-1}. We obtain τ_{cond} = 12 µs and therefore losses by thermal conduction are negligible over the time scale of our measurements.

Regarding radiation losses, it was shown for a 15-mJ laser spark that radiation dissipates 22% of the deposited energy (Phuoc, 2005). A lower limit for the characteristic time of radiation cooling, τ_{rad}, can be obtained by assuming the plasma to be a blackbody. At $T = T_e$ = 45,000 K and with σ, the Stefan constant, we calculate $\tau_{rad} = \rho c_p r/2\sigma T^3 \approx 60$ ns. As can be clearly[2] seen in Figure 4.6, the radiation is far below the blackbody emission and therefore τ_{rad} should be much longer than 60 ns. Therefore, radiation losses are not expected to be the primary mechanism of plasma cooling from 0 to 100 ns. However, they could be taken into account to refine the spark model, see for instance the work in (Shneider, 2006).

---

[1] Calculated on https://cearun.grc.nasa.gov/ in January 2020 (McBride and Gordon, 1992)

[2] Anticipating the calibrated spectrum showed in Figure 6.17, the continuum radiation of the thermal spark remains in the range 1 – 10 W·sr^{-1}·cm^{-2}·nm^{-1} whereas the maximal blackbody emission is above 10^3 W·sr^{-1}·cm^{-2}·nm^{-1} for temperatures higher than 20,000 K.

Regarding state-to-state ionization, state-to-state recombination, and volume expansion, the rate of electron decay can be modeled with Eq. 4.2:

$$\frac{dn_e}{dt} = \left(k_{i,N(^4S)}n_{N(^4S)} + k_{i,N(^2D)}n_{N(^2D)} + k_{i,N(^2P)}n_{N(^2P)} + \cdots\right)n_e - \left(k_{rec,N(^4S)} + k_{rec,N(^2D)} + k_{rec,N(^2P)} + \cdots\right)n_{N^+}n_e^2 - \frac{dV}{dt}\frac{1}{V}n_e \quad \text{Eq. 4.2}$$

where $k_{i,N(X)}$ is the ionization rate coefficient of state X, $k_{rec,N(X)}$ the recombination rate coefficient of N^+ in state X, n_{N^+} the N^+ density, and V the plasma volume. We already showed that the last term on the right-hand side of Eq. 4.2 is driving the decrease of n_e in Figure 4.14. We now demonstrate with a state-to-state model that ionization compensates the chemical recombination of electrons during the expansion. Assuming isochoric dissociation during the discharge, the total heavy particle density at t = 8 ns is 5×10^{19} cm^{-3}. From t = 8 ns to t = 12 ns, T_e decreases from 48,000 to 40,000 K. In an isentropic expansion, the quantity $T_eV^{\gamma-1}$ is conserved, implying an increase of the plasma volume by a factor of 2. Thus, the total heavy particle density is 2.5×10^{19} cm^{-3} at t = 12 ns. We assume that the dominant ion is N^+ and that the remaining heavy particles are atomic nitrogen. Thus, at t = 12 ns, $T_e \approx$ 40,000 K (Figure 4.11), $n_e \approx n_{N^+} \approx 2\times10^{19}$ cm^{-3} (Figure 4.10), and $n_N \approx 0.5\times10^{19}$ cm^{-3}. The populations of the excited states are computed using the partition functions of NIST [31], assuming a Boltzmann distribution. The ground state number density, $n_{N(^4S)}$, represents 10% of the atomic nitrogen number density, whereas the metastable states, $n_{N(^2D)}$ and $n_{N(^2P)}$, represent 12% and 5%, respectively. The remaining 73% occupy higher excited states. Using the rate coefficients of (Ciccarino and Savin, 2019) and detailed balancing, we find that the ionization rate of N(^{4}S) is comparable with the recombination rate of N^+ into N(^{4}S) ($k_{i,gs}n_{N(^4S)}n_e \sim k_{rec,gs}n_{N^+}n_e^2 \sim 10^{27}$ cm^{-3} s^{-1}). The same conclusion is obtained for metastable ($\sim 10^{27}$ – 10^{28} cm^{-3}s^{-1}) and higher excited states up to E = 11.8 eV ($\sim 10^{28}$ – 10^{29} cm^{-3}s^{-1}). We repeated this calculation up to the last point for which we measured T_e and found that ionization balances recombination until t = 100 ns. Therefore, up to at least t = 100 ns, the thermal spark is in chemical equilibrium.

At longer timescales (t > 1 µs), hydrodynamic effects lead to the formation of a torus and the mixing of the plasma column with fresh gas (Olsen, Edmonson and Gayhart, 1952; Kono *et al.*, 1989; Xu, 2013; Bane, Ziegler and Shepherd, 2015; Stepanyan *et al.*, 2017). In the numerical study of (Dumitrache *et al.*, 2019), a dimensionless number, defined in Eq. 4.3, was introduced to predict the discharge conditions for which recirculation occurs.

$$\Pi_{Tr} = \frac{\mathrm{E_{uh}}}{p_0 S d} \quad \text{Eq. 4.3}$$

The Π_{Tr} number depends on E_{uh} the energy deposited into fast gas heating, p_0 the initial pressure, S the plasma cross-section, and d the interelectrode gap distance. This number can be seen as the ratio of the

energy deposited into fast gas heating and the energy already contained in the discharge volume prior to breakdown. As shown in (Dumitrache *et al.*, 2019), a torus forms when $\Pi_{Tr} > 60 - 80$. In our case, E_{uh} = 2.5 mJ, $p_0 = 10^5$ Pa, S = 0.025 mm^2 and d = 2 mm, which gives Π_{Tr} = 500. This indicates that a torus will be formed and therefore that fresh gases recirculate into the plasma column. However, this recirculation does not occur before 1 µs, as can be clearly seen from Figure 5 of (Stepanyan *et al.*, 2019), obtained for discharge under similar conditions, see Figure 4.15. Therefore, recirculation does not affect the decay of n_e shown in Figure 4.13.

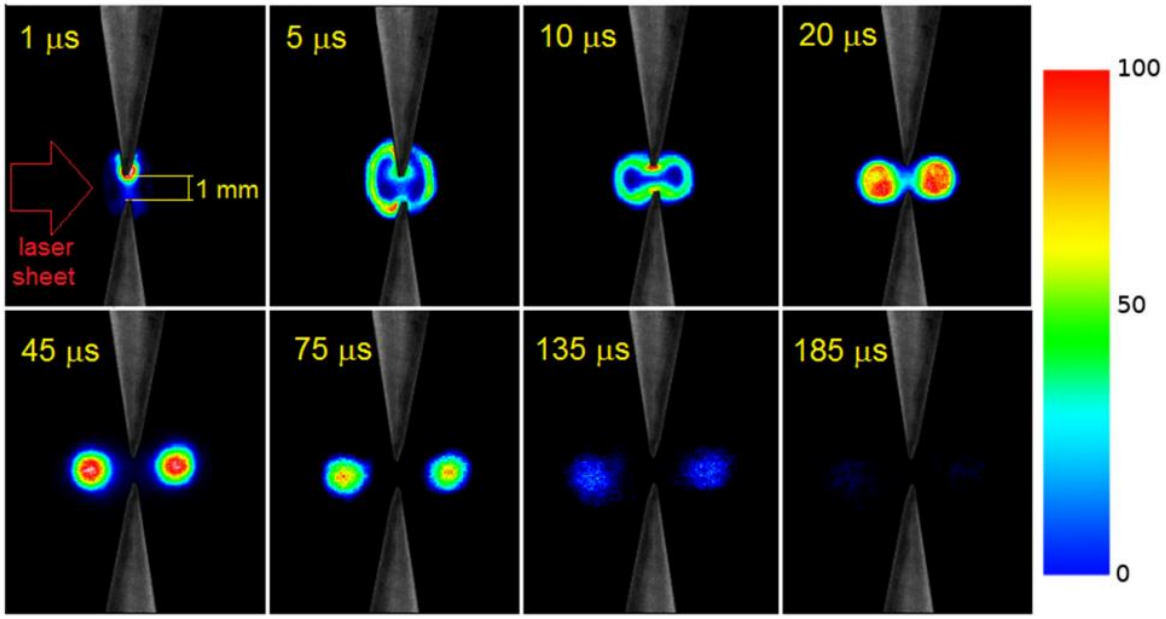

Figure 4.15 Phase-locked OH-PLIF images obtained at different moments in the afterglow of a single nanosecond spark initiated in ambient humid air. Reproduced from (Stepanyan *et al.*, 2019).

4.4 Comparison with the literature

4.4.1 Comparison with other nanosecond thermal sparks

In this section, we compare and discuss the electron density decay curves presented in Figure 4.13. These results were obtained in ambient air or N_2, using nanosecond discharges with fairly similar characteristics, as reported in Table 4.2. In all cases, nearly fully ionized plasmas were produced.

As can be seen in Figure 4.13, the electron density curves all start with a nearly fully ionized plasma at the end of the pulse, and then follow the same evolution after the pulse. It is important to note that the initial discharge radii vary from 20 µm (Orrière *et al.*) to around 100-120 µm (van der Horst *et al.*, Lo *et al.*, and present work). A small radius (30 µm at t = 15 ns) was also reported by (Albrecht *et al.*, 1977).

The reasons explaining these different radii[1] are not known. The small discharge radius reported by Orrière *et al.* cannot be explained by their small gap (200 µm), because Orrière obtained a similar discharge radius with a 1-mm gap (Orriere, 2018). Nevertheless, the rate of volume expansion is related to the hydrodynamic timescale, which is proportional to the initial radius of the discharge channel, and Figure 4.13 confirms that electrons recombine faster when the initial discharge radius is smaller. For a more quantitative comparison, one would have to consider other parameters, such as the energy per unit volume, and the effect of a spherical expansion (in short gaps) compared to cylindrical one (in long gaps).

As shown in Figure 4.13, the electron density decay measured by (Orriere, Moreau and Pai, 2018) and the one measured in the present work follow approximately the same trend. The slightly faster decay reported in (Orriere, Moreau and Pai, 2018) could be due to their smaller initial plasma radius, or to the fact that the volume expansion of their plasma is spherical (*versus* cylindrical in our case), and to the presence in our case of a second pulse (at $t \approx 70$ ns). Like van der Horst *et al.*, Orriere *et al.* fitted the electron decay with Reac. 4.1 only (i.e. neglecting the ionization of N and the plasma expansion). However, using the cross-sections of Wang *et al.* (Wang, Zatsarinny and Bartschat, 2014), it was also shown in Ref. (Orriere, Moreau and Pai, 2018) that the characteristic ionization times of $N(^2P)$ and $N(^2D)$ were comparable with the experimental recombination time for $t < 100$ ns. We obtained the same conclusions using the ionization rate coefficients derived by Ciccarino *et al.* (Ciccarino and Savin, 2019). Furthermore, in his thesis (Orriere, 2018, Fig. 74), Orriere reported the discharge radius evolution, measured by OES. Between $t = 10$ ns and $t = 100$ ns, the discharge volume increased by a factor 3 – 5 while n_e was divided by 25. Based on these two observations, we conclude that Reac. 4.1 is not sufficient to model n_e decay for $t < 100$ ns, and that ionization (reverse of Reac. 4.1) and volume expansion should also be considered.

[1] The discharge radius was measured by OES in (Albrecht *et al.*, 1977; van der Horst *et al.*, 2012; Lo *et al.*, 2017; Orriere, Moreau and Pai, 2018) and this work. In (Lo *et al.*, 2017), the radius measured by OES corresponded to the radius of the electron distribution.

Table 4.2 Parameters of the thermal sparks studied by van der Horst et al., Orriere et al., Lo et al. , and in the present work. The voltage pulse in the work of Lo et al. is 20 ns in duration, whereas the current lasts for hundreds of nanoseconds.

Ref.	Gas (Pressure)	T (K)	Gap (mm)	V_{max} (kV)	PRF (kHz)	Pulse length (ns)	Initial radius (μm)	Energy (mJ)	$n_{e,max}$ (cm^{-3})	$T_{e,max}$ (K)
(Orriere, Moreau and Pai, 2018)	Air (1 atm)	370	0.2	2.5	8	30	20 ± 4 (t < 15 ns)	0.1	$1x10^{19}$ (t = 12 ns)	70,000
(van der Horst *et al.*, 2012)	N_2 N_2+0.9% H_2O (1 atm)	350	2	9	1	170	~ 100	1.0	$4x10^{18}$ (t = 100 ns)	–
(Lo *et al.*, 2017)	Air (1 atm)	300	3	30	0.01	20	120 (t = 15 ns)	> 55	$9x10^{18}$ (t = 15 ns)	44,000
Present work	Air + 1.6% H_2 (1 atm)	300	2	5.5	0.05	10	~ 100 (t = 10 ns)	2.5	$4x10^{19}$ (t = 8 ns)	45,000

As detailed before, (van der Horst *et al.*, 2012) calculated that if only Reac. 4.1 is considered, a temperature of 2.3 eV = 27,000 K would be necessary to explain the relatively slow decay of n_e. Van der Horst *et al.* considered this value to be unrealistically high for a nonequilibrium plasma. However, in light of the present work and of the measurements reported in Table 4.2, it appears likely that the electron temperature could indeed reach such high values, and perhaps even higher. For t < 100 ns, n_e was not measured by van der Horst *et al.* Given the similarities between this discharge and the others in Table 4.2, it is expected that n_e reached 10^{19} cm^{-3} during the 100-ns pulse of (van der Horst *et al.*, 2012).

In (Lo *et al.*, 2017), Lo *et al.* showed that the decay of n_e in the afterglow of their thermal spark was due to an isentropic expansion. Their 2D-resolved measurements of n_e clearly demonstrated an expansion of the plasma channel, beginning at t = 15 ns. They also found a homogeneous electron density distribution along the interelectrode gap, as in our experiments. However, T_e was higher at the electrodes than in the middle of the gap. The T_e values measured in (Lo *et al.*, 2017) are close to those reported in this work. Chemical equilibrium is therefore expected at least up to t = 100 ns. For t > 300 ns, the electron decay is slower than in the other references, see Figure 4.13, possibly because the current lasted for more than 500 ns in their experiment. Also, the n_e inferred from the Stark broadened N^+ lines might be somewhat overestimated at t > 300 ns because Van der Waals broadening was not taken into account in their lineshape analysis.

4.4.2 Comparison with spark discharges used for combustion ignition

The transition in a few nanoseconds from a N_2-emission dominated spectrum to a continuum/N+-dominated spectrum is also observed in discharges of longer durations, in particular the discharges used for combustion ignition in car engines. The latter ones are typically a few milliseconds long and evolve in three phases, as described by Maly *et al.* in (*Flow and combustion in reciprocating engines*, 2009): the "breakdown" phase (≈ 10 ns), the "arc" phase (≈ 1-10 µs) and the "glow" phase (≈ 1 ms). (Albrecht *et al.*, 1977) recorded the emission of N^+ lines already at 7 ns in these discharges, and showed that it became dominant after 15 ns. The comparison of T_e and n_e measured by Albrecht *et al.* and in this work is shown in Figure 4.16. The electron number density measurements agree remarkably, within better than a factor of 1.5. The temperatures profiles are also comparable, albeit about 30%. It is difficult to determine the reason for this difference (potentially due to an overlap of O^+ and N^+ lines, or to inaccurate Einstein coefficients) because Albrecht *et al.* do not give the details of their measurements and analysis. The energy deposited during (i) the "breakdown" phase of millisecond discharges and (ii) the nanosecond discharges is also similar and equal to a few mJ (Albrecht *et al.*, 1977; Lacour *et al.*, 2016). The early phase of longer sparks used for combustion ignition has therefore the same characteristics as the nanosecond thermal spark reported here.

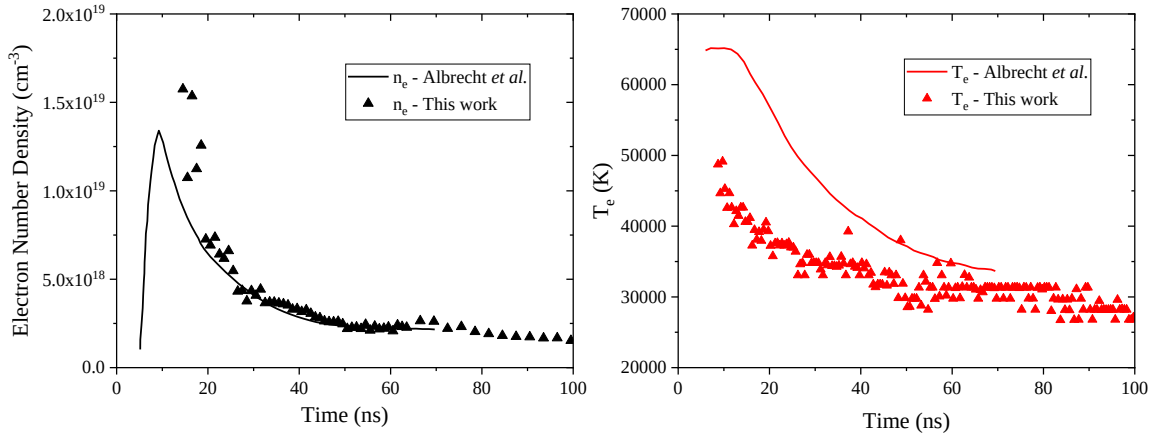

Figure 4.16 Comparison between the measurements of (Albrecht *et al.*, 1977), full lines, and this work, triangles. The data of this work corresponds to the measurements presented in Figure 4.13 and Figure 4.11.

4.5 Conclusion

We showed that, under certain conditions, nanosecond discharges in air can produce a fully ionized plasma ($n_e \sim 10^{19}$ cm^{-3}), with intense N^+ lines and continuum emission in the interelectrode gap. We call this regime the thermal spark, to distinguish it from the previously observed corona, glow, and non-thermal spark regimes observed in (Pai, Lacoste and Laux, 2010b). Through fast imaging, the following steps of formation of the thermal spark in air were evidenced:

1. Formation of a weakly ionized non-equilibrium plasma i.e. the non-equilibrium spark. The typical diameter at these early instants is 200-300 µm and the emission is dominated by the N_2(C→B) radiative transition.
2. Generation of a filament at the cathode on a timescale below 0.5 ns. The typical diameter of the filament is 100 µm; its emission is dominated by N^+ and a broadband continuum. The length and diameter of the filament is found to be independent of the pressure but varies with the applied electric field.
3. A few nanoseconds later, formation of an anode filament with dimensions similar to those of the cathode filament.
4. Propagation of the two filaments in the interelectrode gap. The typical speed of propagation ranges between 10^4 and 10^5 m s^{-1} and is pressure dependent.
5. The filaments merge: the thermal spark is formed.

At low pressures (i.e. p < 300 – 400 mbar), the thermal spark formation is interrupted at step 4. However, step 5 could possibly occur with a longer discharge pulse. We showed that for the same deposited energy, at low and high pressures, the spark can be thermal or in non-equilibrium. The total deposited energy is therefore not an indicator of the transition to a thermal spark.

The electron number density evolution in the post-discharge of a thermal spark in air at 1 atm was measured by Stark broadening of H_α and N^+ lines. Other line broadening processes were found negligible or small. The electron temperature, T_e, was measured by fitting the emission of excited electronic states of N^+, with energies ranging from 21 to 30 eV. The electron number density was found to reach a maximum value of 4×10^{19} cm^{-3} at the end of the pulse, and to then decay to 10^{17} cm^{-3} in 1000 ns. We showed that the three-body recombination of electrons with N^+ is equilibrated by the reverse process of ionization of nitrogen excited states, even after the end of the voltage pulse. The decay of the electron number density is explained by isentropic expansion alone up to t = 100 ns. Heat removal by conduction is found to be negligible on this timescale. Heat removal by radiation is more important but remains secondary. Therefore, for a complete simulation of the thermal spark afterglow, it is sufficient to consider a plasma in chemical equilibrium subject to volume expansion (and radiation losses). These conclusions are found to apply to other measurements performed in the recombination phase of thermal sparks (van der Horst *et al.*, 2012; Lo *et al.*, 2017; Orriere, Moreau and Pai, 2018). Finally, a comparison of n_e and T_e with values measured in a discharge typical of spark plugs used for internal combustion engine ignition showed that the nanosecond thermal spark is equivalent to the "breakdown phase" of the spark discharges used for flame ignition.

The formation of the thermal spark has yet not been discussed. In the following sections, we described the kinetics of a 0-D simulation used for that purpose.

Chapter 5

Kinetic mechanism for air discharges

5.1 Reaction set

In this chapter, 0-D numerical simulations of plasma kinetics are performed using ZDPlasKin (Pancheshnyi *et al.*, 2008) as a function of the reduced electric field. We assumed an isochoric transformation of the plasma, which is typically the case for nanosecond discharges. The Electron Energy Distribution Function (EEDF) is calculated by solving the Boltzmann equation with BOLSIG+ using cross-sections of electron reactions taken mostly from the LXCat[1] database (Hagelaar and Pitchford, 2005; Hagelaar, 2016). We use a baseline kinetic mechanism that was initially applied for non-thermal plasmas (Laux *et al.*, 1999).

Nowadays, several baseline mechanisms for low-temperature plasmas are available in the literature (Kossyi *et al.*, 1992; Capitelli *et al.*, 2000; Bak and Cappelli, 2015) and could have been used. The reaction set of Capitelli *et al.* was used in our previous work[2] (Minesi, Mariotto, *et al.*, 2020). However, these mechanisms include hundreds of reactions, such as the formation of negative ions and N_yO_x with $(x, y) \geq 2$, which are unnecessary to describe the thermal spark formation. Instead, we use a simpler set based on the 38 reactions listed in (Laux *et al.*, 1999) supplemented with 62 additional reactions. The set of Laux *et al.* is adequate for the present study because only the essential reactions and species driving the ionization and recombination of plasma discharges in air are included. However, the rate coefficients of reactions involving electrons, given in Laux *et al.* as a function of T_e, are replaced here by rate coefficients calculated with BOLSIG+. The additional reactions include:

- ionization and dissociation of N_2(X, A, B, C, and a') by electron impact.
- ionization of N^+ and O^+ (to N^{++} and O^{++}) by electron impact.
- quenching of N_2 excited electronic states.

We describe next the complete mechanism used in the present work.

---

[1] Namely: the BSR database, the IST-LISBON database, and the Itikawa database.

[2] The simulations and conclusions of the AIAA conference proceeding (Minesi, Mariotto, *et al.*, 2020) are extended in a recent submission to Plasma Sources Science and Technology (October 2020).

Table 5.1 The baseline kinetic mechanism used in this work is mainly taken from (Laux *et al.*, 1999). The forward reaction coefficients are given, with their dependence on either the gas temperature or the electron temperature. The backward reaction rates are always calculated by detailed balance. With an asterisk (*), we indicate the forward reaction rates identical to those reported in Table 1 of (Laux *et al.*, 1999).

Reaction & Temperature dependence		k_f =A T^b exp(-E/RT)				Ref.	
		k_f k_r	A (cm^3 s^{-1})	b	E/R (K)		
	O_2, NO, N_2 Dissociation / Recombination (Laux *et al.*, 1999)						
(R1)	$O_2 + N_2 \leftrightarrow 2O + N_2$	T_g T_g	$3.32\ 10^{-3}$	-1.5	59,500	(Park, 1993)	*
(R2)	$O_2 + O_2 \leftrightarrow 2O + O_2$	T_g T_g	$3.32\ 10^{-3}$	-1.5	59,500	(Park, 1993)	*
(R3)	$O_2 + NO \leftrightarrow 2O + NO$	T_g T_g	$3.32\ 10^{-3}$	-1.5	59,500	(Park, 1993)	*
(R4)	$O_2 + N \leftrightarrow 2O + N$	T_g T_g	$1.66\ 10^{-2}$	-1.5	59,500	(Park, 1993)	*
(R5)	$O_2 + O \leftrightarrow 2O + O$	T_g T_g	$1.66\ 10^{-2}$	-1.5	59,500	(Park, 1993)	*
(R6)	$O_2 + e \leftrightarrow O + O(^3P) + e$	T_e T_e	BOLSIG+			(Phelps, 1985)	
(R7)	$O_2 + e \leftrightarrow O + O(^1S) + e$	T_e T_e	BOLSIG+			(Phelps, 1985)	
(R8)	$NO + N_2 \leftrightarrow N + O + N_2$	T_g T_g	$8.30\ 10^{-9}$	0.0	75,500	(Park, 1993)	*
(R9)	$NO + O_2 \leftrightarrow N + O + O_2$	T_g T_g	$8.30\ 10^{-9}$	0.0	75,500	(Park, 1993)	*
(R10)	$NO + NO \leftrightarrow N + O + NO$	T_g T_g	$1.83\ 10^{-7}$	0.0	75,500	(Park, 1993)	*
(R11)	$NO + N \leftrightarrow N + O + N$	T_g T_g	$1.83\ 10^{-7}$	0.0	75,500	(Park, 1993)	*
(R12)	$NO + O \leftrightarrow N + O + O$	T_g T_g	$1.83\ 10^{-7}$	0.0	75,500	(Park, 1993)	*
(R13)	$N_2 + N_2 \leftrightarrow 2N + N_2$	T_g T_g	$1.16\ 10^{-2}$	-1.6	113,200	(Park, 1993)	*
(R14)	$N_2 + O_2 \leftrightarrow 2N + O_2$	T_g T_g	$1.16\ 10^{-2}$	-1.6	113,200	(Park, 1993)	*
(R15)	$N_2 + NO \leftrightarrow 2N + NO$	T_g T_g	$1.16\ 10^{-2}$	-1.6	113,200	(Park, 1993)	*
(R16)	$N_2 + N \leftrightarrow 2N + N$	T_g T_g	$4.98\ 10^{-2}$	-1.6	113,200	(Park, 1993)	*
(R17)	$N_2 + O \leftrightarrow 2N + O$	T_g T_g	$4.98\ 10^{-2}$	-1.6	113,200	(Park, 1993)	*
	Zeldovich reactions (Laux *et al.*, 1999)						
(R18)	$N_2 + O \leftrightarrow NO + N$	T_g T_g	$1.06\ 10^{-6}$	-1.0	38,400	(Park, 1993)	*
(R19)	$NO + O \leftrightarrow O_2 + N$	T_g T_g	$1.39\ 10^{-11}$	0.0	19,400	(Park, 1993)	*
	Associative ionization / Dissociative recombination (Laux *et al.*, 1999)						
(R20)	$N + O \leftrightarrow NO^+ + e$	T_g T_e	$1.46\ 10^{-15}$	1.0	31,900	(Park, 1993)	
(R21)	$N + N \leftrightarrow N_2^+ + e$	T_g T_e	$9.97\ 10^{-17}$	1.5	67,500	(Park, 1993)	
(R22)	$O + O \leftrightarrow O_2^+ + e$	T_g T_e	$1.18\ 10^{-21}$	2.7	80,600	(Park, 1993)	
	Electron Impact Ionization of O_2 and NO (Laux *et al.*, 1999)						
(R23)	$O_2 + e \leftrightarrow O_2^+ + 2e$	T_e T_e	BOLSIG+			(Itikawa, 2009)	
(R24)	$O_2 + e \leftrightarrow O^+ + O + 2e$	T_e T_e	BOLSIG+			(Itikawa, 2009)	
(R25)	$NO + e \leftrightarrow NO^+ + 2e$	T_e T_e	BOLSIG+			(Itikawa, 2016)	
(R26)	$NO + e \leftrightarrow N + O^+ + 2e$	T_e T_e	BOLSIG+			(Itikawa, 2016)	

(R27)	$NO + e \leftrightarrow O + N^+ + 2e$	T_e T_e	BOLSIG+		(Itikawa, 2016)		
	Charge Exchange (Laux *et al.*, 1999)						
(R28)	$N^+ + N_2 \leftrightarrow N + N_2^+$	T_g T_g	$1.66\ 10^{-12}$	0.5	12,000	(Park, 1993)	
(R29)	$NO^+ + O \leftrightarrow N^+ + O_2$	T_g T_g	$1.66\ 10^{-12}$	0.5	77,200	(Park, 1993)	*
(R30)	$NO + O^+ \leftrightarrow N^+ + O_2$	T_g T_g	$2.32\ 10^{-19}$	1.9	26,600	(Park, 1993)	
(R31)	$NO^+ + N \leftrightarrow N_2 + O^+$	T_g T_g	$5.65\ 10^{-11}$	-1.08	12,800	(Park, 1993)	
(R32)	$O^+ + N_2 \leftrightarrow N_2^+ + O$	T_g T_g	$1.49\ 10^{-12}$	0.36	22,800	(Park, 1993)	
(R33)	$NO^+ + N \leftrightarrow N_2^+ + O$	T_g T_g	$1.20\ 10^{-10}$	0.0	35,500	(Park, 1993)	*
(R34)	$O_2^+ + N \leftrightarrow N^+ + O_2$	T_g T_g	$1.44\ 10^{-10}$	0.14	28,600	(Park, 1993)	
(R35)	$O_2^+ + N_2 \leftrightarrow N_2^+ + O_2$	T_g T_g	$1.64\ 10^{-11}$	0.0	40,700	(Park, 1993)	
(R36)	$NO^+ + O_2 \leftrightarrow NO + O_2^+$	T_g T_g	$3.99\ 10^{-11}$	0.41	32,600	(Park, 1993)	
(R37)	$NO^+ + O \leftrightarrow N + O_2^+$	T_g T_g	$1.20\ 10^{-11}$	0.29	48,600	(Park, 1993)	

Most of the reactions used by Laux *et al.* are taken from (Park, 1993; Yu *et al.*, 2001). The reaction rate coefficients in (Yu *et al.*, 2001) are, however, calculated for T_{gas} = 2000 K, which is not suited for the present work. The reaction rates calculated by Yu *et al.* are therefore replaced by calculations performed with BOLSIG+ with the cross-sections specified in Table 5.1. In the case of (R28), $N^+ + N_2 \leftrightarrow N + N_2^+$, the rate constant is taken from (Park, 1993). Note that some of the rate coefficients of charge exchange reactions were rounded off in Table 1 of (Laux *et al.*, 1999), but the exact values were used in their simulation.

The ionization of NO by electron impact was initially limited to (R25), $NO + e \leftrightarrow NO^+ + 2e$, in (Laux *et al.*, 1999). We added here the formation of O^+ and N^+, (R26) and (R27) (Itikawa, 2016). The cross-section of NO dissociation by electron impact is, to our knowledge, not available in the literature (Itikawa, 2016). BOLSIG+ computes the rate of O_2 dissociation by electron impact based on the cross-sections[1] provided in (Phelps, 1985). In this model, the N_2 dissociation and ionization by electron-impact are state-specific and more details are given in Table 5.2.

For electron-heavy reactions, the rate constant is a function of the electron temperature. For heavy-heavy reactions, the rate constant is a function of the gas temperature. As discussed in Section 5.3.2, this is critical for associative ionization and dissociative recombination, whose rate constants depend on T_g and T_e, respectively.

[1] Available in the LXCat *Phelps database* or the LXCat *LISBON-IST database*

Finally, the dissociative recombination of N_2^+, (R21), is calculated with detailed balance using Park's rate of associative ionization. One could also take the cross-sections calculated by (Bacri and Medani, 1982) or measured by (Peterson *et al.*, 1998).

Table 5.2 Supplementary reactions of molecules calculated with BOLSIG+. The backward reaction rates are always calculated by detailed balance.

Reaction		Cross-section
	Electronic Excitation of N_2	
(R37)	$N_2 + e \leftrightarrow N_2(Y) + e$	(Pitchford and Phelps, 1982)
	Y = A, B, C, a'	
(R38)	$N_2(Z) + e \leftrightarrow N_2(Y) + e$	(Bacri and Medani, 1982)
	Z = A, B, C, a'	
	Y = B, C, a'	
	Ionization and dissociation of N_2	
(R39)	$N_2(X) + e \leftrightarrow N_2^+(Y) + 2e$	(Isola, Gómez and Guerra, 2010)
	Y = X, B	
(R40)	$N_2(X) + e \leftrightarrow N_2^+(Y) + 2e$	(Bacri and Medani, 1982)
	Y = A, C	
(R41)	$N_2(Z) + e \leftrightarrow N_2^+(Y) + 2e$	(Bacri and Medani, 1982)
	Z = A, B, C, a'	
	Y = X, A, B, C	
(R42)	$N_2(Z) + e \leftrightarrow N + N + e$	(Bacri and Medani, 1982)
	Z = X, A	
(R43)	$N_2(Z) + e \leftrightarrow N + N(^2D) + e$	(Bacri and Medani, 1982)
	Z = B, a', C	
	Electronic transitions of N_2^+	
(R44)	$N_2^+(Z) + e \leftrightarrow N_2^+(Y) + e$	
	Z = X, A, B, C	(Bacri and Medani, 1982)
	Y = X, A, B, C	

The cross-sections of electronic excitation of $N_2(X)$ to higher excited states were measured by (Cartwright *et al.*, 1977) and later renormalized by (Trajmar, Register and Chutjian, 1983). Usually, these cross-sections are associated with the *LXCaT Phelps Database* (Phelps and Pitchford, 1985). In our kinetic simulations, the cross-section of electron-impact excitation of N_2 to $N_2(A^3\Sigma_u^+)$ is the sum of the cross-sections to the $N_2(A, v')$ levels taken from (Pitchford and Phelps, 1982). The $N_2(B^3\Pi_g, B^3\Sigma_u^-, W^3\Delta_u)$ states are lumped together in the $N_2(B)$ state, using the renormalized cross-sections of (Cartwright *et al.*, 1977). This is also the case for $N_2(C)$, which is the sum of $N_2(C^3\Pi_u, E^3\Sigma_g^+)$ states. The $N_2(a'^1\Sigma_u^-,$

$a^1\Pi_g$, $w^1\Delta_u$) singlet states are lumped together in the $N_2(a')$ state. This grouping was initially proposed in (Kossyi *et al.*, 1992) and used in the simulations[1] of (Flitti and Pancheshnyi, 2009). In future work, the $N_2(a'^1\Sigma_u^-)$ and $N_2(a^1\Pi_g)$ should be distinguished because their dissociation cross-sections differ by one order of magnitude.

The electronic transitions between N_2(A, B, C, a') by electron impact are taken from (Bacri and Medani, 1982). The transitions between the N_2^+(X, A, B, C) states by electron impact are also taken from (Bacri and Medani, 1982). The ionization cross-sections of N_2(X) to N_2^+(X, B), (R39), were estimated in (Isola, Gómez and Guerra, 2010) based on the (renormalized) measurement of Cartwright *et al.* and the recommendations of Itikawa[2]. The ionization cross-sections of N_2(A, B, a', C), (R41), are taken from (Bacri and Medani, 1982). The dissociation cross-sections of N_2 electronic states, (R42) and (R43), are all taken from (Bacri and Medani, 1982). In electron-impact dissociation of N_2, the formation of either N ground state, i.e. N(^{4}S), or N(^{2}D) is based in our kinetics on energy and spin conservation[3]. Therefore, we assume that N_2(X, A) dissociates into two N(^{4}S) atoms, (R42), whereas N_2(B, a', C) dissociates into N(^{4}S) and N(^{2}D), (R43). Reactions involving the excited electronic states of NO and O_2 are neglected in this work because these species are not dominant in these air[4] plasmas.

---

[1] Available online: www.zdplaskin.laplace.univ-tlse.fr/author/sergey-pancheshnyi/index.html

[2] The ionization cross-sections of Cartwright *et al.* and Guerra *et al.* are overestimated because they also include dissociative ionization cross-sections. In future work, we intend to separate these two channels of ionization, although the impact is limited in the present case. This aspect is discussed further in Appendix C.3.

[3] In the work of (Guerra *et al.*, 2019), the branching ratio of (Zipf and McLaughlin, 1978) is used. We prefer to not follow this choice, because Zipf & McLaughlin specifically stated that "The measurements described in this paper do not provide detailed information on the specific yield of N(^{2}P), N(^{2}D), and N(^{4}S) atoms" and only provided an upper bound for N_2(X) dissociation by electron impact. See also Appendix C.2 where this question is discussed.

[4] If O_2 excited states were to be included in a simulation, we recommend using the cross-sections of the LXCat *Phelps database* as done in (Flitti and Pancheshnyi, 2009). It was argued, however, that these states have a minor impact on the chemistry (Bak and Cappelli, 2015). For NO excitation cross-sections, note that non-investigated discrepancies exist between the LXCat *Itikawa database* and the LXCat *Hayashi database*.

Table 5.3 Transitions between atomic excited states and their ionization. The backward reaction rates are always calculated by detailed balance. The electron configuration and term are provided with each state. Rate coefficients are rounded in the present table and non-rounded values can be found in (Ciccarino and Savin, 2019).

Reaction		$k_f = A\ T_e^b \exp(-E/RT)$			Ref.
		A (cm^3s^{-1})	b	E/R (K)	
	Atomic electronic state transitions				
(R45)	$N(^4S^0) + e \leftrightarrow N(Y) + e$	BOLSIG+			(Wang *et al.*, 2014)
	$Y = {}^2D^0, {}^2P^0, {}^4P, {}^2P, {}^4P, {}^2S^0, {}^4D^0$				
(R52)	$N(^2D^0) + e \leftrightarrow N(Y) + e$	BOLSIG+			(Wang *et al.*, 2014)
	$Y = {}^2P^0, {}^4P, {}^2P, {}^4P, {}^2S^0, {}^4D^0$				
(R58)	$N(^2P^0) + e \leftrightarrow N(Y) + e$	BOLSIG+			(Wang *et al.*, 2014)
	$Y = {}^4P, {}^2P, {}^4P, {}^2S^0, {}^4D^0$				
(R63)	$N(^4P, 3s) + e \leftrightarrow N(Y) + e$	BOLSIG+			(Wang *et al.*, 2014)
	$Y = {}^2P, {}^4P, {}^2S^0, {}^4D^0$				
(R67)	$N(^2P, 3s) + e \leftrightarrow N(Y) + e$	BOLSIG+			(Wang *et al.*, 2014)
	$Y = {}^4P, {}^2S^0, {}^4D^0$				
(R70)	$N(^4P, 2s^22p^4) + e \leftrightarrow N(Y) + e$	BOLSIG+			(Wang *et al.*, 2014)
	$Y = {}^2S^0, {}^4D^0$				
(R72)	$N(^2S^0, 3p) + e \leftrightarrow N(^4D^0) + e$	BOLSIG+			(Wang *et al.*, 2014)
(R73)	$O(^3P) + e \leftrightarrow O(^1D, {}^1S) + e$	BOLSIG+			(Tayal *et al.*, 2016)
(R75)	$O(^1D) + e \leftrightarrow O(^1S) + e$	BOLSIG+			(Tayal *et al.*, 2016)
	Atomic electronic state ionization				
(R76)	$N(^4S^0) + e \leftrightarrow N^+ + 2e$	BOLSIG+			(Wang *et al.*, 2014)
(R77)	$N(^2D^0) + e \leftrightarrow N^+ + 2e$	BOLSIG+			(Wang *et al.*, 2014)
(R78)	$N(^2P^0) + e \leftrightarrow N^+ + 2e$	BOLSIG+			(Wang *et al.*, 2014)
(R79)	$N(^4P, 3s) + e \leftrightarrow N^+ + 2e$	$9.33\ 10^{-10}$	0.49	49,120	(Ciccarino *et al.*, 2019)
(R80)	$N(^2P, 3s) + e \leftrightarrow N^+ + 2e$	$1.67\ 10^{-9}$	0.45	45,090	(Ciccarino *et al.*, 2019)
(R81)	$N(^4P, 2s^22p^4) + e \leftrightarrow N^+ + 2e$	$6.57\ 10^{-11}$	0.74	41,660	(Ciccarino *et al.*, 2019)
(R82)	$N(^2S^0, 3p) + e \leftrightarrow N^+ + 2e$	$3.74\ 10^{-9}$	0.42	34,580	(Ciccarino *et al.*, 2019)
(R83)	$N(^4D^0, 3p) + e \leftrightarrow N^+ + 2e$	$4.82\ 10^{-9}$	0.41	32,820	(Ciccarino *et al.*, 2019)
(R84)	$O(^3P) + e \leftrightarrow O^+ + 2e$	BOLSIG+			(Tayal *et al.*, 2016)
(R85)	$O(^1D) + e \leftrightarrow O^+ + 2e$	BOLSIG+			(Tayal *et al.*, 2016)
(R86)	$O(^1S) + e \leftrightarrow O^+ + 2e$	BOLSIG+			(Tayal *et al.*, 2016)

In the present work, we only consider the ionization of O and N to the ground state of the $N^+(^3P)$ and $O^+(^4S)$ ions, because the ionization to other states is negligible[1] (Wang, Zatsarinny and Bartschat, 2014).

The forward rate coefficients of electron-impact ionization of the first three levels of N and O, (R45-R47) and (R84-86), are calculated with BOLSIG+ using the ionization cross-sections obtained by the B-spline R-matrix (BSR) approach (Wang, Zatsarinny and Bartschat, 2014; Tayal and Zatsarinny, 2016). For states above $N(^2D)$ and up to $N(^4D^0)$, the ionization rate coefficients calculated by (Ciccarino and Savin, 2019) are used. We will show in Section 6.1.3 that the reactions listed in Table 5.3 drive the final stage of thermal spark ionization. A summary of the electronic levels of N_2, N, and O modeled in the present mechanism is given in Table 5.4.

Table 5.4 Electronic levels of N_2, N, and O included in the present work. The energy is given relative to the ground state (Huber and Herzberg, 1979; Kramida *et al.*, 2018), g is the level statistical weight.

State	Configuration	g	E_{up} (eV)
$N(^4S^0)$	$2s^22p^3$	4	0
$N(^2D^0)$	$2s^22p^3$	10	2.38
$N(^2P^0)$	$2s^22p^3$	6	3.575
$N(^4P)$	$2s^22p^2(^3P)3s$	12	10.33
$N(^2P)$	$2s^22p^2(^3P)3s$	6	10.68
$N(^4P)$	$2s^22p^4$	12	10.92
$N(^2S^0)$	$2s^22p^2(^3P)3p$	2	11.60
$N(^4D^0)$	$2s^22p^2(^3P)3p$	20	11.75
$O(^3P)$	$2s^22p^4$	9	0
$O(^1D)$	$2s^22p^4$	5	1.97
$O(^1S)$	$2s^22p^4$	1	4.19

State	g	E_{up} (eV)
$N_2(X\ ^1\Sigma_g^+)$	1	0
$N_2(A\ ^3\Sigma_u^+)$	3	6.23
$N_2(B\ ^3\Pi g)$	6	7.40
$N_2(a'\ ^1\Sigma_u^-)$	1	8.45
$N_2(C\ ^3\Pi_u)$	6	11.06
$N_2^+(X\ ^2\Sigma_g^+)$	2	0
$N_2^+(A\ ^2\Pi_u)$	4	1.13
$N_2^+(B\ ^2\Sigma_u^+)$	2	3.16
$N_2^+(C\ ^2\Sigma_u^+)$	2	8.02

[1] We also neglected the three-body recombination with heavy colliders, and therefore did not consider the following reaction, where A = N, O, and M is any heavy collider.

$$A + M \leftrightarrow A^+ + e + M$$

Table 5.5 Supplementary reactions for the thermal spark transition. Quenching reactions are taken from (Popov, 2016b) and the ionization rate coefficients of N^+ and O^+ are calculated in this thesis. The forward rate coefficients are given by $k_f = A\,T^b \exp(-E/RT)$ and backward reaction rates are calculated by detailed balance.

	Reaction & Temp. dependence		A ($cm^3\ s^{-1}$)	b	E/R (K)	Ref.
	Quenching of N_2 electronic excited states (Popov, 2016b)					
(R87)	$N_2(A) + O_2 \leftrightarrow N_2(X) + 2O$	T_g	$9.81\ 10^{-14}$	0.5	0	(Kossyi *et al.*, 1992)
(R88)	$N_2(A) + O_2 \leftrightarrow N_2(X) + O_2$	T_g	$4.33\ 10^{-14}$	0.5	0	(Kossyi *et al.*, 1992)
(R89)	$N_2(A) + O \leftrightarrow NO + N(^2D)$	T_g	$4.00\ 10^{-11}$	0.0	0	(Thomas *et al.*, 1996)
(R90)	$N_2(B) + N_2 \leftrightarrow N_2(A) + N_2$	T_g	$1.00\ 10^{-11}$	0.0	0	(Kossyi *et al.*, 1992)
(R91)	$N_2(B) + O_2 \leftrightarrow N_2(X) + 2O$	T_g	$3.00\ 10^{-10}$	0.0	0	(Kossyi *et al.*, 1992)
(R92)	$N_2(B) + O \leftrightarrow NO + N(^2D)$	T_g	$3.00\ 10^{-10}$	0.0	0	(Shkurenkov *et al.*, 2014)
(R93)	$N_2(C) + N_2 \leftrightarrow N_2(B) + N_2$	T_g	$1.00\ 10^{-11}$	0.0	0	(Kossyi *et al.*, 1992)
(R94)	$N_2(C)+O_2 \leftrightarrow N_2(X)+O+O^*$	T_g	$1.73\ 10^{-11}$	0.3	0	(Rusterholtz *et al.*, 2013)
(R95)	$N_2(C) + O \leftrightarrow NO + N(^2D)$	T_g	$3.00\ 10^{-10}$	0.0	0	(Shkurenkov *et al.*, 2014)
(R96)	$N_2(a') + N_2 \leftrightarrow N_2(B) + N_2$	T_g	$2.00\ 10^{-13}$	0.0	0	(Piper, 1987)
(R97)	$N_2(a')+O_2 \leftrightarrow N_2(X)+O+O^*$	T_g	$2.80\ 10^{-11}$	0.0	0	(Piper, 1987)
(R98)	$N_2(a') + O \leftrightarrow NO + N(^2D)$	T_g	$3.00\ 10^{-10}$	0.0	0	(Shkurenkov *et al.*, 2014)
	Formation of doubly ionized ions					
(R99)	$N^+ + e \leftrightarrow N^{++} + 2e$	T_e	$5.10\ 10^{-12}$	0.68	349,690	This work
(R100)	$O^+ + e \leftrightarrow O^{++} + 2e$	T_e	$9.42\ 10^{-14}$	0.98	381,240	This work

The quenching of N_2 excited states is taken from the work of (Popov, 2016b), which is, to our knowledge, the most complete set of reactions for the simulation of non-thermal nanosecond discharges. It was shown in (Popov, 2016b) that this set reproduces the ultrafast heating observed in (Rusterholtz *et al.*, 2013) and (Lo *et al.*, 2014; Lo, Cessou and Vervisch, 2014) with good accuracy.

The quenching rate coefficients of $N_2(A)$ given in Table 5.5 are slightly modified compared to those of Popov because our model is not vibrational specific and does not include O_2 excited states. Therefore, it was assumed in (R88) that O_2 is not excited to the $O_2(b^1\Sigma_g^+)$ state, which is different from the *(R2)* reaction in (Popov, 2016b).

Also, we discarded the *(R3)*, *(R4)* and *(R6)* reactions of (Popov, 2016b) because they involve vibrationally excited molecules. The formation of NO by $N_2(A)$ quenching, (R92), was initially neglected in the early work of Popov (Popov, 2001). However, it was shown by (Thomas and Kaufman, 1996) and later

by (Burnette *et al.*, 2014; Shkurenkov *et al.*, 2014) that the formation of NO has a higher impact than what was expected.

For the conditions of Rusterholtz *et al.*, Popov showed that the dissociative quenching of N_2(A, B, C, a') represent 63% of the total oxygen dissociation (Rusterholtz *et al.*, 2013; Popov, 2016b). Regarding the production of metastable oxygen by N_2(C), Popov used the branching ratio (46% / 52% / 2%) of metastable argon quenching by O_2 (Balamuta and Golde, 1982; Popov, 2011a). The quenching of metastable xenon, which has a similar energy as N_2(B), does not produce excited atomic oxygen (Balamuta and Golde, 1982). Therefore, we assume that only O(^{3}P) is produced in N_2(B) quenching. Note that Popov used a constant rate coefficient for N_2(C) quenching, although it was shown that the rate varies with $T_g^{0.3}$ (Rusterholtz *et al.*, 2013). The product of N_2(a') quenching is assumed to be O(^{3}P) + O(^{1}D) with a probability of one (Popov, 2016b). Finally, we neglected the quenching of N(^{2}D) and O(^{1}S, ^{1}D), reactions *(R16)* to *(R34)* in (Popov, 2016b), because these reactions induce vibrational excitation which is not included in the present mechanism. The quenching of N(^{2}P) measured by (Salmon *et al.*, 2018) was also neglected.

Finally, the formation of N^{++} and O^{++} by electron-impact of N^+ and O^+ is included, (R99) and (R100). We integrated the cross-sections reported in (Tawara and Kato, 1987) with a Maxwellian EEDF and fitted the results with Arrhenius laws. The ionization rate coefficients fit the integrated results within 1% in the 40,000 – 73,000 K range, see Table 5.6.

Table 5.6 Accuracy of the Arrhenius fits for N^+ and O^+ ionization by electron impact.

	23,000 K	30,000 K	40,000 K	73,000 K
N^+ ionization	~ 1%	< 1%	< 1%	< 1%
O^+ ionization	~ 30%	~ 10%	~ 1%	< 1%

Note that this set of reactions is incomplete if one is interested in the heating generated by *non-thermal* sparks. For that purpose, the quenching of atomic metastable states may have to be included (Popov, 2016a) along with other species such as O^-, O_3, and N_4^+ (Bak and Cappelli, 2015). We aim to pursue this task in future work.

5.2 Detailed balance

In these simulations, the reverse rates are computed by detailed balance (Dresvin, 1977; Alberty and Silbey, 1992). Let us define Reac. 5.1 involving four fictitious species: A, B, C, and D.

$$A + B \leftrightarrow C + D \qquad \text{Reac. 5.1}$$

If k_f, the forward rate coefficient of Reac. 5.6, is known, then, k_r, the reverse rate coefficient can be computed using Eq. 5.1, where Z_X is the partition function of species X.

$$\frac{k_f}{k_r} = \frac{Z_C Z_D}{Z_A Z_B}(T) \qquad \text{Eq. 5.1}$$

The definition of the partition function is given in Chapter 3 where its energy reference is set to the energy of the atomic ground state.

As stated before, if the collision partners are heavy particles, we must set $T = T_{gas}$ in Eq. 5.1. However, if one electron is involved, then we must set $T = T_e$. For instance, in Reac. 5.2 the forward rate is a function of T_{gas} and the reverse rate depends on T_e.

$$N + N \leftrightarrow N_2^+ + e \qquad \text{Reac. 5.2}$$

A particular treatment must be applied for three-body reactions involving two heavies and one electron but does not concern this work (Annaloro *et al.*, 2017).

For instance, we take the case of ionization/recombination of atomic nitrogen N(^{4}S), detailed balance is equivalent to the Saha formula (Eq. 5.2), where m_e is the electron mass, k_b the Boltzmann constant, T_e the electron temperature, h the Planck constant, g_X the degeneracy of X, I the ionization energy of N(^{4}S), and $k_{f,i}$ the ionization rate computed with BOLSIG+.

$$k_{r,i} = \frac{1}{2}\left(\frac{2\pi m_e k_b T_e}{h^2}\right)^{-\frac{3}{2}} \frac{g_{N(^4S)}}{g_{N^+}} \exp\left(\frac{\mathrm{I}}{k_b T_e}\right) k_{f,i} \qquad \text{Eq. 5.2}$$

The first term in Eq. 5.2 is the inverse of the electron partition function and the factor 1/2 accounts for the electron degeneracy. The Saha formula is exact if the EEDF is a Maxwellian (the use of T_e requires to have a Maxwellian EEDF).

5.3 Tests of the kinetic mechanism

5.3.1 Equilibrium composition

To test the present mechanism, we compute the equilibrium composition of air at temperatures ranging from 300 to 40,000 K. The initial composition of the mixture is synthetic air (79% of N_2 and 21% of O_2) at 1 atm and 300 K. The simulation is run for a sufficiently long time (≥ 1 s) as to reach equilibrium. In the first set of simulations, we assume an isochoric transformation from ambient air (p = 1 atm, T = 300 K) to a given temperature up to 40,000 K.

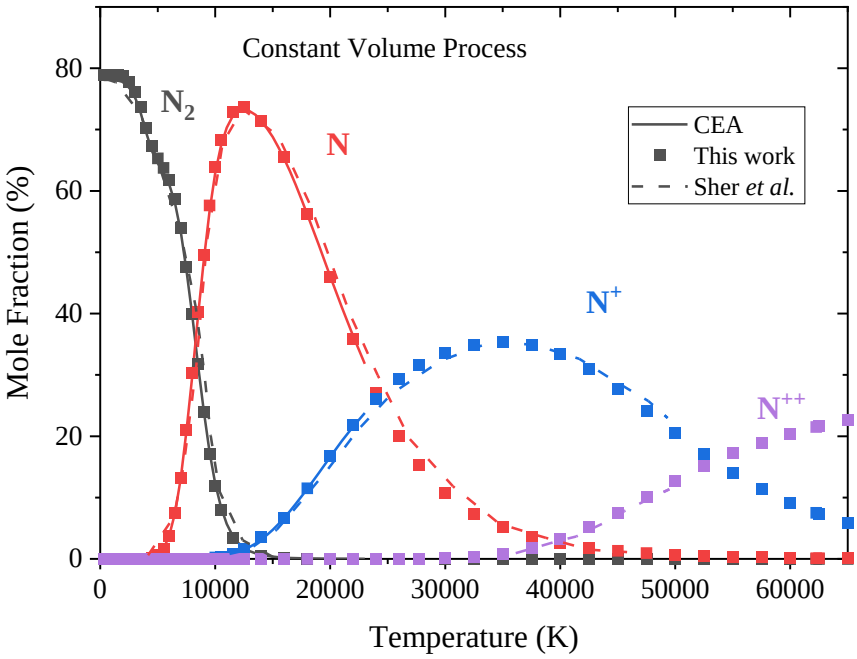

Figure 5.1 Equilibrium composition of synthetic air as a function of the temperature in a constant volume process. Comparison of N_2, N, and N^+ mole fractions according to the CEA (solid line), the data in Sher *et al.* (dashed line), and this work (squares).

In Figure 5.1, the mole fractions of N_2, N, and N^+ are compared with the calculations performed with the "Chemical Equilibrium with Applications" (CEA) NASA code[1] (McBride and Gordon, 1992). N_2 is fully dissociated around 10,000 K and N is almost completely ionized at 40,000 K. Our values are in close agreement with those of CEA up to 23,000 K (upper limit of CEA). They also compare well with the values reported by (Sher, Ben-Ya'ish and Kravchik, 1992) up to 50,000 K. A comparison of the O_2, NO, O, and O^+ mole fractions presented in Figure 5.2. Notably, the NO mole fraction computed by Sher *et al.* is not consistent with our values and those of CEA. We therefore consider the results of CEA as a reference up to around T = 20,000 K, and we compare with the results of Sher *et al.* otherwise.

[1] The code is available at cearun.grc.nasa.gov (consulted in April 2020)

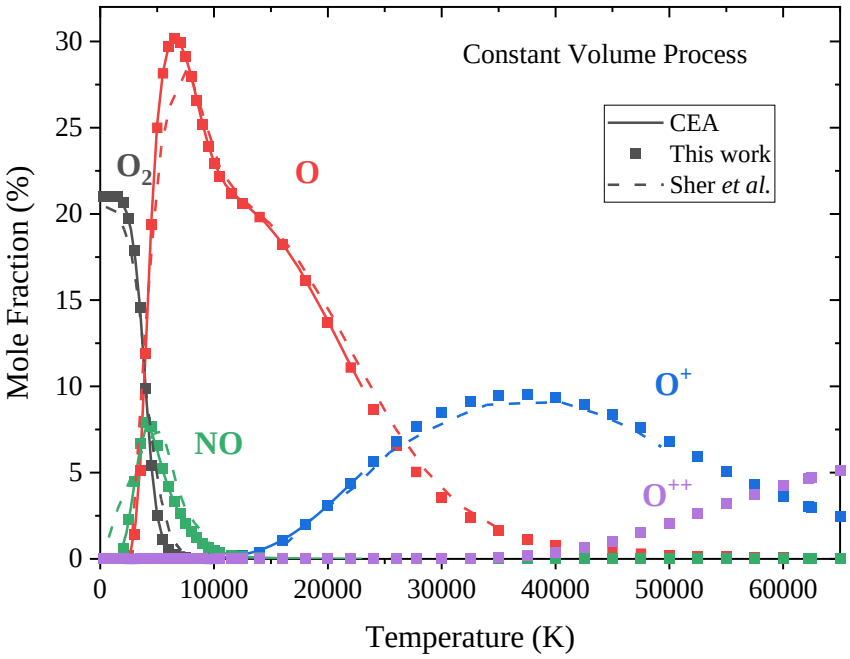

Figure 5.2 Equilibrium composition of synthetic air as a function of temperature in a constant volume process. Comparison of O_2, NO, O, and O^+ mole fractions according to the CEA (solid line), the data in Sher *et al.* (dashed line), and this work (squares).

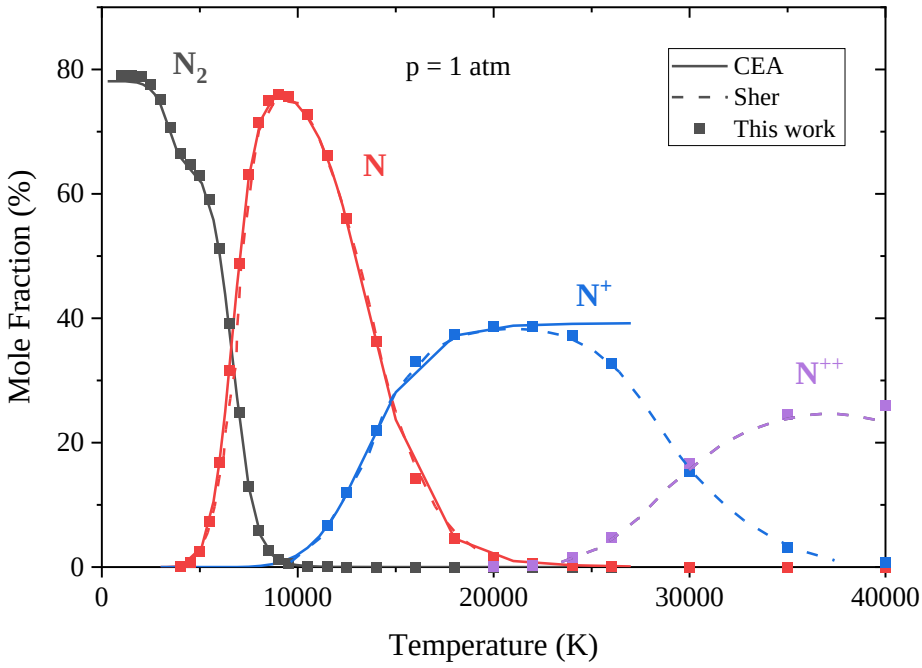

Figure 5.3 Equilibrium composition of synthetic air as a function of temperature at 1 atm. Comparison of N_2, N, N^+, and N^{++} mole fractions according to the online calculation of CEA (solid line), the values in Sher *et al.* (dashed line), and this work (squares).

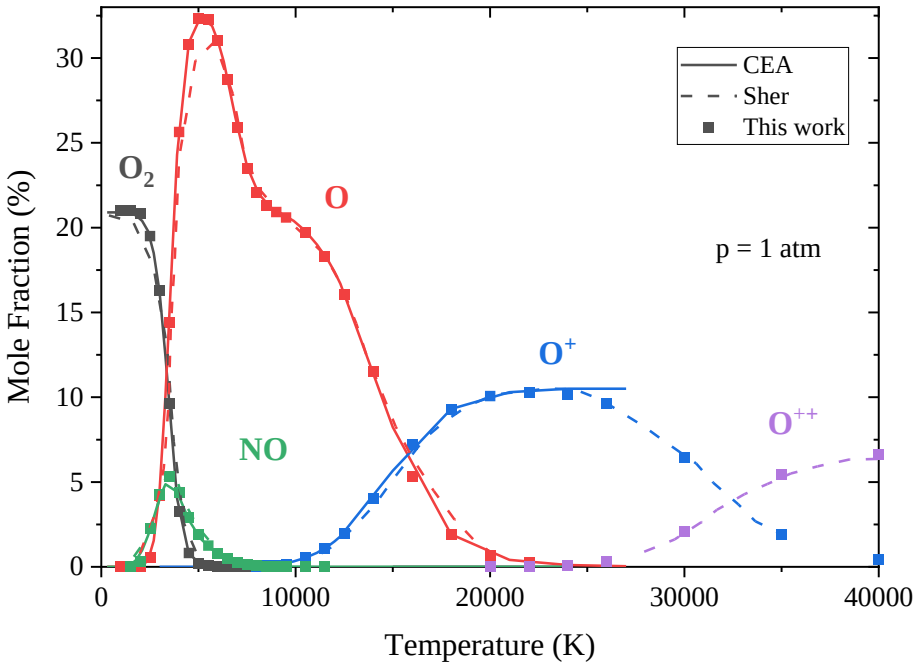

Figure 5.4 Equilibrium composition of synthetic air as a function of temperature at 1 atm. Comparison of O_2, O, O^+, and O^{++} mole fractions according to the online calculation of CEA (solid line), the values in Sher *et al.* (dashed line), and this work (squares).

In Figure 5.3 and Figure 5.4, the equilibrium composition of synthetic air at constant pressure (1 atm) agrees closely with the calculations of CEA and Sher *et al.*. The differences between our results and those of CEA above 20,000 K are due to the formation of doubly ionized ions, not included in the CEA calculations. However, doubly ionized ions were considered in the work of Sher *et al.*, and our results are in close agreement with theirs. Thus, these results validate the correct implementation of detailed balance in our kinetic mechanism. All species needed to describe ionization up to 40,000 K are taken into account. Above 40,000 K, in a constant pressure transformation, the formation of triply ionized ions should be included (Sher, Ben-Ya'ish and Kravchik, 1992).

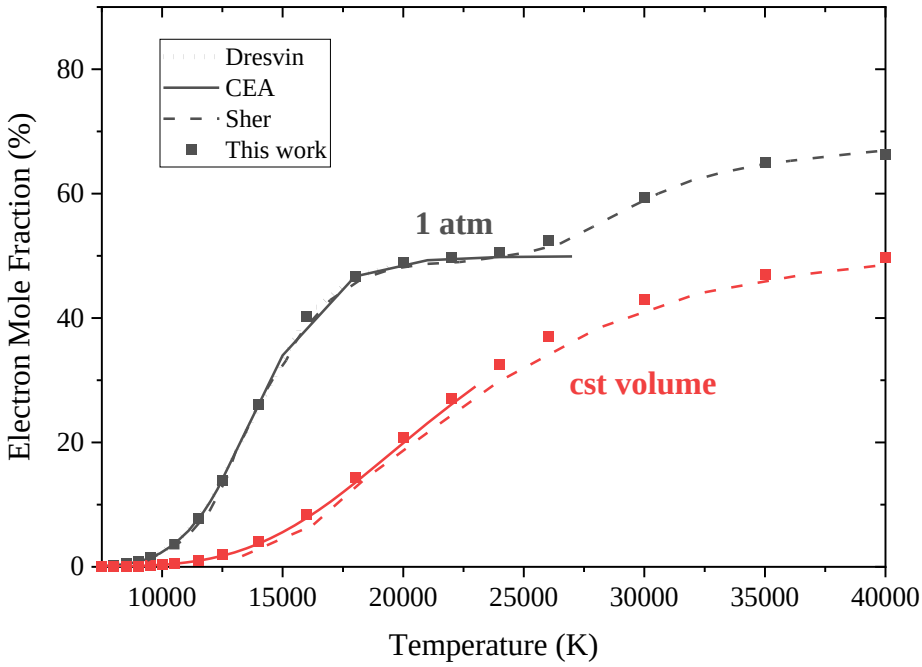

Figure 5.5 Equilibrium ionization of synthetic air N_2 : O_2 (0.79 : 0.21) as a function of temperature for isochoric and isobaric processes. Our data (squares) are compared to the CEA (solid line), the data of Sher *et al.* (dashed line), and the values reported by Dresvin (dotted line).

The full ionization of the plasma occurs at ~ 20,000 K in a constant pressure process, but above 30,000 K in a constant volume one. In constant volume heating, the pressure is indeed higher than 1 atm for T_{gas} > 300 K. Ionization and molecular dissociation increase the pressure and are therefore unfavored at high pressure. This result is also known as Le Châtelier's principle. Accordingly, we show in Figure 5.5 that higher ionization fractions are obtained at constant pressure. Along with the calculations of CEA and Sher *et al.*, we also show in Figure 5.5 the values reported in (Dresvin, 1977, p. 22).

In this section, we ran an equilibrium composition test up to 40,000 K, in a constant pressure transformation, and up to 50,000 K, in a constant volume transformation. Up to these limits, our results agree with three references. The equilibrium composition calculated in the constant volume approximation is valid up to 65,000 K because the mole fraction[1] of N^{+++} remains below 5%.

[1] We computed the equilibrium composition of a Saha-equilibrium composition assuming that the plasma is only composed of nitrogen, T = 65,000 K, and n_e = 8×10^{19} cm^{-3} (physics.nist.gov/PhysRefData/ASD). The output of the calculation gives the following mole fractions: N (2.4%), N^+ (29%), N^{++} 64%, N^{3+} (4.1%), and N^{4+} (<0.1%).

5.3.2 Two-temperature steady-state

In (Laux *et al.*, 1999), a set of 38 reactions was used to study a non-thermal plasma at T_{gas} = 2000 K (fixed) and 2000 K < T_e < 18,000 K. Laux *et al.* showed that in non-equilibrium conditions, the ionization is driven by Reac. 5.3 – Reac. 5.6 (included in our kinetic mechanism, see Table 5.1 and Table 5.3). The rates of these reactions are controlled by T_e.

$$N_2 + e \rightarrow N_2^+ + 2e \quad \text{Reac. 5.3}$$
$$O_2 + e \rightarrow O_2^+ + 2e \quad \text{Reac. 5.4}$$
$$O_2 + e \rightarrow O + O + e \quad \text{Reac. 5.5}$$
$$O + e \rightarrow O^+ + 2e \quad \text{Reac. 5.6}$$

The recombination of electrons is mainly[1] due to Reac. 5.9, the dissociative recombination of NO^+ molecules, which are formed by charge exchange, Reac. 5.7 and Reac. 5.8. The rates of Reac. 5.7 and Reac. 5.8 are, however, controlled by T_g and the recombination is ultimately limited by Reac. 5.7.

$$N_2 + O^+ \rightarrow NO^+ + N \quad \text{Reac. 5.7}$$
$$NO + O_2^+ \rightarrow NO^+ + O_2 \quad \text{Reac. 5.8}$$
$$NO^+ + e \rightarrow N + O \quad \text{Reac. 5.9}$$

In (Laux *et al.*, 1999), two initial conditions were chosen:

1. Equilibrium air composition at $T_{gas} = T_{e0}$ = 2000 K and p = 1 atm.
2. Steady-state air composition at T_{gas} = 2000 K, T_{e0} = 18,000 K, and p = 1 atm.

Then, the gas temperature remained at T_{gas} = 2000 K and T_e was varied between 8000 and 18,000 K. It was shown numerically and analytically that if $T_e \neq T_{gas}$, *the pressure and the temperatures do not entirely determine the steady-state composition of air*. Instead, the initial composition of the gas plays a role[2].

[1] Note however that, in non-thermal sparks at $n_e > 10^{15}$ cm^{-3} , the dominant ions are N_2^+, O_2^+, NO^+, and N_4^+, see Figure 4 in (Bak and Cappelli, 2015).

[2] This result was also recently demonstrated in argon (Annaloro *et al.*, 2017)

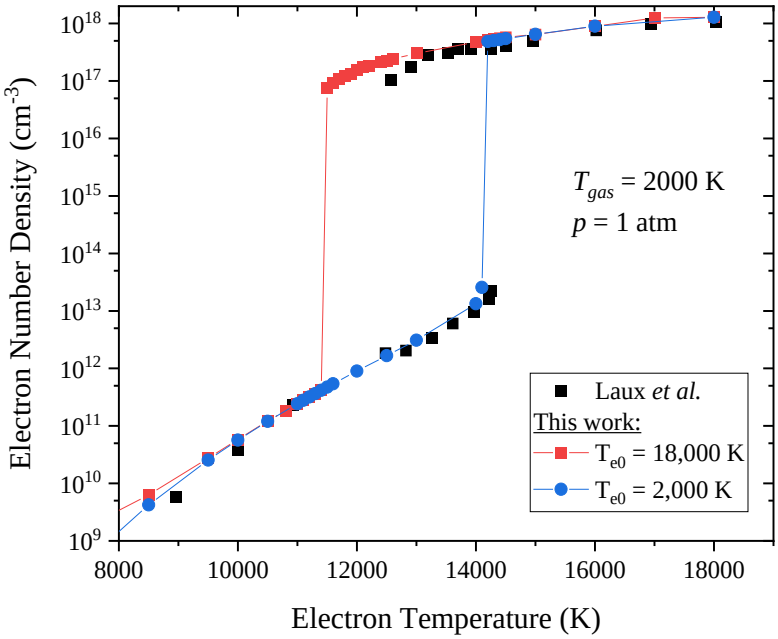

Figure 5.6 Comparison of the steady-state n_e obtained by Laux *et al.* (in black) and with the present kinetic mechanism. The steady-state electron number density is shown for a gas mixture initialized with the equilibrium composition at $T_{gas} = T_e = 2000$ K (in blue), and at $T_{gas} = 2000$ K and $T_e = 18{,}000$ K (in red).

In Figure 5.6, for T_{e0} = 2000 K and T_e < 14,300 K, at steady state, the electrons recombine with NO^+ and the plasma remains partially ionized. For T_e > 14,300 K, ionization by electron impact is faster than the charge exchange reaction. All the molecules are thus dissociated, and the ionization is eventually balanced by three-body recombination. The three-body recombination is slower than NO^+ dissociative recombination. Thus, the steady-state n_e is significantly higher at T_e > 14,300 K.

For T_{e0} = 18,000 K, the plasma is initially close to full ionization[1]. Therefore, the number density of molecules (N_2, O_2, NO) is low and the formation of NO^+ by charge exchange is strongly limited by Reac. 5.7. Ultimately, for electron temperatures below 12,000 K, n_e falls below 10^{17} cm^{-3}. Thus, the N_2 number density is high enough to activate Reac. 5.7 - Reac. 5.9 and the electrons recombine efficiently with NO^+.

[1] Note that the gas and electron temperatures are fixed numerically. At T_{gas} = 2000 K, T_{e0} = 18,000 K, and p = 1 atm, the steady-state electron number density is $n_e \sim 10^{18}$ cm^{-3}. Thus, the gas is fully ionized, and it is expected that $T_{gas} = T_e$ in the upper limb in Figure 5.6. This aspect has however no influence on the transition from the lower to the higher limb of the curve.

In Figure 5.6, we reproduced the results of Laux *et al.* with the kinetic mechanism[1] presented in Section 5.1. The EEDF is taken to be Maxwellian at a given temperature T_e. For T_{e0} = 2000 K, we obtained identical results. This agreement is expected because the rates of charge exchange are identical to those of Laux *et al.* Also, the rate coefficients of ionization used by Laux *et al.* were obtained by integration of the ionization cross-sections by a Maxwellian EEDF, which is strictly equivalent to what is performed in our simulations. However, for T_{e0} = 18,000 K, the abrupt fall of the steady-state n_e is obtained at 12,500 K by Laux *et al.* and at 11,500 K in the present work. This difference is due to the inclusion of N and O excited states in our mechanism. These electronic states store N and O atoms that are not available for N_2 and O_2 formation. The recombination of electrons with NO^+ is therefore shifted to lower temperatures.

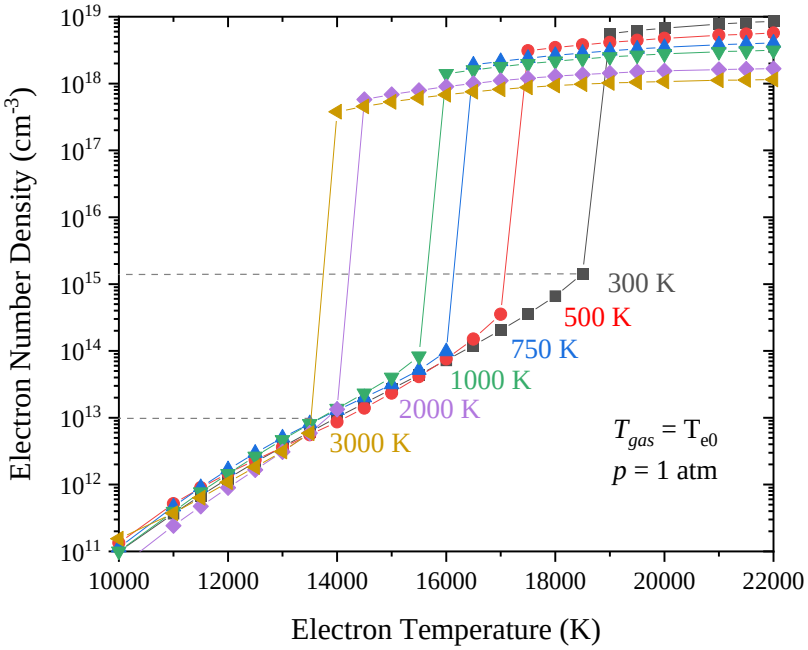

Figure 5.7 Influence of T_{gas} on the S-curve. The gas temperature is given next to each curve with the corresponding color (*e.g.* the calculation at T_{gas} = 500 K are performed in red).

We showed in Figure 5.6 that at T_{gas} = 2000 K, the maximal ionization of a two-temperature steady-state plasma is 10^{13} cm^{-3}. At higher n_e, the electron recombination with NO^+ is too slow and the plasma

[1] N^{++} and O^{++} formations are however not included because the rates we computed in Table 5.5 are not accurate enough at these temperatures.

reaches full ionization. In Figure 5.7, calculations are performed [1] at ambient pressure with 300 K < T_{gas} < 3000 K. We show the two-temperature steady state is common for all plasmas for T_e < 14,000 K. However, for decreasing T_{gas}, the transition to fully ionized plasmas shifts to higher T_e. For instance, at T_{gas} = 300 K, the highest electron number density in the low-limb of the S-curve is obtained at T_e = 18,000 K and reaches $n_{e,steady} \approx 10^{15}$ cm^{-3} ≈ 100 ppm. However, with T_{gas} = 3000 K, we obtain at most $n_{e,\,steady} \approx 10^{13}$ cm^{-3} ≈ 10 ppm at T_e = 13,000 K, which is two orders of magnitude lower in absolute density. Indeed, at 300 K, the conversion of O_2^+ to NO^+ is slower. This difference is visible in Figure 5.8 where the number density of positive ions is compared to the electron number density. At 300 K, electrons equilibrate with N_2^+, O_2^+, and NO^+ ions. Instead, at 3000 K, the N_2^+ and O_2^+ number density is negligible because they are converted to NO^+. Thus, at T_{gas} = 300 K, more channels of recombination are open, which makes it theoretically possible to sustain a partially ionized plasma with n_e = 10^{15} cm^{-3}. However, such a state would be challenging to sustain in practice because, at n_e = 10^{15} cm^{-3}, ultrafast-heating would increase the gas temperature unless the gas is flown through the discharge at very high velocity.

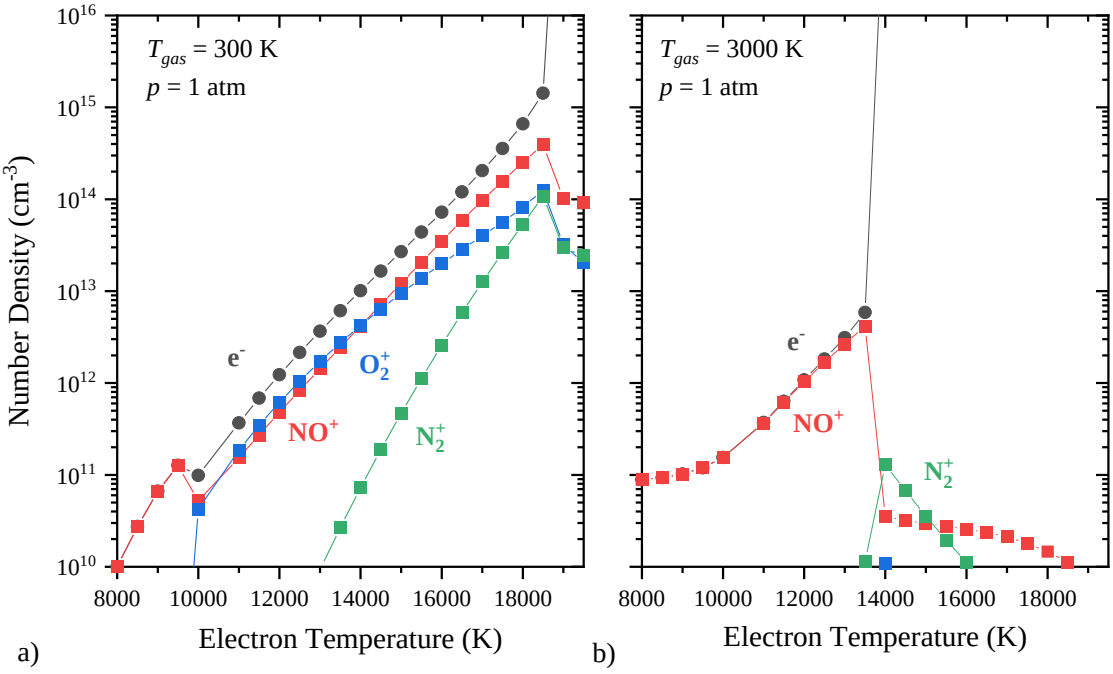

Figure 5.8 Steady-state number density of positive ions compared to the electron number density. The gas temperature is equal to 300 K (left, a) and 3000 K (right, b).

[1] The formation of some negative (O^-, O_2^-, O_3^-, O_4^-, $N_xO_y^-$) and positive ions (N_4^+, O_4^+, N_xO^+) are neglected in the present work but could have an impact below 2000 K (Kossyi *et al.*, 1992). Their addition to our mechanism could slightly shift the transition from the lower to the higher limb of the curve in Figure 5.7.

5.4 Conclusion

We built a kinetic mechanism for air discharges near ambient conditions. The baseline kinetic mechanism is mainly taken from the work of (Park, 1993; Laux *et al.*, 1999; Popov, 2016b). Additional reactions and species were added:

- The excitation of N_2 electronic states. Their ionization and dissociation were also included.
- The transitions between N_2^+ excited states.
- The ionization of N and O excited states.
- The ionization of N^+ and O^+.

This mechanism is tested at equilibrium up to 40,000 K in the isochoric and isobaric approximations. However, we expect this kinetic model to be correct up to 60,000 K in the isochoric approximation. Further tests are performed by comparing our results to those of Laux *et al.* on two-temperature plasmas. The latter test was also the opportunity to show that, at atmospheric conditions, an electron number density of up to 10^{15} cm^{-3} could be sustained at steady-state.

Chapter 6

Transition from a non-thermal to a thermal nanosecond spark

In this chapter, the thermal spark formation is described using the kinetic mechanism developed in Chapter 5. In Section 6.1, the full ionization mechanism is first detailed on an academic example. The ionization of excited atomic states is found to drive a sudden increase of the electron number density from 10^{17} to 10^{19} cm^{-3} in 0.5 ns. During the transition, the frequency of elastic collisions between ions and electrons increases, leading to the thermalization of the heavy species (atoms, ions) with the electrons. Then, in Section 6.2, the formation of a fully ionized plasma is studied experimentally in the cathode vicinity. The electron number density is measured with three methods and compared to the numerical results.

6.1 Fast full ionization of the thermal spark

6.1.1 Formation of a fully ionized plasma

In this section, the initial gas temperature is equal to 300 K, and the initial electron temperature to 1000 K. The initial number density of the gas (79% N_2 and 21% O_2) is equal to the Loschmidt number at 300 K and 1 atm, $n_{Los} = 2.45\times10^{19}$ cm^{-3}. The initial[1] electron number density is equal to $n_{e0} = 10^6$ cm^{-3}. The time-integration step is 5 ps. A field of 6 kV.mm^{-1} is applied, which corresponds to $(E/N)_0$ = 240 Td in ambient conditions. This field is representative of setup #2 in Chapter 4 (Minesi, Stepanyan, *et al.*, 2020).

In BOLSIG+, the reduced field E/N is the ratio of the electric field to the neutral particle density, $N_{neutral}$. As we will see in the present work, however, the neutral particle density can drop to negligible values, and the reduced field tends toward infinity. Thus, the electron temperature increases above reasonable values. Therefore, we define N as the heavy particle density, i.e. $N = N_{ion} + N_{neutral}$. Another approach

[1] The variation of the initial electron number density will only shift the kinetic curves in time. Apart from this aspect, it is found to have a minor influence on the results, up to $n_{e0} = 10^{10}$ cm^{-3}.

consists, instead, to impose the electron temperature. This procedure produces similar results as detailed in Section 6.1.5.

The plasma recombination phase (t > 10 ns) is not studied with the present model. It was shown in Chapter 4 that the decay of n_e in the thermal spark afterglow is, at least up to t = 100 ns, due to the plasma channel cooling during an isentropic expansion.

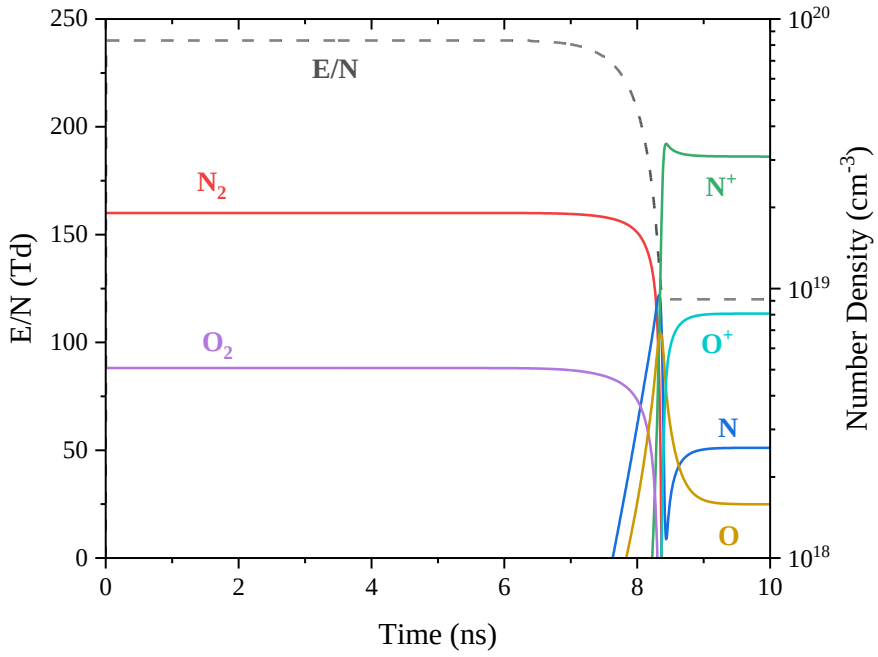

Figure 6.1 Diminution of the reduced field (dashed grey line) due to the dissociation of molecules. The number density of major species (solid lines) is also given.

The evolution of E/N and the number density of major species (N_2, O_2, O, N, N^+, and O^+) are shown in Figure 6.1. Up to t = 8 ns, E/N = 240 Td and the gas composition does not change much. At t = 8 ns, the reduced field begins to decay due to molecular dissociation. During a short period of 0.5 ns, the plasma undergoes an abrupt transition from a molecular to an atomic composition. Shortly after, the atoms are ionized and E/N remains constant. The plasma is fully ionized at t = 9 ns. In the following, the discussion focuses on the transition between a partially and a fully ionized plasma.

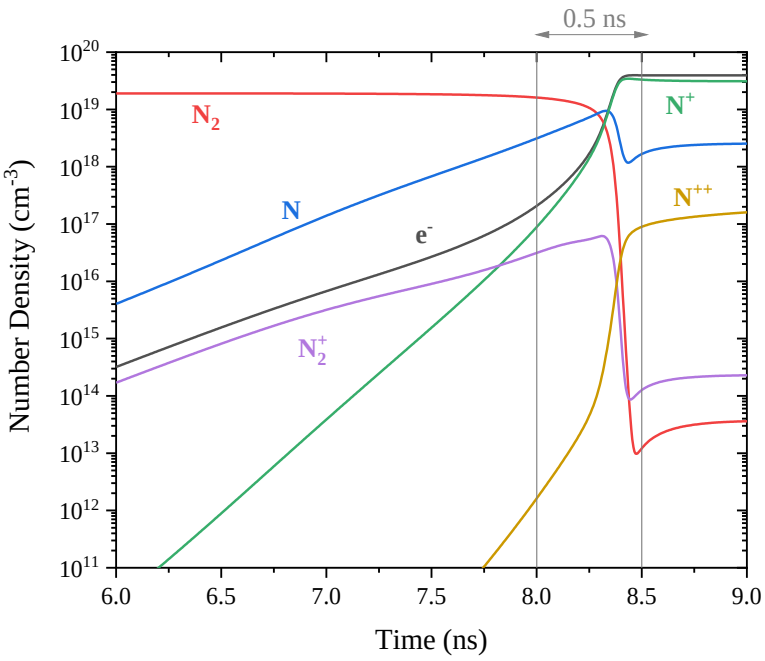

Figure 6.2 Detailed evolution of the number density of nitrogen species during a 10-ns pulse of 6 kV/mm.

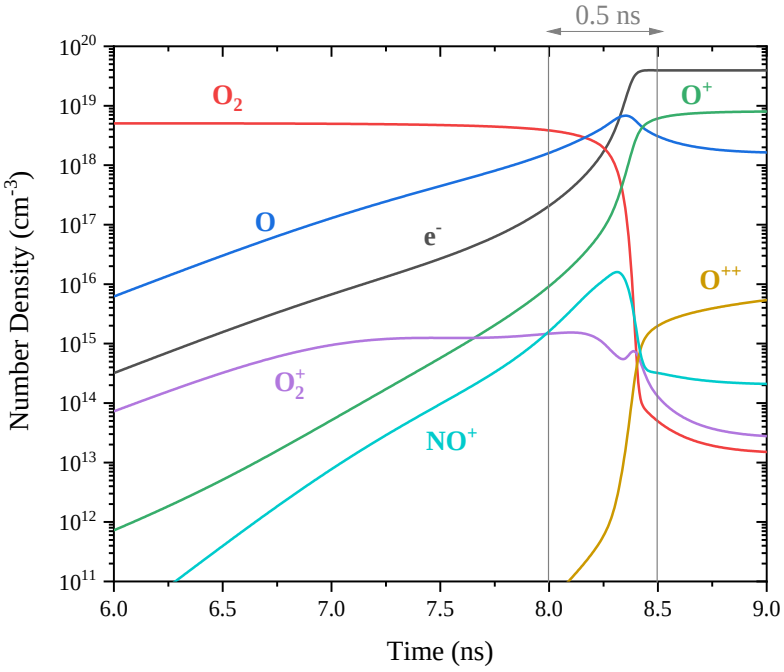

Figure 6.3 Detailed evolution of the number density of oxygen species and NO^+ during a 10-ns pulse of 6 kV/mm.

The abrupt transition at $t = 8$ ns is also visible in Figure 6.2 and Figure 6.3, where the plasma composition is more detailed. We emphasize the interval 8.0 ns – 8.5 ns by two grey lines. During this short period, the electron number density gains two orders of magnitude, as also shown in Table 6.1. This result corresponds to earlier experimental observations of fully ionized filaments, abruptly generated by nanosecond discharges in less than 0.5 ns in (Minesi, Stepanyan, *et al.*, 2020), 2 ns in (Orriere, Moreau

and Pai, 2018), and less than 5 ns in (Lo *et al.*, 2017). Comparing Figure 6.2 and Figure 6.3, oxygen and nitrogen species follow approximately the same evolution with time.

Table 6.1 Plasma parameters before (t = 8.0 ns) and after (t = 8.5 ns) the fast ionization phase. At t = 8.5 ns, we calculate that only 39% of atomic nitrogen is in the ground state (1.7×10^{18} cm^{-3}).

t (ns)	E/N (Td)	T_e (K)	T_{gas} (K)	N_2 (cm^{-3})	N (cm^{-3})	N^+ (cm^{-3})	n_e (cm^{-3})
8.0	208	39,800	1500	$1.6\ 10^{19}$	$4.9\ 10^{18}$	$8.8\ 10^{16}$	$2.1\ 10^{17}$
8.5	120	34,900	34,700	$1.2\ 10^{13}$	$4.3\ 10^{18}$	$3.3\ 10^{19}$	$3.9\ 10^{19}$

6.1.2 Increase of the gas temperature

The results of this section are used notably in Sections 8.5.3.

When the plasma is weakly ionized (t < 8 ns), the electron temperature is constant around T_e ~ 45,000 K and the gas (or heavy) temperature remains below 1500 K, see Figure 6.4. As the electron number density increases, the gas temperature jumps from 1500 to 34,700 K in 0.5 ns (see Table 6.1). The decrease of the reduced field (due to molecular dissociation) induces a global decrease of T_e between 6 ns and 10 ns. Near t = 8.5 ns, T_e increases and then decreases because the EEDF calculation depends on T_{gas} (see Eq. (27) in (Hagelaar and Pitchford, 2005)). These variations vanish if we perform the simulation assuming T_{gas} = 300 K (see cyan curve in Figure 6.4). Soon after, at t = 10 ns, the electrons are thermalized with the heavy particles at T_{gas} = T_e = 32,500 K.

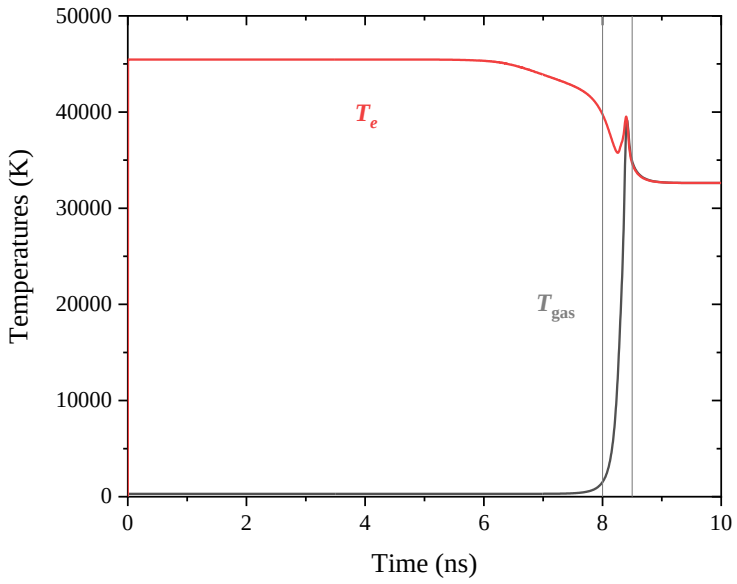

Figure 6.4 Comparison of the gas temperature increase (in grey) with the electron temperature (in red). The evolution of T_e is also calculated assuming T_{gas} = 300 K (in cyan).

In non-equilibrium nanosecond spark discharges, the gas is weakly ionized (n_e = 10^{15} – 10^{16} cm^{-3}) and the temperature of the heavy particles increases ($\Delta T \sim 1000$ K) mainly due to the ultrafast heating mechanism (Rusterholtz *et al.*, 2013). Models to determine the temperature evolution of non-equilibrium discharges are available in the literature (Bak and Cappelli, 2015; Popov, 2016a). In the present model of thermal spark discharges, we incorporate only energy transfer through elastic and inelastic collisions between electrons and heavy particles (calculated using BOLSIG+). Heating associated with chemical reactions is neglected. We show in the following that the increase of T_{gas} is only due to electron collisions.

The electron-electron, ν_{ee}, and electron-ion, ν_{ei}, collision frequencies can be calculated in Eq. 6.1, where the average velocity of electrons is $\sqrt{8k_bT_e/\pi m_e} \sim 10^8$ cm s^{-1}.

$$\nu_{ei} = \nu_{ee} = n_e \sigma_{Coul} \sqrt{\frac{8k_bT_e}{\pi m_e}} \qquad \text{Eq. 6.1}$$

The Coulomb cross-section, σ_{Coul}, is approximated in Eq. 6.2 by the where the Coulomb logarithm[1] is given by $\ln(\Lambda) = 13.57 + 1.5 \log_{10}(T_e) - 0.5 \log_{10}(n_e)$ (Raizer, 1991).

$$\sigma_{Coul} = 2.87 \times 10^{-14} \frac{\ln\Lambda}{(T_e[\text{eV}])^2} [\text{cm}^2] \qquad \text{Eq. 6.2}$$

The frequency of energy exchange between electrons and ions (assumed to be mostly N^+) in elastic collisions is given by the following relation:

$$\nu_{ei}^E \approx \frac{m_e}{m_{N^+}} \nu_{ee}$$

Thus, the ion-electron thermalization time, τ_{ei}^E, is given in Eq. 6.3 and plotted in Figure 6.4.

$$\tau_{ei}^E \sim \left(\frac{m_e}{m_{N^+}} \nu_{ee}\right)^{-1} \qquad \text{Eq. 6.3}$$

with $m_{N^+}/m_e = 25{,}700$. The electron-neutral thermalization time, τ_{en}^E, is calculated in Eq. 6.4, where $\sigma_{tr} = 10^{-16}$ cm^2 (Raizer, 1991).

$$\tau_{en}^E \sim \left(\frac{m_e}{m_N} \nu_{ee}\right)^{-1} = \left(\frac{m_e}{m_N} n_{neutral} \sigma_{tr} \sqrt{\frac{8k_bT_e}{\pi m_e}}\right)^{-1} \qquad \text{Eq. 6.4}$$

[1] In the present application, the Coulomb logarithm ranges between 4.5 and 7.5.

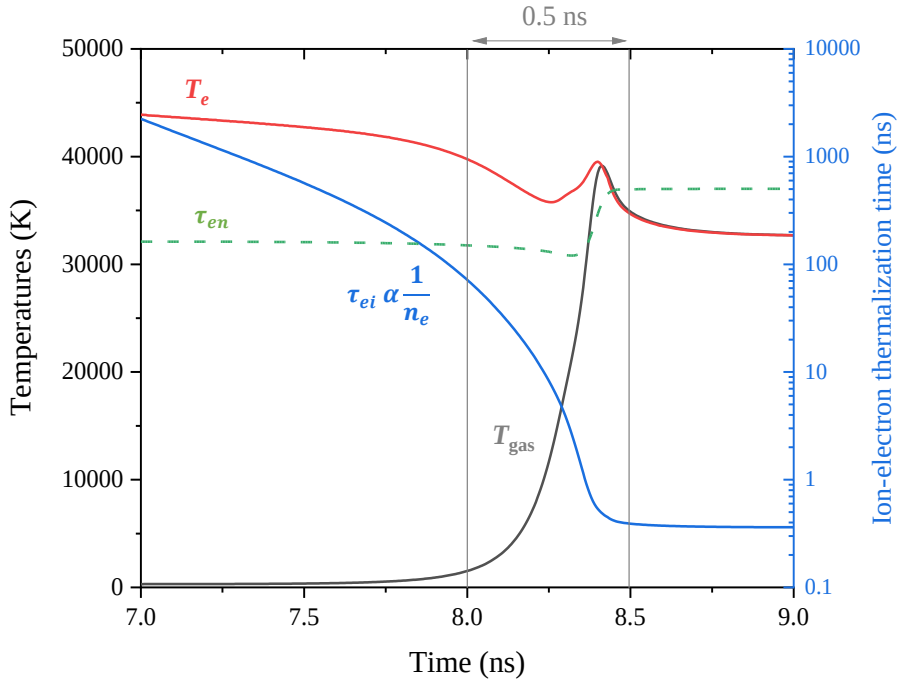

Figure 6.5 Comparison of the temperature increase with the ion-electron thermalization time (in blue). The electron-neutral thermalization time is provided for reference (dashed green).

The electron-neutral thermalization time, τ_{en}^E, remains above 200 ns and becomes much longer than τ_{ei}^E after t = 8.0 ns, as shown in Figure 6.5. At t = 8.0 ns, $n_e \approx 10^{17}$ cm^{-3} and τ_{ei}^E decreases by two orders of magnitude until it reaches approximately 0.4 ns at t = 8.5 ns. At the same time, the gas temperature reaches 10,000 K in 0.25 ns, then 35,000 K in 0.5 ns. Once accelerated, ions can efficiently transfer their energy to the remaining neutral particles because their masses are similar[1]. The thermalization by electron-ion collisions has already been discussed in the literature (Bastien and Marode, 1979; Almazova *et al.*, 2020) and the critical electron number density was found to be around $n_e = 10^{16} – 10^{17}$ cm^{-3} (Barreto, Jurenka and Reynolds, 1977; Stritzke, Sander and Raether, 1977), which is consistent with the present simulations.

[1] The typical thermalization time between N and N^+ is approximately $\sqrt{m_{N^+}/m_e} = 160$ times smaller than τ_{en}.

6.1.3 Influence of the N excited states

The origin of the fast ionization stage and the impact of the ionization of N electronic states on the plasma kinetics are now discussed. Figure 6.6 and Figure 6.7 show the net rates of the dominant ionization processes and their relative contributions. The net ionization rate, R_{net}, is given in Eq. 6.5, where the recombination rate of A is subtracted to its ionization rate.

$$R_{net}\left[\mathrm{cm^{-3}s^{-1}}\right] = k_{ion} n_A n_e - k_{recomb} n_{A^+} n_e^2 \qquad \text{Eq. 6.5}$$

The ionization of N_2 ground and excited states are summed for clarity and represented by a single curve. The importance of N_2 excited states ionization is discussed later.

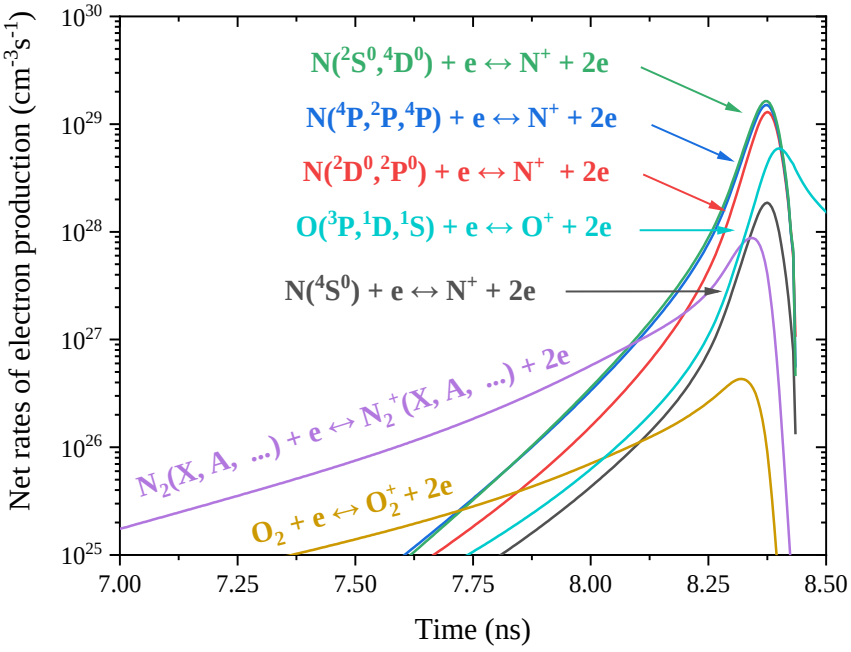

Figure 6.6 Net ionization rates of dominant processes (backward rates subtracted). The net ionization rates of the two metastable states of N at 2.38 and 3.57 eV (in red) are added together. The next 5 levels are combined into two groups: E_i = 10.33, 10.68, 10.92 eV (in blue) and E_i = 11.60, 11.75 eV (in green). The net ionization rates of all N_2 and O electronic levels are also combined in two groups (in purple and cyan, respectively).

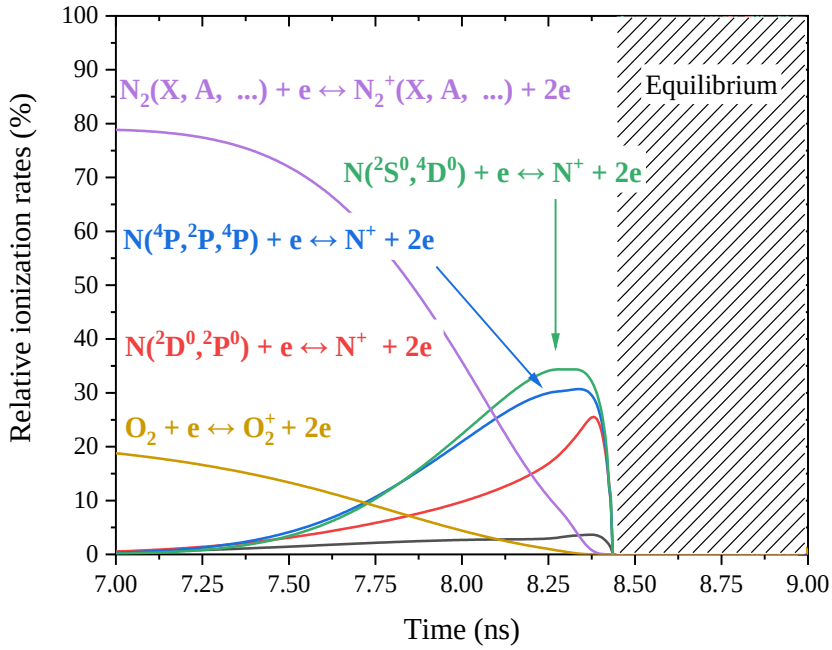

Figure 6.7 Net ionization rates relative to the net electron production rate, for the conditions of Figure 6.6.

At t < 6.5 ns, the plasma is still partially ionized ($n_e < 10^{15}$ cm^{-3} in Figure 6.3) and the electron production is dominated by the ionization of N_2, N_2^*, and O_2. At t = 7 – 7.5 ns, the ionization of N excited states already represents ~ 10% of the total ionization, but the ionization of N(^{4}S) is still negligible. At t = 8.0 ns, the electrons are now mainly (~ 70%) produced by electron-impact ionization of N excited states. Finally, at t = 8.4 ns, the peak of ionization is reached, more than 10^{20} cm^{-3} ns^{-1}, and the gas is already ionized above 50%. The fall of N_2 and O_2 ionization rates is due to the fast decay of N_2 and O_2 number densities at this moment (see Figure 6.2). The contribution of O(^{3}P, ^{1}D, ^{1}S) ionization rates, shown in Figure 6.6, reaches its maximum after the ionization peak. This delay, compared to N ionization, could be reduced if higher excited states of O were added to the kinetics. The ionization of O(^{3}P, ^{1}D, ^{1}S) remains however below 5% in terms of relative importance[1].

[1] Addition of higher excited states is planned for future work, although it will not have major consequences on the model.

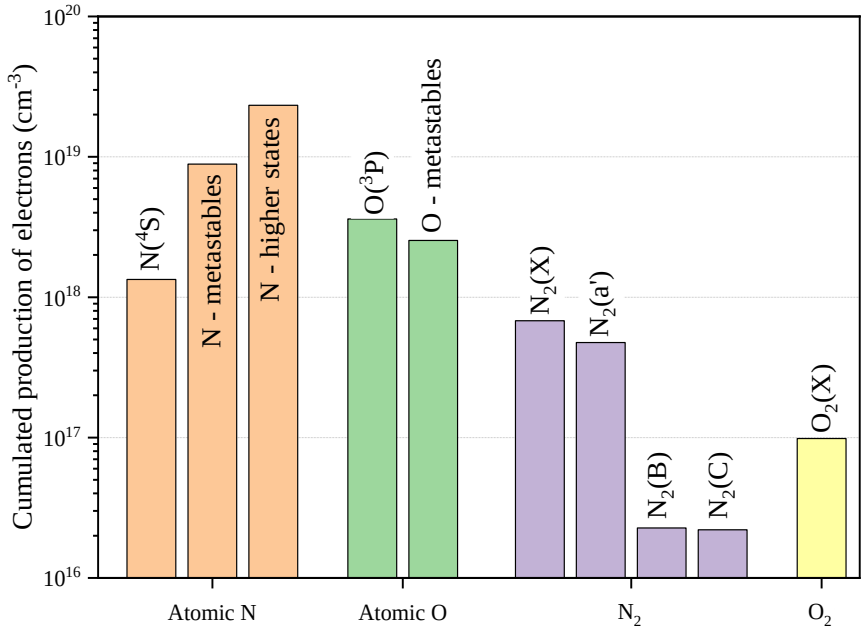

Figure 6.8 Cumulated production of electrons for the main ionization pathways. The cumulative values are integrated in the range 0 – 8.5 ns.

The relative importance of the rates of ionization is also shown in Figure 6.8 with a column graph. The total number of electrons produced by the N excited states is above 2×10^{19} cm^{-3} and most of the ionization through these channels occurs in 0.5 ns. O metastable states' electron production is lower than that of the ground state, which could be due to the low energy and low ionization cross-sections of these states (compared to N). The ionization of N_2 spans several nanoseconds and occurs before the fast ionization phase. The role of N_2(B) and N_2(C) is relatively negligible compared to that of N_2(a'). This is due to the differences in the dissociation cross-sections shown in Figure 6.9. As the energy of the electrons increases, the N_2 excited states are expected to dissociate before they ionize. The dissociation cross-section of N_2(a') in Figure 6.9, however, remains low compared to the other excited states. N_2(a') is thus less affected by electron-impact dissociation and is efficiently ionized compared to N_2 other states. Finally, the O_2 ionization reaches 10^{17} cm^{-3} and corresponds to the early phase of the nanosecond pulse (not shown in Figure 6.6).

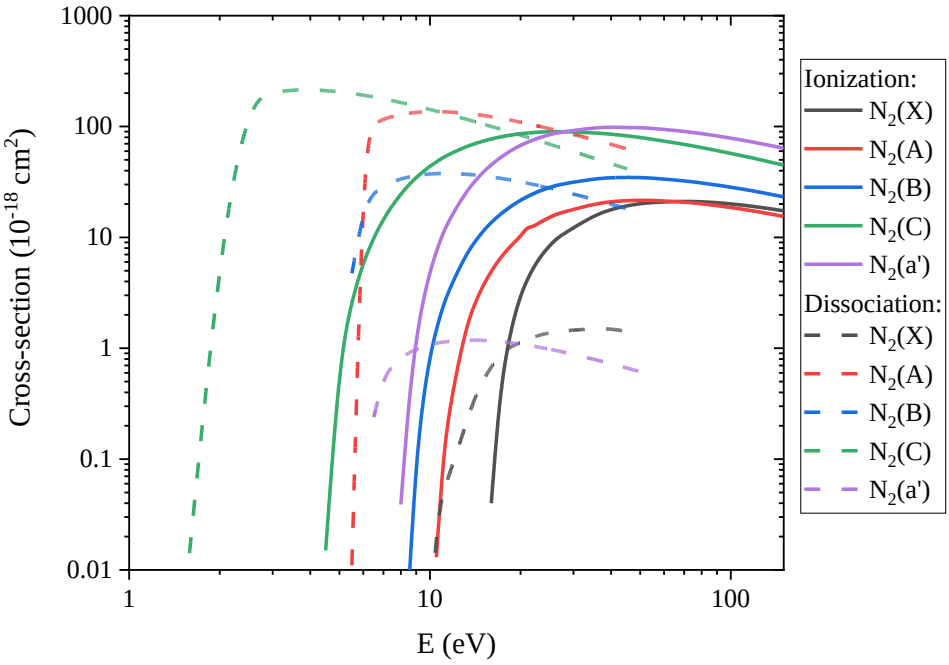

Figure 6.9 Ionization (full lines) and dissociation (dashed lines) cross-sections of N_2(X), N_2(A), N_2(B), N_2(C), and N_2(a') by electron impact (Bacri and Medani, 1982).

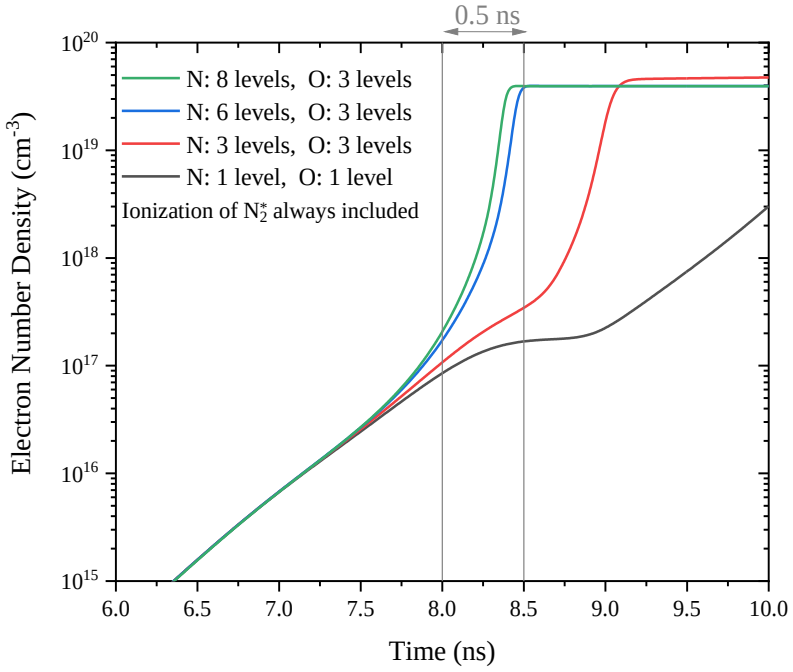

Figure 6.10 Temporal evolution of n_e from simulations including three electronic states of O and three, six, and eight electronic states of N (in red, blue, and green, respectively). The n_e evolution computed considering only N(^{4}S) and O(^{3}P) is also shown (in black). The region of fast ionization of the 8-level model is delimited by the gray lines at 8.0 and 8.5 ns.

To further underscore the role of atomic excited states, additional simulations are performed, changing the number of N and O atomic excited states included in the kinetic mechanism. The evolution of the

electron number density is shown in Figure 6.10. The 8-level model will be the reference for comparison. Simulations with only the first six excited states of nitrogen (E_{up} < 11.61 eV in Table 5.4) lead to similar results as in previous sections: the fast ionization stage now lasts 0.75 ns (instead of 0.5 ns). If only the first three levels of nitrogen are included, full ionization is reached by the end of the 10-ns pulse. However, the fast ionization phase is 1-ns long instead of 0.5 ns. An intermediate result is obtained by including four or five levels.

Finally, if only the ionization of N(^{4}S) and O(^{3}P) is included, the dynamics of ionization are dramatically altered. After a 1-ns stabilization at $n_e = 10^{17}$ cm^{-3}, n_e increases at a rate similar to what was observed at $t < 7$ ns, principally due to N ionization. Full ionization is not reached by the end of the pulse. Note that the ionization of N_2 excited states is always included. The deviation between the models starts at $t = 7.25 – 7.75$ ns, corresponding to $n_e = 10^{16} – 10^{17}$ cm^{-3}. Therefore, we conclude that if $n_e \geq 10^{16}$ cm^{-3}, the correct description of the plasma kinetics must include at least the first six electronic states of N and the first three electronic states of O.

Qualitatively, the model of (Shcherbanev *et al.*, 2019) corresponds to the grey curves in Figure 6.14. In (Shcherbanev *et al.*, 2019), the ionization of N_2 electronic excited states was claimed to be responsible for the full ionization of the gas (nanosecond SDBD in pure N_2 at 5 atm), which seems to be in disagreement with our present conclusions. Indeed, by the time the simulation is stopped in (Shcherbanev *et al.*, 2019), the ionization reaches ~ 1%, which corresponds to the moment at which the ionization of atomic excited states dominates. Also, in (Shcherbanev *et al.*, 2019), the heat released by the recombination of N_2^+ and O_2^+ was stated to be responsible for gas thermalization in their conditions, which is not in agreement with our findings. Although N_2^+ and O_2^+ recombination could have an impact, the heating due to electron-ion collisions is sufficient to explain the increase of temperature in the present simulations (see Figure 6.4).

6.1.4 EEDF deviation from the Maxwellian distribution

As mentioned in Section 5.2, the computation of the recombination rates relies on detailed balance, Eq. 5.2, valid only if the EEDF is Maxwellian. Also, the ionization rate constants of the highest excited states of N (those with energies above 10 eV) were computed assuming a Maxwellian EEDF. In this section, we show that these approximations are valid when these processes are critical.

Departure from a Maxwellian distribution is expected in non-equilibrium plasmas generated by nanosecond discharges. The short period between $t = 8.0$ ns and $t = 8.5$ ns marks the thermalization of the electron and heavy particles. The deviation $\delta(\varepsilon)$ from the Maxwellian distribution is defined in Eq. 6.6, where ε is the electron energy, $f(\varepsilon)$ the EEDF, and $f_M(\varepsilon)$ the corresponding Maxwellian distribution with the same mean energy as $f(\varepsilon)$.

$$\delta(\varepsilon) = \frac{f(\varepsilon)}{f_M(\varepsilon)} \qquad \text{Eq. 6.6}$$

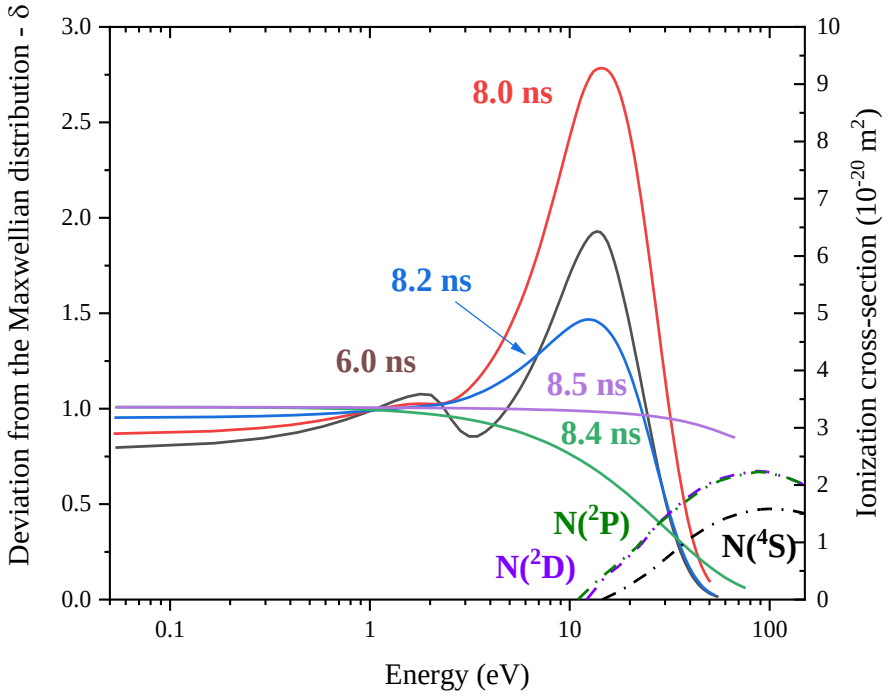

Figure 6.11 Deviation (δ) of the EEDF from a Maxwellian EEDF of the same mean energy. The ionization cross-sections of N(^{4}S), N(^{2}D) and N(^{2}P) , taken from (Wang, Zatsarinny and Bartschat, 2014), are also shown for reference.

A set of δ(ε) functions are shown in Figure 6.11 for several instants. From *t* = 6.0 ns to *t* = 8.5 ns, the EEDF progressively thermalizes due to the high electron-electron collision frequency. At t = 8.5 ns, the electron number density is above 10^{19} cm^{-3} and the EEDF is very close to Maxwellian (i.e. δ(ε) ≈ 1).

The ionization rate coefficients of excited electronic states of N with energy above 10 eV (noted N**) are given by Arrhenius laws based on BEB cross-sections integrated with a Maxwellian EEDF in (Ciccarino and Savin, 2019). We now show that this approximation is valid when these rates are critical. The threshold of the N** ionization cross-sections lies at ε ≈ 3 eV. In Figure 6.11, we show that, in the 6 – 8.2 ns interval, $\delta(\varepsilon) = 1^{+1.5}_{-0.2}$ up to ε = 25 eV. The deviation from the corresponding Maxwellian EEDF is small and the ionization rates are at most overestimated by a factor of 2.5. At later times, the EEDF rapidly becomes Maxwellian and its deviation is below 50% up to ε = 30 eV. The use of Arrhenius rates for N** ionization is therefore reasonable.

The recombination to excited electronic states becomes important only at *t* > 14.2 ns, as shown by the decay of the ionization rates in Figure 6.11. After 14.2 ns, the EEDF approaches a Maxwellian. It is, therefore, valid to use detailed balance for recombination rate calculations at these times.

6.1.5 Comparison with an early Boltzmann EEDF

To our knowledge, BOLSIG+ was tested up to an ionization fraction of 1% (Hagelaar, 2016). Also, we assumed[1] that N is the total heavy particle density in the E/N formulation, i.e. $N = N_{ions} + N_{neutrals}$. Therefore, we conducted a verification of our numerical results by assuming T_e = 34,900 K at t > 8 ns. The EEDF is assumed to be Maxwellian at t > 8 ns. Thus, in this special case, the results are independent of BOLSIG+ calculations and referred to as "early Maxwellian EEDF".

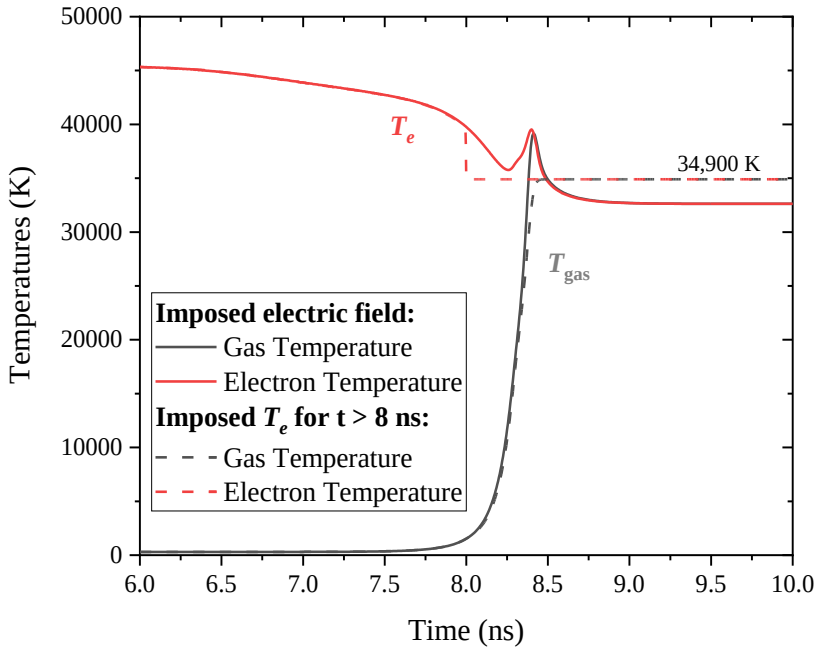

Figure 6.12 Comparison of the temperatures evolution if: (solid lines) a field of 6 kV/mm corresponding to E/N_0 = 240 Td or (dashed lines) T_e is set to 34,900 K at t = 8 ns.

The initial conditions of the early Maxwellian EEDF simulation are taken at t = 8.5 ns, see Table 6.1. In this specific simulation and only for t > 8.0 ns, the EEDF is Maxwellian with T_e = 34,900 K. The variations of T_{gas} and T_e in the early Maxwellian EEDF model is compared with the 8-level model in Figure 6.12. The moment T_e is imposed is easily noticeable at t > 8 ns and has little effect on T_{gas}. The equilibrium temperature is imposed by T_e = 34,900 K and is 2300 K above the reference model.

[1] It is worth noting that for $n_e < 10^{18}$ cm^{-3}, this formulation does not influence the results of the present work.

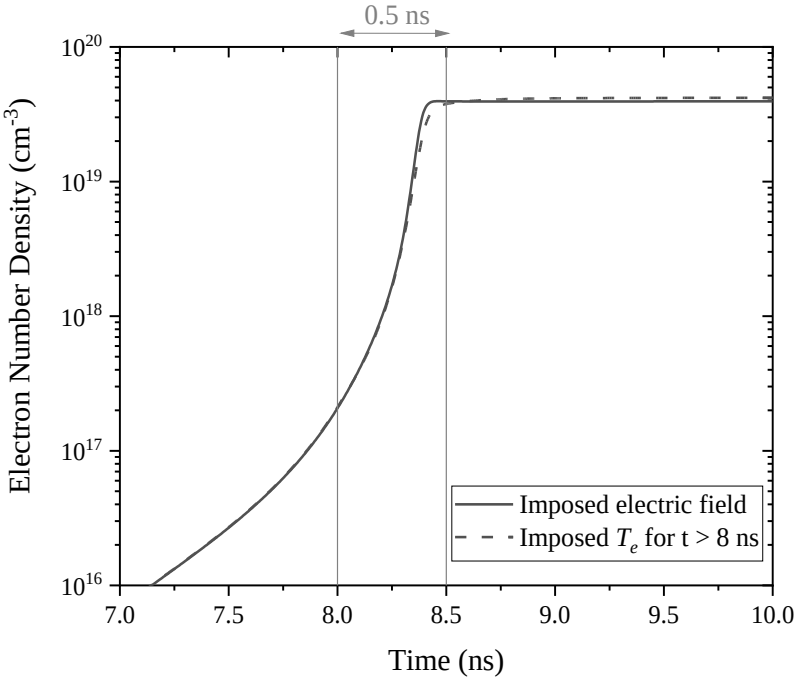

Figure 6.13 Comparison of the electron number density increase in the conditions of Figure 6.12.

In Figure 6.13, the same fast increase of n_e is observed with the early equilibrium model (2 decades increase in 0.5 ns). The steady-state number density of n_e is slightly above the reference model (6%) due to the 2000-K increase induced by choice of T_e. Comparable results are also obtained if T_e is set to 38,900 K instead of 34,400 K in the early Maxwellian EEDF simulation.

Thus, the plasma kinetics could have been computed assuming T_e = 35,000 – 40,000 K during the entire simulation. However, the use of E/N allows comparison with the experimental electron temperatures obtained in the literature. Indeed, the temperatures we obtain here are close to what was experimentally measured by a fit of N^+ lines in previous works (Minesi *et al.*, 2019; Minesi, Stepanyan, *et al.*, 2020). A temperature of T_e = 39,000 ± 4000 K was obtained in the early afterglow of a 10-ns discharge of 8-kV applied between pins separated by 3 mm (Minesi *et al.*, 2019), and T_e = 45,000 ± 5000 K was measured in a 2-mm discharge after a 5.5-kV pulse (Minesi, Stepanyan, *et al.*, 2020). In a pin-to-pin configuration, (Orriere, Moreau and Pai, 2018) measured an electron temperature of 72,000 ± 10,000 K and 37,000 ± 4,000 K at t = 15 ns and t = 30 ns, respectively, during a ns-discharge of 2.5 kV across a 200-µm gap. A longer duration discharge was applied by (Lo *et al.*, 2017) across a gap of 3 mm, and a temperature ranging from 30,000 K to 45,000 K was measured. Also, in the early phase (t < 30 ns) of a spark-plug discharge of 3 kV in a 1-mm gap, (Albrecht *et al.*, 1977) measured an electron temperature ranging between 60,000 and 30,000 K. All the experiments mentioned above reached full ionization within a few nanoseconds. A more exhaustive comparison between these experiments is given in (Minesi, Stepanyan, *et al.*, 2020). Therefore, we conclude that the temperature obtained (in the 8-level

model) or imposed (in the early Maxwellian model) adequately represents the experiments reported above.

6.1.6 Effect of pressure and transition map

In this section, we discuss the influence of the pressure and the reduced field on the thermal spark formation. Several experiments have been performed at the LPP laboratory using Dielectric Barrier Discharges (DBD) (Stepanyan *et al.*, 2014; Shcherbanev *et al.*, 2016; Ding *et al.*, 2019). They showed that an increase of pressure induced the transition to a fully ionized plasma, called “filament” in their work. We performed several simulations in air, varying the initial pressure. The reduced field is kept constant at 200 Td for simplicity.

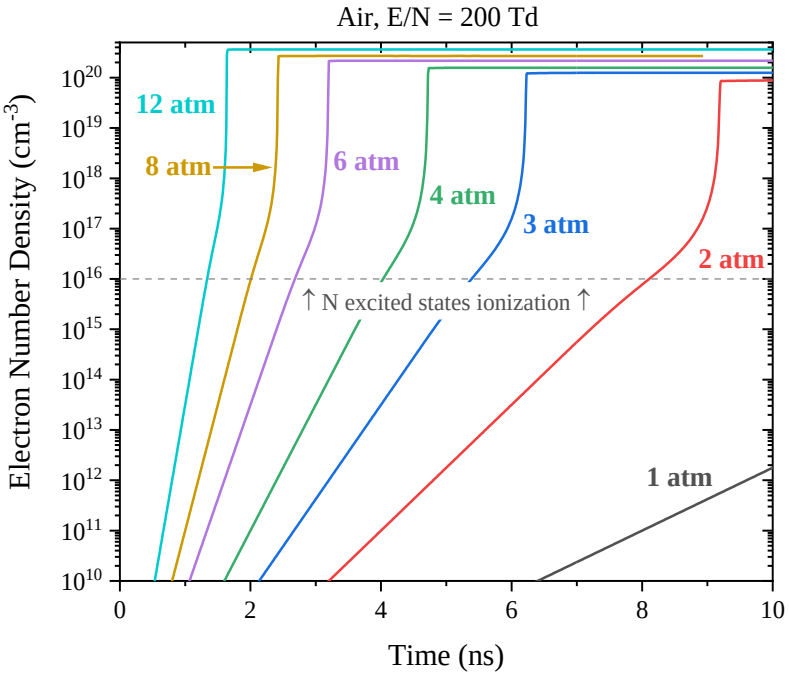

Figure 6.14 Evolution of the electron number density under a 10-ns pulse of 200 Td. The initial pressure is indicated next to each curve. The dashed grey line at 10^{16} cm^{-3} shows the beginning of the fast ionization phase.

In Figure 6.14, the evolution of n_e computed with initial pressures varying from 1 to 12 atm is given. In all cases, if $n_e < 10^{16}$ cm^{-3}, the electron number density increases exponentially with a constant characteristic time. As shown before, the initial n_e increase is due to N_2 and O_2 ionization by electron impact

(see Figure 6.7). For a given electron number density, the increase of n_e is faster at higher pressure because the ionization rate is proportional[1] to the target number density. Two situations can occur:

- The net ionization rate is not sufficiently fast and n_e remains below 10^{16} cm^{-3} at the end of the pulse.
- An electron number density of 10^{16} cm^{-3} is reached during the pulse. In this case, the gas temperature increases and the N excited states ionize. This phase is 0.5-ns long, as detailed before.

Therefore, increasing the pressure accelerates the crossing of the threshold at $n_e = 10^{16}$ cm^{-3}.

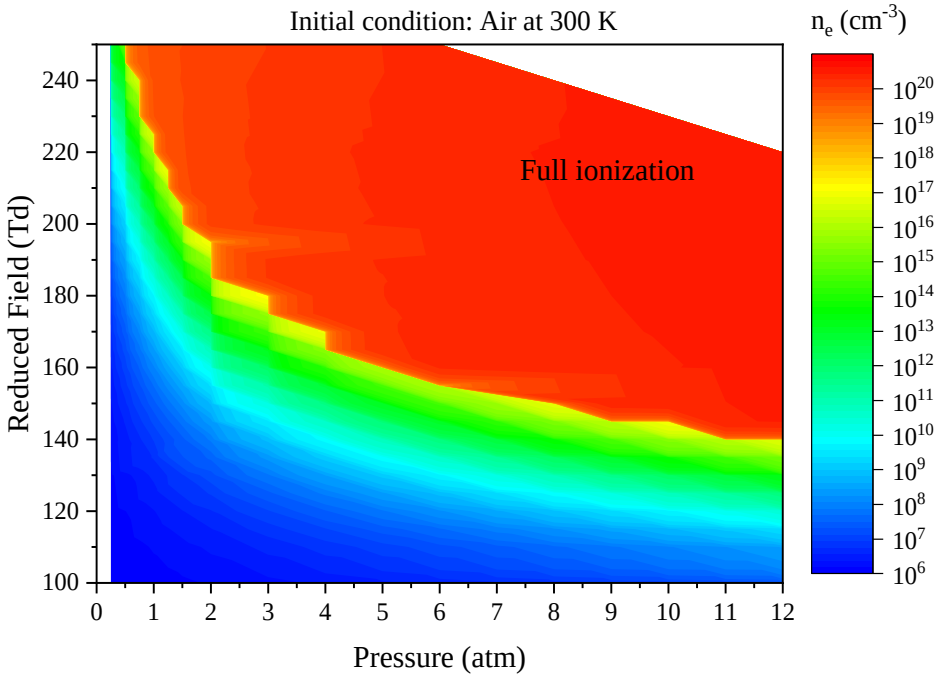

Figure 6.15 Maximal (final) electron number density for a 10-ns pulse under a constant reduced field. Initial condition is air at 300 K and $n_{e0} = 10^6$ cm^{-3}. Full ionization is reached in the red zone.

These calculations have been performed for p in the range 0.25 – 12 atm and E/N below 250 Td. The results are shown in Figure 6.15 where the maximal n_e obtained in a 10-ns discharge under a given electric field is plotted. Full ionization at 0.5 atm by a 10-ns spark can be obtained for E/N > 250 Td. Also, the plasma never reaches full ionization up to 12 atm if the reduced field is below 140 Td.

In Section 4.2, the measurements showed that the increase of pressure accelerated the formation of the thermal spark. The numerical investigations demonstrate that the increase of pressure has, indeed, a

[1] For instance, at $t = 0$ ns and for the same E/N, the N_2 ionization rate at 2 atm is twice higher than that at 1 atm.

positive effect on the thermal spark formation. However, these simulations are performed under a constant reduced field, instead of a constant applied voltage, as in the experiments. At constant applied voltage, increasing the pressure decreases E/N, but it also reduces the cathode sheath length, which increases E/N (Stepanyan *et al.*, 2014). Thus, a comparison of the effect of pressure obtained in experiments and simulations should account for the sheath formation, which is left for future work.

6.2 Comparison of four methods for electron number density measurements

In this section, we compare measurements of the electron number density evolution during the ionization phase of the thermal spark. The experimental setup is similar to setup #1 in Table 4.1, also presented in Figure 4.1. The electrical characteristics are slightly different. A nanosecond pulse of approximatively 8-kV is applied across a 1.2-mm gap in air at atmospheric pressure (see also Figure 6.21 described later). The pulse repetition frequency is equal to 1 kHz, which allows for fast data acquisition. The deposited energy is 3 mJ per pulse. The air is premixed with 3.6% of H_2, which increases the H_α signal compared to the study in Chapter 4.

The optical setup is identical to the one presented in Chapter 4, see Figure 4.1. The temporal resolution is 0.5 ns. We use two gratings, with 1800 gr/mm and 300 gr/mm, to record the H_α emission so that small and large Stark broadening widths can be captured on the CCD array. The 300-gr/mm grating is also used to record the N^+ emission at 500 nm. After numerical binning, the spectra are acquired from five locations along the interelectrode axis, resulting in a spatial resolution of 240 µm. In this section, the full ionization of the cathode filament is described. The electron number density is measured using four methods:

1. H_α Stark broadening, see Section 6.2.1
2. N^+ Stark broadening, see Section 6.2.2
3. Calibrated line intensity of N^+ and O^+, see Section 6.2.2
4. Calibrated continuum emission of electrons, see Section 6.2.3

6.2.1 Stark broadening of H_α

The subtraction of the Van der Waals, resonant, Doppler, and natural broadening is similar to that performed in Section 4.3. In the present conditions, the resonant, Doppler and natural broadening are negligible. We now show that Van der Waals is negligible. The Van der Waals HWHM is obtained in Eq. 6.7 by summing the contribution of the perturbers.

$$\Delta\lambda_{Van\ der\ Waals}[nm] = \frac{n_{total}}{2.7\times10^{19}\ cm^{-3}}\left(\frac{T_{gas}}{273\ K}\right)^{0.3}\sum_{pert}\left(\frac{\gamma_{pert}}{100}x_{pert}\right) \qquad \text{Eq. 6.7}$$

The γ_{pert} coefficients were calculated in Table A3-A5 of (Minesi, Stepanyan, *et al.*, 2020) and reported in Section 1.3. We simplify the sum in Eq. 6.7 using γ_{mean} defined in Eq. 6.8.

$$\gamma_{mean} = \sum_{pert}\left(x_{pert}\gamma_{pert}\right) \qquad \text{Eq. 6.8}$$

In Table 8.4, the value of γ_{mean} is calculated in air. During the thermal spark formation, the gas composition varies from N_2 / O_2 at 300 K, to N / O at 20,000 K and finally N^+ / O^+ at 40,000 K. For these compositions, the Van der Waals HWHM varies from 34 to 267 pm. For comparison, during the partially a Stark HWHM of 34 pm corresponds to $n_e \sim 10^{14}$ cm^{-3}, which is well below our sensitivity limit. When the gas is fully ionized and T = 40,000 K, a Stark HWHM of 267 pm corresponds to 3×10^{16} cm^{-3} which is three orders of magnitude lower than the measured electron number density.

Table 20 Estimated γ_{mean} coefficient and Van der Waals broadening HWHM of the H_α line in ambient air at 300 K, dissociated air at 20,000 K, and fully ionized air at 40,000 K.

Composition	γ_{mean}	T (K)	n_{total} (cm^{-3})	$\Delta\lambda_{VdW}$ (HWHM – pm)
N_2 / O_2	3.36	300	2.7×10^{19}	34
N / O	3.64	20,000	5.4×10^{19}	150
N^+ / O^+	3.26	40,000	5.4×10^{19}	267

In Figure 6.16, the H_α line recorded with an 1800 gr/mm grating is shown and fitted with a Lorentzian convolved with the instrumental broadening function. The H_α width uncertainty is about ±20%, which leads to a 30% uncertainty on the n_e measurement with this technique.

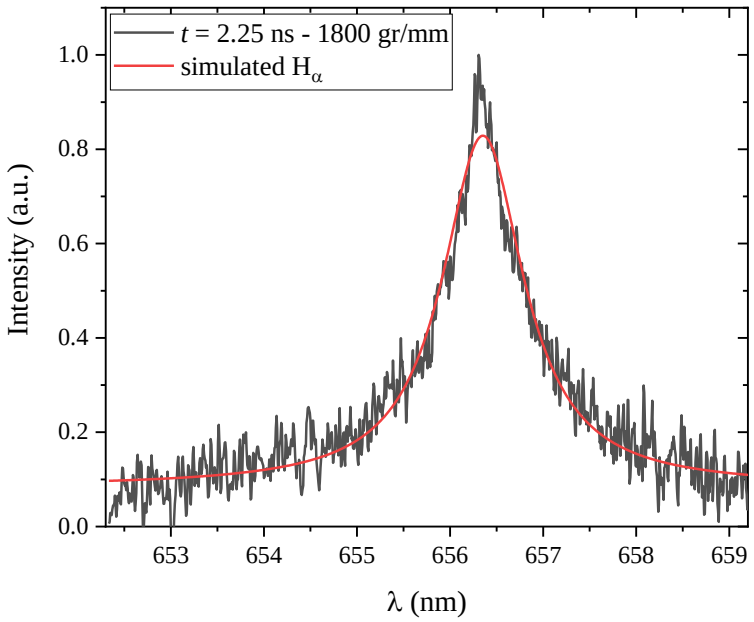

Figure 6.16 Fitting of the H_α line at t = 2.25 ns (1800-gr/mm grating).

In this work, some of the Stark broadening measurements are performed during the high-voltage pulse. In (Bastien and Marode, 1977), it was shown that the applied electric field can have an impact on the Stark broadening. In that case, they showed that the width of the line would be related to the current density instead of the electron number density. In (Bastien and Marode, 1977), expressions are derived for the Stark broadening of H_α and H_β generated by the sum of two fields:

- A microscopic field, arising from the presence of ions and electrons in the plasma. *This is the typical Stark broadening effect.*
- A macroscopic field applied in one direction during the experiment. *This field can interfere with the Stark broadening.*

According to Bastien & Marode, the H_β Stark broadening is mainly due to the shifting of intense external lines caused by the static ions' microfield. The addition of an external field has, therefore, an impact on the H_β Stark broadening. On the other hand, Bastien & Marode showed that the addition of an external field has a weak impact on the H_α lineshape. For instance, at $n_e = 10^{17}$ cm^{-3} and T_e = 10,000 K, the Stark

HWHM of H_α remains independent of the applied field up to at least[1] 12 kV/mm, see Table 1 of (Bastien and Marode, 1977). In our experiments, the maximum applied field is 6.7 kV/mm when $n_e \sim 10^{17}$ cm^{-3}. Therefore, the external applied field does not influence our Stark broadening measurements of H_α during the pulse.

6.2.2 Stark broadening and intensity of the N^+ lines

We showed in Sections 4.3 and 6.1.3 that, after full ionization, the plasma reaches equilibrium at T = 30,000 K – 50,000 K. At these temperatures, after an isochoric transformation, the plasma is mainly composed of electrons (50%), N^+ (40%) and O^+ (10%), see Section 5.3.1. Thus, the number density of the ions (N^+ and O^+) is expected to follow n_e. We measure the densities of several excited states of the ions by calibrated OES and infer the total ion density assuming a Boltzmann distribution of the electronic states at the measured electron temperature. The OES calibration is performed according to the procedure described in Appendix B. A typical spectrum fitted with a Specair calculation is shown in Figure 6.17.

[1] Bastien & Marode calculated the effect of the external field up to four times the Holtsmark field, where the Holtsmark field is, in SI unit:

$$E_{Holzmark} = \frac{e}{4\pi\varepsilon_0 n_e^{2/3}}$$

where e is the elementary charge, ε_0 the dielectric constant, and n_e the electron number density.

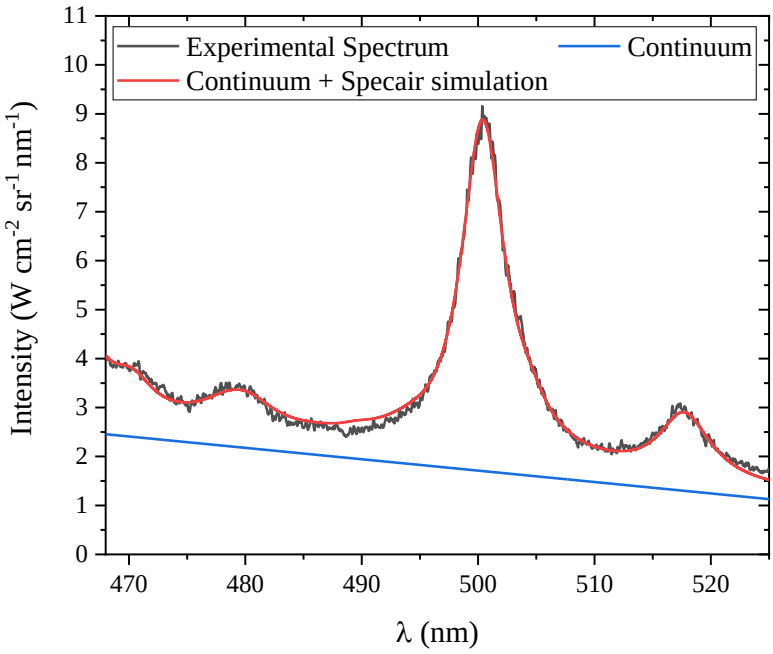

Figure 6.17 Fit of the N^+ and O^+ emission near the cathode at t = 9.75 ns. The continuum emission is approximated by a linear function (in blue) and the N^+ and O^+ emission is calculated by Specair (in red). The fit gives $n_e = 2.0\times10^{19}$ cm^{-3}, $n_{N+} = 3.6\times10^{18}$ cm^{-3}, $n_{O+} = 1.2\times10^{17}$ cm^{-3}, and T_e = 35,000 K (accuracy discussed in the text).

For N^+ lines, the Stark width dominates the others and the lineshape fit provides another measurement of n_e. The uncertainty on the Stark broadening fitting (and n_e determination) remains below 20%. The continuum radiation (assumed to be linear) is subtracted and studied in Section 6.2.3. All electronic states of the ions are assumed to follow a Boltzmann distribution at T_e.

In (Shcherbanev *et al.*, 2019), it was reported that the emission of filamentary SDBD was indeed the sum of two concentric channels. In their case, the intense N^+ and continuum emissions were emitted from the central core, whereas a weaker N_2 emission originated from the outer shell. Shcherbanev *et al.* reported a filament FWHM of 18 ± 2 µm. In configuration similar to ours, Orriere measured the FWHM of a thermal spark (Orriere, 2018, p. 88). He found an FWHM of 50 µm for a 6-kV discharge of 20 ns applied across a 1-mm gap between the electrodes[1]. However, no filter was used and the measurement of Orriere is an upper bound of their thermal spark diameter. Finally, in a 25-kV discharge of 40 ns at ambient conditions, Parkevich *et al.* measured the n_e distribution of a thermal spark by interferometry (Parkevich *et al.*, 2019). Their discharge looked homogeneous with conventional lenses but was indeed composed of several fully ionized filaments, 10 – 50 µm in diameter. Finally, Lo *et al.* clearly observed

[1] For a 2-kV pulse across 200-µm gap, Orriere measured a FWHM of 40 µm.

a constriction of the discharge channel during the transition to the thermal spark in a microsecond pulsed discharge in air (Lo *et al.*, 2017).

In the present study, the plasma column diameter is estimated with a 10-nm bandpass filter centered at 480 nm (Hard Coated OD 4.0 10-nm Bandpass Filter, Edmund Optics). An accurate measurement is challenging with our present setup because of shot-to-shot fluctuations (of the order of a few 10s of microns) and because the column width is comparable with the pixel width, which could result in pixel bleeding. Thus, in the following, we assume that the plasma diameter is constant in time and of the order or less than the pixel resolution, i.e. Δl = 15 µm. We note that this value is comparable with the measurements of Shcherbanev *et al.*, Orriere, and Parkevich *et al.*

The accuracy of the T_e measurements is ± 10%, as shown in Section 4.3. This uncertainty has strong consequences on the number density of the ions. For instance, in Figure 6.18, we show three N^+ spectra calculated at 35,000 K ± 10%. The N^+ number density of each spectrum in Figure 6.18 is adjusted to conserve the peak intensity at λ = 500 nm. This example shows that a 10% variation on T_e results in a factor-two increase/decrease in the N^+ number density.

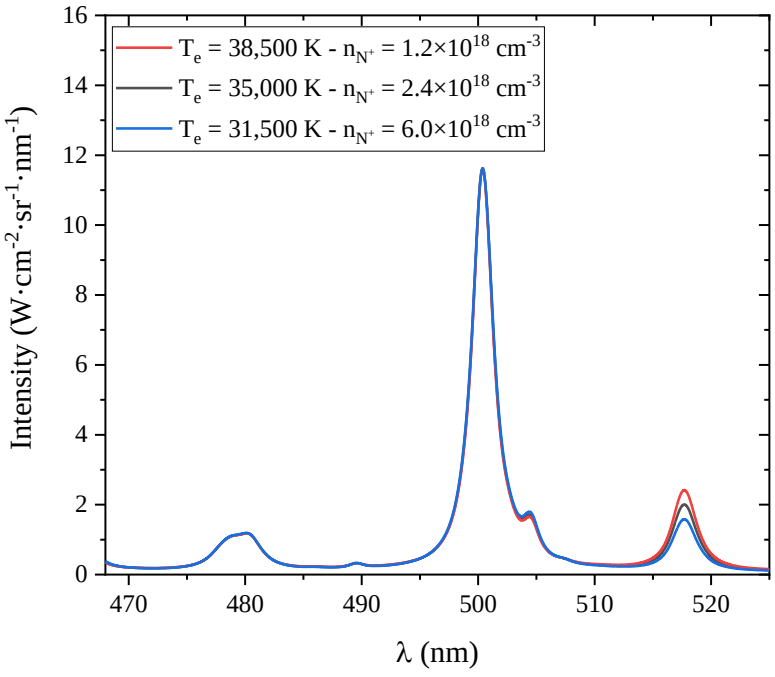

Figure 6.18 Influence of the temperature on the N^+ number density. Three spectra are calculated using Specair at 35,000 K ± 10%, accounting for the slight self-absorption in a 40-µm plasma column.

Note that the Stark broadening constants of the lines at 518 nm are not available in the literature above 28,000 K. Their values were adjusted in previous work, see the appendix in (Minesi, Stepanyan, *et al.*, 2020), and are consistent with the values found at lower temperatures in the literature, but could add

uncertainty to the measurement. Thus, we estimate that the statistical error on the measurements of N^+ and O^+ number densities is about a factor of two[1]. The impact of the plasma diameter estimation is discussed in Section 6.2.4. Nevertheless, we conclude that the N^+ number density is in the range 10^{18} – 10^{19} cm^{-3}, which is consistent with the maximal electron number density measured by Stark broadening (~ 10^{19} cm^{-3}).

6.2.3 Continuum radiation of electrons

As shown in several works, continuum radiation can be significant in laser-induced plasmas (De Giacomo *et al.*, 2010), DBD discharges (Shcherbanev *et al.*, 2016), or pin-to-pin nanosecond discharges (Minesi *et al.*, 2019). The continuum emission is the sum of the free-free radiation (also called Brems-strahlung) and the free-bound radiation (also called recombination continuum). The continuum emission coefficient is given in Eq. 6.9 where n_e and n_i are the electron and ion number densities, Z_i the ion charge, T_e the electron temperature, ξ the free-bound Gaunt factor, and G the free-free Gaunt factor (Bastiaans and Mangold, 1985).

$$\varepsilon_c(\lambda, T_e, n_e) = C_8 Z_i \frac{n_e n_i}{\lambda^2 \sqrt{T_e}} [\xi(1 - e^{-u}) + G e^{-u}] \qquad \text{Eq. 6.9}$$

If more than one ion is present in the mixture, the total continuum radiation will be a sum over Z_i, i being the ion species. In the present case, we consider that N^+ is the dominant ion and $Z_i = 1$. If the plasma is mainly composed of neutral atoms, another formulation must be used, see (Wilbers *et al.*, 1991; Iordanova *et al.*, 2009). The C_8 constant can be determined with Eq. 6.10, where e is the electron charge, k_b the Boltzmann constant, c the speed of light, and m_e the electron mass.

$$C_8 = \frac{16\pi e^6}{3c^2\sqrt{6\pi m_e^3 k_b}} = 1.63 \times 10^{-34} \left[\mathrm{W \cdot m^3 \cdot nm \cdot K^{0.5} \cdot sr^{-1}}\right] \qquad \text{Eq. 6.10}$$

The dimensionless variable u is defined in Eq. 6.11, where h is the Planck constant, k_b the Boltzmann constant, c the speed of light and λ the wavelength.

$$u = \frac{hc}{\lambda k_b T_e} \qquad \text{Eq. 6.11}$$

[1] Added to this, deviations from a Boltzmann distribution could arise due to losses by radiation. A collisional-radiative model would be necessary to go beyond the Boltzmann equilibrium assumptions.

The free-free Gaunt factor of N^+ (or O^+) at $\lambda = 500$ nm varies from $G = 1.08$ to $G = 1.1$ for T in the range 32,000 – 42,000 K, interpolating[1] the results of (Sutherland, 1998). The free-bound Gaunt factor should be averaged on the final states of the atom (i.e. after the electron has recombined with the ion). The free-bound gaunt factors at $\lambda = 500$ nm = 0.18 Ry range between $\xi = 0.8$ and $\xi = 1.2$ depending on the final bound state, see the values calculated for any ions in Table 1 in (Karzas and Latter, 1961). Therefore, we assume $\xi = 1$ and $G = 1.09$ in the present application. These coefficients are assumed to be accurate[2] within 10%.

Assuming $n_e = n_i$, we obtain n_e [m^{-3}] as a function of λ [nm], the volumetric emission coefficient ε_c [$W \cdot m^{-3} \cdot sr^{-1} \cdot nm^{-1}$], and T_e [K] (Bastiaans and Mangold, 1985):

$$n_e^2 = \frac{\lambda^2 \sqrt{T_e}}{C_8} \frac{1}{\xi(1 - e^{-u}) + Ge^{-u}} \varepsilon_c \qquad \text{Eq. 6.12}$$

We can relate ε_c with the continuum intensity I_c [$W \cdot m^{-2} \cdot sr^{-1} \cdot nm^{-1}$], the absorption coefficient k [m^{-1}], and the plasma width Δl [m].

$$I_c = \varepsilon_c \frac{1 - \exp(-k\Delta l)}{k} \qquad \text{Eq. 6.13}$$

For a plasma diameter of 15 µm and $n_e = n_{N+} = 10^{19}$ cm^{-3}, we calculated with Specair that $k\Delta l = 0.5$., Based on this estimation, the plasma is optically thin, i.e. $I_c \approx \varepsilon_c \Delta l$. This approximation leads to, at most, an overestimation of ε_c by 40%. *We will see in the next paragraph that this uncertainty is acceptable.* Finally, Eq. 6.11 can be further simplified as Eq. 6.14 where n_e [m^{-3}] is given as a function of Δl [m] the plasma width, I_c [$W \cdot m^{-2} \cdot sr^{-1} \cdot nm^{-1}$] the continuum intensity, T_e [K] the electron temperature, and λ [nm] the wavelength of observation.

$$n_e = \left(\frac{\lambda^2 \sqrt{T_e}}{C_8} \frac{1}{\xi(1 - e^{-u}) + Ge^{-u}} \frac{I_c}{\Delta l} \right)^{\frac{1}{2}} \qquad \text{Eq. 6.14}$$

The uncertainty of this measurement is now discussed. Thanks to the power 1/2 on the right-hand side of Eq. 6.14, the large uncertainties mentioned earlier will be halved. As shown in Figure 4.9, the uncertainty on T_e is about 10%. The free-free and free-bound coefficients vary slowly with T_e and, in this case, are known within ±10%. The intensity calibration of the absolute spectrum is assumed to be accurate within about ±20%. Thus, considering the thin plasma maximal uncertainty, the maximal

---

[1] We used the *ChiantiPy* Python package (Dere *et al.*, 1997, 2019) at https://github.com/chianti-atomic/ChiantiPy.

[2] If needed, a more precise value could be obtained using the summation performed by the *ChiantiPy* Python Package with the values of (Verner *et al.*, 1996). As described later, the dominant uncertainty is on the plasma thickness.

uncertainty on ε_c is +20% and -60%. The plasma thickness, Δl, is assumed to be exact and discussed later. After propagation of uncertainty, we find that n_e measurement by continuum emission is accurate by -50% and +30%.

6.2.4 Comparison of the four methods for electron number density measurement

In Figure 6.19, we compare electron number densities measured with the four different techniques applied in this section. From t = 1.25 ns to t = 8 ns, n_e increases from 10^{16} to 3×10^{19} cm^{-3}. Then the electron density slowly decays to 5×10^{18} cm^{-3} at 24 ns.

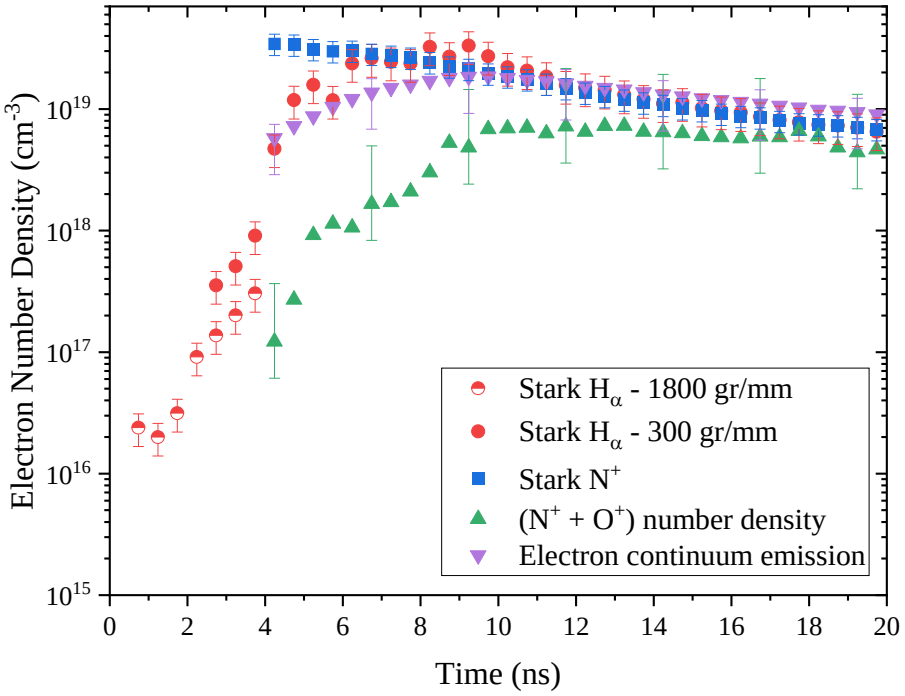

Figure 6.19 Evolution of the electron number density near the cathode measured with Stark broadening of H$_\alpha$ (red circles), Stark broadening of N$^+$ (blue squares), intensity of N$^+$ lines (green triangles), and continuum radiation (purple triangles). We assumed an optically thin plasma for continuum radiation (uncertainty propagated in the error bars). The plasma width is taken to be constant and equal to 15 µm.

We note that the measurements from the Stark broadening of H$_\alpha$ and N$^+$ are in excellent agreement. The electron number densities measured with the continuum emission and the intensity of N$^+$ and O$^+$ lines agree within the uncertainties of each technique for t > 12 ns. At earlier times, however, the electron densities measured from the absolute OES measurements underestimate the electron number density. This could be because the diameter of the plasma column was overestimated. Since the plasma is neutral, we can use the absolute OES measurements to infer the diameter of the plasma column. To do so, we assume that the ion density is equal to the electron density measured by Stark broadening of N$^+$, and we adjust the plasma diameter so that the OES measurements yield the same number density as the Stark

broadening measurements. This method enables us to determine the evolution of the plasma diameter as a function of time. The inferred plasma diameter evolution is shown in Figure 6.20. The same procedure is applied for the continuum radiation measurement, using the electron density determined from the Stark broadening of N^+ as a reference. As shown in Figure 6.20, the two methods provide a plasma diameter evolution that agrees within a factor of about 2 at times greater than 10 ns. This level of agreement is actually quite good, considering the uncertainties on each of these two independent, absolute emission-based techniques.

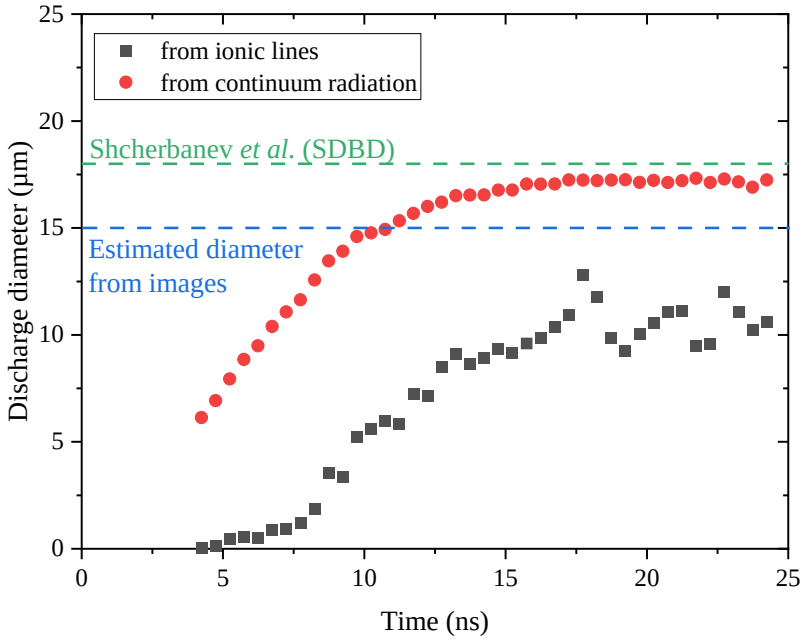

Figure 6.20 Discharge diameter estimation from the continuum and atomic line radiations.

According to the measurement of ionic lines, the measurements obtained with the filtered images overestimated the plasma diameter at all times. According to the continuum radiation, the 15-µm diameter was overestimated for $t < 10$ ns and underestimated at later times. From the graphical comparison, we conclude that a 15-µm diameter was a reasonable approximation.

We now estimate the value of magnetic pressure in the filaments. The magnetic pressure, P_m, can be estimated from Eq. 6.15, where μ_0 is the magnetic susceptibility and B the tangential magnetic field.

$$P_m = \frac{B^2}{2\mu_0} \qquad \text{Eq. 6.15}$$

The tangential magnetic field on the filament boundary can be approximated by the magnetic field generated by an infinitely thin straight wire. We get the magnetic pressure in Eq. 6.16, where I is the electrical current, and R_f is the filament radius. (Shcherbanev *et al.*, 2019).

$$P_m = \frac{(\mu_0 I)^2}{8\pi^2 R_f^2}; \quad P_m = 0.15 \left\{ \frac{I[\mathrm{A}]}{R_f[\mu\mathrm{m}]} \right\}^2 \mathrm{atm} \qquad \text{Eq. 6.16}$$

In our case, the maximal current is $I \approx 200$ A and the radius $R_f \approx 1$ µm, which gives $P_m \approx 6000$ atm. If we assume an isochoric heating from 300 K to 40,000 K, complete dissociation and ionization, the kinetic pressure is at most equal to $P_k \approx 533$ atm. Thus, the magnetic pressure is well above the kinetic one and a z-pinch effect is likely to occur.

6.3 Comparison of experimental and numerical electron densities

The electron number densities obtained with the Stark-broadened lineshapes and the electron continuum are now compared to the result of numerical simulations. Initial conditions and numerical parameters are listed in Table 6.21.

Table 6.21 Initial conditions and numerical parameters. The initial N_2 and O_2 number densities correspond to air at 1 atm and 300 K, and the initial electron and N_2+ number densities to typical ionization in streamer discharges.

Initial gas state						Numerical parameters
N_2 (cm^{-3})	O_2 (cm^{-3})	N_2^+ (cm^{-3})	e- (cm^{-3})	T_{gas} (K)	T_e (K)	Time step (ps)
1.90×10^{19}	5.06×10^{18}	1.00×10^{14}	1.00×10^{14}	300	1000	1.0

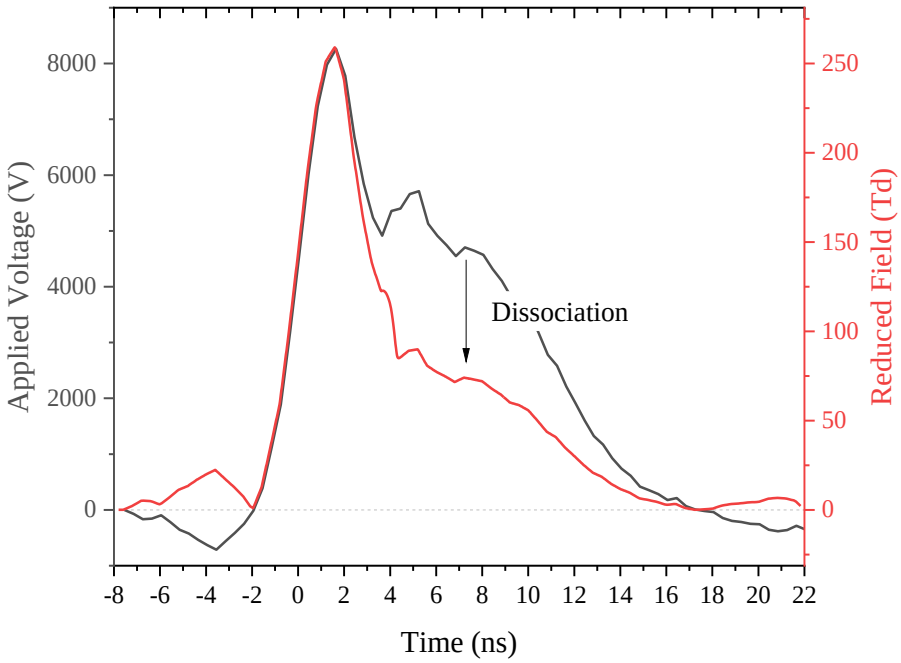

Figure 6.21 Applied voltage (across a 1.2-mm gap) reconstructed from the difference of incident and reflected voltage (grey line) and reduced field in the simulation (red line).

The incident voltage is measured in the middle of a 6-m coaxial cable, as described in Chapter 4. The applied voltage is reconstructed by summing the incident and reflected pulses, see also Figure 2.5. The peak voltage difference across the 1.2-mm gap is 8 kV, which corresponds to 275 Td (at $N_{tot} = 2.4\times10^{19}$ cm^{-3}) if we assume that the field is Laplacian. The reconstructed voltage is shown in Figure 6.21. The evolution of E/N is calculated from the reconstructed voltage, arbitrarily reduced by 6% to account for the cathode fall (represents a 500-V fall at maximal applied voltage), and from the calculated total density, N, which increases after 4 ns due to dissociation. The maximal E/N applied in the simulation is thus equal to 255 Td.

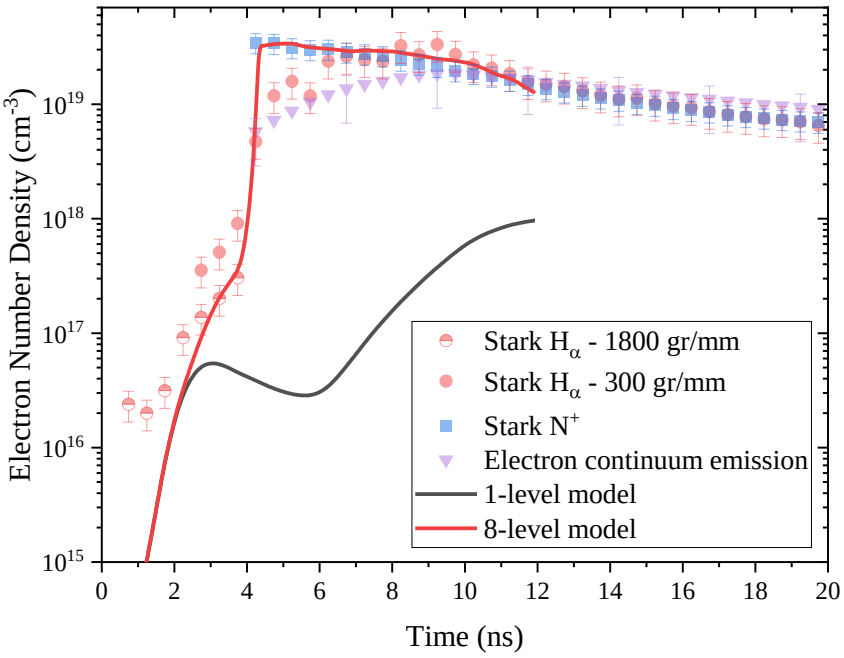

Figure 6.22 Comparison of the electron number density obtained by simulation (red solid line) with that measured by Stark broadening and continuum emission. If the simulation is run without the ionization of O and N excited states (grey solid line), full ionization is not reached.

In Figure 6.22, we compare the evolution of the electron number density measured with Stark broadening of N^+, Stark broadening of H_α, and the free-free/bound-free continuum, with the electron number density calculated with the kinetic mechanism presented in Chapter 5. The initial conditions can be found in Table 6.21 and the applied voltage in Figure 6.21. Without the ionization of N and O excited states, n_e reaches at most 10^{18} cm^{-3} at the end of the 10-ns pulse. However, with the complete mechanism of Chapter 5, full ionization is reached at $t = 4$ ns. As detailed in Section 6.1, for $t < 4$ ns, the production of electrons is primarily due to the ionization of N_2 excited states. Then, at $t \approx 4$ ns, enough N_2 molecules are dissociated and N^+ atoms are produced through stepwise ionization of N. This ionization phase is as abrupt as in Section 6.1, even though the applied field is decreasing at this instant. The simulation is stopped at $t = 10$ ns. After this instant, the constant volume approximation does not hold anymore, and the radial expansion of the plasma should be considered in the simulation.

The simulations closely reproduce the measured electron density profile. This comparison thus provides strong support to our proposed mechanism of thermal spark formation.

6.4 Conclusions on the thermal spark formation

In this chapter, we studied the thermal spark formation under a nanosecond pulse using a 0-D model developed in Chapter 5. We showed that, in air at atmospheric pressure and for $n_e > 10^{16}$ cm^{-3}, the fast increase of the electron number density (two decades in 0.5 ns) is mainly driven by the ionization of N excited states, whereas that of O metastable states and $N_2(a')$ is important but remains secondary.

As n_e increases, the rate of electron-ion collisions increases as well. At $n_e \sim 10^{17}$ cm^{-3}, the characteristic time of the energy transfer between electron and ions is below 1 ns. Hence, the ions thermalize with the free electrons. The plasma is then at LTE and the dominant species are N^+ and O^+, with traces of N^{++} and O^{++}.

For pressures ranging between 1 to 12 atm, the onset of N excited states ionization is marked by an acceleration of the net electron production rate. Therefore, for any pressure conditions, we recommend to include the atomic excited states ionization $n_e > 10^{16}$ cm^{-3}.

We compared experimental and numerical electron density profiles during the thermalization of a nanosecond spark. Experimentally, the electron number density near the cathode is measured with four methods:

1. Stark broadening of N^+
2. Stark broadening of H_α
3. Continuum emission from free-free and free-bound radiation
4. Line emission of N^+ and O^+

These four measurements agree and show that n_e jumps from 10^{17} to 10^{19} cm^{-3} in less than 0.5 ns. Numerically, applying the experimental field, a similar evolution of n_e is retrieved, confirming our proposed mechanism for thermal spark formation.

Part III: Application of NRP discharges to plasma-assisted combustion

Chapter 7

Introduction to plasma-assisted combustion

7.1 Background

Gaseous and liquid combustibles are inexpensive to produce, easily transported, and energy dense. The production infrastructures, transportation, and consumption of fossil fuels have been installed in our society for more than a century. Thus, any need for energy can be quickly supplied using fossil fuels, which explains why their worldwide use increases every year. In the meantime, most governments[1] set a target for a reduction of equivalent CO_2 emission in the next 20 years, which is not compatible with our growing appetite for energy. The reduction of CO_2 emissions can be achieved by working in several directions, including, among others:

- a reduction in our global energy consumption, which requires dramatic societal changes against the current trend[2];
- alternate energy sources, such as nuclear, wind, solar energy which present many advantages (low-carbon, local) but also significant drawbacks (intermittency, cost, security);
- technological improvements in fuel conversion efficiency, which require massive investments from industry and governments.

Concerning the latter, the combustion efficiency of automotive engines can be improved by using high rates of Exhaust Gas Recirculation (EGR). This technique is ultimately limited by the impossibility to

[1] European Union targeted to reduce the 2030 greenhouse gas emission by 40% compared to the levels of 1990, see https://ec.europa.eu/clima/policies/strategies/2030_en

[2] In the US, the current trend is the opposite. Indeed, the 'total primary energy consumption' increased by nearly 30% from 1974 to 2019, while the 'total primary energy production' increased by more than 50% (U.S. Energy Information Administration, 2020).

ignite at too lean ratios (Neame *et al.*, 1995). In the meantime, the use of biofuels is intensively increasing[1] and their composition remains quite variable[2]. Therefore, the author expects that the industry will face a high demand for fuel-flexible burners/motors with strong resistance to lean regimes. This challenge can be achieved by Plasma-Assisted Combustion (PAC), as it will be shown in this introduction. We focus the following discussion on the potential improvements in the combustion area using plasma sources, and more specifically, nanosecond discharges.

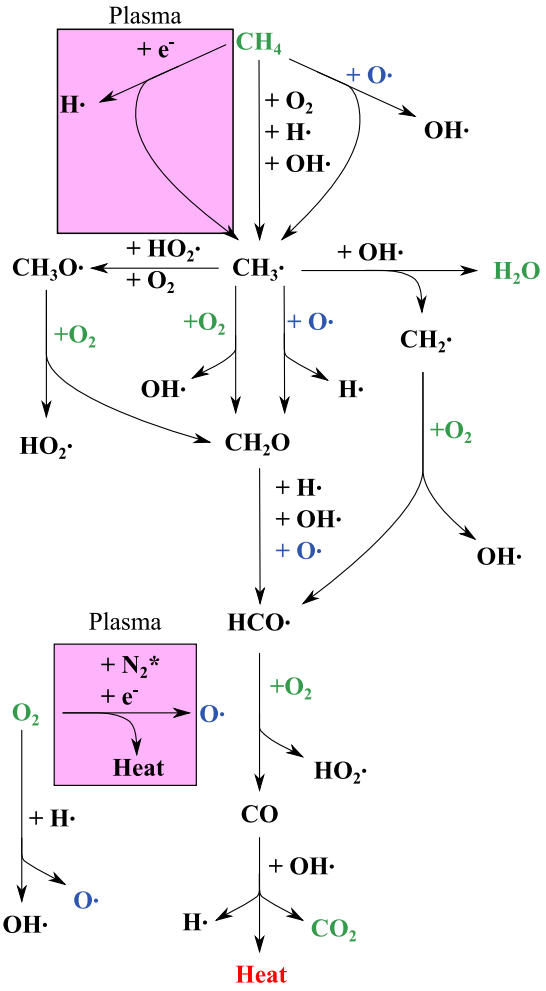

Figure 7.1 Simplified combustion mechanism of CH_4 at high temperature based on (Wang, 2015), the GRI-Mech 3.0 (Smith *et al.*, 2000), and the PAC mechanism of (Sun *et al.*, 2013). The O radicals are colored in blue and the stable reactants and products (CH_4, H_2O, O_2, CO_2) in green.

[1] The production (and consumption) of biofuels has increased by an order of magnitude from 2010 to 2019 (U.S. Energy Information Administration, 2020).

[2] For instance, diesel biofuels can be composed of 2 to 40% of bioadditive in volume (Panteleev, Panteleeva and Panteleev, 2013).

In Figure 7.1, a simplified mechanism of CH_4 combustion at high temperature (T_{gas} > 1000 K) is given based on (Wang, 2015) and GRI-Mech 3.0 (Smith *et al.*, 2000). Most reactions involve a stable molecule and a radical (marked by a dot, e.g. $OH\cdot$). In non-assisted combustion, the process begins by *chain initiation*, such as Reac. 7.1, usually triggered by an increase of T_{gas}.

$$CH_4 + O_2 \rightleftharpoons CH_3\cdot + HO_2\cdot \qquad \text{Reac. 7.1}$$

Then, CH_3 reacts with stable molecules or radicals. Some reactions generate more radicals than they consume and are thus part of the chain propagation. For instance, in Reac. 7.2, H is converted to OH and forms two new radicals:

$$H\cdot + O_2 \rightleftharpoons OH\cdot + O\cdot \qquad \text{Reac. 7.2}$$

Among the radicals, OH is of primary importance in combustion, as the oxidation of CO is principally due to the OH radical:

$$OH\cdot + CO \rightleftharpoons H\cdot + CO_2 \qquad \text{Reac. 7.3}$$

In Reac. 7.3, one[1] radical is consumed and one radical produced; the reaction is part of the *chain propagation*. This reaction is also responsible for most of the heat generated by combustion, ΔH_r = - 104 kJ/mol (Wang, 2015).

Significant combustion improvement can be reached if the radicals density is artificially increased because most of the reactions in Figure 7.1 involve OH, O, or H. Note that in Figure 7.1, two plasma reactions are added: electron impact on CH_4 and the dissociation of O_2 by N_2^* quenching or electron impact. Sun *et al.* found that the production of O was critical to control the radical production and promote the chain branching effect in the reaction zone (Sun *et al.*, 2013). In the conditions of Sun *et al.*, atomic oxygen either forms OH, used in Reac. 7.3, or H, which participates in the chain branching reaction, Reac. 7.2. It was also shown that the plasma can be a source of radicals, which enhance chain initiation at lower temperatures than for non-assisted combustion (Sun *et al.*, 2013; Ju and Sun, 2015).

The field of PAC has been reviewed several times in the last decade. In her last review, Starikovskaia summarized recent experiments performed in a wide range of pressures (0.01 – 10 atm) and temperatures (300 – 2000 K) for Plasma-assisted Ignition (PAI) and PAC (Starikovskaia, 2014). In the conclusion, the author stressed that kinetic models of PAC could predict the shortening of autoignition delay time but failed by several orders of magnitude to predict the absolute concentration of radicals and active species. There is, therefore, a need for the development and validation of PAC kinetics models (Starikovskaia, 2014; Ju and Sun, 2015).

---

[1] Strictly speaking, the CO and NO molecules are also radicals. Nevertheless, they are more stable than O, OH, and H.

Indeed, over the last years, significant improvements in the fundamental understanding of PAC were achieved. The impact of ozone on combustion efficiency was, for instance, reviewed in (Sun *et al.*, 2019). Ozone addition to combustible mixtures pre-processes the fuel and thus extends flammability limits and enhances flame propagation/stabilization (Sun *et al.*, 2019). The positive effect of ozone is mainly due to ozonolysis (and atomic oxygen formation depending on the case). However, the positive impact of ozone is restricted to the low temperatures typically encountered in PAI (Sun *et al.*, 2019).

Also, it was shown in various mixtures and conditions that atomic oxygen has a dominant role in PAC (Ju and Sun, 2015). In (Popov, 2016a), Popov summarized the recent advances in PAC and PAI models. This study notably shows that atomic oxygen has more effect on combustion than O_2 excited states or vibrational excitation. Thus, for effective plasma-assistance, Popov recommended loading energy in the electronic states of N_2. This loading of energy leads to O_2 dissociation and heating and can be efficiently achieved with E/N > 100 Td.

In the next section, we shortly review recent PAC experiments performed with NRP discharges. We focus on experiments conducted at high thermal power compared to typical lab-scale experiments.

7.2 Review of high-power PAC experiments

Four high-power experiments are reviewed in this section. The first one was performed at the EM2C laboratory (Barbosa *et al.*, 2015). In that experiment, a two-stage swirled injector is connected to a rectangular combustion chamber with optical access ports. The combustion chamber has a square cross-section of 100 × 100 mm^2 and a length of 500 mm. Both stages are supplied with air, while only the primary stage is fed with fully premixed air and C_3H_8. The maximal flowrates correspond to a maximal power of 52 kW. The outlet of the combustion chamber is open to the atmosphere. A refractory steel anode is introduced in the combustion chamber through its upper wall and placed less than 1 cm down-stream of the outlet of the primary stage mixing area. The NRP discharges are applied at 30 kHz using a pulse generator (FID FPG 30-100MS) with 10-ns pulse width for electrical power of 350 W. The initial conditions are set to Q_{air} = 105 $N{\cdot}m^3{\cdot}h^{-1}$ and Q_{C3H8} = 2.1 $N{\cdot}m^3{\cdot}h^{-1}$ (P = 52 kW, Φ = 0.47). Then, the fuel flow rate is gradually decreased until the Lean Blow Out (LBO) limit. Figure 7.2 shows CH* images of the flame as Φ is decreased with and without plasma. The NRP discharges extend the LBO limit from Φ_g = 0.40 to Φ_g = 0.11 (global equivalence ratio), which corresponds to an extension from Φ_p = 2.05 to Φ_p = 0.57 (pilot equivalence ratio),

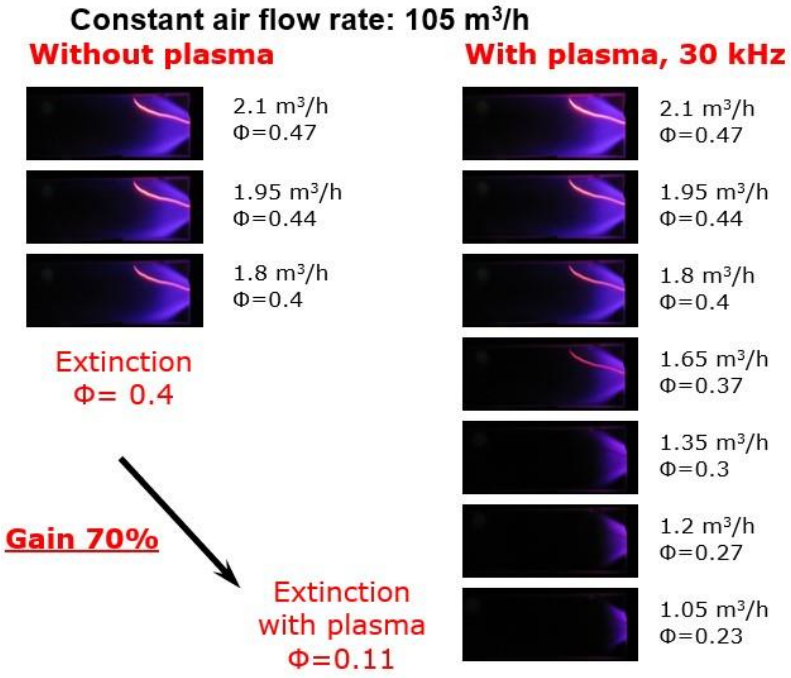

Figure 7.2 Illustration of the LBO reduction by CH* imaging (Barbosa *et al.*, 2015). The bright filament visible in the photos is the anode heated by burnt gases.

In another experiment, a plasma-assisted multipoint Lean Direct Injection (LDI) system was designed and tested at the NASA Glenn Research Center's Combustion Dynamics Facility (Del Campo *et al.*, 2017). Del Campo *et al.* inserted a high-voltage electrode in the CE-13 facility, typically using Jet A or JP-8 liquid fuels (Hicks *et al.*, 2012). The experiments were performed at a flame thermal power of 50 kW. Unfortunately, there are very few reported details on the plasma energy measurements or the flame topology for this experiment. The LBO was reached by decreasing the fuel flow rate and a 24% improvement of the LBO was obtained by Del Campo *et al.* Note also that a significant reduction of thermo-acoustic instabilities was measured by Del Campo *et al.*

PAC was also performed on the MERCATO burner at ONERA (Heid *et al.*, 2009). The Mercato test facility comprises a square cross-section combustion chamber fed with air and kerosene (liquid) by a swirl injector. The injection system is located upstream, inside a plenum chamber, supplied with air at 423 K (150°C) in this particular experiment. The chamber pressure is set to 3 bar and the kerosene is supplied directly to the injector. An FID pulser (FPG 30-100MS) generates 10-ns discharges at 30 kHz with an average electrical power[1] below 500 W. The plasma is produced between a ring electrode (an-

[1] This electrical power is not given by Heid *et al.* and corresponds to the maximal power that can be delivered with this pulser. This value therefore grossly overestimates the actual plasma power. Nonetheless, the ratio between the *overestimated* electrical power and the thermal power remains below 1%.

ode) and the injector (grounded) – called "configuration c" (Heid *et al.*, 2009). The flame is first stabilized at $\Phi = 2.0$ and P ~ 150 kW; then, the kerosene flow rate is progressively decreased down to extinction. In configuration c, a reduction of the LBO limit from $\Phi = 0.39$ to 0.27 occurred when the NRP discharges were applied. Although they were quite short (32 s) due to the absence of cooling, these tests achieved the highest flame power in PAC experiments.

The fourth set of flame stabilization experiments was performed on the mini-PAC burner at the EM2C laboratory (Galley *et al.*, 2005; Pilla *et al.*, 2006; Pilla, 2008). (Note that the experiments described in Chapter 8 were performed on a new version of this mini-PAC burner.) A bluff-body configuration anchors a propane flame at a maximal theoretical power of 25 kW. The diameter of the bluff-body and the external diameter of the burner outlet are 10 and 16 mm, respectively. Each discharge deposits 2.5 mJ, corresponding to an average power of 75 W at 30 kHz repetition frequency. The pulses are delivered by a cylindrical electrode made of refractory steel[1] (anode) in the recirculation zone of the bluff-body (grounded cathode). With plasma assistance, it was found that a stable flame regime could be obtained at equivalence ratios 10% leaner than without the NRP discharges. It was also shown that the flame was not completely extinguished for even leaner conditions and remained confined near the recirculation zone. Although most of the fuel was unburnt in this regime, the small flame could serve as "pilot flame" to reignite the combustor. A summary of the four configurations is given in Table 7.1.

[1] This electrode was a commercially available domestic heater electrode. Note that in Chapter 8, a thinner tungsten electrode is used.

Table 7.1 Experimental conditions of selected PAC experiments (Laux, 2017). In the experiments of Pilla *et al.*, the LBO was improved by about 10% for a wide range of air flowrates, see also Figure III.21 of (Pilla, 2008). P_{LBO} corresponds to the maximal power at LBO without plasma assistance.

Configuration	Swirled	7-LDI	Swirled	Bluff-body
Fuel	C_3H_8	Jet fuel	Kerosene (L)	C_3H_8
Pressure	1 bar	1 bar	3 bar	1 bar
Flow speed	40 m/s	?	?	10-20 m/s
$P_{flame,\ max}$	52 kW	> 200 kW	~ 80 kW	25 kW
P_{plasma}	350 W	< 500 W	< 500 W	75 W
P_{plasma} /P_{flame}	0.7%	< 1%	< 0.4%	0.3%
Frequency	30 kHz	?	30 kHz	30 kHz
Φ_{LBO}	0.40→0.11	0.21→0.16	0.39→0.27	10% improv.
P_{LBO} w/o plasma	45 kW	50 kW	63 kW	19 kW
Ref.	(Barbosa *et al.*, 2015)	(Del Campo *et al.*, 2017)	(Heid *et al.*, 2009)	(Pilla *et al.*, 2006)

7.3 Objectives of this study

We shortly reminded in Section 7.1 that the generation of radicals (OH) and atomic species (O, H) could chemically accelerate the combustion chemistry. These species can be efficiently generated at fields above 100 Td, typically encountered in NRP discharges. Also, NRP discharges can achieve significant heating, which enhances the combustion chemistry. These effects have been mostly studied in gaseous mixtures of air and simple hydrocarbons. Methane and propane mix easily with air, their chemical kinetics are fairly well known, and experiments with these mixtures are widely documented in the PAC literature. However, besides recent advances (Popov, 2016a), the thermal and chemical effects of NRP discharges on methane-air combustion are still not fully understood.

Then, in Section 7.2, we reviewed four high-power PAC experiments performed in propane (Pilla *et al.*, 2006; Barbosa *et al.*, 2015) and liquid fuels (Heid *et al.*, 2009; Del Campo *et al.*, 2017). Fundamental studies with liquid fuels are scarce in the literature, with few details on the plasma characteristics because they face complex technical difficulties. For instance, liquid droplets increase the computational cost for simulations, the kinetic mechanisms are not as well known, and the possible accumulation of fuel imposes strict safety rules during the experiments. Identifying the dominant chemical effects of the plasma is even more challenging because of the increased number of species and reactions. Thus, PAC is less studied in liquid fuels than in simple gaseous hydrocarbons.

Plasma-Assisted Combustion has been investigated at the EM2C laboratory since the mid-2000s, starting with experiments conducted on the bluff-body configuration called Mini-PAC (Pilla, 2008; Xu, 2013). Some key results are summarized here. NRP discharges were applied at tens of kHz in the recirculation zone of the Mini-PAC burner. Pilla *et al.* characterized the temperature increase and active species formation in the middle of the discharge (Galley *et al.*, 2005; Pilla *et al.*, 2006; Pilla, 2008). A study on the effect of the frequency and the applied voltage was performed. At 30 kHz, Pilla *et al.* showed that for 6.5-kV discharge, the number density of $N_2(C)$ increased up to 2×10^{14} cm^{-3}. The peak density of atomic oxygen was estimated to be about 3×10^{15} cm^{-3}. Pilla concluded that the flame enhancement was due to the temperature increase coupled with the atomic oxygen formation. In a complementary study, Xu studied the formation of OH using PLIF in a propane-air flame in the mini-PAC burner (Xu, 2013). Xu showed that OH radicals generated along the discharge axis were convected by flow recirculation toward the shear layer of incoming fresh gases. The fresh gases were then ignited, and the lifted flame attached back to the bluff-body.

Based on these grounds, in Chapter 8, new experiments are conducted on the Mini-PAC burner to answer several remaining questions. A methane-air mixture is chosen to simplify the PAC chemistry. The following objectives will be addressed:

- Determine the nature of the NRP spark used to stabilize the mini-PAC flame: non-thermal or thermal?
- Measure OH(X) density profiles during the temporal sequence, going from the pilot flame to the stable flame, pulse after pulse.
- Use these profiles to guide the development of an LES model of PAC, developed in parallel (Bechane, 2021), and make quantitative comparisons about the production of OH by the plasma-flame interaction?
- Measure with high temporal and spatial resolution the electron and excited species number densities, to guide and validate the construction of a detailed model of PAC chemistry.
- Identify the critical heating and cooling mechanism thanks to space and time-resolved temperature measurements.

In Chapter 9, PAC is also studied in another configuration, the SICCA-spray burner, to demonstrate the versatility of NRP discharges in a swirl-stabilized, confined flame with a variety of fuels. The extension of the lean blow-out limit is measured for:

- Perfectly premixed methane-air, as in most fundamental studies on PAC.
- Liquid heptane, representative of diesel for automotive applications, injected as hollow cone sprays.

- Liquid dodecane, representative of kerosene for aeronautical applications, also injected as hollow cone sprays.

Chapter 8 was conducted under the PASTEC[1] project (ANR-16-CE22-0005), and Chapter 9 is an extended version of our recently published article (Vignat *et al.*, 2020).

[1] PASTEC is the acronym of Plasma AssiSTEd Combustion.

Chapter 8

Study of a bluff-body configuration: Mini-PAC

We will first describe the experimental setup and the conditions we chose for the experiments presented in Section 8.1. Qualitative observations of the transition from a non-assisted weak flame to a plasma-stabilized flame are performed by chemiluminescence. Then, the same observations are carried out by OH Laser-Induced Fluorescence (LIF) in Section 8.2. We show that the NRP discharges increase the OH number density several times. In Section 8.3, the electrical characteristics of the discharges are presented, followed by the identification of the lines emitting in the spectrum. The latter demonstrates that the discharge is a non-equilibrium plasma. In Section 8.4, the electron number density is measured by Stark broadening of H_α. Most of the discharge volume remains at a limited ionization degree ($n_e < 10^{15}$ cm^{-3}), whereas the near-cathode region is more strongly ionized ($n_e \sim 10^{16}$ cm^{-3}). In Section 8.5, the gas temperature is measured by OES. We discuss the gas cooling mechanism, due to fresh gas recirculation during the interpulse, and the gas heating, due to electron-ion collisions and dissociative quenching during the discharge. With calibrated OES, we measure in Section 8.6 the number density of N_2(B), N_2(C), OH(A), CN(B), NH(A), and N_2^+(B). We finally conclude this study in Section 8.7.

8.1 The Mini-PAC configuration

8.1.1 Experimental setup

This section describes the setup used for the Mini-PAC burner, which stands for "mini Plasma Assisted-Combustion." The burner is similar to the configuration of (Pilla *et al.*, 2006; Pilla, 2008), but the experiments are conducted with methane instead of propane. The schematic of the burner exit is presented in Figure 8.1. The internal diameter of the injection tube of the burner is 16 mm, and the bluff-body diameter is 10 mm. The Reynolds number, based on the diameter of the burner outlet, the bulk velocity, and the gas kinematic viscosity is about 14,000. The gas flow is therefore in the turbulent regime. A recirculation zone above the bluff-body stabilizes the generated turbulent flame.

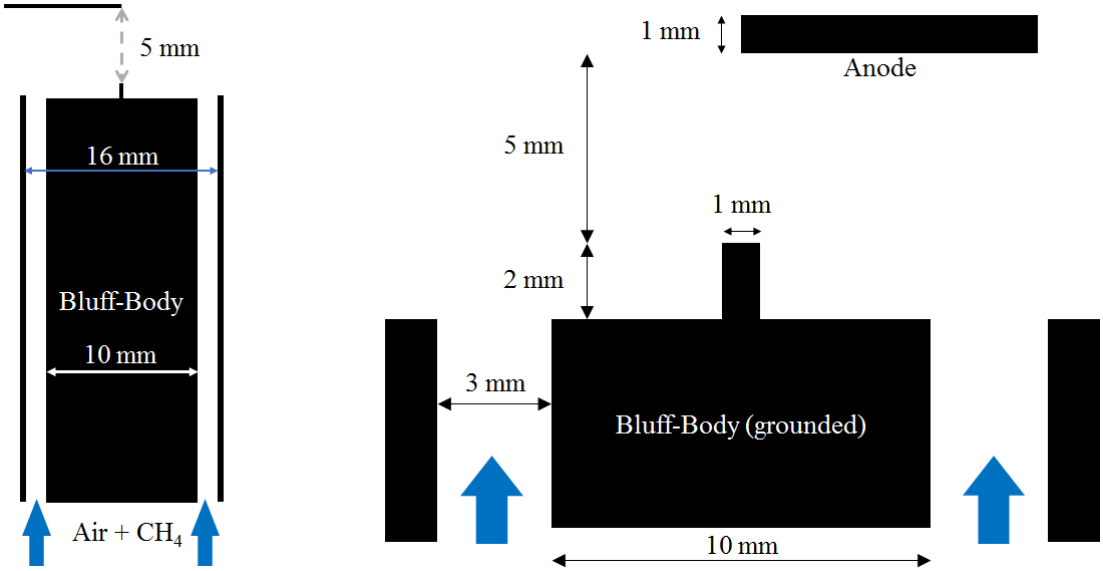

Figure 8.1 Schematic of the Mini-PAC burner and electrode configuration, reproduced from (Perrin-Terrin, 2020)

The NRP discharges are initiated in the recirculation zone, which is mainly composed of burnt gas. High-voltage nanosecond pulses are applied across a gap of 5 mm, between a horizontal tungsten electrode and a vertical tungsten electrode (see Figure 8.1). The vertical electrode is mounted on the grounded bluff-body. The diameter of the electrodes is 1 mm. No significant distortion of the flame structure by the electrode is observed. All measurements without plasma are, however, performed with the electrodes in place to allow comparisons between the non-assisted and plasma-assisted flames.

The use of tungsten electrodes allows for operating with slow erosion. In the PASTEC conditions (20 kHz, 2 mJ per pulse – detailed later), the length of the grounded electrode decreases by 23 ± 9 µm per hour. Therefore, each nanosecond discharge removes 0.3 ± 0.1 nm of tungsten, which corresponds[1] to the depletion of one tungsten atomic layer per pulse. The experiment can, therefore, be run for hours without noticeable erosion.

A map of the burner operating conditions is shown in Figure 8.2. Three series of measurements are performed at the EM2C (2) and CORIA (1) laboratories[2]. The "Stable Flame" region corresponds to a developed, stable, V-shape flame (Pham, Lacoste and Laux, 2011). A typical V-shape flame close to

[1] The interatomic distance of the body-centered cubic structure of tungsten is $a = 4R/\sqrt{3}$, where the radius of the tungsten atom is R = 0.14 nm. The erosion of the tungsten electrode per pulse is thus equivalent to a layer of atoms a = 0.32 nm.

[2] In the PASTEC project, two identical burners have been manufactured for complementary experiments at the CORIA and EM2C laboratories.

stoichiometric conditions is shown in Figure 8.2. In the "Weak Flame" region, a significant part of methane is not burnt, and the flame is confined in the recirculation zone downstream of the bluff-body[1]. The "Intermittent Flame" is between the two previous regions. In this case, the flame oscillates between the Stable and Weak flames. The limits of the different zones are shown in Figure 8.2. Finally, the limit of extinction lies between $\Phi = 0.7 – 0.8$ in the considered range. The operating point investigated in this work is represented in Figure 8.2 by a black triangle ("Weak Flame" region, $\Phi = 0.8$, $Q_{air} = 16\ m^3 \cdot h^{-1}$).

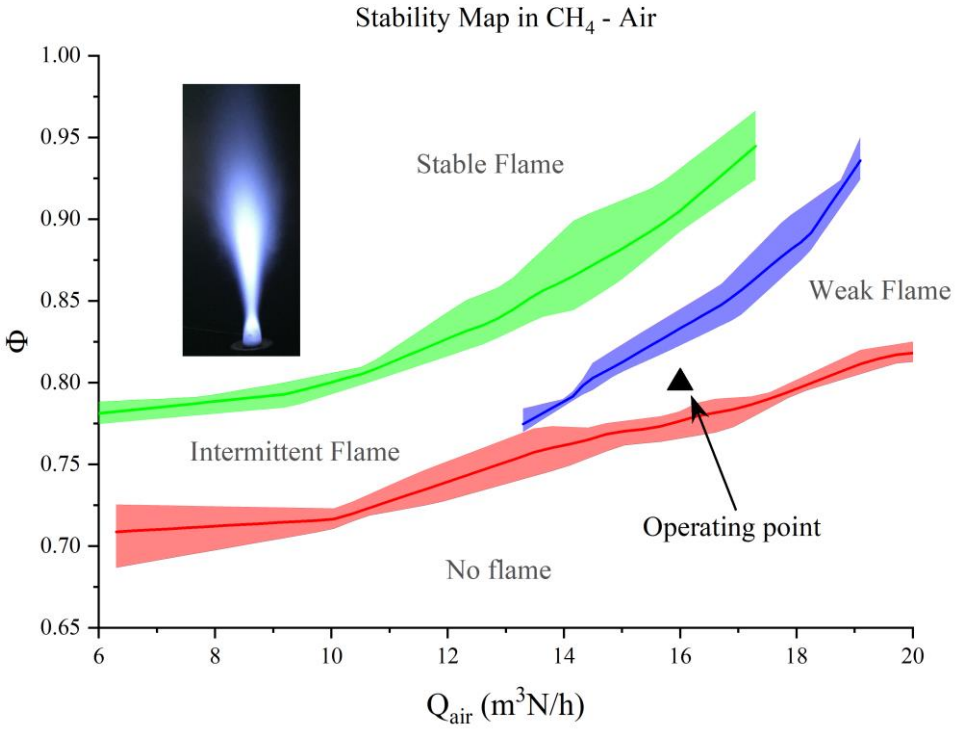

Figure 8.2 Operating conditions of the mini-PAC burner (no NRP discharge applied). The "PASTEC flame" is represented by a black triangle and lies in the "Weak Flame" zone if no NRP discharges are applied. Pictures of the flame are inserted in the top left (stable) and bottom right (weak) corners. The filled areas represent the measurement uncertainty.

The experimental setup for optical and electrical diagnostics is presented in Figure 8.3. The discharge emission is focused on a monochromator (Acton SP2500i) slit via two 10-cm plano-convex lenses for the OES measurements. The focal length of the spectrometer is 500 cm. The monochromator is coupled with an ICCD camera (PI-MAX 2, Princeton Instruments) with a minimal gate exposure of 2 ns. Another ICCD camera (PI-MAX 2, Princeton Instruments) is focused on the burner to perform flame imaging and Laser-Induced Fluorescence (LIF) experiments. A complete description of the LIF experimental setup is given in Section 8.2.1. The electrical characteristics of the NRP discharges are monitored on an

[1] This regime was also called "pilot flame" in (Pilla *et al.*, 2006; Pilla, 2008).

oscilloscope (HDO 6000 – Lecroy) using voltage (Lecroy PPE 20kV) and current (Pearson Coil Model 2877) probes. The interpretation of the oscillograms is presented in Section 8.3.1.

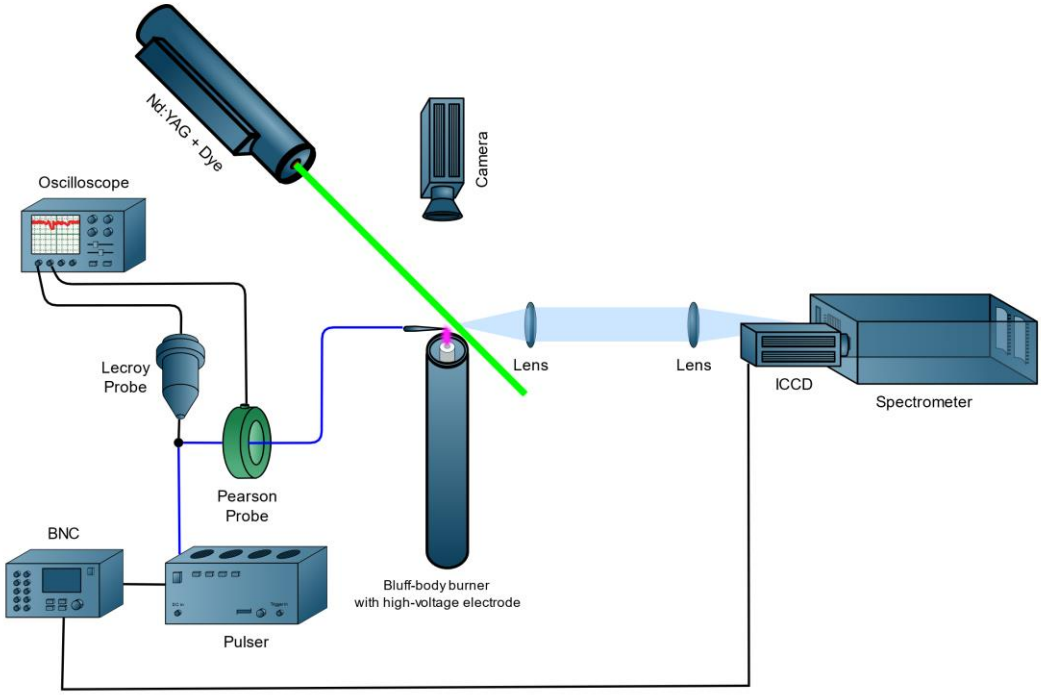

Figure 8.3 Experimental setup, including the OES, electrical measurements, and the LIF setup.

The nanosecond discharges are generated by an FID 10-30NM10 generator, denominated “pulser #4” in the rest of the manuscript. The output of the pulser is connected to a plasma reactor by a 75-Ω coaxial cable (Alphawire 9011a).

The results of the next sections are obtained under the following conditions (“PASTEC conditions”):

- Air flowrate: Q_{air} = 16 m^3h^{-1}
- CH_4 flowrate: Q_{CH4} = 1.34 m^3h^{-1} (Φ = 0.8)
- Voltage amplitude of the incident pulses: 3.5 kV
- Discharge repetition rate: 20 kHz

The flowrates can be converted to masse rates such as $\dot{m}_{air}$ = 5.75 $g{\cdot}s^{-1}$ and $\dot{m}_{CH4}$ = 0.27 $g{\cdot}s^{-1}$.

The theoretical power of this lean flame (Φ = 0.8) is equal to 13.3 kW if the methane is completely burnt[1]. Under these conditions, the deposited energy at steady state is equal to 2 mJ per pulse (see Section 8.3.1), which results in an average electric power of 40 W. These conditions are referred to as the "PASTEC conditions" or "PASTEC flame".

8.1.2 Flame characterization: chemiluminescence

Images of the PASTEC flame with and without plasma assistance are shown in Figure 8.4. The first objective of our study is to investigate the transition from the PASTEC flame, burning in the vicinity of the bluff-body, to the PASTEC flame stabilized by NRP discharge. In other words, we aim to understand the transition from left to right in Figure 8.4.

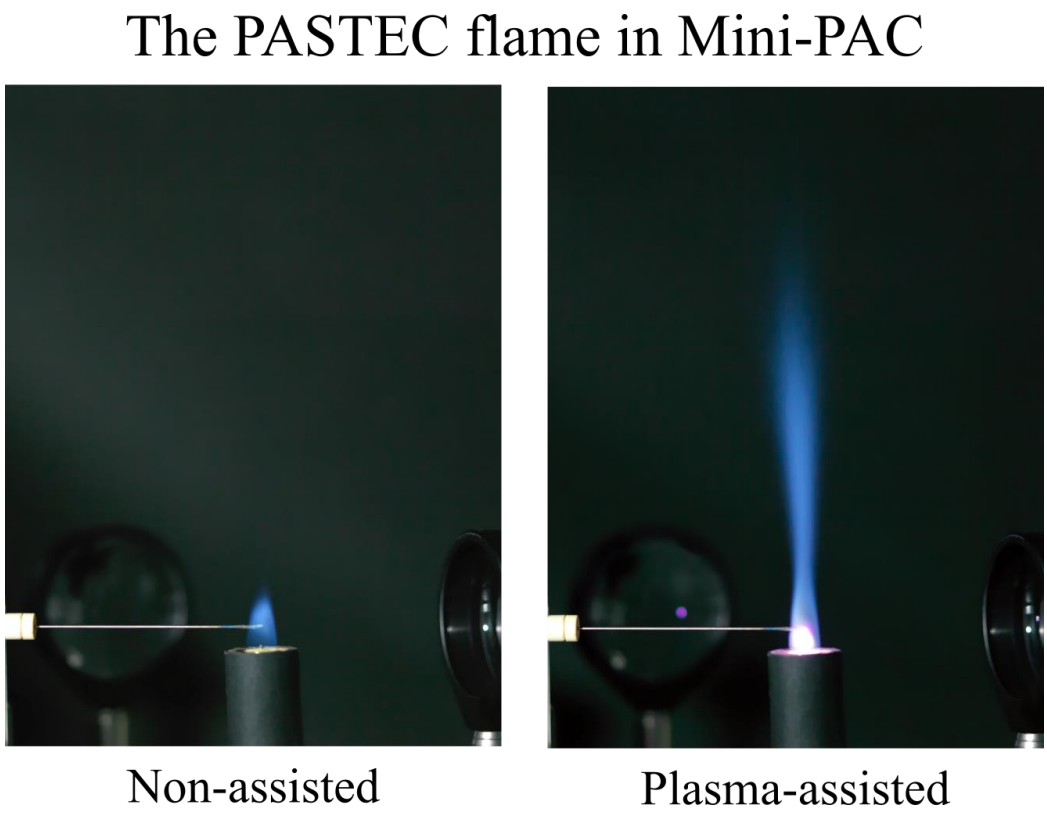

Figure 8.4 Pictures of the non-assisted (left) and plasma-assisted (right) PASTEC flame using a digital camera (Hasselblad H3DII-31) with an obturation time of 1/20 s (Cécile Oriot, CentraleSupélec). For the plasma-assisted flame, the CCD is overexposed in the plasma region.

---

[1] Stoichiometry is obtained at $Q_{air} / Q_{CH4} = 9.52$, with the following reaction:

$$CH_4 + 2\ (O_2 + 3.76\ N_2) \rightarrow CO_2 + 2\ H_2O + 7.52\ N_2$$

A Lower Heating Value (LHV) of 803 kJ/mol is used to compute the released power.

The effect of NRP discharges on the PASTEC flame is probed by chemiluminescence of OH* and CH*, as shown in Figure 8.5 and Figure 8.6, respectively. For each experiment, we apply a train of 300 nano-second pulses separated by 50 µs (20 kHz) from t = 0 ns to t = 15 ms. Then, the discharges are stopped for about 1 second to get back to the conditions of the non-assisted flame (left of Figure 8.4). Then the train of 300 pulses is repeated. The emission of the flame between each discharge is averaged 100 times. These images are taken with different filters mounted on the camera:

- Filter centered on the OH(A-X) emission at 310 nm with a FWHM of 10 nm (ZHQA - High transmission Bandpass 310 nm, Asahi Spectra Co.)
- Filter centered on the CH(A-X) emission at 430 nm with a FWHM of 10 nm (ZBPA - Bandpass 430nm, Asahi Spectra Co.)

OH is present in the flame and CH is mainly present at the flame front. In the Figure 8.5 and Figure 8.6, the origin of the z-axis is the tip of the bluff-body electrode. During the experiments, a rectangular mask hides the emission of the discharge to prevent camera saturation. The horizontal electrode is visible on the left at (r < 5 mm, z = 5 mm). The emission is Abel-inverted to provide the radial distribution of OH* and CH* emission.

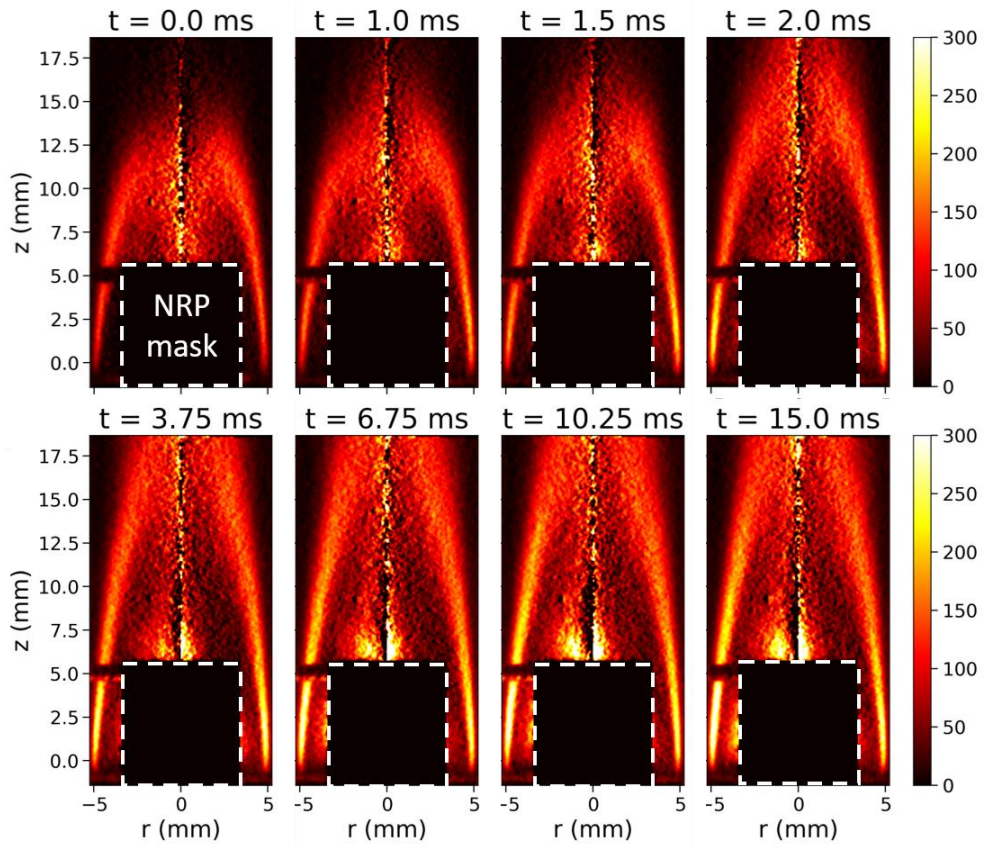

Figure 8.5 OH* chemiluminescence of the PASTEC flame (Φ = 0.8, f = 20 kHz, E_{pulse} = 2 mJ). The time displayed above the images is the delay with respect to the first discharge. The images are Abel-inverted and the emission of the discharge is hidden behind a mask. The electrode on the left at z = 5 mm is visible.

At t = 0 ms, the first discharge is applied. The flame is still confined to the recirculation zone and the plasma assistance has no effect yet. At t = 1 ms in Figure 8.5, corresponding to the 20th pulse, the flame height has increased by approximately 2 mm. In the range of 1 – 2 ms, the top of the flame image extends beyond the CCD chip (> 18 mm). The emission at the flame boundaries (r = ± 5 mm, z < 5 mm) increases by almost a factor of two. At approximately t = 3.75 ms, a luminous zone is visible above the electrode at (r = 0 mm, z = 5 – 8 mm). The luminous zone is not an artifact of the Abel inversion and shows that combustion began at this location. Its intensity increases until approximately t = 10 ms when the flame emission reaches a steady state. Figure 8.6 shows the CH* emission in the same conditions and the same observations can be made.

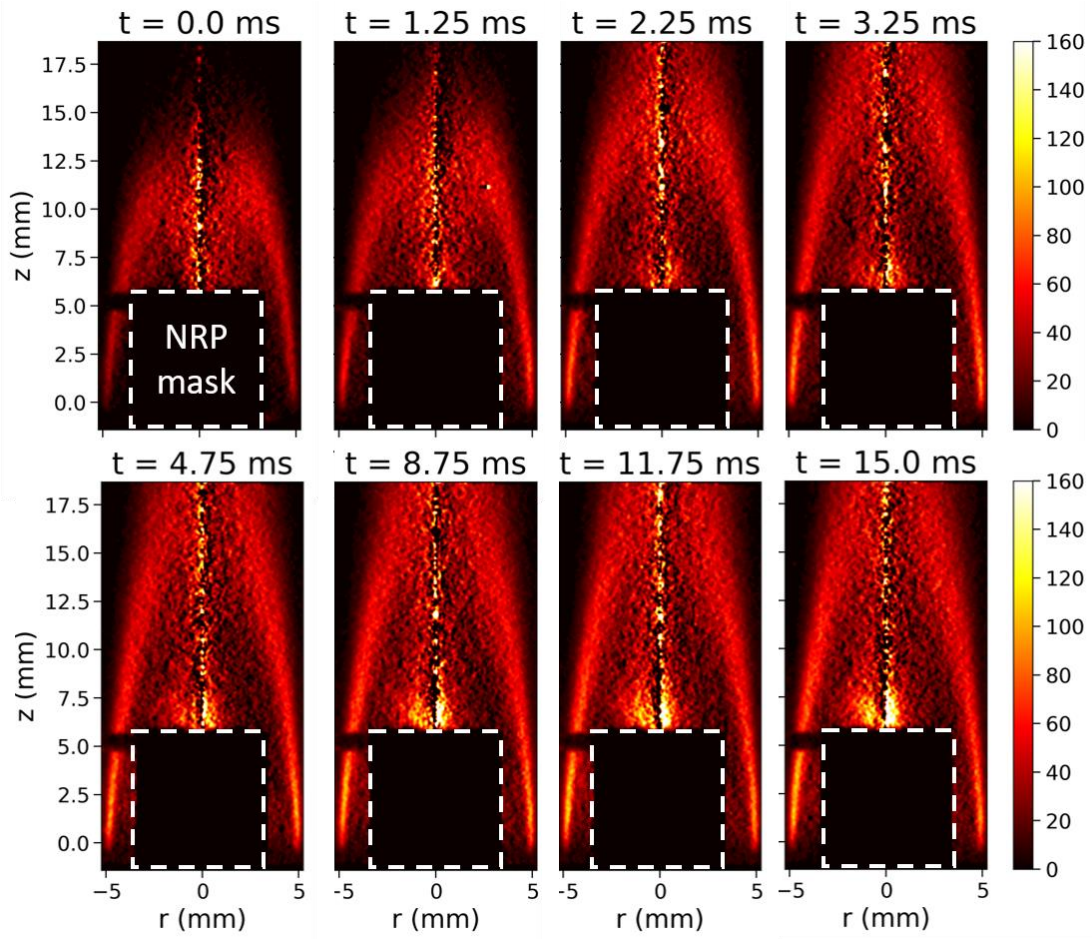

Figure 8.6 CH* chemiluminescence of the PASTEC flame (Φ = 0.8, f = 20 kHz, E_{pulse} = 2 mJ). The time displayed above the results is the delay with respect to the first discharge. The images are Abel inverted.

In this section, the experimental Mini-PAC conditions were presented. Pictures and chemiluminescence images of the turbulent flame are performed. The plasma-assistance increases the luminosity of the flame, which can be qualitatively related to an increase of its thermal power.

8.2 Laser-Induced Fluorescence

8.2.1 Experimental setup

In this section, we characterize the effect of the NRP discharge on the PASTEC flame by OH-LIF. Unlike OES, the LIF diagnostic has the advantage of probing the ground state of OH (see Section 1.4 where the OH-LIF theory is presented). In this section, we detail the LIF setup.

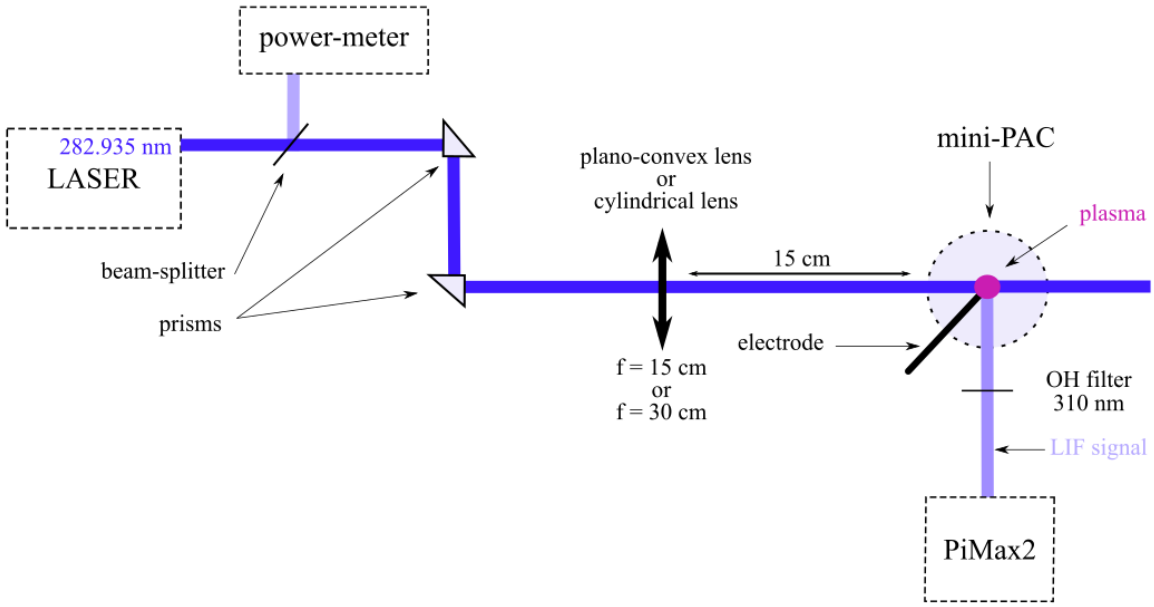

Figure 8.7 LIF setup used in this work. The lens is either plano-convex (for LIF experiments) or cylindrical (for PLIF experiments). The energy of the laser beam is continuously monitored during the operations.

The spatial distribution of OH is studied either by LIF or Planar LIF (PLIF). A frequency-doubled dye laser (Continuum ND6000) with Rhodamine 590 dye pumped by a Nd:YAG laser (Continuum Precision) at 532 nm is used to excite the OH(A) state at 10 Hz. The laser energy per pulse ranges from 0 to 35 mJ and is tuned[1] at 282.937 nm to excite the $Q_2(3)$ transition[2] of OH[($X^2\Pi$, v"=0)→($A^2\ \Sigma^+$, v"=1)] (Luque and Crosley, 1998). The OH fluorescence signal is collected using a bandpass filter (ZBPA 310 - High transmission, Asahi Spectra Co.) centered at 310 nm with 11-nm FWHM placed before the ICCD

[1] Wavelength in air, not in vacuum.

[2] Note that in previous publications (Sainct, 2014; Sainct *et al.*, 2014; Stepanyan *et al.*, 2019), it was argued that this wavelength corresponded to the $Q_1(6)$ transition. However, in the LIFBASE database, the $Q_1(6)$ transition is reported at 282.927 nm. Other authors also do not provide the wavelength to the last decimal, e.g. 282.93 nm in (Sun *et al.*, 2013). Whether the $Q_1(6)$ or $Q_2(3)$ transition is excited has minor implications on the conclusions of (Sainct, 2014; Sainct *et al.*, 2014; Stepanyan *et al.*, 2019).

camera (PiMax2, Princeton Instruments). The peak transmission of the filter is about 60%, with an optical density of 4 outside of the 290 – 350 nm wavelength range. The PLIF laser sheet is generated by a cylindrical lens (f = 30 cm). The height of the sheet is 8 mm, and its thickness is approximately 0.2 mm. In LIF, the laser beam is focused on the middle of the interelectrode gap by a plano-convex lens (f = 15 cm), see Figure 8.7. The beam waist is close to 0.2 mm.

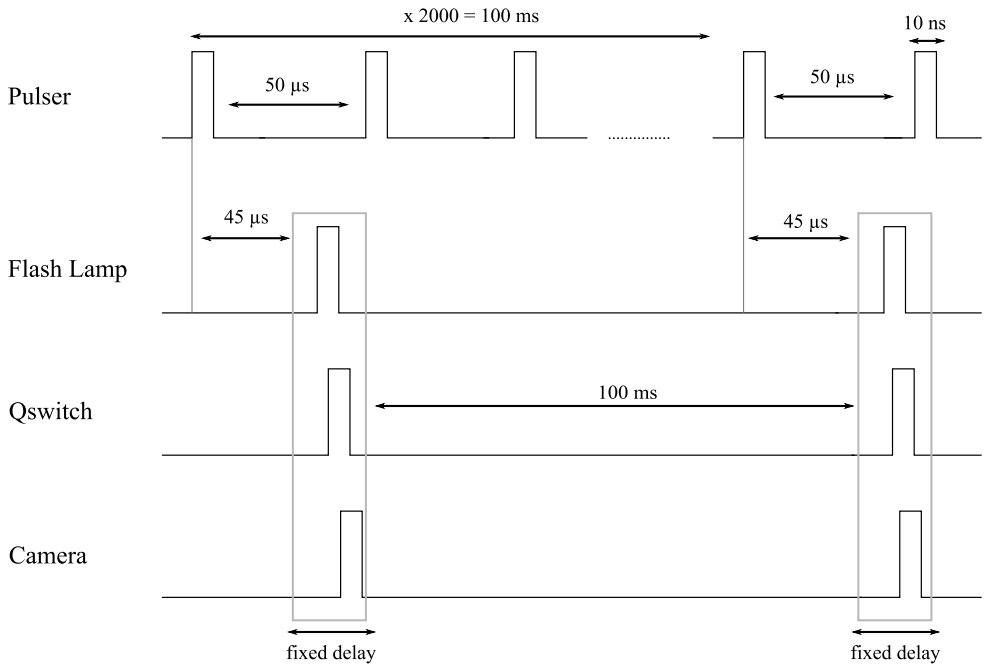

Figure 8.8 Synchronization scheme. The pulser #4 (which operates at 20 kHz) is synchronized with the LIF diagnostic performed at the 10-Hz laser frequency.

The discharge, the laser, and the camera are synchronized with a gate-and-delay generator (BNC Model 575), see Figure 8.8. The delay between the camera gating and the laser components (flash-lamp and Q-switch) is kept constant.

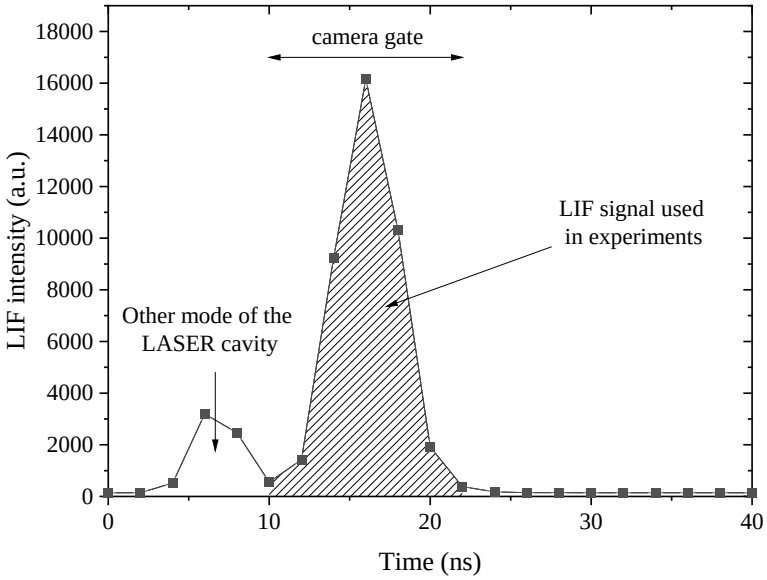

Figure 8.9 LIF intensity variation. The hatched area indicates the laser pulse used in the LIF experiments.

In Figure 8.9, the evolution of the LIF signal during the laser pulse is measured with a 2-ns gate. The LIF signal presents two peaks[1]. In the present measurements, a camera gate of 12 ns is centered on the second peak. Under the PASTEC conditions, the effective lifetime of OH(A) is determined by the quenching processes (Bruggeman *et al.*, 2014) which have rate coefficients in the range of $5 \times k_{Q,N_2} \sim k_{Q,CO_2} \sim k_{Q,H_2O} \sim 5 \times 10^{-10}$ cm^3s^{-1}, for the N_2, CO_2 and H_2O quenchers. From these values, we compute $\tau_{eff,OH} \approx 1.5$ ns in a burnt stoichiometric mixture ($CO_2/H_2O/N_2$). Therefore, the LIF signal is expected to follow the laser intensity profile.

[1] The first peak is due to a laser feature independent of the PASTEC flame.

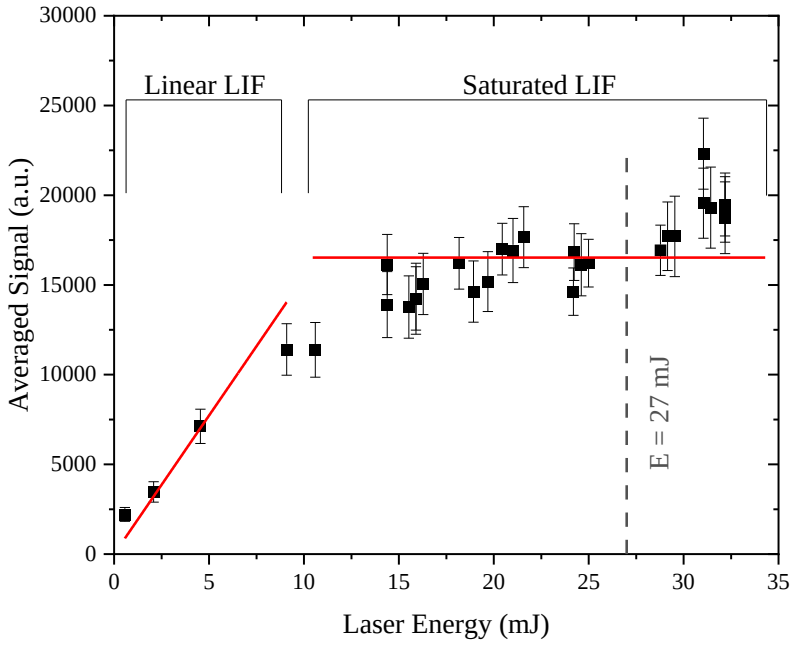

Figure 8.10 Saturation curve of the LIF signal in the PASTEC non-assisted flame (Φ = 0.8, f = 20 kHz, E_{pulse} = 2 mJ). The error bars of the LIF signal are mostly due to turbulence.

The energy of the laser beam is monitored by a powermeter with a low time response (typically around 1 second). Therefore, the measured energy is the sum of the energy of the principal pulse used for the experiments and the spurious pulse measured before. In Figure 8.10, we obtained a saturation curve with a camera gate of 12 ns. The camera gate is shown in Figure 8.9. The curve presents two distinct zones: the linear regime and the saturated regime. The slight increase of the LIF signal above 15 mJ is due to the spatial and temporal wings of the laser, which are not saturated. However, the uncertainty raised by this effect is small compared to the statistical fluctuations due to turbulence (see also Section 8.2.2).

As shown in Figure 8.7, a fraction of the laser beam is separated with a beam splitter to measure the laser energy. A laser pulse of 27 mJ is used in the LIF experiments. Approximately 80% of the laser energy is into the second peak (~ 22 mJ). The LIF signal is therefore saturated for laser pulses of more than 15 mJ. The fluence of the laser beam is about 1.8 GW.cm^{-2} in the LIF configuration, which according to the estimates of Section 1.4 corresponds to saturated LIF. On the other hand, saturation could not be reached in PLIF (fluence of 0.4 MW·cm^{-2}). As detailed in Section 1.4, the conversion of the fluorescence signal into OH number density requires the knowledge of the OH quenching rates in the linear regime. These rates depend on the temperature and the gas composition, which makes the linear LIF interpretation challenging.

8.2.2 OH distribution

In this section, the PLIF measurements are first used to qualitatively characterize the Mini-PAC flame in the vicinity of the electrodes.

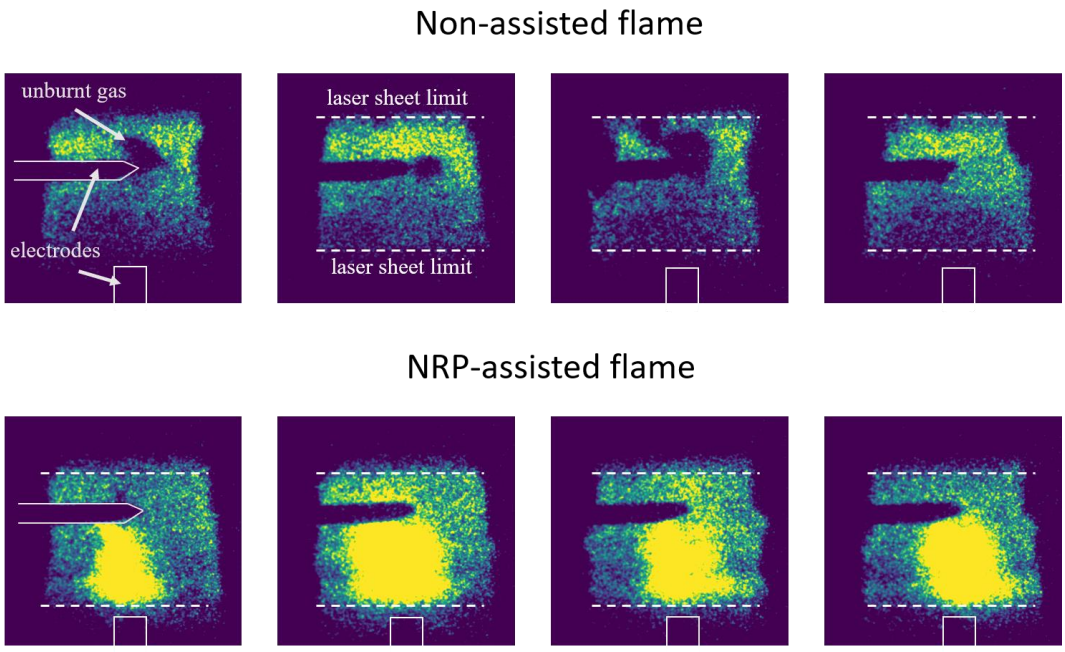

Figure 8.11 Single-shot OH-PLIF images obtained in the PASTEC flame (Φ = 0.8, f = 20 kHz, E_{pulse} = 2 mJ) (same color scale in all images). (top) Four single-shot measurements without NRP discharges. (bottom) Four single-shot measurements with 2-mJ NRP discharges applied at 20 kHz.

In Figure 8.11, single-shot PLIF measurements are presented. The highest value of the color scale is artificially reduced to highlight the location of the active species generated by the discharges. The horizontal electrode is sketched on the top left picture. The electrode is positioned between the laser sheet and the camera (see setup in Figure 8.7), thus no PLIF emission is visible in this area.

In the assisted flame, the measurements are performed 45 µs after the discharge when plasma emission is negligible. The strong LIF signal between the electrodes indicates the OH species produced by the discharges. The extent of the OH volume generated by the discharges is variable, possibly because of turbulence.

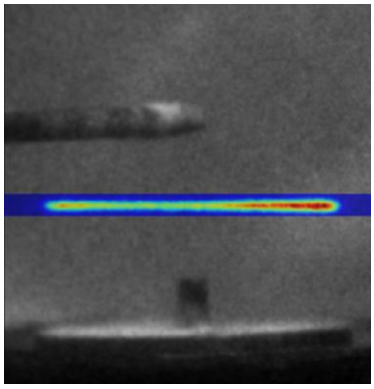

Figure 8.12 Picture of the Mini-PAC burner taken with the ICCD camera (black and white) with a non-saturated LIF signal superimposed (false colors).

In the following experiments, the laser beam is focused with a plano-convex lens. For a laser pulse of ~ 27 mJ (at 282.937 nm), the LIF signal is in the saturated regime and is proportional to the OH number density. In the middle of the interelectrode gap (see Figure 8.12), the laser beam is perpendicular to the discharge axis and can be approximated by a cylinder of 200-µm radius, whose axis lies at z = 2.5 mm.

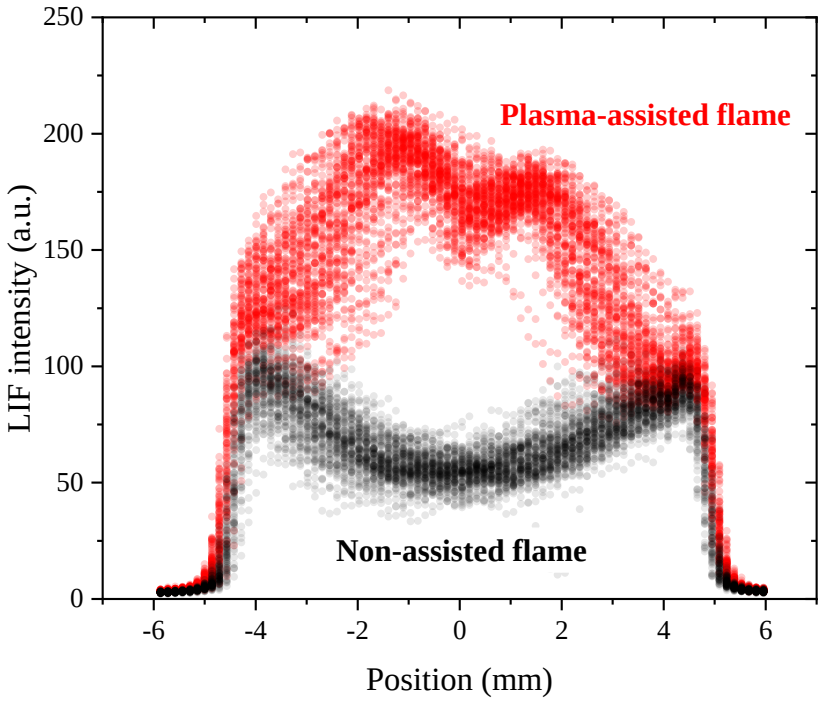

Figure 8.13 LIF signal along the bluff-body under the PASTEC conditions (Φ = 0.8, f = 20 kHz, E_{pulse} = 2 mJ). The data are acquired before the application of the NRP discharges (black dots) and when the NRP discharges are applied at steady state (red dots). Each set comprises 100 shots.

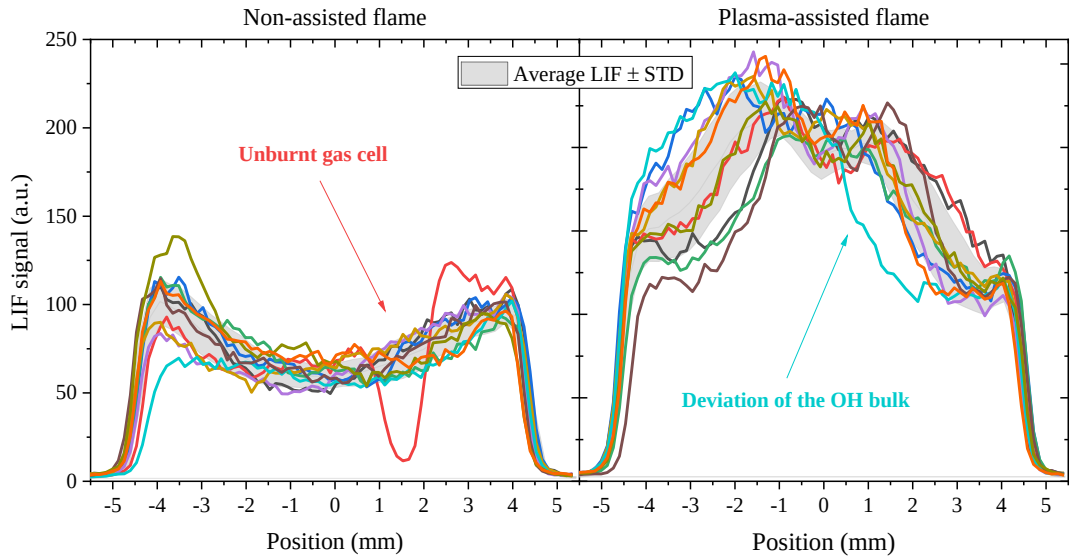

Figure 8.14 Comparison of the average LIF signal (the light grey swath indicates the standard deviation) and 10 instantaneous measurements (colored solid lines) under the PASTEC conditions (Φ = 0.8, f = 20 kHz, E_{pulse} = 2 mJ). The measurements are shown with and without plasma-assistance.

The LIF signal obtained in the non-assisted flame and during the application of the NRP discharges are shown in Figure 8.13. In the non-assisted flame, the OH concentration is minimal at the center and reaches a maximum at at the flame boundaries, r = ± 5 mm. When the NRP sparks are applied, the OH concentration increases by a factor of up to 3 at the center and the shot-to-shot standard deviation of the OH number density increases. This trend is more visible if one compares single-shot experiments and the average LIF signal in Figure 8.14. When the NRP discharges are applied, the OH region oscillates within r = ± 2.5 mm, see for instance the deviation of the cyan curve in Figure 8.14 compared to the average OH distribution. Without plasma assistance, we already showed in Figure 8.11 that unburnt gas cells exist within the flame. This unburnt gas is also detected in single-shot LIF measurements, see for instance the red curve in Figure 8.14.

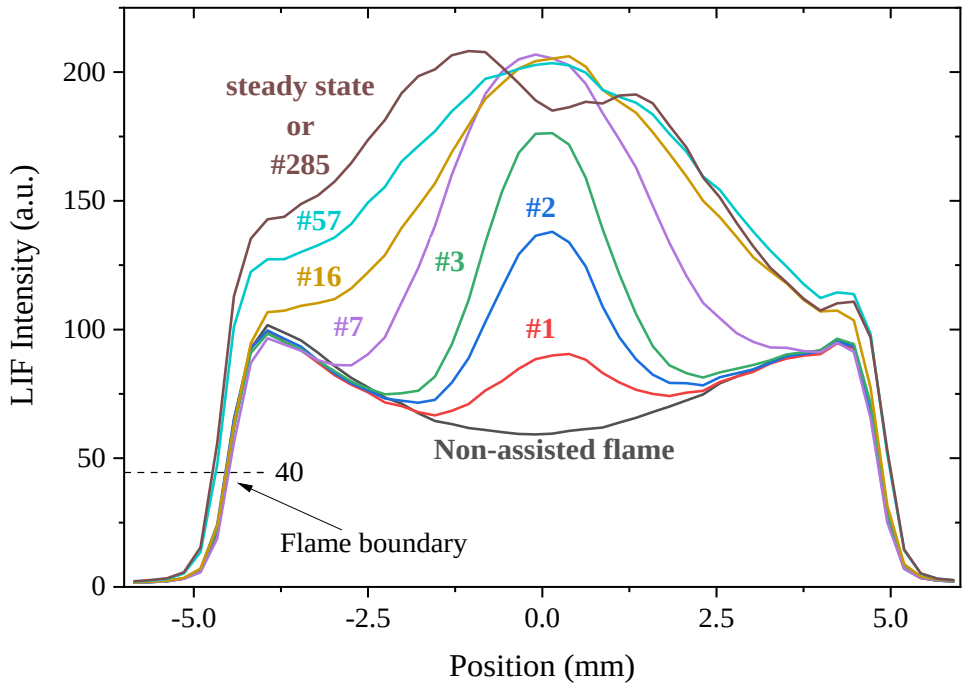

Figure 8.15 Evolution of the OH-LIF signal when NRP discharges are applied under the PASTEC conditions (Φ = 0.8, f = 20 kHz, E_{pulse} = 2 mJ). The numbers displayed correspond to the number of pulses applied before the measurement (e.g. the purple curve "#7" is obtained between the 7th and 8th pulses). The LIF value used to determine the flame width in Figure 8.16 is shown.

Figure 8.15 shows the pulse-to-pulse evolution of the relative OH LIF signal. These measurements are averaged 100 times. For clarity, the standard deviation of the LIF signal (similar to that of the data in Figure 8.14) is not shown in Figure 8.15. During the first pulses, OH is produced by the discharges around r = 0 mm. At the bluff-body boundaries (r = ± 5 mm), the OH number density increases after pulse #16. This increase can have two origins. Either the OH molecules produced in the discharge region are transported to the bluff-body borders, or they are chemically produced, for instance due a temperature increase. The measurements are stopped after pulse #285 (= 14.25 ms) when the LIF signal reaches steady state.

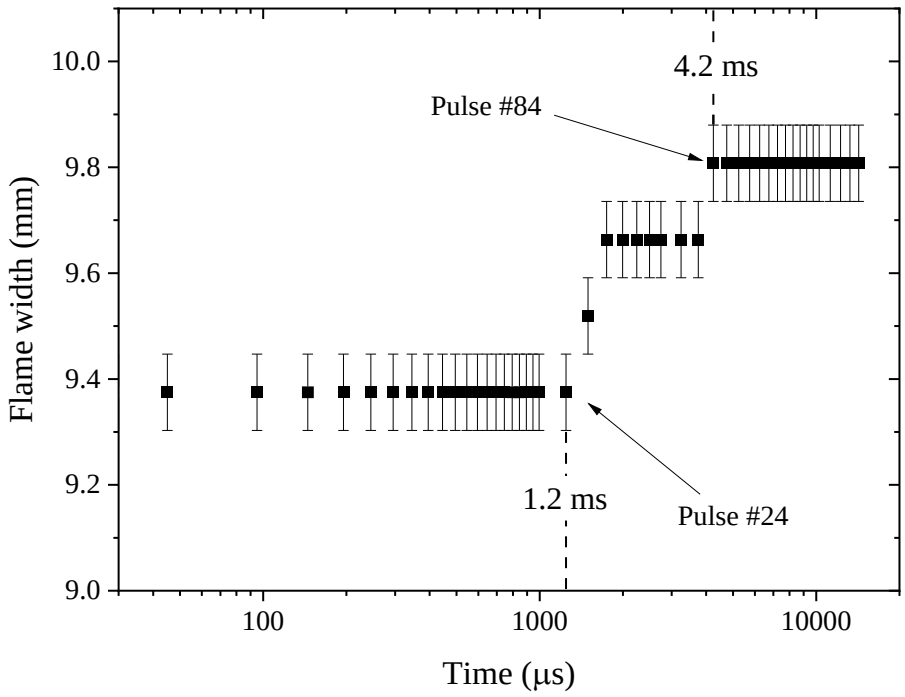

Figure 8.16 Evolution of the flame width based on the OH radius. PASTEC conditions: Φ = 0.8, f = 20 kHz, E_{pulse} = 2 mJ. Vertical bars represent the spatial resolution of the measurement.

Figure 8.15 shows that the flame width increases between pulse #16 and #285. The flame boundary is arbitrarily chosen to be marked at 40 a.u. in the scale of Figure 8.15 (corresponding to 40% of the maximal OH density in the non-assisted flame). The increase of OH number density at the flame border being very steep, the value of the threshold does not significantly influence the flame width variations reported in Figure 8.16. The flame width is constant up to t = 1.2 ms and then increases by 0.4 mm. The steady-state flame width is reached at t = 4 ms.

The advection of OH radicals and heat from the discharge region to the bluff-body boundaries (shear layer) was already reported by (Xu, 2013, chap. 6). Xu showed that this transport of OH and heated species induced the anchoring of a propane flame, otherwise lifted several millimeters above the bluff-body. Our case is slightly different, because here the flame is already anchored to the bluff-body. Nonetheless, our measurements show that the flame diameter increases after about 1 ms, which corresponds to the advection time of the (heat and species). Thus, the stabilization process is similar.

8.2.3 Comparison with Large Eddy Simulations

Our experimental results are compared to numerical simulations of the Mini-PAC configuration. The numerical strategy relies on implementing a low CPU-cost model of plasma-assisted combustion (Castela *et al.*, 2017) in a Large Eddy Simulations (LES) flow solver. The model has recently been used

to simulate ignition in a configuration close to the Mini-PAC experiment (Bechane and Fiorina, 2020). In the numerical model, the electric energy of each pulse is distributed into:

- Ultra-fast heating (timescale of ~ 50 ns)
- Oxygen dissociation (timescale of ~ 50 ns)
- Slow heating by VT transfer (timescale > 1 µs)

In this section, we compare the OH number densities calculated by the model and measured by OH-LIF.

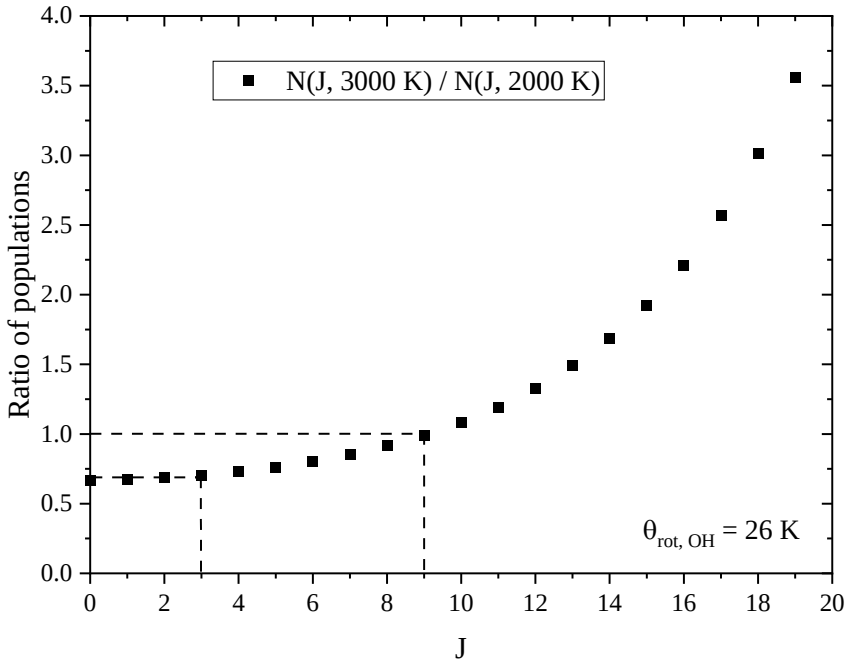

Figure 8.17 Relative variation of the OH rotational population at T_{rot} = 3000 K relative to T_{rot} = 2000 K. The population of the J = 3 state decreases by 30% when the temperature increases, whereas the population of J = 9 remains constant.

As stated before, in the saturated regime, the LIF intensity is proportional to the density of the rotational state excited by laser radiation, in this case, OH(X, v = 0, J = 3). The spatial variations presented in Figure 8.15 are therefore representative of the OH(X, v = 0, J = 3) number density. The ratio of the rotational populations at 3000 K (maximum temperature in the plasma, see Section 8.3) and 2000 K (the flame temperature at ϕ = 0.8) are provided in Figure 8.17 to simulate an extreme case scenario. As shown in Figure 8.17, the spatial variation of the OH(X, v = 0) number density can vary by at most 32%

due to temperature variations[1]. With the same arguments, LIF signal corrections due to the changes in the vibrational population are estimated to be, at most, 10%.

To picture the effect of such a correction, we used the temperature of Bechane's simulations to correct the LIF signal (Bechane, 2021). Using Eq. 8.1, where $\Theta_{rot,\,OH}$ = 27 K and $\Theta_{vib,\,OH}$ = 5378 K (Huber and Herzberg, 1979), we can determine the total OH density from the measured OH(J = 3, v = 0) number density.

$$\frac{OH_{J=3,v=0}}{OH_{tot}} = \frac{(2\mathrm{J}+1)\exp\left(-\frac{J(J+1)\Theta_{rot,OH}}{T}\right)}{T/\Theta_{rot,OH}} \frac{1}{\left[1-\exp\left(-\frac{\Theta_{vib,OH}}{T}\right)\right]^{-1}} \qquad \text{Eq. 8.1}$$

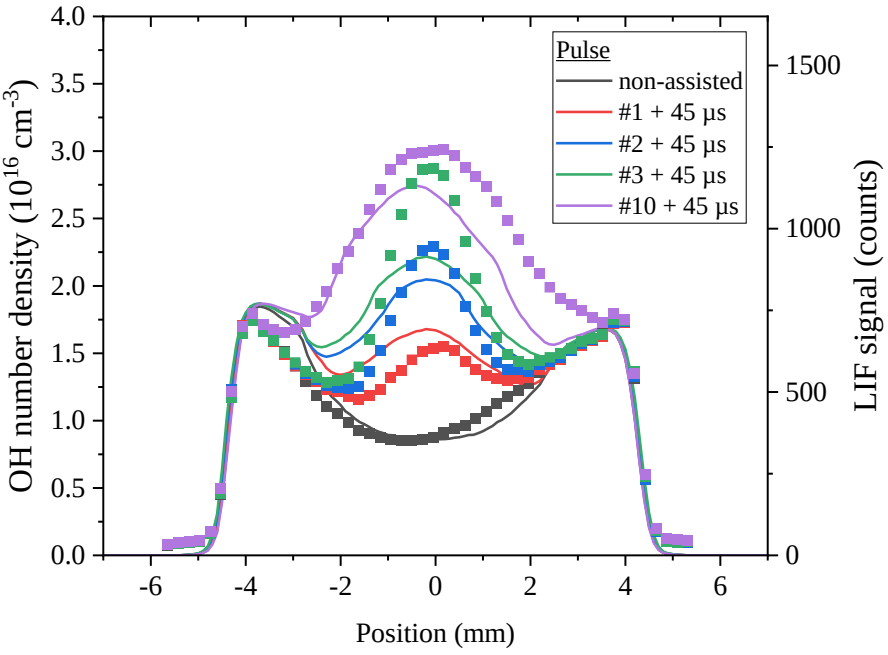

Figure 8.18 Comparison of the temperature-corrected OH-LIF signal (squares) with LES simulations (solid lines) of OH number density obtained in Bechane's numerical simulations (Bechane, 2021) after the 1st, 2nd, 3rd, and 10th pulses.

In Figure 8.18, the corrected LIF signal is compared with the simulated OH number density for the first 10 pulses. The LIF signal is normalized to match the densities computed by Bechane at the flame front at r = ± 5 mm. The measured and predicted values are in good agreement for the case without plasma and for the first two pulses. The shapes and magnitudes of the profiles are particularly well matched. In

[1] No correction would be necessary if the J = 9 state were pumped instead of J = 3. Therefore, we recommend for future work to use the $R_1(9)$ line at 281.377 nm (air wavelength) which is intense and isolated from other transitions within 20 pm.

the central region, the OH number density increases three-fold in three pulses. Although it takes ten pulses in the simulation, the same increase is obtained numerically.

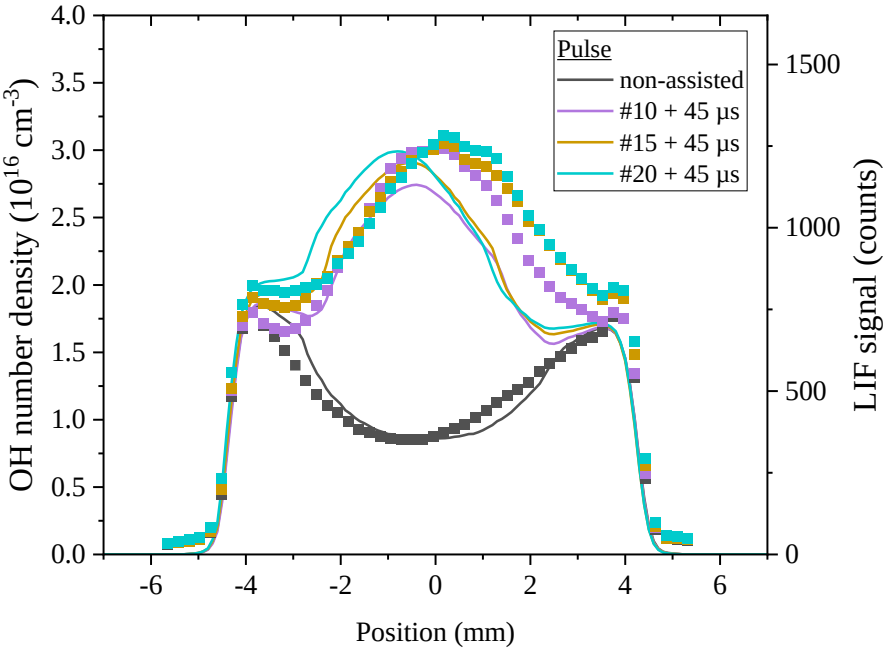

Figure 8.19 Comparison of the temperature-corrected OH-LIF signal (squares) with LES simulations (solid lines) of OH number density obtained in Bechane's simulation (Bechane, 2021) after the 10th, 15th, and 20th pulses.

The OH number density profiles for subsequent pulses are shown in Figure 8.19. After the 10th pulse, at r = 0, the OH number density has increased by:

- 3.5 times according to the experiment and
- 3.0 times according to the simulation.

At later times, the OH density continues increasing in the wings of the distribution, both in simulations and experiments. Between the 10th and the 20th pulses (in the interval 0.5 – 1.0 µs), the agreement between simulations and experiments is excellent.

8.2.4 Conclusions on LIF experiments

After correcting for the temperature effect, the OH LIF measurements show that the NRP discharges increase the OH number density up to a factor of three on the bluff-body axis. Approximately 1 ms after the first discharge, the flame width begins to increase, along with the OH number density at the bluff-body borders. This effect is synchronized with the increase of the flame height measured by chemiluminescence in Section 8.1.2. Our experimental LIF profiles agree remarkably well with the LES simu-

lations performed by Bechane. The increase in OH number density is first located in the discharge vicinity. After the 10th pulse (t = 500 µs), the OH number density also increases near r = ± 5 mm, as demonstrated by the simulations and the experimental results.

In the next sections, we will study at the nanosecond scale the increase of temperature and the species generated during the pulse.

8.3 Discharge characterization

8.3.1 Deposited energy

The results of the following sections are performed at steady state in the PASTEC conditions. Incident pulses of 3.5 kV are generated at 20 kHz by pulser #4 and delivered to the anode through a 6-m, 75-Ω coaxial cable. The voltage and current probes are placed either (i) in the middle of the 6-m cable or (ii) at the electrode. The voltage, current, and deposited energy measured at steady state are shown in Figure 8.20 for the two positions of the probes. The curves are averaged values (practically, at least 1000 measurements were acquired). The standard variation of the current and voltage are below 7%. Once integrated, these variations lead to a 12% statistical fluctuation of the measured energy. The differences between these two arrangements of the probes are described in Chapter 2.

For the measurements presented in Figure 8.20 a), the probes are placed at the electrode. Thus, the applied voltage (sum of the incident and reflected pulses) and the total current passing through the discharge are measured. We start the time counter t = 0 ns at the breakdown, i.e. when the current is above 1 A. The peak current is measured at t = 11 ns. At this moment, the abrupt fall of both current and voltage marks the end of the energy deposition. Therefore, the instant t = 11 ns is used for discharge/OES synchronization and matches the peak of the OES signal, see also (Rusterholtz *et al.*, 2013). For the results presented in Figure 8.20 b), the probes are placed upstream in the cable, 3 meters away from the discharge. Thus, the incident pulse and its reflections on the electrode can be measured. The incident pulse propagates from the measuring point to the electrode in 15 ns, and this delay is taken into account when synchronizing the time axis of Figure 8.20 b) with Figure 8.20 a).

For the considered steady-state regime at 20 kHz, the total deposited energy is equal to 2 mJ per pulse. The vertical bars on the peak voltage, peak current, and total deposited energy correspond to the standard deviation of the measurements. It can be seen in Figure 8.20 b) that an incident pulse of 2.5 mJ is generated and that only 1.7 mJ is deposited at the first passage. The remaining 0.9 mJ is reflected back toward pulser #4. This reflection results from impedance mismatch between the coaxial cable (75 Ω)

and the interelectrode gap (infinite resistance before the plasma is formed). When the number of electrons increases in the plasma, the gap conductivity increases as well, and the impedance decreases. Hence, the energy is no longer reflected and can be efficiently deposited in the plasma.

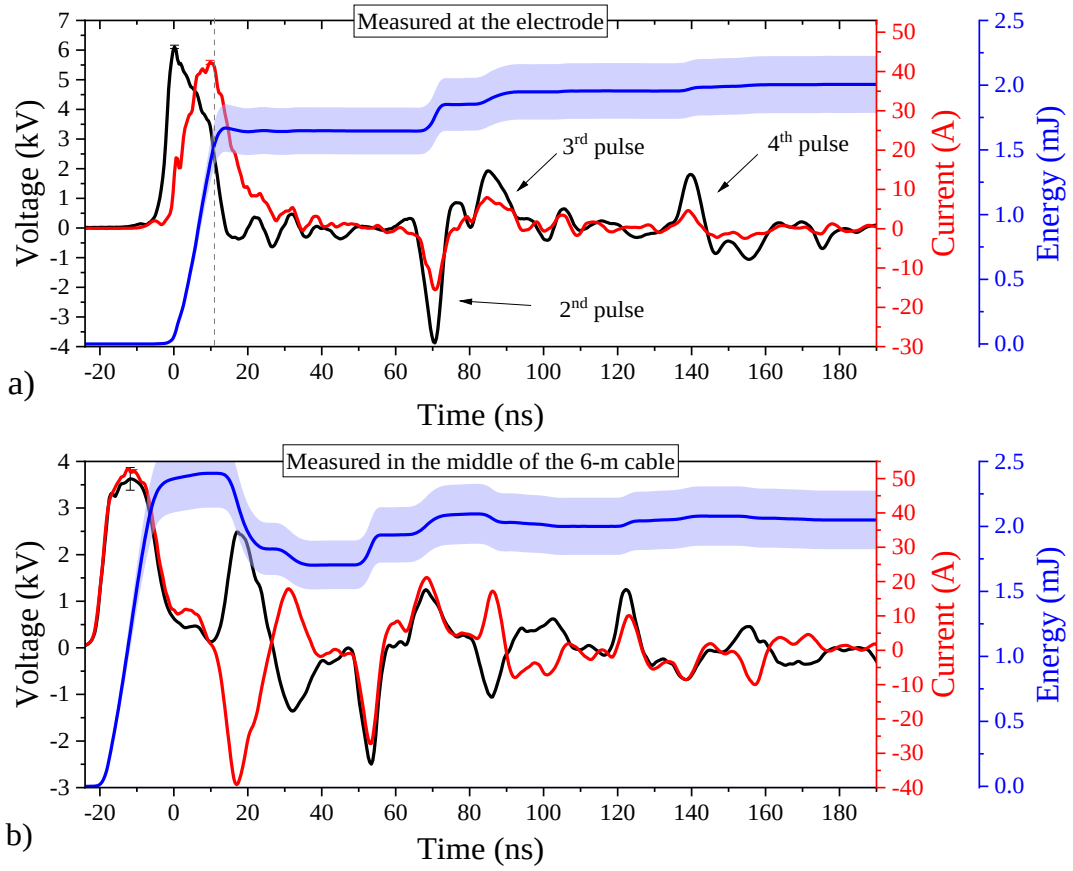

Figure 8.20 Voltage (black) and current (red) measured a) at the electrode or b) in the middle of a 6-m cable connecting the generator and the electrodes. The energy deposited in plasma is obtained by integrating the product of the voltage and the current (the light blue swath indicates the standard deviation). The dashed grey line represents the current peak at t = 11 ns used for OES synchronization. PASTEC conditions: Φ = 0.8, f = 20 kHz, E_{pulse} = 2 mJ.

In Figure 8.20 a), at t = 70 ns, a negative voltage pulse of -4 kV is measured at the electrode, rapidly followed by a positive pulse of +2 kV at t = 80 ns. Between 70 and 85 ns, approximately 0.2 mJ is deposited by these two pulses. At t = 140 ns, 0.1 mJ is deposited in a 4th pulse (+2 kV). The origin of the 3rd pulse is not known, but it is likely related to the pulser electronics. The 2nd and 4th pulses are reflections of the initial pulse, after traveling along the 6-m coaxial cable and the internal circuit of the pulser. Their polarities are alternated (1st: positive, 2nd: negative, 4th: positive) because pulser #4 must have a negligible impedance compared to the cable one (75 Ω). The total energy is thus deposited in four main pulses within 150 ns. The ratio of the plasma electric power (40 W) and flame maximal thermal power (13.3 kW) is, therefore, equal to 0.3%.

A low power budget of plasma-assistance is essential for most practical applications[1]. Here we compare the energy (i) produced by the generator, and (ii) deposited in the plasma. As shown in Figure 8.20 a) and b), the energy deposited into the plasma is practically the same for both probe configurations (2.01 mJ *versus* 2.05 mJ). The standard deviation of the present measurement (± 0.2 mJ) is due to the generator and the plasma state fluctuations; they remain independent of the location of the probes. Both methods are, therefore, equivalent to measure the deposited energy. In Figure 8.20 b), we showed that the incident pulse carries 2.4 mJ. Therefore, the energy produced by pulser #4 is deposited in the gas mixture with an efficiency[2] of 83%. Without the 2nd, 3rd, and 4th pulses, this efficiency would drop[3] to 70%.

8.3.2 Species identification

In this section, we identify most of the species emitting between 180 and 800 nm for the PASTEC point (methane/air, Φ = 0.8, f = 20 kHz, Epulse = 2 mJ). The area of light collection is shown in Figure 8.21. The diameter of the discharge (FWHM) is 1 mm, which is large compared to the typical slit widths we use in this study (50 – 150 µm). With this configuration, the measurements are spatially resolved along the gap axis. However, the radial resolution is lost. The identification begins with the species emitting in the ultraviolet (UV).

---

[1] See for instance the study of (Neame *et al.*, 1995) who extended the EGR tolerance of an automotive engine with a 1.2-J discharge. The authors admitted, however, that the power cost of their system (454 W) was too high for practical applications.

[2] We define "efficiency" as the deposited energy compared to the incident energy. For monitoring the total efficiency of this NRP generation, one would have to also consider the losses during transformation of AC power to NRP discharges.

[3] We show in Chapter 9 (SICCA experiment) that a near-100% efficiency can be achieved with a higher voltage.

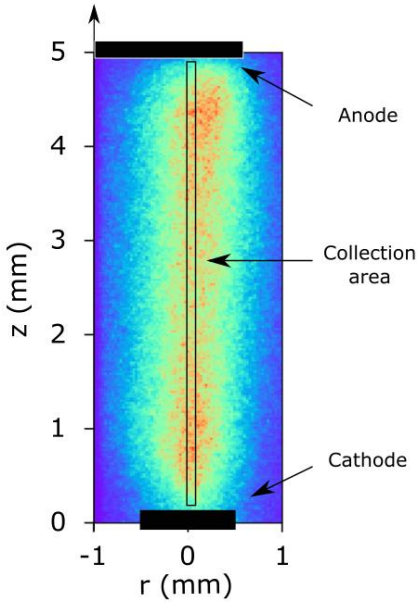

Figure 8.21 Collection area compared to the typical emission of the nanosecond discharge under the PASTEC conditions (Φ = 0.8, f = 20 kHz, E_{pulse} = 2 mJ).

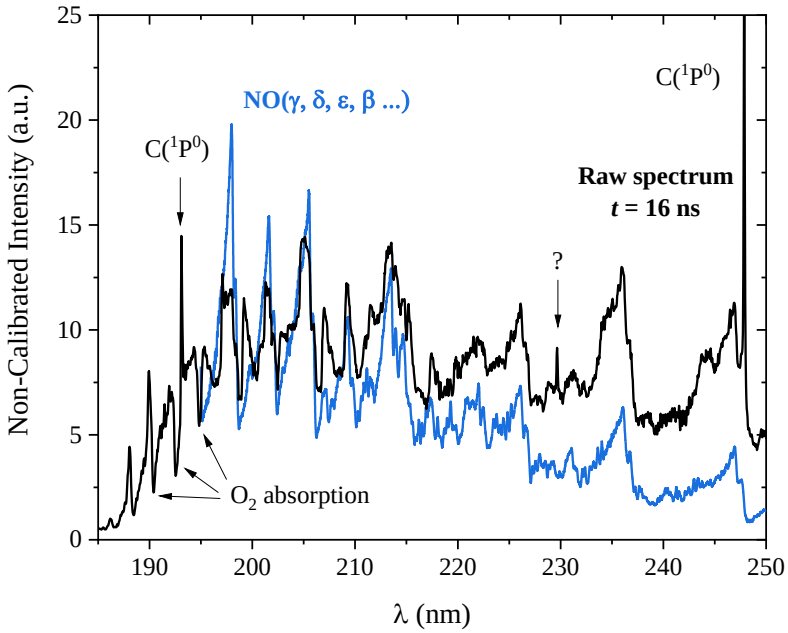

Figure 8.22 Non-calibrated spectrum (in black) recorded between 185 and 250 nm under the PASTEC conditions (Φ = 0.8, f = 20 kHz, E_{pulse} = 2 mJ). The emission of the discharge is spatially averaged along the interelectrode gap at t = 16 ns. For comparison, the NO spectrum is simulated with Specair.

In Figure 8.22, a non-calibrated spectrum measured in the interval 180 – 250 nm at t = 16 ns is compared to the emission of NO bands simulated with Specair (Laux *et al.*, 2003). In this wavelength range, the CCD response, grating response, and optics transmissivity sharply vary and air strongly absorbs in the VUV region (below λ = 190 nm). Thus, Figure 8.22 serves for comparison purposes. We identify NO emission features of NO γ (A – X), NO β (B -X) NO δ(C – X) and NO ε(D – X) (Laux *et al.*, 2003).

Possibly, two unexplained bands at 199 and 207 nm could be related to CO(A – X) emission (McGuire *et al.*, 2020), although no other features of CO were found in the spectrum. Two atomic lines are visible at 193 and 247 nm and correspond to the atomic carbon lines from the excited state C($^1P^0$) at 7.68 eV.

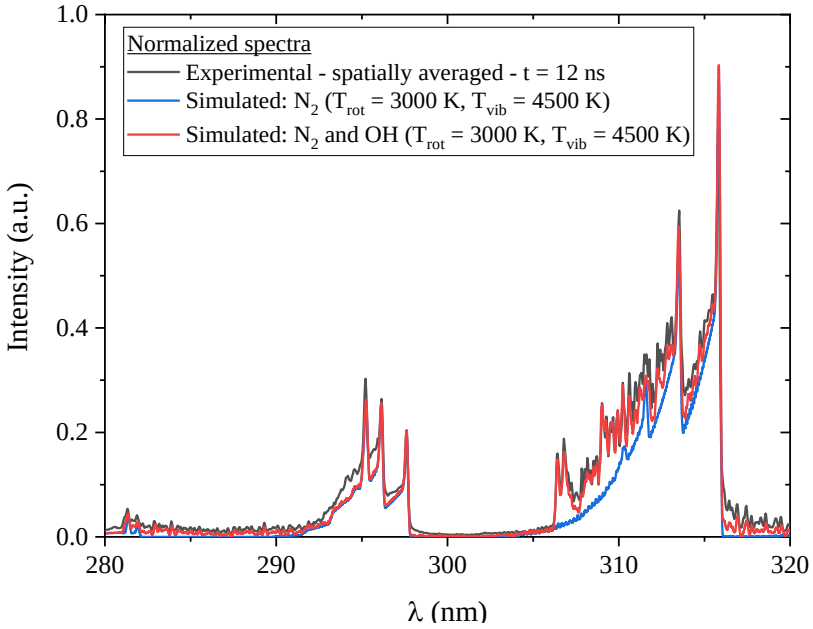

Figure 8.23 Identification of the OH spectrum at t = 12 ns in the PASTEC conditions (Φ = 0.8, f = 20 kHz, E_{pulse} = 2 mJ) with Specair simulations. The experimental and simulated spectra are normalized at 316 nm. The experimental spectrum is spatially averaged and not calibrated. The inclusion of the OH(A-X) emission (in red) provides a better agreement than the simulation N_2(C-B) emission only (in blue).

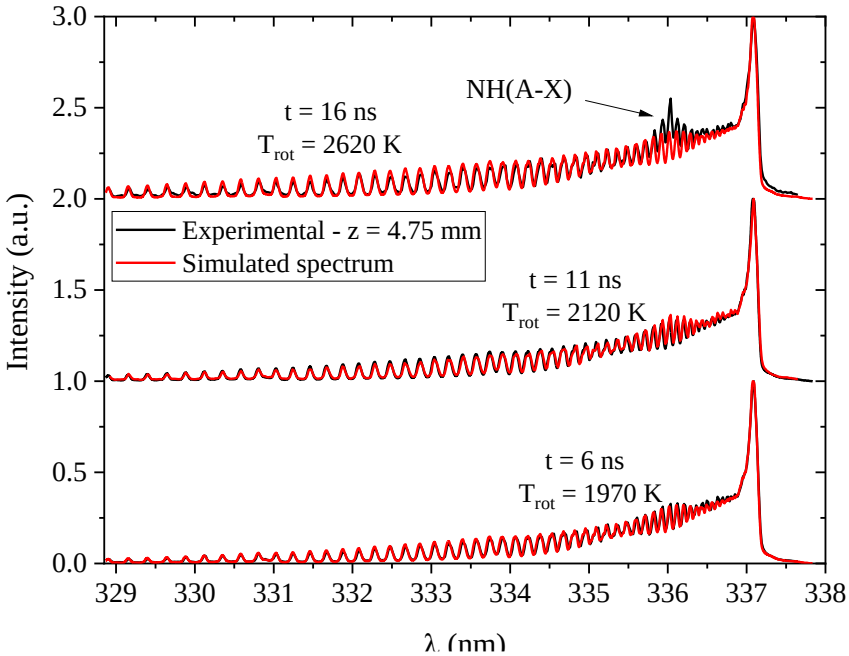

Figure 8.24 Normalized experimental spectra and Specair simulated spectra of the N_2(C-B) (0-0) vibrational band at t = 6, 11, and 16 ns. These measurements are performed near the anode (z = 4.75 mm) under the PASTEC conditions (Φ = 0.8, f = 20 kHz, E_{pulse} = 2 mJ). The emission at 336 nm is due to the NH(A-X) transition.

In Figure 8.23, a non-calibrated emission spectrum between 280 and 320 nm is presented. The experimental emission matches the simulated spectrum (Laux *et al.*, 2003) only if OH emission is added to the N_2 second positive system. The rotational temperatures of OH(A) and N_2(C) are assumed to be equal in this example. Note however that the OH(A) rotational temperature is sometimes not representative of the gas temperature (Bruggeman *et al.*, 2014; Sainct *et al.*, 2014). The measurement of OH(A) rotational temperature and density is presented in Section 8.6.2.

The N_2(C-B, 0-0) band dominates the overall spectrum and is used in Section 8.3.2 to determine the gas temperature. For t ≥ 16 ns, we also observe NH(A-X) emission at λ = 336 nm (Figure 8.24). Measurements of NH(A) rotational temperature and number density are presented in Section 8.6.2.

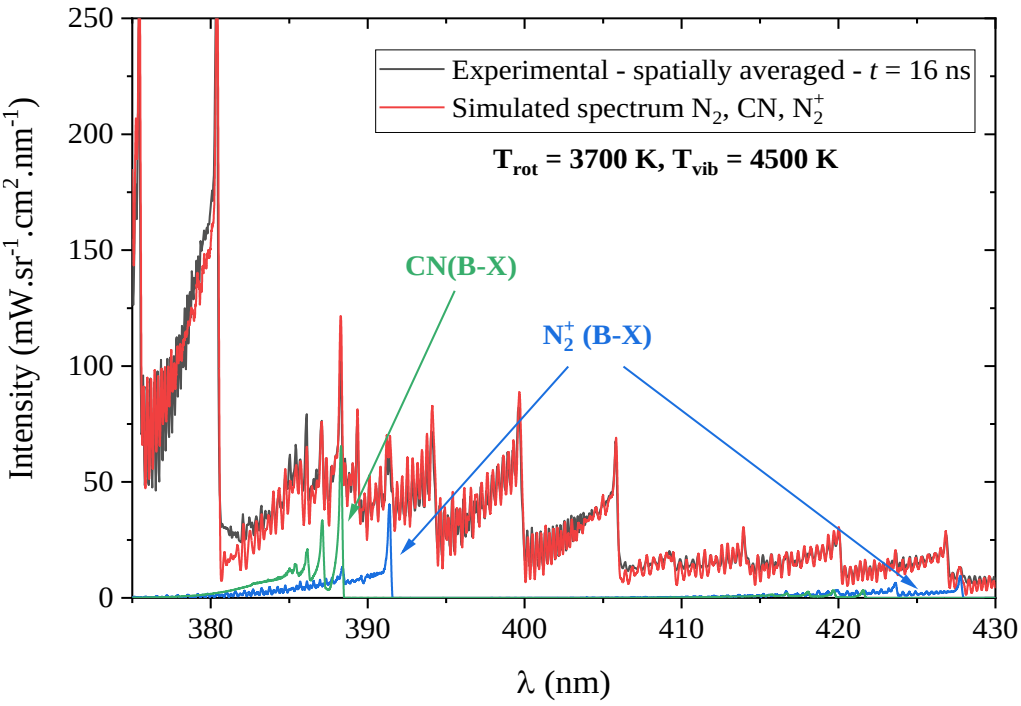

Figure 8.25 Calibrated spectrum (in grey) compared with a simulated spectrum (in red) composed of N_2, CN, and N_2^+. The experimental spectrum is spatially averaged and measured at t = 16 ns under the PASTEC conditions (Φ = 0.8, f = 20 kHz, E_{pulse} = 2 mJ). The Specair spectra are simulated with T_{vib} = 4500 K and T_{rot} = 3700 K.

In the wavelength range 300 – 500 nm, the emission is dominated by the second positive system of N_2. However, for t ≥ 12 ns, other features can be detected such as CN violet emission, i.e. CN(B-X), and N_2^+ first negative system, i.e. N_2^+(B-X). In Figure 8.25, the emission spectra of these three species are simulated and compared with the spatially averaged spectrum acquired at t = 16 ns. In this case, we assumed all species have the same rotational and vibrational temperatures (T_{rot} = 3700 K and T_{vib} = 4500 K).

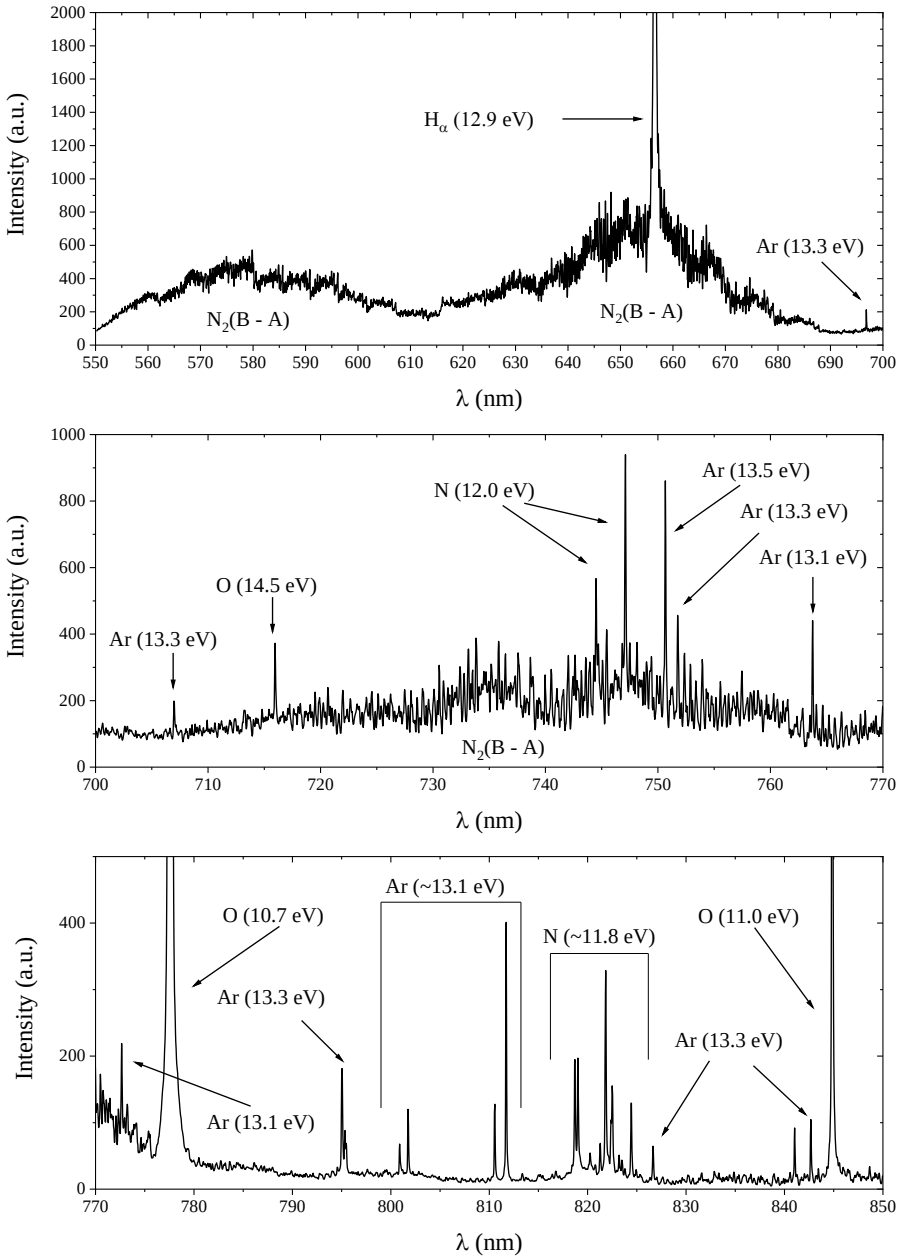

Figure 8.26 Non-calibrated emission spectrum recorded between 550 and 850 nm at t = 16 ns under the PASTEC conditions(Φ = 0.8, f = 20 kHz, E_{pulse} = 2 mJ). The emission is spatially averaged along the interelectrode gap.

We show the emission spectrum of the discharge between 550 and 700 nm under the PASTEC conditions and t = 16 ns in Figure 8.26. The visible wavelength range is dominated by the N_2(B-A) emission and the H_α line. However, for t > 10 ns, the N_2 emission decays and several atomic lines are visible up to 850 nm. Several argon lines are identified in between 680 and 850 nm. Oxygen lines (at 777 nm and 846 nm) and nitrogen lines (at 742 – 746 nm and 820 nm) demonstrate the dissociation of air molecules. The production of atomic species such as N and O usually leads to the formation of NO, see Reac. 8.1 (Ombrello, Ju and Fridman, 2008).

$$N + O_2 \rightarrow NO + O$$ Reac. 8.1

It was indeed shown that NO molecules accelerate CH_4 and H_2 ignition at low temperature (Ombrello, Ju and Fridman, 2008). We already showed in Figure 8.22 that NO is produced in the discharge vicinity. Kim et al. demonstrated using simulations in similar conditions that NO can also be formed in a plasma-assisted flame by Reac. 8.2 (Kim et al., 2007).

$$N + OH \rightarrow NO + H$$ Reac. 8.2

However, Kim et al. also found that N atoms can later consume NO via Reac. 8.3.

$$N + NO \rightarrow N_2 + O$$ Reac. 8.3

The impact of atomic species on NO concentration could therefore be moderate and needs more investigations that are beyond the scope of this thesis.

8.3.3 Short conclusions on the discharge characterization

In this section, the discharge was characterized by electrical OES measurements. The energy measurements show that each 2-mJ discharge comprises four energy depositions. Most of the energy is deposited in the first pulse (1.7 mJ).

The list of species detected by OES in the PASTEC conditions is given in Table 8.1 and Table 8.2. The presence of atomic species in the spectra indicates that these discharges are in the NRP-spark regime, whereas the simultaneous presence of N_2 excited states and atomic species indicates that thermal equilibrium is not reached. *Therefore, this discharge is a non-thermal spark.*

Table 8.1 List of the molecular species identified by OES. The emitting state is given in brackets. The NO emission is due to multiple states, principally the NO(A,B,C,D) states.

Emitting species	NO(A,B,C,D)	OH(A)	NH(A)	CN(B) N_2^+(B)	N_2(B) N_2(C)
Wavelength (nm)	< 250	310	336	380 – 390	550 – 750 290 – 410
Example	Figure 8.22	Figure 8.23	Figure 8.24	Figure 8.25	Figure 8.26 Figure 8.24

Table 8.2 List of the atomic species identified by OES.

Emitting species	C	H (H_α, H_β)	N^+	O	N	Ar
Wavelength (nm)	193, 247	656 486	500	777	742 – 746 818 – 825	750 794
Example	Figure 8.22	Figure 8.26 Figure 8.30	Figure 8.30		Figure 8.26	

The same measurement will be performed in Chapter 9 in the SICCA experiment for discharge characterization. In the present chapter, a more detailed analysis is completed. In the next section, time-resolved OES is performed to measure the electron number density of the plasma.

8.4 Electron number density

8.4.1 The H_α line broadening

The electron number density can be measured from the Stark broadening of the H_α line at 656 nm. As described in Section 1.3, the total width[1] of H_α is the sum of several broadening mechanisms: Doppler, resonance, natural, Van der Waals, Stark, and instrumental.

Under the PASTEC conditions, the Doppler width is small compared to our instrumental broadening, and the increase in temperature has a negligible effect. Thus, the Doppler HWHM will be considered constant and equal to 0.012 nm. The number density of atomic hydrogen is estimated to be below 10^{15} cm^{-3}, resulting in negligible resonance broadening (< 0.001 nm). Natural broadening is negligible.

The Van der Waals HWHM is obtained in Eq. 6.7 by summing the contributions of the perturbers listed in Table 8.3.

$$\Delta\lambda_{Van\ der\ Waals}[nm] = \frac{p}{1\ atm}\left(\frac{273\ K}{T_{gas}}\right)^{0.7}\sum_{pert}\left(\frac{\gamma_{pert}}{100}x_{pert}\right) \qquad \text{Eq. 8.2}$$

The γ_{pert} Van der Waals coefficients were calculated in Table A3-A5 of (Minesi, Stepanyan, *et al.*, 2020) and reported in Section 1.3. In Table 8.3, the dominant mole fractions in a CH_4 – air flame at

[1] By convention, the term "width" always refers to the Half-Width at Half Maximum (HWHM) in this thesis.

$\Phi = 0.8$ are given. The flame composition is calculated at equilibrium for T_{gas} = 2000 K and T_{gas} = 3000 K, the limits of the flame temperature in the interelectrode region (see the temperature measurements in Section 8.5). The compositions are calculated with the "Chemical Equilibrium with Applications" (CEA) NASA code[1] (McBride and Gordon, 1992).

Table 8.3 Mole fractions in an equilibrium mixture of CH_4 – air ($\Phi = 0.8$) at 2000 and 3000 K calculated with the CEA NASA code (McBride and Gordon, 1992) and γ factors taken from Section 3.3

Species	N_2	O_2	CO_2	CO	H_2O	H_2	H	NO	OH
Mole fraction at 2000 K	72%	3.7%	7.7%	0.05%	15%	0.2%	0.00%	0.3%	0.2%
Mole fraction at 3000 K	66%	4.3%	2.7%	4.3%	9.4%	2.0%	2.2%	2.0%	3.7%
$\gamma_{\text{Van der Waals}}$	2.9	5.2	3.4	3.1	2.7	3.6	-	5.9	-

Using data of Table 8.3, the average gamma coefficient on the right-hand side of Eq. 6.7 is equal to γ_{2000K} = 3.0 and γ_{3000K} = 2.8. Thus, the total Van der Waals HWHM is 7 pm and 5 pm. We assume, therefore, that the Van der Waals HWHM is constant and equal to 6 pm in our analysis.

The Stark HWHM can be calculated with Eq. 8.3 (Gigosos, González and Cardeñoso, 2003; Konjević, Ivković and Sakan, 2012).

$$\frac{n_e}{10^{17} cm^{-3}} = \left(\frac{\Delta\lambda_{HWHM,\mathrm{H}\alpha}}{0.549\ \mathrm{nm}}\right)^{1.47134} \qquad \text{Eq. 8.3}$$

At $n_e = 5\times10^{14}$ cm^{-3}, the Stark HWHM is 0.014 nm; we consider this value to be the lower detection limit of the experiment. The Van der Waals, resonant, natural, Stark, and Doppler HWHM calculated previously are summarized in Table 8.4. The measurements are performed with a 2400-gr/mm grating and a slit width of 50 µm at the spectrometer entrance. The instrumental HWHM measured with a HeNe laser at λ = 632.8 nm is approximately equal[2] to 0.025 nm.

[1] The code is available at cearun.grc.nasa.gov (consulted in April 2020)

[2] Given that the spectrometer focal length is 500 mm, the system has a dispersion, $d\lambda/dx = g / (m \times f)$ = 0.83 nm·mm^{-1} where g is the number of grooves per mm, m the diffracting order, and f the focal length of the spectrometer. The pixel pitch is 13 µm and the slit aperture is 50 µm. Thus, the instrumental function can theoretically be approximated by a trapezoidal shape (in the wavelength space, top: 31 pm and bottom: 52 pm) which roughly corresponds to the experimental instrumental function.

Table 8.4 H_α line HWHM at $n_e = 5\times10^{14}$ cm^{-3} based on the composition of an atmospheric pressure CH_4 – air flame (Φ = 0.8) at 2000 and 3000 K.

T_{gas} (K)	Instrumental broadening (nm)	Resonant (nm)	Van der Waals (nm)	Doppler (nm)	Stark (nm)
2000	0.025	<0.001	0.007	0.011	0.014
3000		<0.001	0.005	0.013	

8.4.2 One-Lorentzian fit of H_α

Figure 8.27 presents a typical fit of the H_α emission by a convolution of:

(i) the profile of the instrumental broadening,

(ii) the Doppler broadening simulated with a constant Gaussian profile (HWHM = 12 pm), and

(iii) the Van der Waals and Stark broadenings simulated with a Lorentzian profile.

The Lorentzian width is varied until the simulated line and the data agree. The Stark width is finally obtained after the Van der Waals HWHM (6 pm) is subtracted from the total Lorentzian HWHM. The error in the Stark width determination is estimated to be ± 15%, see Figure 8.27. The uncertainty in the n_e measurement is ± 20% because of the uncertainty propagation in Eq. 8.3.

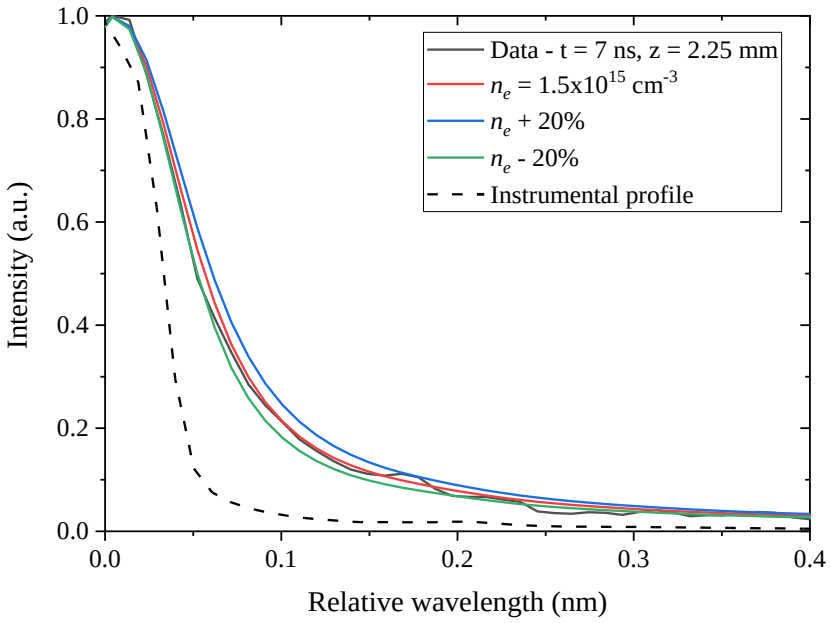

Figure 8.27 Fit of the H_α emission line at t = 7 ns, z = 2.25 mm, under the PASTEC conditions (Φ = 0.8, f = 20 kHz, E_{pulse} = 2 mJ). The wavelength is relative to the H_α line center. The error on the n_e estimation is 20%. The dashed line represents the instrumental function.

The discharge spectra are obtained by collecting the average emission of H_α at various distances z from the cathode. The distribution of the electron number density at several instants is shown in Figure 8.28. The initial electron distribution is relatively homogeneous along the gap: $n_e(t = 2\text{ ns}) \approx 10^{15}$ cm^{-3}. During the applied pulse, n_e increases up to 3×10^{15} cm^{-3} in the middle of the gap. Interestingly, Pilla obtained an electron number density of 10^{15} cm^{-3} at the same location, albeit his conditions were different (Pilla, 2008, p. 125). The ionization degree is higher near the electrodes where, at the end of the pulse, n_e reaches about 10^{16} cm^{-3}. This electron number density at 1 bar and 3000 K represents an ionization of ~ 1%.

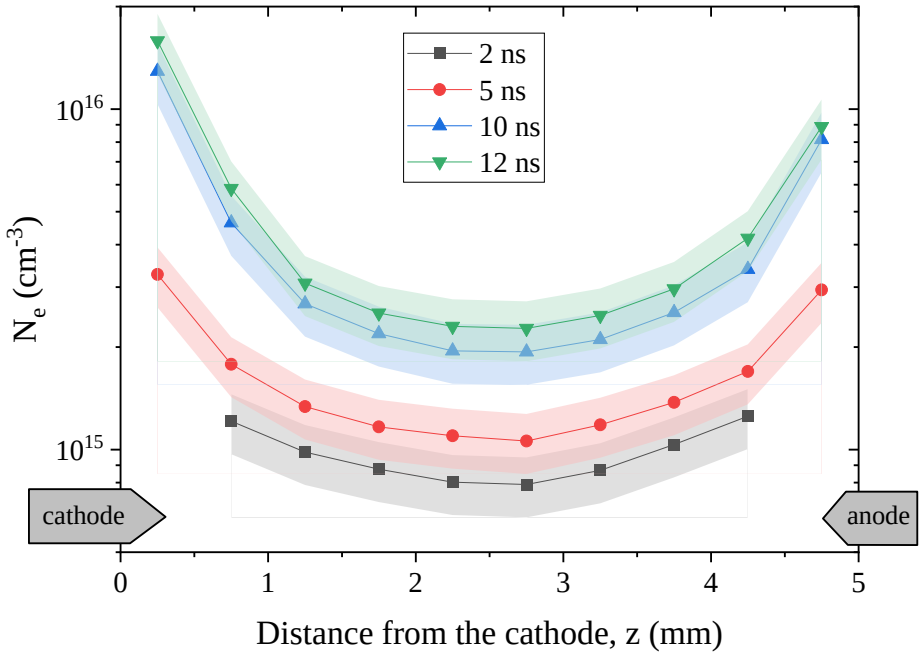

Figure 8.28 Map of the electron number density distribution at t = 2, 5, 10, and 12 ns under the PASTEC conditions (Φ = 0.8, f = 20 kHz, E_{pulse} = 2 mJ).

In Figure 8.20 b), at t = 27 ns, the reflected voltage is equal to zero, which indicates that the plasma impedance is close to the cable impedance[1] (75 Ω) at t = 12 ns. In Section 2.2.2, we calculated the relationship between the plasma impedance and the average electron number density. The optical diameter

[1] We showed in Section 8.3.1 that the electrical measurements performed upstream of the discharge are delayed by 15 ns. Therefore, the measurements acquired at t = 27 ns correspond to events occurring at t = 12 ns.

of the discharge is approximately 1 mm and we assume T_e ~ 1 eV. Applying Eq. 2.10, we get an ionization fraction of 4% at t = 12 ns, which corresponds[1] to the order of magnitude measured here.

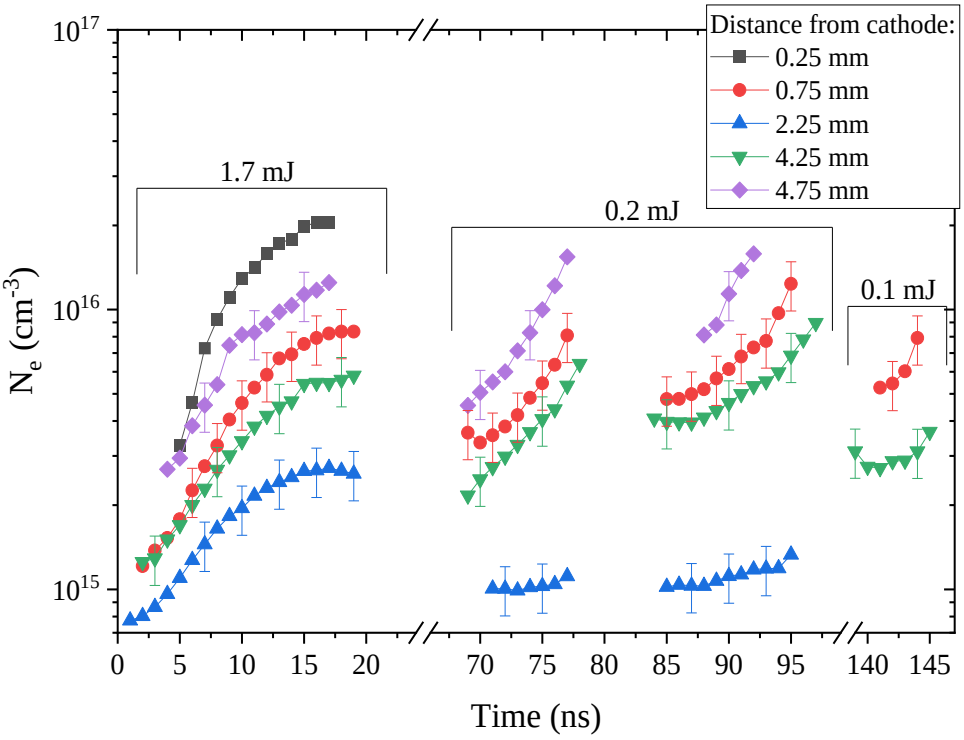

Figure 8.29 Evolution of the electron number density at z = 0.25, 0.75, 2.25, 4.25, and 4.75 mm under the PASTEC conditions (Φ = 0.8, f = 20 kHz, E_{pulse} = 2 mJ). The energy deposited by the pulses is given above the brackets. The result of the two-Lorentzian fits are provided for z = 0.25 mm in Figure 8.33.

In Figure 8.29, the detailed evolution of n_e is plotted on a longer timescale. We see three successive periods corresponding to:

- the 1st incident pulse of 1.7 mJ (t = 0 – 17 ns),
- the 2nd and 3rd pulses of 0.2 mJ (t = 70 – 95 ns),
- the 4th pulse of 0.1 mJ (t = 140 – 145 ns).

As stated before, the increase in n_e is faster close to the electrodes. At t = 17 ns, a maximum of n_e (2×10^{16} cm^{-3}) is reached at the cathode. After this moment, the discharge emission drops and the decay of n_e cannot be measured. At t ~ 69 ns, the 2nd pulse reaches the electrodes, and the H_α emission is visible again. During the period between the 1st and 2nd pulses, we measure a decrease of 50% in the electron

[1] Eq 2.10 is applicable for homogeneous plasmas. For a better characterization, the inhomogeneity of the plasma (e.g. the cathode and anode sheaths) must be considered. Also, at such ionization fractions, electron-ion collisions should be considered (Orriere, Moreau and Pai, 2018).

number density. Then n_e rises during the 2nd pulse in the same manner as the 1st: faster close to the electrodes. The same scenario repeats during the 3rd and the 4th pulse.

Approximately 1.7 mJ are spent for the initial ionization. Then, 0.3 mJ is deposited, which allows for keeping n_e above 10^{15} cm^{-3} during at least 150 ns. Thus, nanosecond discharges can sustain an ionization of 1% at a low power cost. A strategy to efficiently increase the plasma lifetime at such ionization would therefore be to generate additional pulses with an energy ~ 0.2 mJ with a repetition frequency of about 10 MHz.

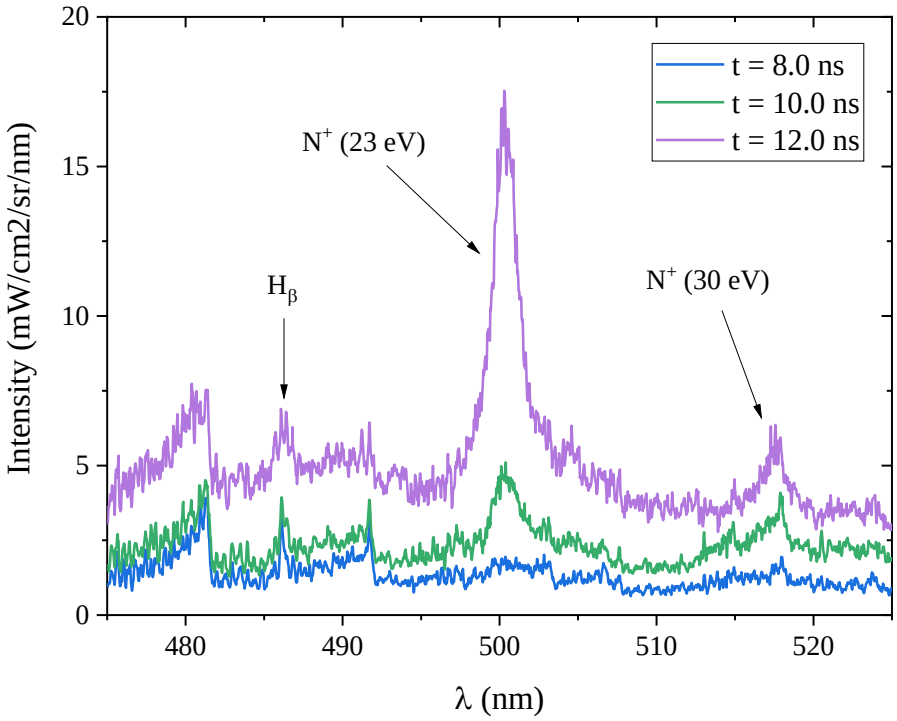

Figure 8.30 Near-cathode emission (z = 4.75 mm) at t = 8, 10, and 12 ns recorded with a 1200-gr/mm grating under the PASTEC conditions (Φ = 0.8, f = 20 kHz, E_{pulse} = 2 mJ).

The increase of n_e is correlated with the appearance at the cathode of the N^+ emission at 500 and 519 nm, shown in Figure 8.30. The N^+ line is visible for t > 10 ns, when the electron number density near the cathode reaches 1.3×10^{16} cm^{-3}. The N^+ line at 567 nm is also detected but not shown here. We note that the H_β emission is also visible at 486 nm. No N^+ line is detected near the anode, which is indeed consistent with the fact that the electron number density measured at this location remains below 1.2×10^{16} cm^{-3} (at t = 17 ns).

8.4.3 Two-Lorentzian fit of H_α

The fitting accuracy being relatively lower near the cathode (z = 0.25 mm), we fitted these data by the sum of two Lorentzians. Both fitting procedures (one or two Lorentzian) are applied to the same dataset in Figure 8.31.

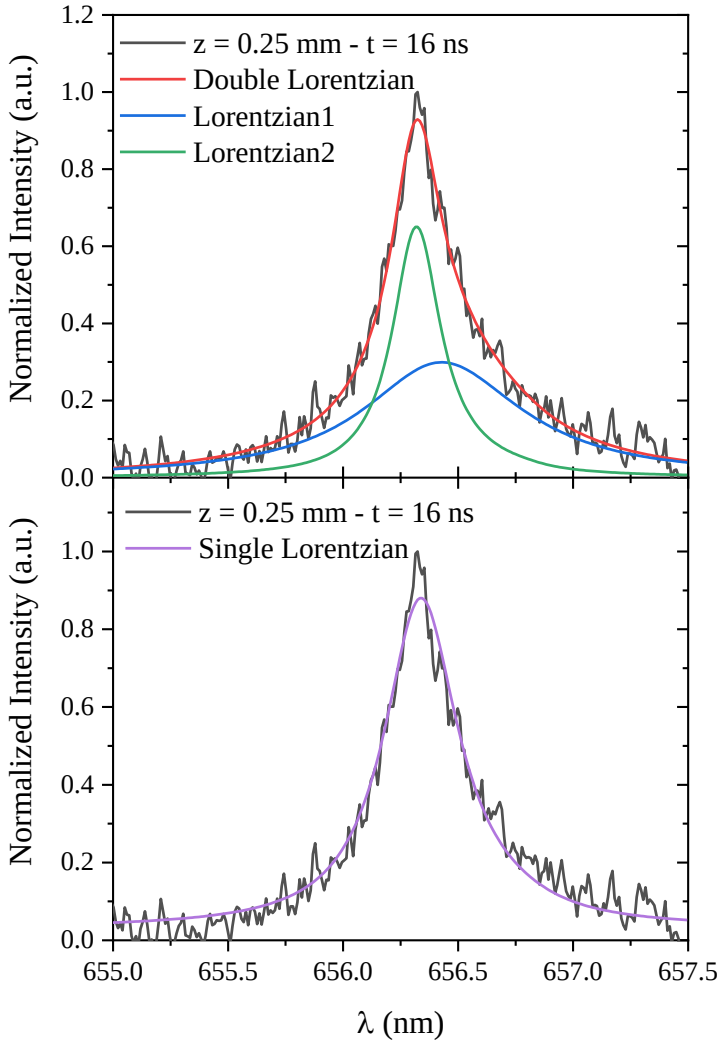

Figure 8.31 Fitting of the H_α line at z = 0.25 mm and t = 15 ns under the PASTEC conditions (Φ = 0.8, f = 20 kHz, E_{pulse} = 2 mJ) with two (top) or one Lorentzian (bottom). A 19% reduction of the residual is obtained with the two-Lorentzian fit.

Two-Lorentzian fitting is typically performed when the electron number density presents fast spatial and temporal variations that cannot be captured by the experimental setup (Sainct, 2014; Sainct *et al.*, 2020). In the present case, this effect is due to the non-repeatability of the filament formation. In Figure 8.32, the total emission of the discharge is reported, and we observe the formation of a filament at the cathode (bottom, z = 0). There is no filament at t = 10 ns, but we clearly see its presence at t = 9, 11, and 12 ns. This instability is not surprising, given that the initial conditions of each spark vary due to the turbulent flow field in this region.

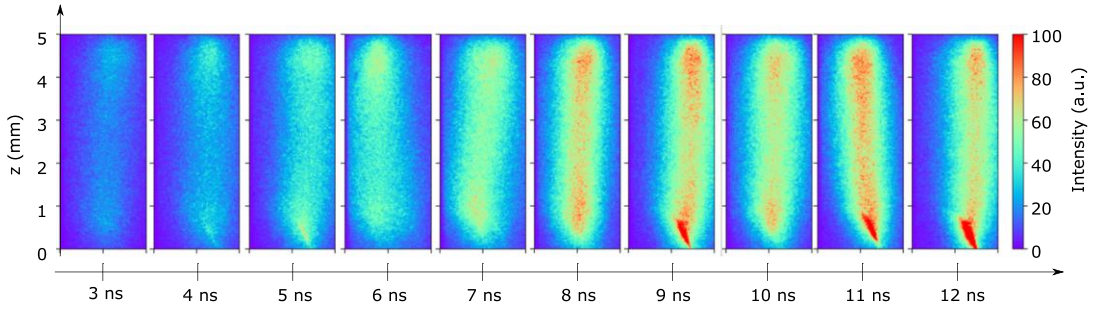

Figure 8.32 Phase-locked single-shot images of the filament formation (the cathode is at the bottom). The total emission is acquired with 2-ns gates under the PASTEC conditions (Φ = 0.8, f = 20 kHz, E_{pulse} = 2 mJ).

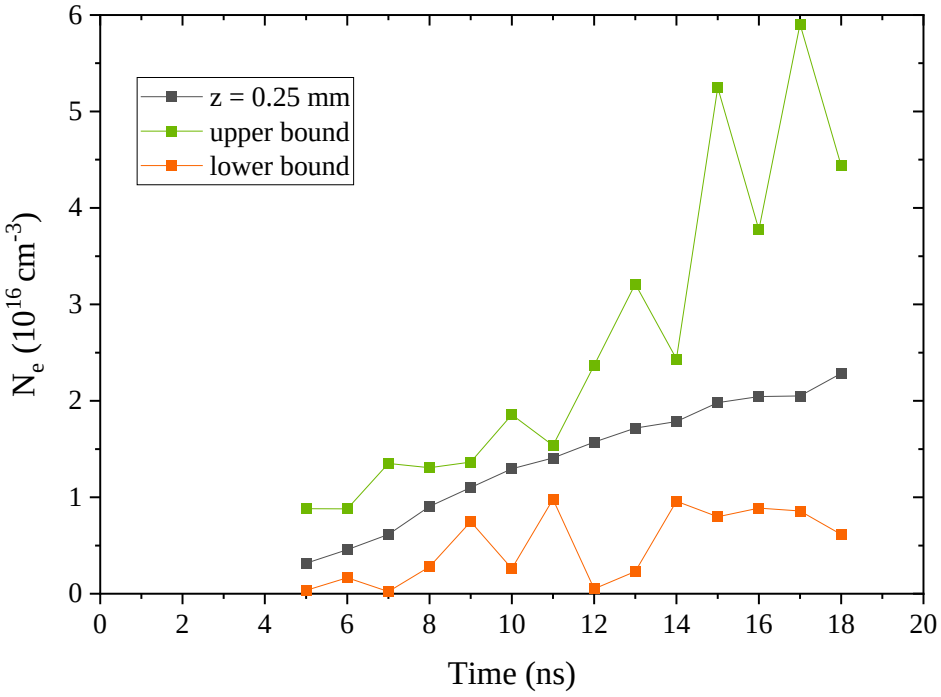

Figure 8.33 Evolution of n_e at the cathode under the PASTEC conditions (Φ = 0.8, f = 20 kHz, E_{pulse} = 2 mJ). The results obtained with a single Lorentzian (in grey) are bracketed by those obtained fitting two Lorentzians to the signal (in green and orange).

The results of the two-Lorentzian fit are shown in Figure 8.33 and compared to the previous results (one-Lorentzian fit). According to this new procedure, the electron number density can be as high as 6×10^{16} cm^{-3}. As shown in Figure 8.33, the fitting of the H_α line by a single Lorentzian provides a measurement of n_e, which is approximately the average of the values obtained with two Lorentzians.

8.4.4 Conclusion on the electron number density

The electron number density was measured in a 2-mJ spark applied at 20 kHz in a CH_4-air flame. At steady-state, the ionization is initially homogeneous in the interelectrode gap $n_e \sim 10^{15}$ cm^{-3}. Then, the

increase of n_e is moderate in the middle of the gap, whereas n_e reaches 10^{16} cm^{-3} at the anode and 2×10^{16} cm^{-3} at the cathode.

In the cathode region, the electron number density increases above 10^{16} cm^{-3} for t > 9 ns, synchronized with the formation of a filament and N^+ lines emission. The H_α line is fitted by two Lorentzians to account for the intermittent nature of the filament formation. The larger component of the fit typically indicates twice higher ionization than the one-Lorentzian fit, reaching a maximum of 5×10^{16} cm^{-3}. The increase of n_e is rather slow, compared to the thermal spark formation described in Part II, which could be due to the number density, below that of ambient air by one order of magnitude. These results also confirm that the NRP discharges used in Mini-PAC are non-thermal sparks.

8.5 Gas temperature

8.5.1 Gas temperature by OES

In this section, the second positive system of N_2 is measured with a 2400-gr/mm grating and an entrance slit of 50 µm (instrumental HWHM of 50 pm). The measurements are also spatially resolved along the interelectrode gap. The N_2(C-B) spectra are fitted with Specair (Laux *et al.*, 2003). The fitting accuracy is demonstrated in Figure 8.34 by comparing the experimental spectrum with the best fit and two other spectra calculated at $T_{rot} = T_{fit} \pm 200$ K. The spectrum presented in Figure 8.34 is performed at z = 4.75 mm (close to the anode), t = 10 ns, and under the PASTEC conditions. The upper bound of the measured temperature is given by the low rotational levels (≈ 337 nm), and the lower bound by the high rotational levels (≈ 330 nm). This difference could be caused by (i) a faster relaxation of the lower rotational numbers (Bruggeman *et al.*, 2014), or (ii) a superposition of two spectra at two different temperatures integrated along the line of sight. In this section, the accuracy in the fitting procedure is, therefore, equal to ± 200 K.

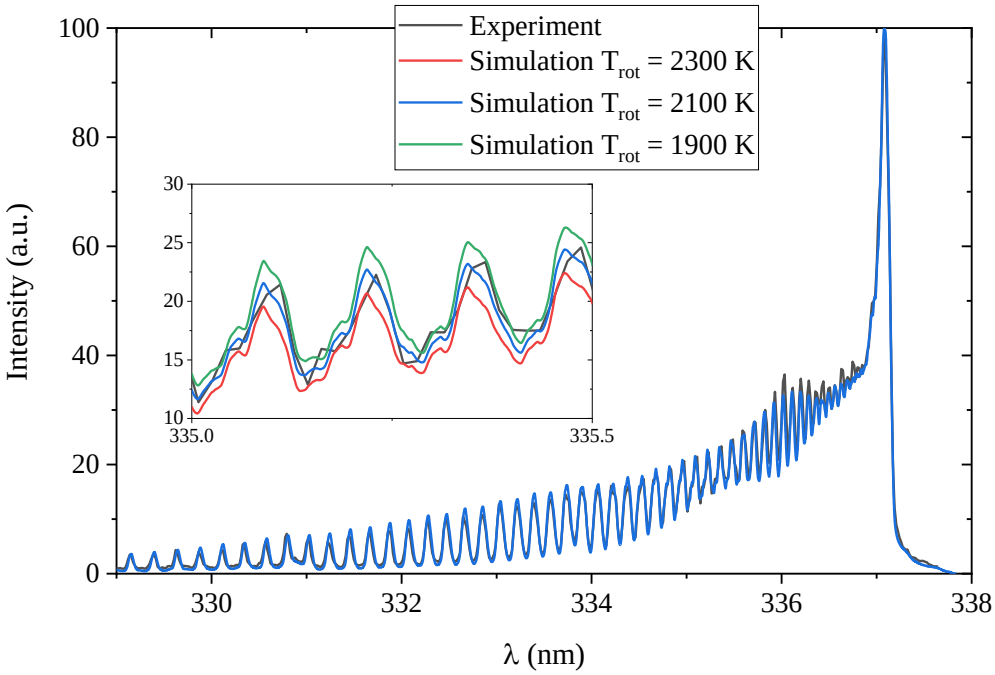

Figure 8.34 Sensitivity of the N_2(C-B) (0-0) spectrum to the rotational temperature. The measurement performed under the PASTEC conditions (Φ = 0.8, f = 20 kHz, E_{pulse} = 2 mJ), z = 4.75 mm, and t = 10 ns, is shown in grey. The best fit, shown in blue, is obtained at T_{rot} = 2100 K.

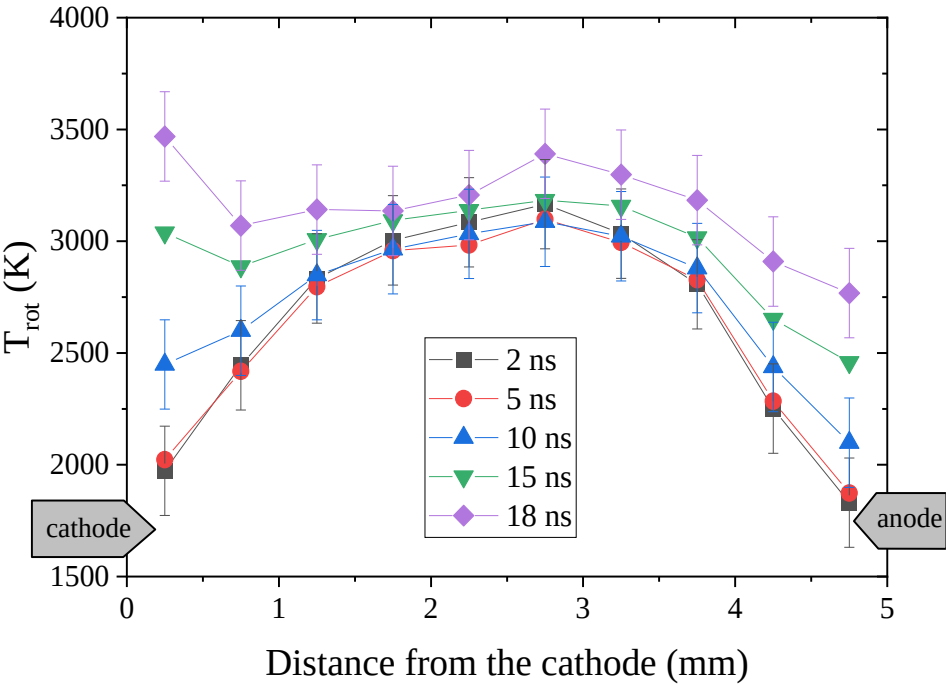

Figure 8.35 Map of the rotational temperature along the interelectrode gap at t = 2, 5, 10, 15, and 18 ns. PASTEC conditions: Φ = 0.8, f = 20 kHz, E_{pulse} = 2 mJ.

The distribution of the rotational temperature along the inter-electrode axis is shown in Figure 8.35 for different delays after the discharge breakdown. During the first nanoseconds, the temperature is maximal in the middle of the interelectrode gap and minimal at the electrodes. From 0 to 18 ns, no noticeable heating is measured in the middle of the gap. However, at the electrodes, for t > 5 ns, the temperature increases from 2000 to 3000 K in 15 ns. Consequently, the temperature becomes more homogeneous at the end of the pulse.

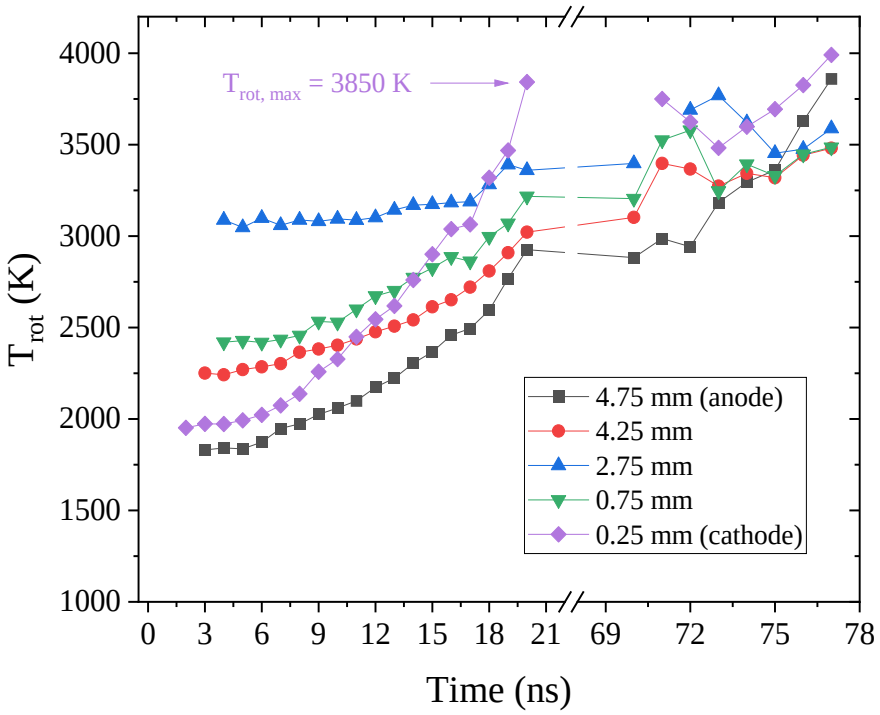

Figure 8.36 Evolution of the rotational temperature along the interelectrode gap. Another temperature measurement is performed at t = 70 – 80 ns with the 2nd pulse. PASTEC conditions: Φ = 0.8, f = 20 kHz, E_{pulse} = 2 mJ.

The evolution of the rotational temperature of $N_2(C)$ is shown in Figure 8.36. The measurements are performed during the 1st (0 – 20 ns) and 2nd pulses (70 – 80 ns). The rotational temperature close to the anode (z = 4.25 mm) increases in 20 nanoseconds from ~ 2200 K to ~ 3000 K. The temperature in the middle of the gap (z = 2.25 mm) increases by less than 300 K. However, the temperature near the cathode (z = 0.25 mm) escalates and reaches 3500 K at t = 18 ns.

In Section 8.4, during the 2nd pulse, the electron number density increased significantly at the electrodes and remained nearly constant in the middle of the gap. A similar situation is encountered with the temperature. During the 2nd pulse, the temperature increases by nearly 800 K near the anode but only by 300 K near the cathode. However, it remains constant at z = 2.25 mm. We note the temperatures measured at $t \approx 70$ ns are equal or slightly higher than the temperature measured at the end of the 1st pulse. Assuming the gas cannot cool in such a short period, this indicates no heating occurred during the 20 –

70 ns interval. During the 3rd and 4th pulses, $N_2(C)$ emission is not intense enough for a reliable interpretation of its spectra and is therefore not presented.

The gas temperature can be deduced from the emission of electronically excited molecules and particularly by the second positive system of nitrogen. For the NRP discharges initiated in the Mini-PAC flame, the $N_2(C)$ state is mostly populated by electron impact excitation of $N_2(X)$. This reaction maps the rotational distribution of $N_2(X)$, which is in equilibrium with the gas temperature at the considered conditions (Popov, 2011b; Rusterholtz *et al.*, 2013). The nascent rotational distribution of $N_2(C)$ is therefore at T_{gas} multiplied by $\theta_C/\theta_X = 1.10$ (Rusterholtz *et al.*, 2013). As described in Section 1.2, T_{rot} will be close to T_{trans} if τ_{RT}, the rotational-translational relaxation time, is fast compared to τ_{eff}, the effective lifetime of $N_2(C)$. For unburnt or burnt CH_4 – air mixtures, we showed in Table 1.3 that $\tau_{eff} \sim \tau_{RT}$. We can therefore consider that T_{trans} is bracketed according to Eq. 8.4.

$$T_{rot}(\mathrm{N_2(C)}) < T_{trans} < \frac{\theta_C}{\theta_X} T_{rot}(\mathrm{N_2(C)}) \qquad \text{Eq. 8.4}$$

The evolution of the gas temperature is shown in Figure 8.37, and compared to 1979 K, the adiabatic flame temperature[1] at $\Phi = 0.8$. Error-bars accounts the fit uncertainty (±200 K) and the +10% uncertainty obtained in Eq. 8.4.

At $t \sim 69$ ns, we observe a further temperature rise due to the 2nd pulse. The applied voltage is above 2 kV in a 5 mm gap, see Figure 8.20. At $T_{gas} \sim 3000$ K and ambient pressure, the estimated reduced field[2] is above 700 Td. At E/N > 120 Td, $N_2(C)$ is primarily populated by electron impact and its emission can still be used for temperature determination (Popov, 2011b). This conclusion holds, even considering 1-kV anode and cathode falls.

[1] Calculation based on Cantera, performed at http://elearning.cerfacs.fr/combustion/tools/adiabaticflametemperature/index.php

[2] This value is obtained by dividing the applied voltage by the interelectrode distance and the total gas density. In this estimation, we neglect the cathode and anode fall.

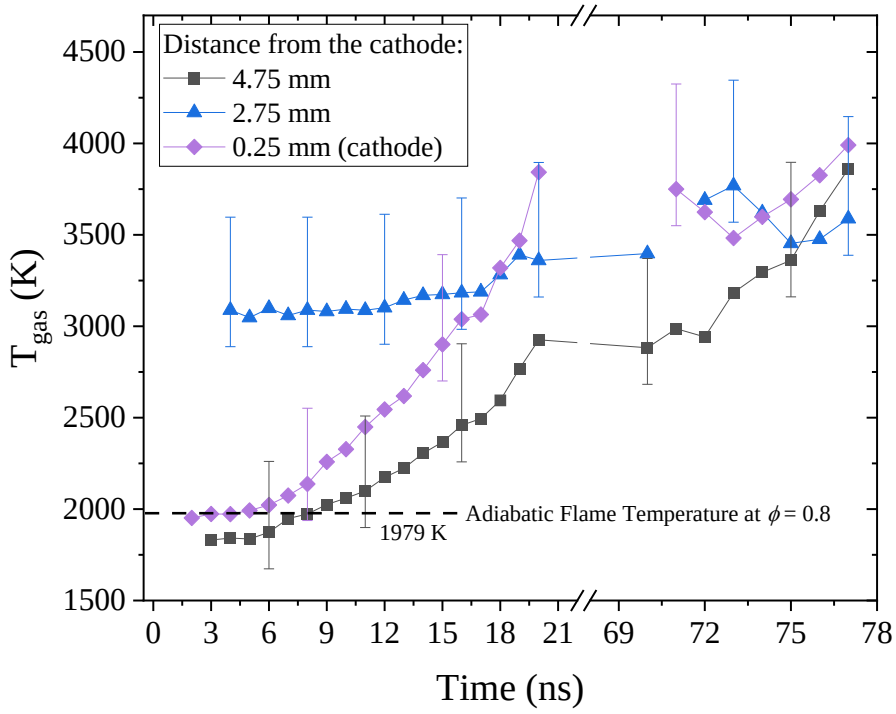

Figure 8.37 Evolution of the gas temperature with time at the cathode (purple), in the middle of the gap (blue), and at the anode (grey). The adiabatic flame temperature at Φ = 0.8 (1979 K) is given for comparison (dashed line). PASTEC conditions: Φ = 0.8, f = 20 kHz, E_{pulse} = 2 mJ.

Using the thermal properties given by the CEA NASA code, we calculate that the energy spent on heating is approximately[1] $c_v/\Delta T \approx 0.9$ mJ, which represents 53% of the energy deposited by the 1st pulse. This result is high compared to previous values (25%) obtained in preheated air (Rusterholtz *et al.*, 2013; Popov, 2016b). Nonetheless, we remark that:

1. The present gas composition is somewhat different from air.
2. The present reduced field, ~500 Td, is higher than that of Rusterholtz *et al.*, ~250 Td. This increase in E/N favors gas heating, as described in (Aleksandrov *et al.*, 2010).

Therefore, a 53% share of energy transferred into heat seems reasonable regarding the two previous arguments.

[1] If we assume a homogeneous cylinder (height: 5 mm, radius: 0.5 mm) heated from 2600 K to 3200 K, the calculation gives 1.0 mJ. We obtain 0.9 mJ after considering the inhomogeneity in the temperature increase.

8.5.2 Near electrode cooling by hydrodynamic effects

The measurements presented in Figure 8.37 demonstrate that, for $t < 4$ ns, the temperature does not rise, and, therefore, is equal to the gas temperature before the discharge onset. Thus, the initial high temperature of 3000 K in the middle of the gap results from the gas heating of previous discharges[1]. Near the electrodes, the temperature at t = 0 – 2 ns is equal to ~ 2000 K, which corresponds to the adiabatic temperature of a lean flame at $\Phi = 0.8$. A similar interpulse cooling was also reported for NRP discharges operated in ambient air, see Figure 72 in (Orriere, 2018). The non-uniform temperature distribution, with lower values of the gas temperature near the electrodes, can be due to:

(i) heat conduction caused by the metallic electrodes in contact with the gas;

(ii) convection caused by hydrodynamic effects (induced by the previous pulses).
We now estimate the phenomenon responsible for this non-uniformity in the temperature.

Characteristic time and volume of cooling by heat conduction can be estimated using $\tau_{cond} = \rho c_p r^2/\lambda$ (p. 199, Raizer, 1991), where ρ is the gas number density, λ the thermal conductivity, and c_p the heat capacity. At $\Phi = 0.8$ and T = 3000 K, we have $\rho = 0.17$ kg·m^{-3}, $\lambda = 0.159$ W·m^{-1}·K^{-1}, and $c_p = 1.6$ kJ·K^{-1}·kg^{-1} (McBride and Gordon, 1992). In 50 µs, corresponding to the period between two consequent pulses, cooling by heat conduction will affect a scale of $r = 170$ µm only. Heat conduction is therefore not responsible for the decay of temperature.

[1] This effect of remnant heat deposited by previous pulses was already observed in preheated air (Rusterholtz *et al.*, 2013).

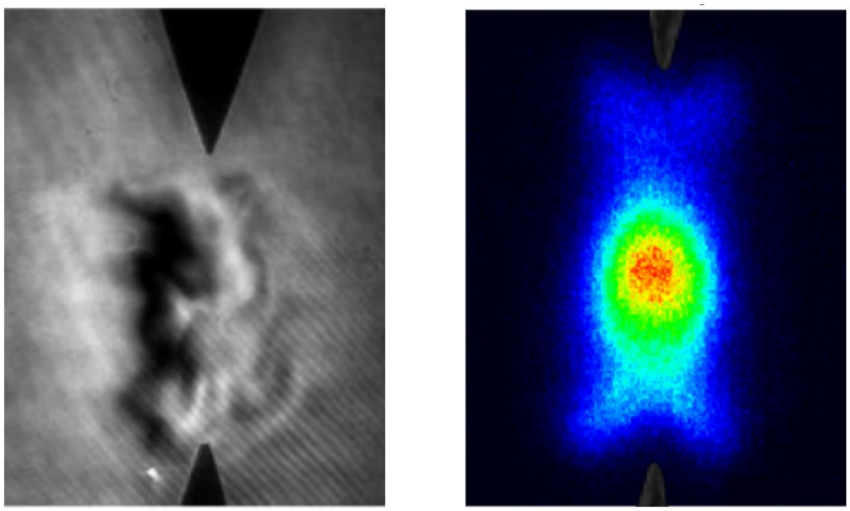

Π = 25 (Dumitrache *et al.* 2019)

Π = 19 (Stepanyan *et al.* 2018)

Figure 8.38 (left) Schlieren experiment taken from Figure 5 in (Dumitrache *et al.*, 2019), Π = 25, t = 32 µs after the spark discharge. (right) OH LIF taken from Figure 6 in (Stepanyan *et al.*, 2019), Π = 19, t = 150 µs after the spark discharge. In both cases, the discharge products are convected to the middle of the gap by entrance of fresh gas along the electrodes.

During the period between two consecutive discharges, the gas hydrodynamic effects following nanosecond discharges can be responsible for the entrance of fresh gas (2000 K) into the near-electrode space. To our knowledge, this phenomenon was first observed in 1952 (Olsen, Edmonson and Gayhart, 1952), with further study in subsequent decades (Albrecht *et al.*, 1977; Kono *et al.*, 1989). The hydrodynamics of nanosecond discharges has recently received particular attention (Castela *et al.*, 2017; Stepanyan *et al.*, 2017, 2019) and baroclinic torque was shown to be responsible for the entrance of fresh gas in the interelectrode gap (Dumitrache *et al.*, 2019). A dimensionless number was introduced in (Dumitrache *et al.*, 2019) to group nanosecond discharges with similar hydrodynamic effects; see Eq. 8.5, where E_{uh} stands for the energy deposited into the fast gas heating, p_0 the initial gas pressure, S the cross-section of the discharge channel, and d the interelectrode gap distance.

$$\Pi_{Tr} = \frac{E_{uh}}{p_0 S d} \qquad \text{Eq. 8.5}$$

In our case, E_{uh} = 0.4 mJ, S = 0.785 mm^2, d = 5 mm, and $p_0 = 10^5$ Pa. We took into account that approximately 50% of the energy deposited in plasma is spent for fast gas heating. We obtain $\Pi \approx 3$. It was shown that for similar Π numbers, fresh gas is introduced near the electrodes and pushes the hot gas to the middle of the gap. This effect is particularly clear in Figure 8.38 where OH PLIF and Schlieren experiments are extracted from previous work (Dumitrache *et al.*, 2019; Stepanyan *et al.*, 2019). In

Figure 8.38, the experiments are performed tens of microseconds after a nanosecond discharge initiated in air[1] with Π = 25 (left, in Figure 8.38) and Π = 19 (right, in Figure 8.38).

The cooling of the near-electrode region is, therefore, due to the hydrodynamic effect following the discharge. The same phenomenon was also reported in air with micrometric gaps (Orriere, 2018). We now examine the origin of the heating during the discharge.

8.5.3 Heating mechanism during the discharge

The two-step mechanism, in Reac. 8.4 and Reac. 8.5, is mainly responsible for the ultrafast gas heating in air (Rusterholtz et al., 2013).

$$N_2(X) + e \rightarrow N_2(B,C) + e \qquad \text{Reac. 8.4}$$

$$N_2(B,C) + O_2 \rightarrow N_2(X) + 2O + \varepsilon_{B,C} \qquad \text{Reac. 8.5}$$

The energy released during ultrafast heating is approximately ε_C = 4.57 eV for the quenching of N_2(C), and ε_B = 0.9 eV for the quenching of N_2(B) (Popov, 2011b). In post-combustion conditions at Φ = 0.8, oxygen represents approximately 4% of the gas mole fraction, see Table 8.3. If oxygen were fully dissociated during the discharge, the temperature increase would reach between 100 K and 600 K (the highest value is reached if all O_2 molecules are dissociated by N_2(C) quenching).

During the pulse, in the middle of the gap, the temperature increases by less than 300 K, possibly due to Reac. 8.4 and Reac. 8.5. However, the temperature increases by 1000 K near the anode and 1500 K near the cathode. A slow thermal spark transition could be associated with the evolution of the temperature close to the electrodes. We recall that the thermal spark is formed in five steps: (i) weak ionization in the interelectrode gap; (ii) formation of a fully ionized filament at the cathode, and (iii) at the anode; then (iv) propagation of the filaments and (v) merge of the filaments. It was shown that the increase of the gas density (or pressure) intensified the transition to a fully ionized plasma (Shcherbanev *et al.*, 2016; Minesi, Stepanyan, *et al.*, 2020). At the breakdown, the gas density is approximately ten times lower than under ambient conditions. The thermalization of the spark is thus less intense than under ambient conditions. Therefore, this increase in temperature at the electrode could be due to a slow filament formation, namely steps (ii) and (iii). It was also shown that the filament formation is faster at the cathode than at the anode (Minesi, Stepanyan, *et al.*, 2020), which is consistent with the present measurements. At $n_e \sim 10^{16}$ cm^{-3} and assuming T_e = 3 eV the electron-ion collision frequency is equal to $\nu_{ei} = 10^{12}$ Hz (see also Section 6.1.2 on the thermal spark formation). Therefore, assuming the dominant

[1] It was shown in (Dumitrache *et al.*, 2019) that the hydrodynamic effects following nanosecond discharges are not particularly sensitive to the gas mixture.

ion to be N_2^+ (or O_2^+), we get an ion-electron thermalization time of τ_{ei} ~ 20 ns, which is consistent with the fast increase of T_{gas} at the cathode.

8.5.4 Conclusions on the gas temperature evolution

In this section, the gas temperature distribution along the interelectrode gap was measured by OES. We showed that the increase of the temperature near the electrode is due to the transfer of energy from electrons to heavy ions through elastic collisions. The moderate temperature increase in the middle of the interelectrode gap is, however, due to dissociative quenching of N_2^*. Between the pulses, fresh gas (2000 K) is introduced near the electrodes by hydrodynamic effects. Thus the near-electrode region is subject to intense temperature variations, whereas the temperature in the middle of the interelectrode gap remains between 3000 and 3500 K.

8.6 Electronic states' number density

In this section, the number density of excited electronic states is measured by calibrated OES. These measurements will be valuable for future comparison against detailed chemistry.

8.6.1 $N_2(B)$ and $N_2(C)$ number density

In the range 0 – 18 ns, under the PASTEC conditions, the emission spectra of $N_2(C)$ and $N_2(B)$ are measured with spatial resolution along the interelectrode gap. Two wavelength ranges are considered, 300 – 420 nm and 550 – 750 nm. For the latter, we use a long-pass filter (λ > 400 nm, Melles Griot 03-FCG-049) to cut the second order of diffraction in the spectrometer. The emission spectra are fitted using Specair (Laux *et al.*, 2003), see Figure 8.39 and Figure 8.40, and provide for $N_2(C)$ and $N_2(B)$:

1. vibrational temperatures,
2. rotational temperatures, and
3. number densities.

The shape of the plasma is approximated by a cylinder of 5-mm height (distance between the electrodes) and 1-mm diameter (Gaussian profile with FWHM of 1 mm). The absolute calibration procedure is detailed in Appendix B.

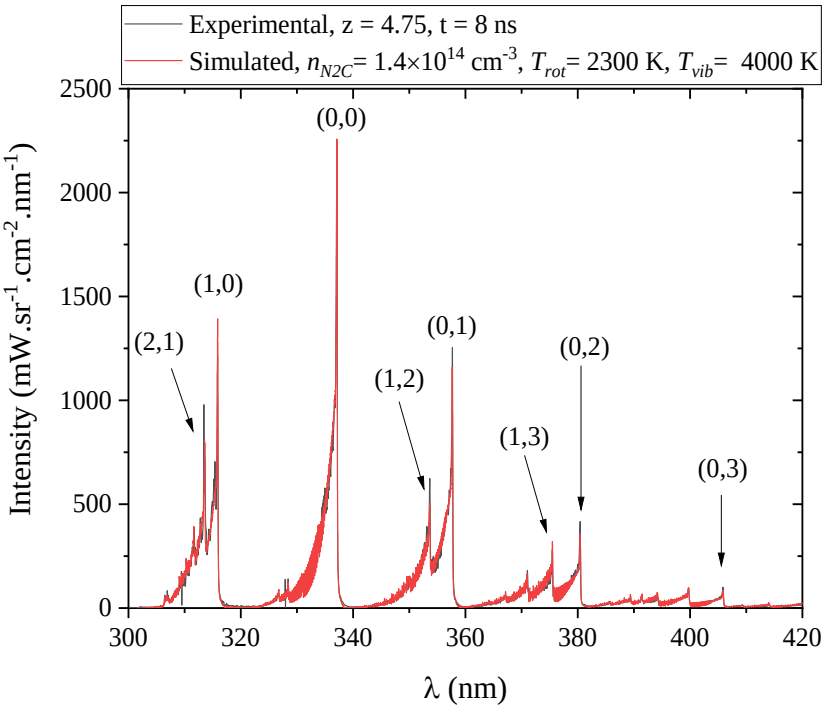

Figure 8.39 Experimental spectrum of N_2(C) (in grey) measured near the anode (z = 4.75 mm), at t = 8 ns under the PASTEC conditions (Φ = 0.8, f = 20 kHz, E_{pulse} = 2 mJ) without optical filter. The spectrum is fitted with a Specair simulation (in red). Vibrational numbers of the upper and lower states are given in brackets.

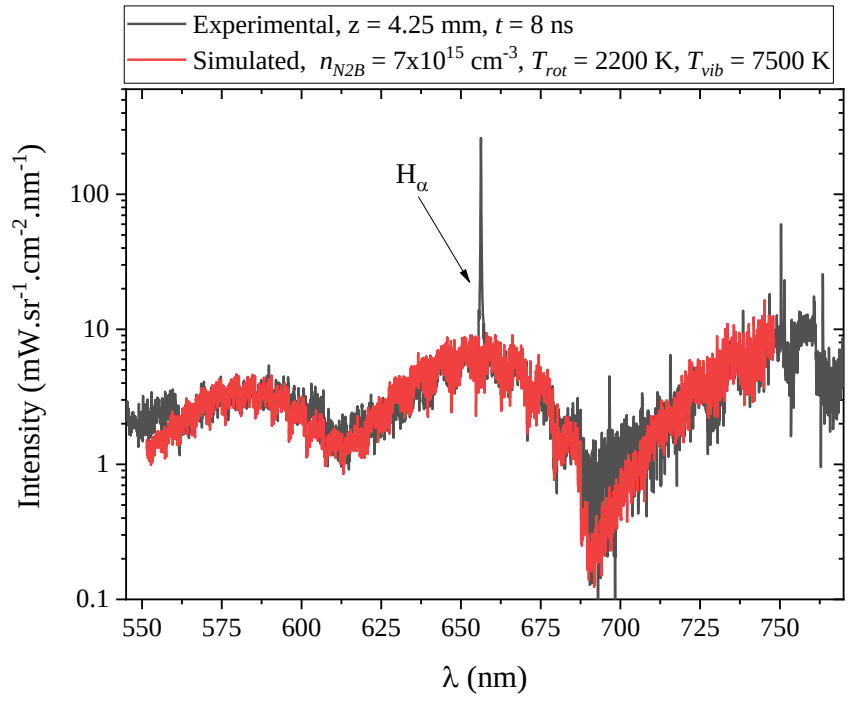

Figure 8.40 Experimental spectrum of N_2(B) (in grey) measured at z = 4.25 mm, at t = 8 ns under the PASTEC conditions (Φ = 0.8, f = 20 kHz, E_{pulse} = 2 mJ). The spectrum is fitted with a Specair simulation (in red). The scale is logarithmic to distinguish H_α and N_2(B) emission. The second order of diffraction is blocked with a long-pass filter (λ > 400 nm, Melles Griot 03-FCG-049)

The spectra presented in Figure 8.39 and Figure 8.40 are obtained with an instrumental HWHM equal to ~ 0.075 nm, which causes a slightly higher inaccuracy in temperature measurements compared to those performed in Section 8.5. The vibrational temperatures of $N_2(B)$ and $N_2(C)$ are found to be constant and homogeneous: $T_{vib}(N_2(B)) = 7500 \pm 1000$ K and $T_{vib}(N_2(C)) = 4000 \pm 500$ K. These results are in agreement with those of (Rusterholtz *et al.*, 2013), although their discharges were applied in different conditions (10 kHz in preheated air and only 0.7 mJ per pulse).

The distribution of $N_2(C)$ number density extracted from calibrated spectra is shown in Figure 8.41 for several instants. At t = 0 ns, the streamer propagation is captured, and the $N_2(C)$ number density is varying from 10^{10} to 10^{11} cm^{-3} between anode and cathode[1]. For $t \geq 2$ ns, the $N_2(C)$ distribution is relatively homogeneous (± 30%) along the discharge channel and increases from 10^{12} to 10^{14} cm^{-3} during the next 8 nanoseconds with the same uniformity.

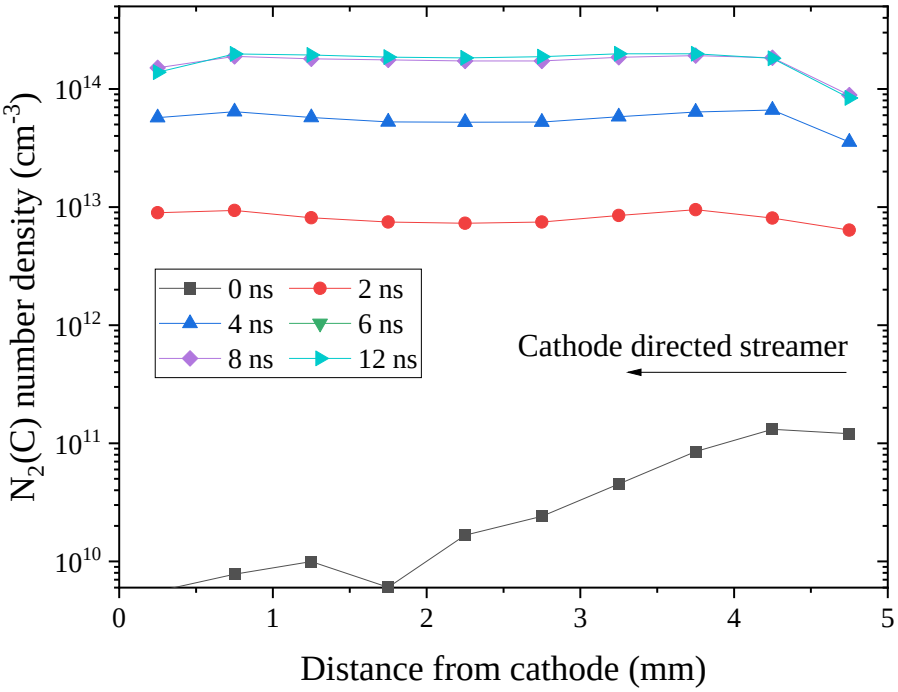

Figure 8.41 Distribution of $N_2(C)$ density along the interelectrode gap at t = 0, 2, 4, 6, 8, 12 ns under the PASTEC conditions (Φ = 0.8, f = 20 kHz, E_{pulse} = 2 mJ). The streamer propagation is shown by a black arrow.

[1] Note that t = 0 ns is the breakdown time, defined in Section 8.3.1, and that the current is already equal to 1 A at this instant.

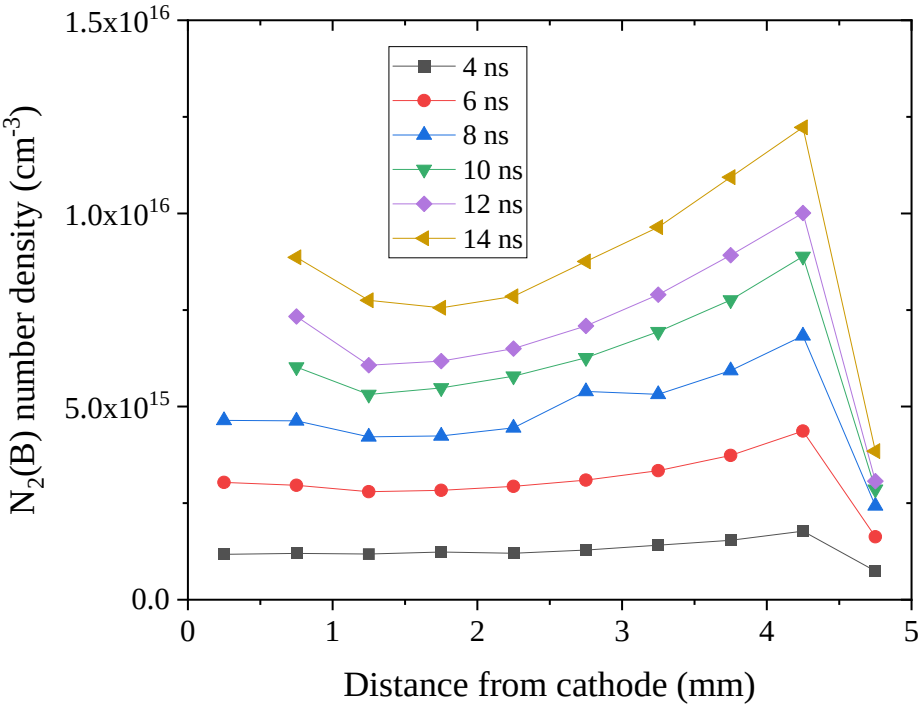

Figure 8.42 Distribution of $N_2(B)$ density along the interelectrode gap at t = 4, 6, 8, 10, 14 ns under the PASTEC conditions (Φ = 0.8, f = 20 kHz, E_{pulse} = 2 mJ).

The distribution of the $N_2(B)$ number density along the discharge channel is given in Figure 8.42 after fitting its emission between 550 nm and 750 nm (see Figure 8.40). The number density of $N_2(B)$ at the anode is almost twice higher than at the cathode. No reason can yet explain this gradient of $N_2(B)$ density. At its maximum, the total $N_2(B)$ number density is equal to 10^{16} cm^{-3}, which represents 0.5% of the total gas number density. The measurements close to the cathode could not be exploited for t > 8 ns due to atomic and continuum emission mixing with the N_2 first positive system, which is particularly clear in Figure 8.43.

We also determined the number density of $N_2^+(B)$ and CN(B) with these measurements (see Figure 8.25 for illustration). The distribution of their number densities up to t = 18 ns is given in the next section.

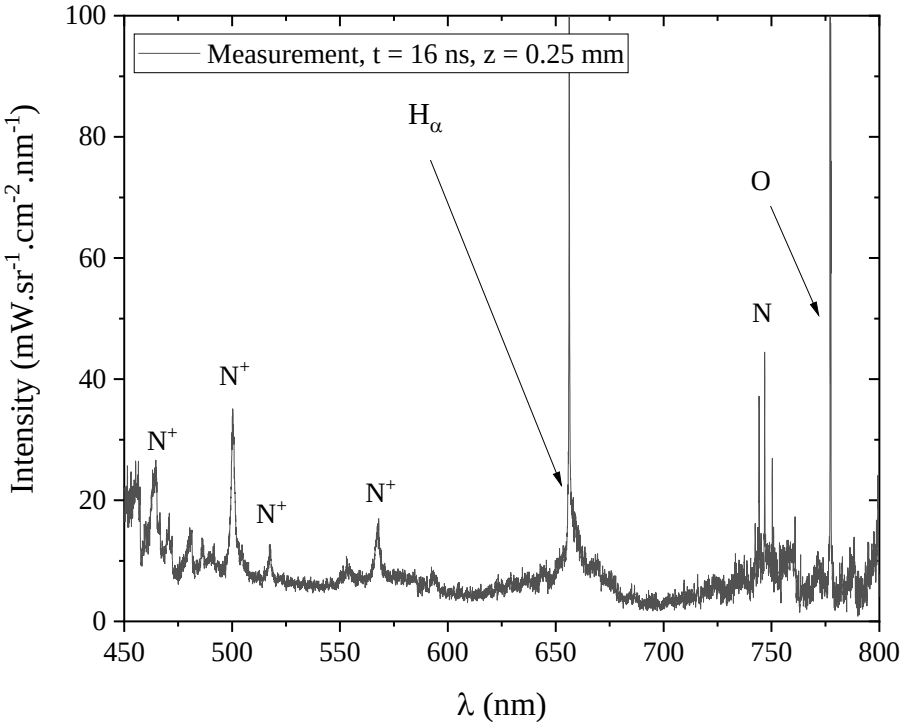

Figure 8.43 Near-cathode emission (z = 0.25 mm) at t = 16 ns under the PASTEC conditions (Φ = 0.8, f = 20 kHz, E_{pulse} = 2 mJ). The N_2(B) spectrum is not visible due to the intense atomic and continuum emission.

8.6.2 CN(B), and N_2^+(B) number density

The number densities of CN(B) and N_2^+(B) also give an insight into the plasma chemistry during and after energy deposition. The determination of the number density of CN, whose spectrum is shown in Figure 8.25, is of primary importance for correct estimation of plasma radiative heat flux on spatial probes in the Titan atmosphere (Walpot *et al.*, 2006). Thus, CN formation has been extensively studied (Magin *et al.*, 2006; Gökçen, 2007; Martin *et al.*, 2010) and the following reactions could significantly contribute to CN radical formation:

$$C + N_2 \rightleftharpoons CN + N \qquad \text{Reac. 8.6}$$

$$CO + N \rightleftharpoons CN + O \qquad \text{Reac. 8.7}$$

According to Reac. 8.7 and Reac. 8.6, the presence of CN is a marker of atomic species formation. The rate coefficient of Reac. 8.7 (Martin *et al.*, 2010) is four times higher than that of Reac. 8.6:

- Reac. 8.6: $k_6 = 5.24\times10^{13}$ cm^3·mol^{-1}·s^{-1}
- Reac. 8.7: $k_7 = 2.41\times10^{14}$ cm^3·mol^{-1}·s^{-1}

However, the N_2 number density is 10 to 100 times higher than CO number density (see equilibrium flame composition in Table 8.3). If we assume that the number densities of N and C are of the same order of magnitude, we can expect both reactions as having the same importance in the CN formation.

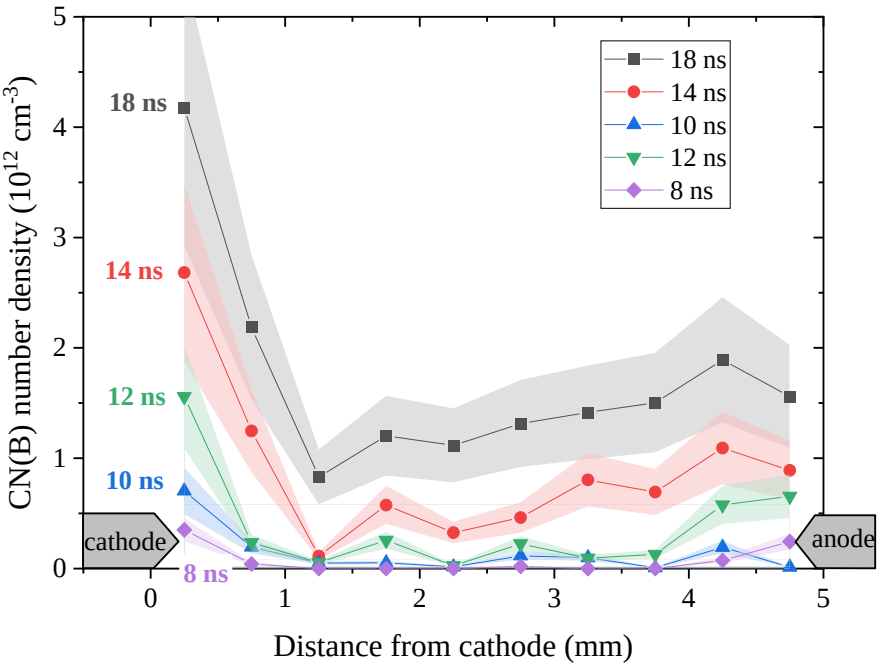

Figure 8.44 Distribution of the CN(B) number density along the interelectrode gap under the PASTEC conditions (Φ = 0.8, f = 20 kHz, E_{pulse} = 2 mJ).

In Figure 8.44, the evolution of the CN(B) number density distribution along the interelectrode gap is shown. By the end of the pulse, the CN number density increases in the entire gap. The effect is most pronounced at the cathode, probably due to a higher number density of N during the filament formation. For future work, confirmation of this CN formation mechanism, based on studies in N_2/CH_4 mixtures, deserves to be further analyzed in the case of NRP discharges applied to $N_2/H_2O/CO_2$ mixtures.

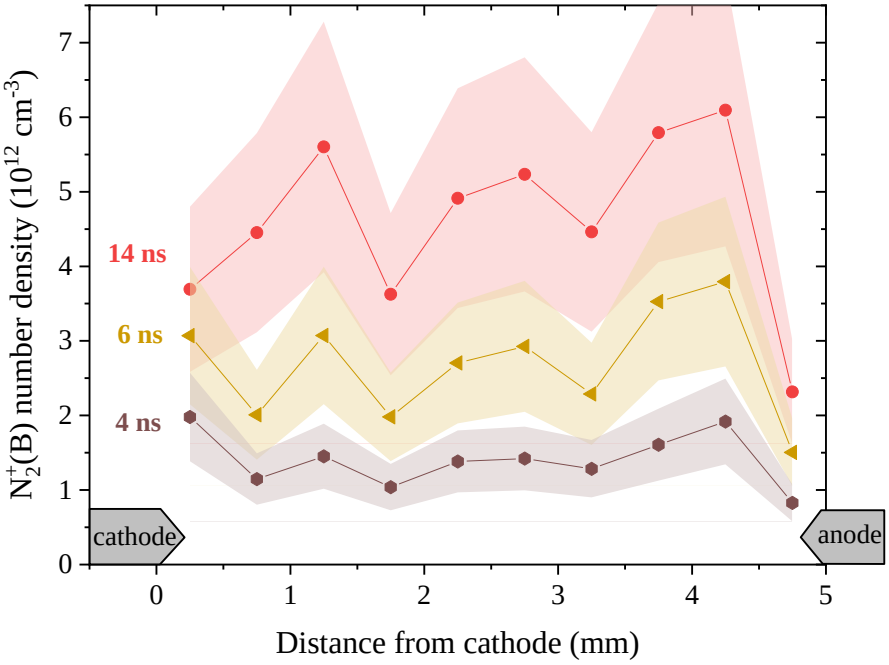

Figure 8.45 Distribution of the N_2^+(B) number density along the interelectrode gap under the PASTEC conditions (Φ = 0.8, f = 20 kHz, E_{pulse} = 2 mJ).

The N_2^+(B) number density is shown in Figure 8.45 and is of the same order of magnitude as CN. The ratio of N_2(C) and N_2^+(B) intensities can be used for reduced field[1] determination in air, as detailed by (Paris *et al.*, 2005). However, the coefficients of Paris *et al.* were determined in synthetic air. To apply this method in the PASTEC conditions, precise knowledge of the N_2(C) and N_2^+(B) quenching rate coefficients is necessary. Therefore, it cannot be applied in this study with current knowledge of the plasma composition and quenching rate dependence with temperature. However, the N_2(C) and N_2^+(B) number densities are both homogeneous along the interelectrode gap. Therefore, the electric field is also expected to be homogeneous.

8.6.3 NH(A) and OH(A) number density – second set for N_2(B) and N_2(C)

The number densities of N_2(C) and N_2(B) were obtained in Section 8.6.1, with a relative error of 30%, including the statistical fluctuation and the error of the fitting procedure. Other sources of error are systematic and challenging to estimate. We list, as potential sources:

[1] These findings were challenged by (Pancheshnyi, 2006), who argued that the three-body quenching of N_2^+ should be taken into account. It was later demonstrated by Paris *et al.* that the relation they determined in 2005 was correct (Paris *et al.*, 2006).

1. Misalignment in the calibration train (e.g. calibration lamp slightly off-focus or not perpendicular to the optical axis)
2. Internal reflections in the spectrometers, also called straylight
3. Variation of the delivered energy by the pulser (typically $<E_{pulse}> = 2.0 \pm 0.1$ mJ)

A second experiment was performed, which resolved items i and iii. The new data were acquired with different filters, which reduced the straylight in the spectrometer (item ii). The measurements were also extended to t = 42 ns, for N_2(C), and t = 35 ns for N_2(B). Moreover, these new data include OH(A) and NH(A) emission and are used to determine their number densities.

Spectral measurements of the plasma radiation are performed on the 300 – 370 nm range. A bandpass filter in the 250 – 400 nm range (Melles Griot – 03 FCG 177) is used to minimize the effect of internal reflections in the spectrometer during calibration. A typical fit of OH(A), N_2(C), and NH(A) is given in Figure 8.46.

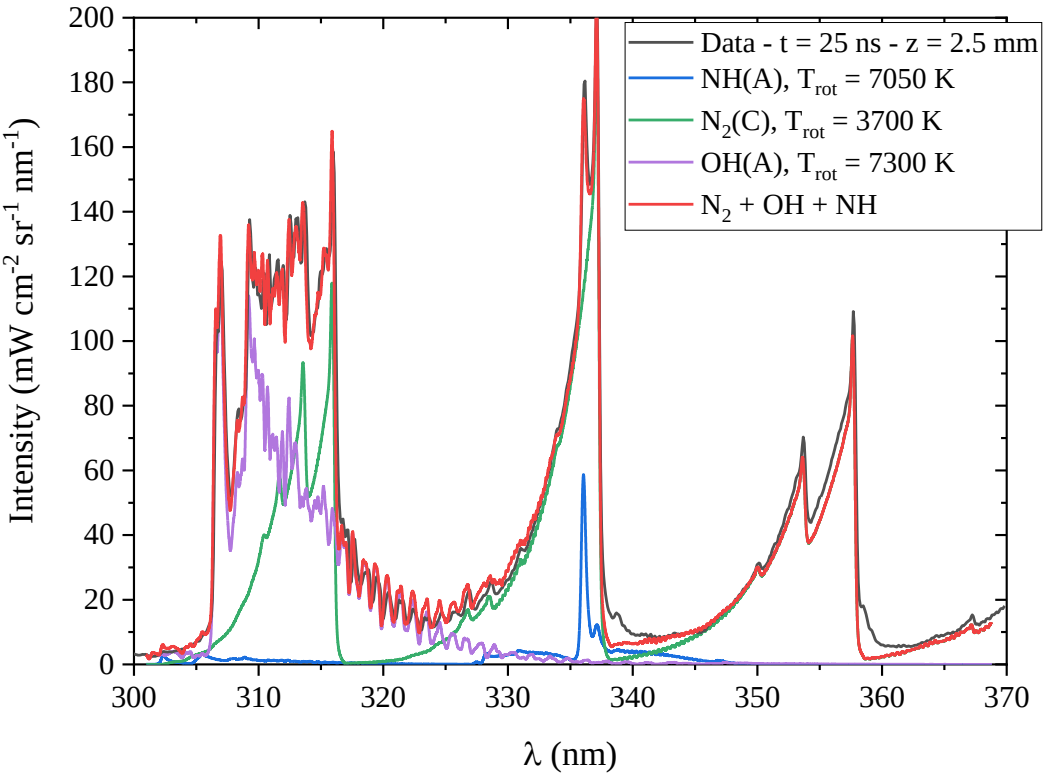

Figure 8.46 Typical fit of OH(A), N_2(C), and NH(A) emission between 300 and 370 nm. The data are acquired under the PASTEC conditions (Φ = 0.8, f = 20 kHz, E_{pulse} = 2 mJ), t = 25 ns, and the emission is spatially averaged between z = 2.5 ± 0.5 mm (middle of the gap). The vibrational temperature of the synthetic spectra simulated with Specair is T_{vib} = 3950 K. The slight disagreement (below 5%) between 350 and 360 nm could be due to N_2^+(B) emission.

The fitting is performed according to a sequential procedure:

- The rotational temperature of $N_2(C)$ is fitted on the normalized spectrum in the 355 – 360 nm wavelength range.
- The vibrational temperature of $N_2(C)$ is fitted on the normalized spectrum in the 340 – 360 nm wavelength range.
- The NH(A) relative intensity compared to $N_2(C)$ is fitted on the normalized spectrum using 320 – 360 nm wavelength range.
- The OH(A) relative intensity compared to $N_2(C)$ is fitted on the normalized spectrum using full wavelength range.
- An optimization algorithm[1] further reduces the L2 distance between the normalized experimental spectrum and the synthetic spectrum, using the previous results as an initial guess. The fitting provides relative densities (OH/N_2 and NH/N_2), rotational temperatures ($T_{rot\_N2(C)}$, $T_{rot\_OH(A)}$, and $T_{rot\_NH(A)}$) and the vibrational[2] temperature of the spectrum content. This step is the longest, given that six parameters are minimized.
- Finally, the number densities of $N_2(C)$, OH(A), and NH(A) are obtained by rescaling the synthetic spectrum to the calibrated experimental spectrum.

The previous algorithm is applied to all spectra acquired from t = 0 ns to 42 ns. A spatial binning of 1 mm is used in this case (in Section 8.6.1, we used a spatial binning of 500 µm). We find that T_{rot}(OH) ranges between 6000 and 8000 K and that T_{rot}(NH) ranges between 2000 and 9000 K. The vibrational temperature of the system is constant around T_{vib} = 4000 ± 500 K. These temperature measurements are, however, approximative given the fairly large instrumental broadening.

[1] We used the *Powell* method of the *scipy.minimize* Python package.

[2] We assumed the vibrational temperature of all species to be equal, because only $N_2(C)$ is sensitive to this parameter in the 300 – 370 nm wavelength range.

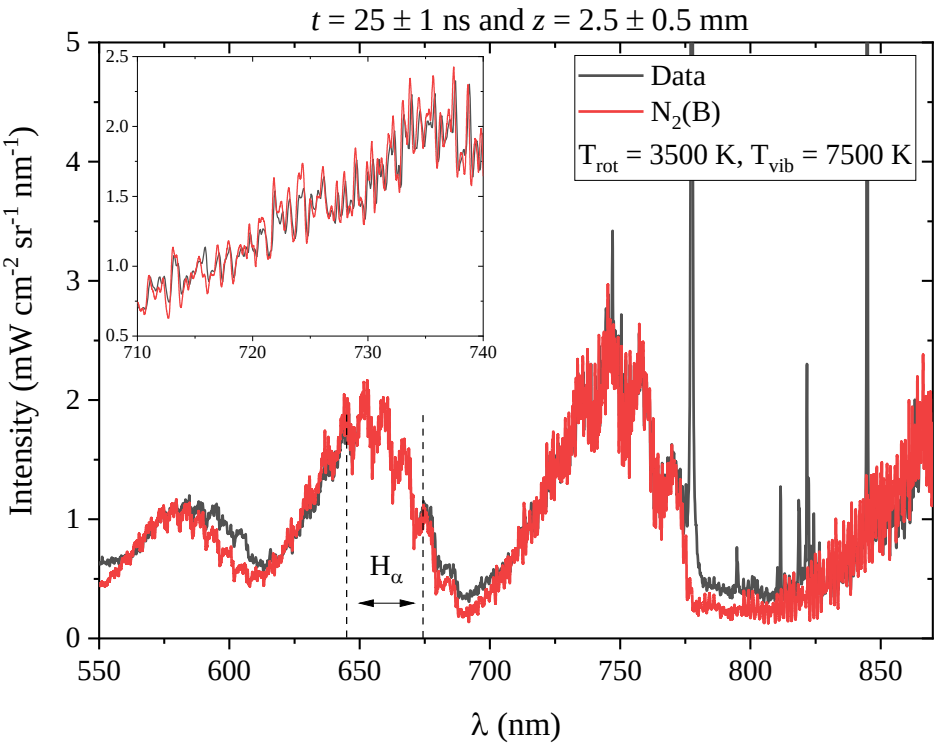

Figure 8.47 $N_2(B)$ emission at t = 25 ns and in the middle of the interelectrode gap under the PASTEC conditions (Φ = 0.8, f = 20 kHz, E_{pulse} = 2 mJ). The synthetic spectrum is generated with Specair at T_{rot} = 3500 K and T_{vib} = 7500 K. No experimental data are acquired in the range 640 – 660 nm range to avoid CCD saturation by the H_α line.

Another set of experiments was also performed to acquire the $N_2(B)$ spectrum. This time, a 550-nm long-pass filter is used (Melles Griot – OG550 – 03 FCG 087). The emission of $N_2(B)$ is fitted according to a simpler procedure. The normalized emission is compared[1] to synthetic spectra of $N_2(B)$, varying T_{rot} and T_{vib}. Then, the number density of $N_2(B)$ is obtained after rescaling the best fit to the calibrated data. As in Section 8.6.1, for t > 10 ns and at the cathode, the continuum and atomic emission cannot be neglected. We therefore discarded these spectra. A typical example of an $N_2(B)$ spectrum fitted with a Specair simulation is shown in Figure 8.47. The emission is recorded from 550 to 870 nm, except at λ = 645 – 675 nm, due to the intensity of the H_α line. The atomic emission in the range 750 – 870 nm is not fitted.

[1] The procedure is accelerated using a database of precalculated spectra using the *RADIS* Python package (Pannier and Laux, 2019) freely available at https://github.com/radis/radis. We stored $N_2(B)$ emission spectra calculated with T_{rot} = 2000, 2250, 2500 … 4250 K and with T_{vib} = 6000, 6500, … 9000 K. The accuracy of the fitting is therefore equal to ±250 K for T_{rot}, and ±500 K for T_{vib}.

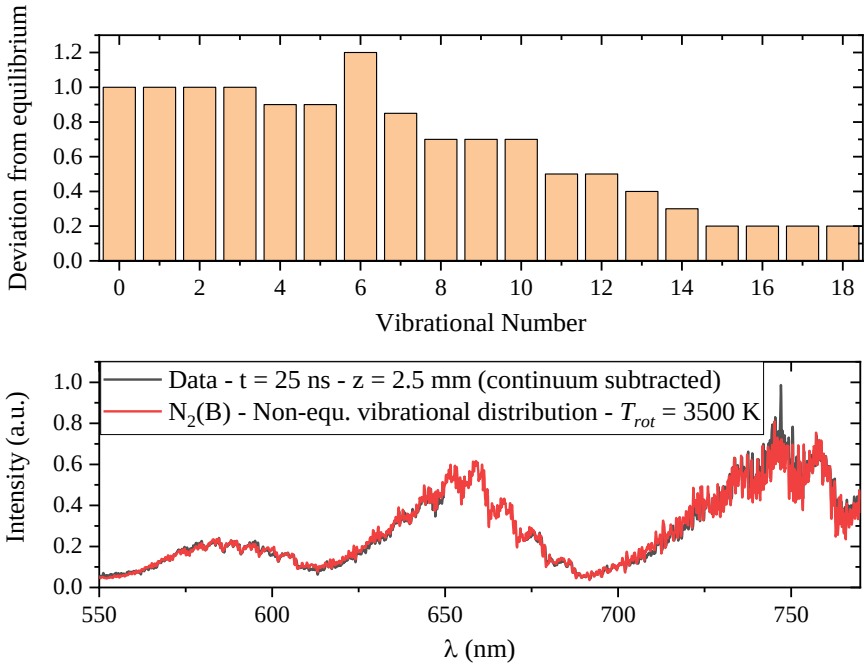

Figure 8.48 (bottom) Spectra of Figure 8.47. A continuum emission (assumed linear) is subtracted from the data and a non-equilibrium vibrational distribution is assumed in the calculation. (top) Deviation of the vibrational populations compared to a Boltzmann distribution at 7500 K.

The slight disagreement near λ = 600 nm and λ = 690 nm can be resolved with a continuum subtraction (less then 0.1 $mW \cdot cm^{-2} \cdot sr^{-1} \cdot nm^{-1}$ at 550 nm) and a non-equilibrium distribution of $N_2(B)$ vibrational levels. Non-equilibrium fitting is performed in Figure 8.48 (same data as in Figure 8.47). The fitting in Figure 8.48 left unchanged the lower vibrational numbers, which are the more populated states. Therefore, the deviation from vibrational equilibrium and the continuum subtraction has a minor impact on the measurement of $N_2(B)$ number density.

To conclude on the accuracy of our measurements, we compare in Figure 8.49 the evolution of $N_2(B)$ and $N_2(C)$ number densities according to the spectra presented in Section 8.6.1 and the present section. The number densities of $N_2(B)$ agree within 30%, which is the expected repeatability of calibrated OES. The number densities of $N_2(C)$ agree remarkably well.

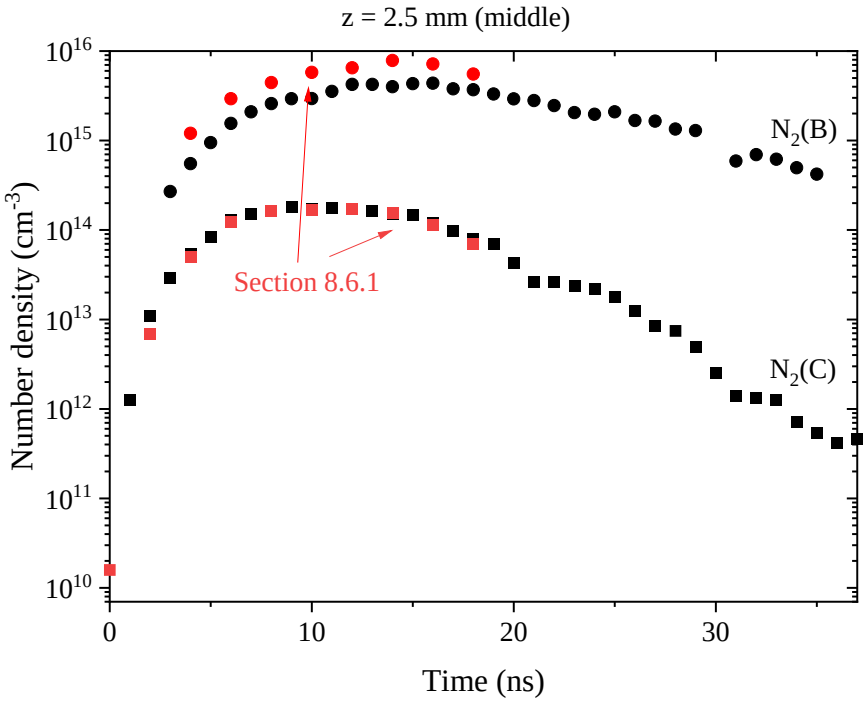

Figure 8.49 Comparison of the number density measurements in the PASTEC conditions (Φ = 0.8, f = 20 kHz, E_{pulse} = 2 mJ) obtained after two calibrated OES experiments.

8.6.4 Conclusion on the excited states' number density

In Figure 8.50, the number densities of N_2(B), N_2(C), OH(A), NH(A), N_2^+(B), and CN(B) are given near the edges of the discharge and in its middle. The electron number density is added for comparison purposes. The densities range from 10^{11} to 10^{16} cm^{-3}. As expected, the densities increase during the energy deposition (0 – 10 ns), flatten, and then decay. These data are essential for the validation of detailed plasma chemistry in a CH_4 – air flame and could extend our observations on:

- the role of atomic species in the CN formation, near the cathode
- the role of N_2(B, C) dissociative quenching by O_2 in the heating, in the middle of the discharge
- the production of OH(A) which is essential for flame chemistry.

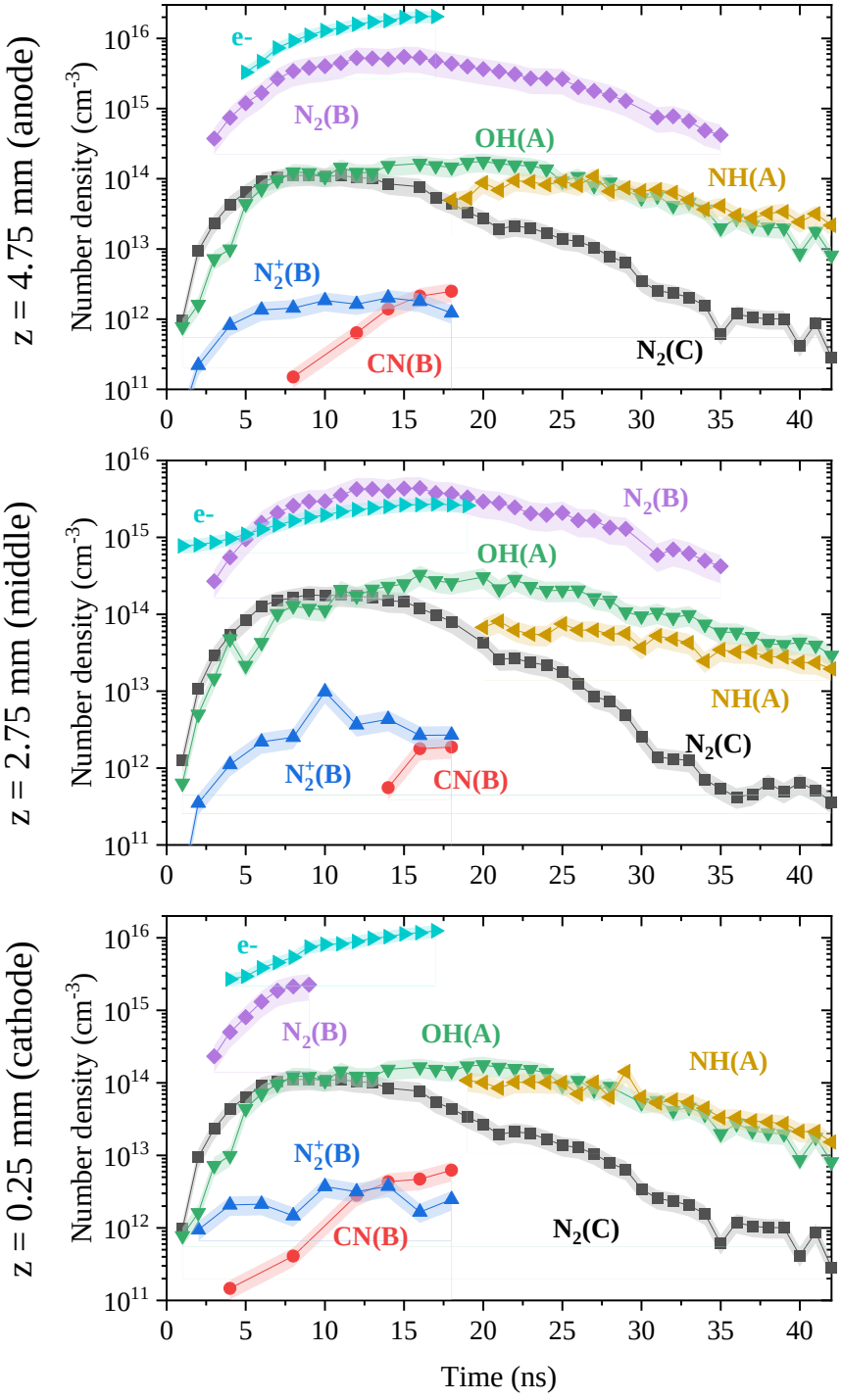

Figure 8.50 Evolution of the $N_2(B)$, $N_2(C)$, OH(A), NH(A), $N_2^+(B)$, and CN(B) number densities under the PASTEC conditions (Φ = 0.8, f = 20 kHz, E_{pulse} = 2 mJ). The results are displayed at three locations: near the anode at z = 4.75 mm (top), in the center of the interelectrode gap at z = 2.75 mm (middle), and near the cathode at z = 0.25 mm (bottom). For comparison, we also include the evolution of the electron number density in cyan.

8.7 Conclusions of the Mini-PAC experiment

NRP spark discharges of 2 mJ were initiated at 20 kHz in the recirculation zone of a CH_4 premixed turbulent flame at $\Phi = 0.8$. Within the transition from a non-assisted to a plasma-assisted flame, OH* and CH* chemiluminescence measurements showed that the NRP discharges have an impact on the flame topology after ~ 1 ms (~ 20 pulses). The chemiluminescence of the plasma-assisted flame reaches a steady-state after approximately 200 pulses.

We measured by Laser-Induced Fluorescence that the OH density increases by a factor of three between the non-assisted and the plasma-assisted flame. The NRP discharges also have an impact on the flame width. This increase of the flame width marks the arrival of the discharge benefits (creation of excited species and increase of the temperature) at the bluff-body boundaries. This increase of OH number density can be due to an increase of the flame temperature, which is indirectly due to the discharge, or the transport of OH radicals directly produced in the discharge.

We showed that the plasma is non-thermal, although the cathode region is close to a thermal regime. Indeed, the electron number density reaches 10^{16} cm^{-3} in the cathode filament, which corresponds to a 1% ionization. Also, the CN number density is remarkably high near the cathode, which is usually related to atomic species formation.

The hydrodynamic effects generated by the nanosecond sparks induce a fast cooling of the near-electrode regions during the interpulse. At $t = 0$ ns, the near-electrode temperature is found to be 2000 – 2500 K, due to the entrance of fresh (2000 K) gas during the interpulse. At the cathode, the temperature increases up to 3500 K, which is due to the thermal spark formation, i.e. heating of the ions by electron impact. The temperature rise in the middle of the interelectrode gap is comparatively lower, from 3000 K to 3500 K in 10 ns. In these conditions, N_2 excited states are likely responsible for the heating through dissociative quenching by O_2. We calculated that 0.9 mJ is spent in the temperature increase during the first pulse. This value represents 53% of the deposited energy. This value is high compared to previous results obtained in preheated air (Rusterholtz *et al.*, 2013; Popov, 2016b). However, this is not surprising, given that the present gas composition and reduced fields are somewhat different from the case of Rusterholtz *et al.* (Aleksandrov *et al.*, 2010).

Chapter 9

The SICCA-spray configuration

In this Chapter, NRP discharges are used to extend the LBO limit of lean swirling flames. Three fuels are considered: premixed methane-air, liquid heptane, and liquid dodecane. The fuel flow rate is kept constant and the flame power is always close to 5 kW. Heptane (C_7H_{16}) is representative of commercial diesel (Foucher *et al.*, 2013), while dodecane is a heavy fuel ($C_{12}H_{26}$) representative of kerosene in aero-engine applications.

In Section 9.1, the experimental setup of the SICCA burner and the NRP discharges is presented. Then, in Section 9.2, the NRP discharges are characterized by OES and found to be non-thermal sparks. Finally, the lean blow-out with methane-air, liquid heptane, and liquid dodecane is measured in Section 9.3. The unsteady behavior of these flames presents periodic oscillations before extinction. Special attention is given to the electrode position in the burner. Finally, the NRP discharges are applied in a burst mode to reduce the plasma power further.

Most of these results are published in (Vignat *et al.*, 2020), apart from those presented in Section 9.3.3.

9.1 SICCA-spray burner

9.1.1 Experimental setup

In most practical systems, the lean blow-out (LBO) limit can be extended by applying NRP discharges, when it is usually dictated by the burner configuration (swirl or bluff-body). The high-voltage electrode is generally located on the centerline of the burner, close to the injector outlet, inside the gas recirculation zone where the flow is relatively slow, see Chapter 8 or (Lacoste *et al.*, 2013; Barbosa *et al.*, 2015). In practical applications, specifically in aero engines, positioning the electrode on the injector centerline may not be practical. The solid electrode will perturb the flow, induce drag, create additional flame anchoring points, and can also get degraded by the resulting heat fluxes. Moreover, liquid fuel atomizers are commonly located on the centerline to ensure a homogeneous spray distribution, and the discharge might form between the electrode and the atomizer head. To avoid damaging this sensitive component, the electrode is placed in the present study close to the side wall and the combustor dome (also called chamber backplane) in the Outer Recirculation Zone (ORZ). Thus, the NRP discharges will occur in hot and burnt gas, which will mix with the fresh unburnt gas.

Experiments are carried out in the SICCA-Spray combustor, see Figure 9.1. The system consists of an air plenum, followed by a swirling injection system (grey area) comprising a tangential channel swirler that leads to a convergent section with a final radius r_{inj} = 4 mm and a conical section of 6 mm. This injector provides a measured swirl number of 0.68. When the system operates in the premixed mode, methane is injected in the air supply 3 m upstream of the plenum to ensure complete mixing. A compact flame is stabilized downstream of the dump plane inside a transparent quartz confinement tube. Two photomultipliers and a high-speed camera mounted with a CH* filter monitor the flame emission.

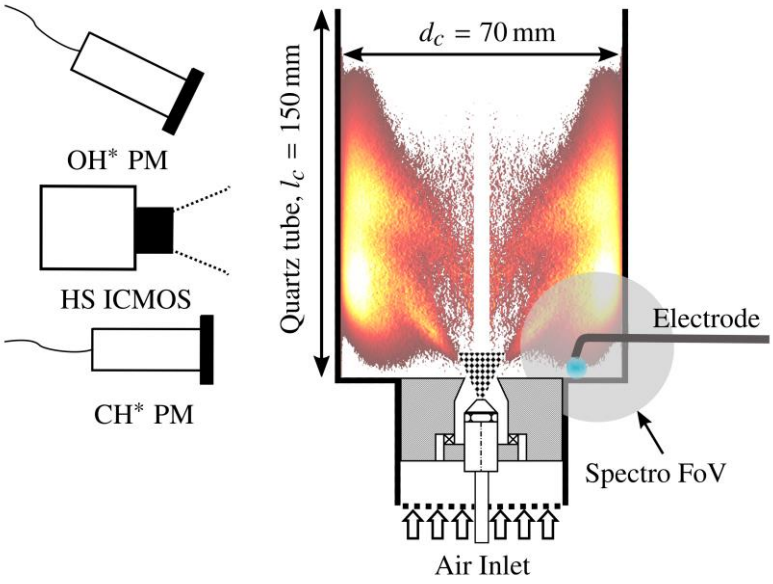

Figure 9.1 SICCA facility with an electrode mounted in the quartz tube. A grey circle represents the Field of View (FoV) of the spectral analysis. An Abel inverted image (see Figure 9.6) obtained at an equivalence ratio Φ = 0.63 is shown in the background. The discharge dimension is to scale with the flame image.

NRP discharges are created between the tip of an Inconel electrode and the combustor backplane. The electrode tip is located 5 mm above the backplane and 24 mm from the centerline of the combustor (see Figure 9.1 and Figure 9.2).

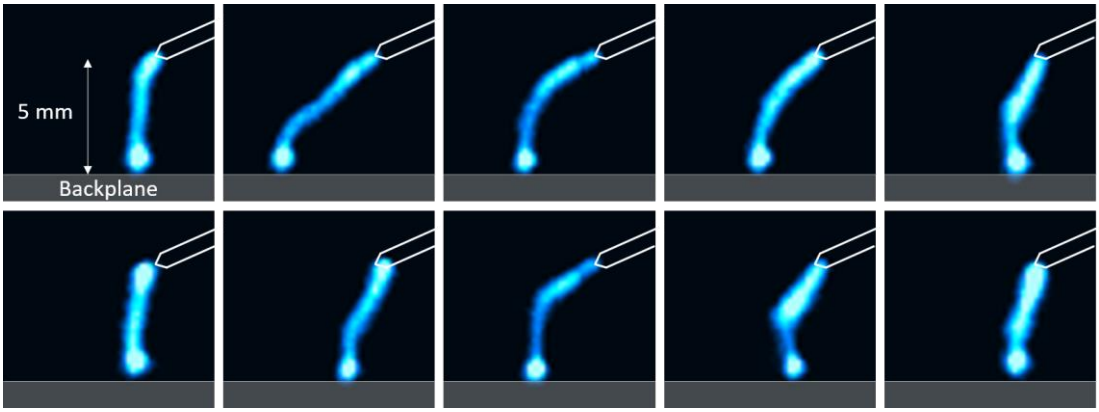

Figure 9.2 Single-shot images of the discharges (false colors). The position of the discharge, between the electrode (anode) and the combustor backplane (grounded), varies due to the turbulent flow in the ORZ.

9.1.2 Deposited energy

A 6-meter long coaxial cable (75 Ω impedance) connects the generator (pulser #4) and the electrode. Two current and voltage probes are placed midway on the cable and are used to monitor the deposited energy. Typical voltage, current and energy curves are shown in Figure 9.3. The voltage is adjusted for every configuration so that the deposited energy remains constant at 5 ± 0.25 mJ, corresponding at 20 kHz to an average electrical power of 100 W. The incident energy of the initial pulse (between 0 and 20 ns) carries 5 mJ ± 0.25 mJ, which is deposited in three pulses of 3.7 mJ, 0.8 mJ and 0.4 mJ, respectively. Another pulse, not shown in Figure 9.3, deposits 0.1 mJ at t ~ 250 ns. This discharge is more energetic than the one used in Section 8.3, where only 2 mJ was deposited, but we note that 100% of the incident energy was deposited in the plasma.

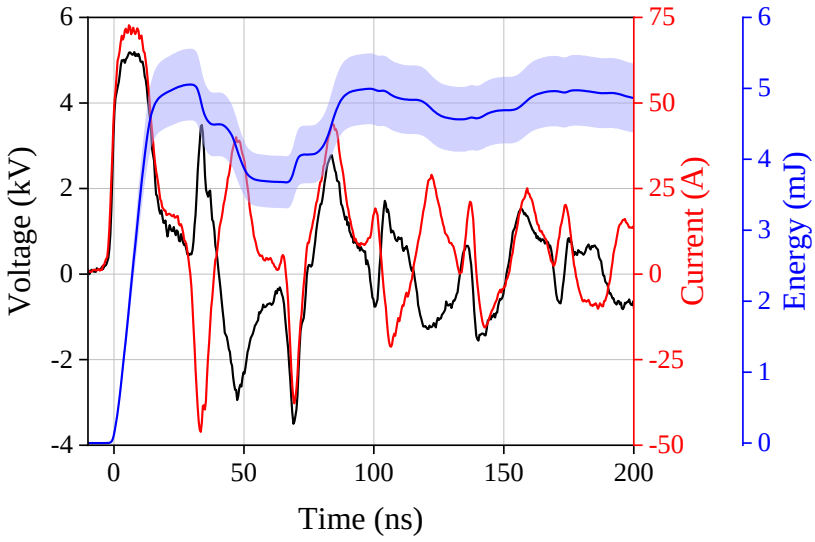

Figure 9.3 Voltage (in black) and current (in red) of a nanosecond discharge measured in a dodecane flame. The energy (in blue) is the integral of the current and voltage product. The light blue swath indicates the standard deviation.

To avoid changing the liquid fuel atomization properties, which are known to be sensitive to fuel flow rate for simplex atomizers, the fuel flow rates are kept constant. They are chosen so that the thermal power (calculated assuming a 100% combustion efficiency) is almost the same for all three fuels at $P_{thermal}$ = 5 kW. The ratio of electrical (NRP) to thermal (combustion) power is, therefore, equal to 2% for all cases.

9.2 Spectroscopic characterization of the discharges

An OceanOptics Maya2000Pro deep-UV spectrometer is used to analyze the spontaneous emission from the combustion process and the plasma. The collection optics consists of a small lens and an optical fiber. The field of view (FoV) schematically shown in Figure 9.1 encompasses the entire discharge area and some of the ORZ with an integration time including several discharges (≈ 1 ms). Therefore, the acquired spectra are representative of the brightest region of the plasma (the core) at the peak of the emission (end of the discharge). At 520 nm, emission from Cr is visible (not to be confused for C_2 Swan emission). It originates from the erosion of the Inconel electrode (constituted of approximately 20% of Cr). This emission might also be caused by titanium (less than 1% in Inconel). For wavelengths longer than 500 nm, a continuum associated with thermal radiation from the burner and the quartz tube is observed.

The acquired spectra displayed in Figure 9.4 give a qualitative idea of the species excited and produced by the discharge and the flame. Typical combustion species, CH(A) and OH(A), are identified in these spectra (Gaydon, 1974; Laux *et al.*, 2003). Strong peaks arising from the emission of CN* are found, a feature reported by Kim *et al.* in a CH_4-N_2 plasma (Kim *et al.*, 2006a, 2006b). However, no emission of C_2 is observed, contrary to the case of Kim *et al.* Atomic emission from oxygen, O*, nitrogen, N*, and hydrogen, H_α, is observed. These features show that the NRP discharges dissociate O_2, N_2 and possibly CO_2, H_2O and the fuel. The dissociation of O_2 by N_2* quenching has already been described in air (Rusterholtz *et al.*, 2013), but the question of dissociation in combustible mixtures is not yet completely solved, see Section 8.6.1.

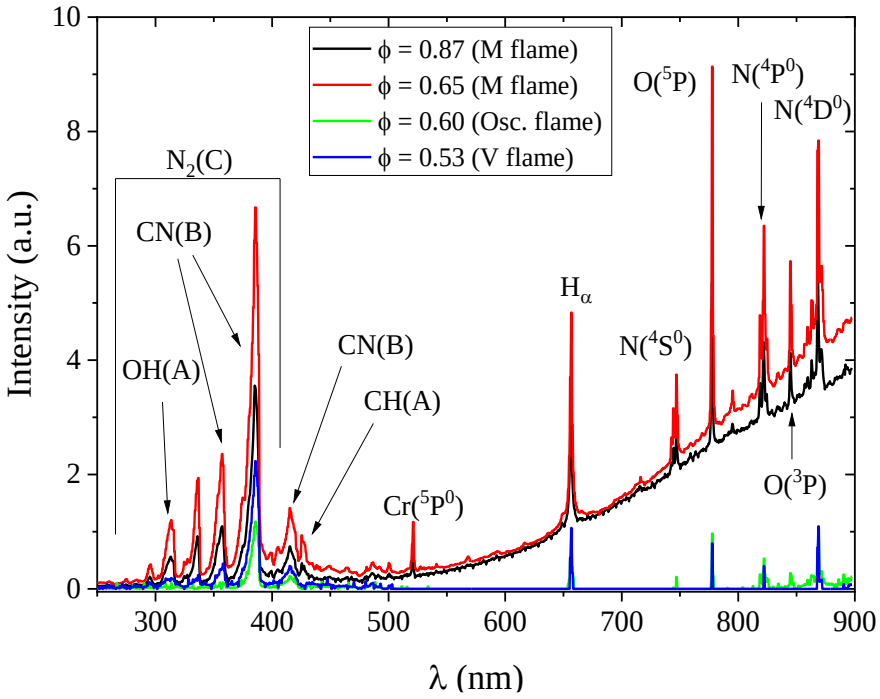

Figure 9.4 Typical emission spectra recorded in a dodecane flame assisted by NRP discharges. In the four regimes (corresponding to ϕ = 0.87, 0.65, 0.60, and 0.53), the emissions of N_2(C), CH, CN, OH, O, H, and N are visible.

Spectral broadening of the H_α line is used to determine the electron number density of the plasma (Gigosos, González and Cardeñoso, 2003). At Φ = 0.87 and 0.65 (attached stable flames), $n_e = 1.4 \pm 0.2 \times 10^{17}$ cm^{-3}. The rotational structure of N_2(C) is used for temperature estimation. Using Specair (Laux *et al.*, 2003), the rotational and vibrational temperatures are estimated to be T_{rot} = 3500 K ± 500 K and T_{vib} = 8000 K ± 1000 K. These temperatures are superior to values reported in Section 8.5.3 or in (Rusterholtz *et al.*, 2013). This difference is consistent with a higher energy deposition used in the present work (1.0 mJ.mm^{-1}) compared to the aforementioned references: 0.18 mJ.mm^{-1} in (Rusterholtz *et al.*, 2013) and 0.4 mJ.mm^{-1} in Section 8.5.3. At Φ = 0.60 and 0.53, the broadening of H_α is equal to the instrumental broadening function and only an upper limit can be estimated: $n_e < 0.2 \times 10^{17}$ cm^{-3}.

The temperature in the plasma $T_{gas} \approx T_{rot} \approx$ 3500 K, greatly superior to the adiabatic flame temperature 1500 – 2000 K, and the dissociation of O_2 indicates that this discharge is neither an NRP-corona nor an NRP-glow discharge (Pai, Lacoste and Laux, 2010b). The level of n_e is found in between the values reported for nonequilibrium NRP-sparks (Rusterholtz *et al.*, 2013), and for thermal sparks (Minesi, Stepanyan, *et al.*, 2020). The vibrational temperature is also higher than what was reported in non-thermal sparks (Pai, Lacoste and Laux, 2010b; Rusterholtz *et al.*, 2013). However, as neither N^+ emission at 500 nm nor an electron continuum is observed in the spectra, the NRP-spark is necessary of the non-thermal type.

The emission spectrum of the M-shape flame without plasma-assistance (Φ = 0.87), in Figure 9.5, presents no atomic emission of O nor N. the C_2 Swan bands are preponderant. No emission of CN is visible. Therefore, the presence of CN in Figure 9.4 is directly attributed to the impact of NRP on the mixture through (i) the increase of electronic temperature of CN and/or (ii) additional production of CN in the plasma.

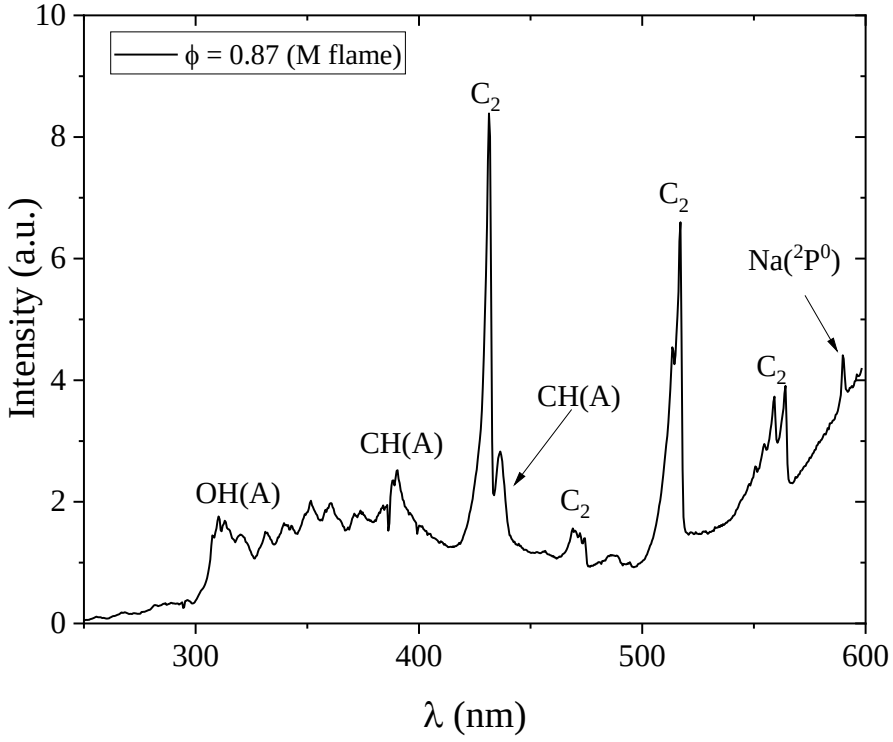

Figure 9.5 Emission spectrum of the flame without NRP assistance.

9.3 Lean Blow-Out

9.3.1 Lean Blow-Out extension by NRP discharges

The LBO limit is determined by linearly increasing the air flow rate, starting from the nominal operating point of $\dot{m}_{air} = 1.94$ g·s^{-1} and going up to $\dot{m}_{air} = 3.77$ g·s^{-1} over a time period of 40 s. Before starting the air ramp, in order to ensure reproducibility, the burner is operated at the steady nominal operating point until thermal equilibrium is reached. For this purpose, the temperature of the quartz tube is monitored using a K-type thermocouple. Operating conditions, in terms of fuel mass flow rate, $\dot{m}_{fuel}$, thermal power, $P_{thermal}$, global equivalence ratio, Φ, and bulk velocity, u_b, are gathered in Table 9.1. The bulk velocity is defined at the cold thermal condition as $u_b = \dot{m}_{tot}/\pi\rho r_{inj}^2$.

Table 9.1 Operating conditions for all three fuels at the start (t_0) and at the end ($t_\infty = 40$ s) of the air flow ramp.

	$\dot{m}_{fuel}$ (g·s^{-1})	$P_{thermal}$ (kW)	Φ		u_b (m.s^{-1})	
			t_0	t_∞	t_0	t_∞
CH_4	0.0997	4.98	0.88	0.46	35	65
C_7H_{16}	0.111	4.95	0.87	0.45	32	62
$C_{12}H_{26}$	0.112	4.97	0.87	0.45	32	62

The flame evolution during the air ramp, depicted in Figure 9.6, shows flame images (CH* filter) for both methane and heptane. The chemiluminescence images are Abel inverted to aid the identification of the flame topology. The evolution of flame shape is essentially the same for all three fuels. Starting from an "M" or "V" shaped flame at the nominal operating condition, the flame changes shape to burn both in the ORZ and at the top of the swirling jet at leaner operating points ($\Phi \approx$ 0.64), leading to an "M+ORZ" shape. Soon after $\Phi \approx 0.64$, the flame starts to oscillate at a frequency close to 12 Hz for methane ($\Phi \approx 0.58$), and 7 Hz for liquid fuels ($\Phi \approx 0.57$ for heptane). The overall evolution is similar for all three fuels during the oscillation, although the oscillation frequency is higher for methane. These oscillations end either by LBO, or by stabilization of the flame in a fairly long "tulip" shape. As the air flow rate is increased, the "stem" part of the flame becomes longer, and the "petals" move downstream until LBO occurs.

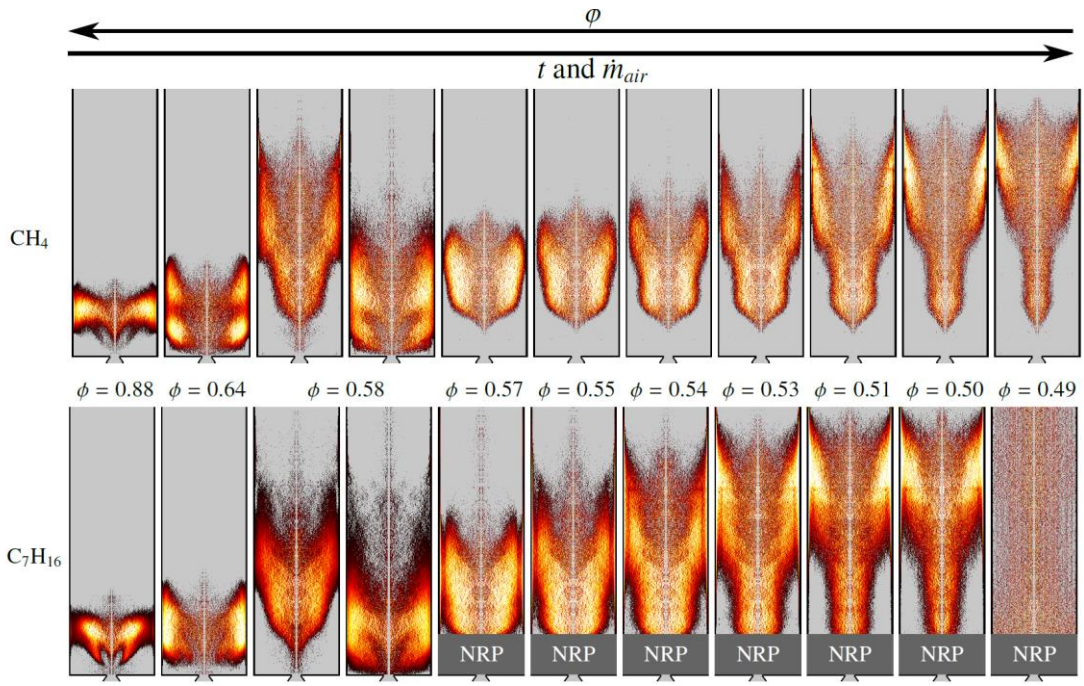

Figure 9.6 Abel inversed chemiluminescence images of CH* acquired using a high-speed camera. From left to right, the air flow is increasing starting at nominal condition of Table 9.1. The first line shows the blow out sequence for a methane flame without NRP assistance. The second line is that for a heptane flame without NRP assistance down to Φ = 0.57, and with NRP assistance for leaner points. In the latter case, a darker band at the bottom of the combustor is added to mask the luminosity of the discharges. The central line is an artifact of the Abel inversion.

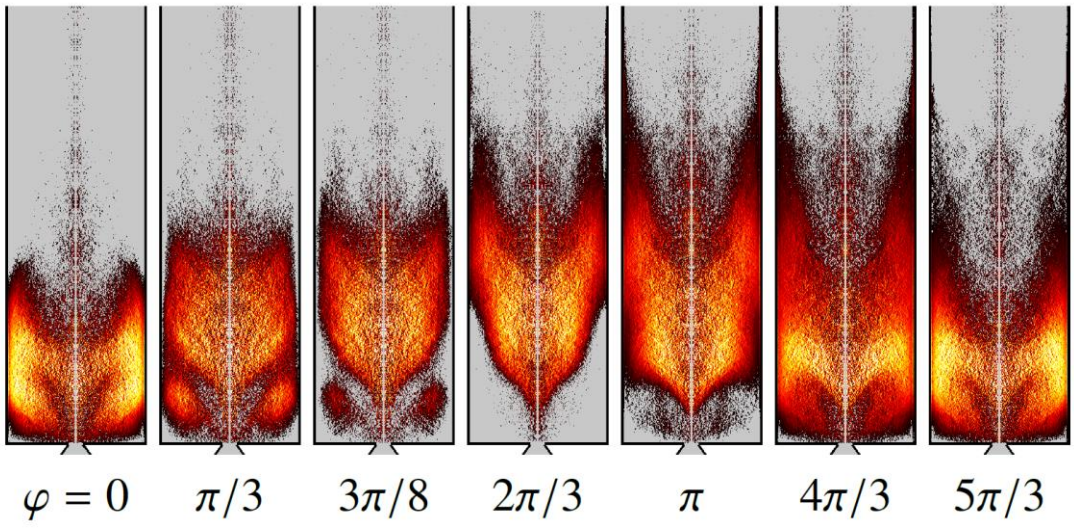

Figure 9.7 Phase averaged images of the flame oscillation cycle with heptane at $\Phi \approx 0.57$. The images are Abel inversed.

The oscillations at Φ = 0.57 are measured at steady state and phase-averaged in Figure 9.7 for heptane. Flame images are acquired with a high-speed camera and a predominant oscillation mode at 7.5 Hz is found by Dynamic Mode Decomposition (DMD) analysis (Schmid, 2010). These low-frequency oscillations are essentially extinction and reignition in the ORZ, as the flame oscillates between an "M+ORZ" and a "tulip"' shape. The ORZ is reignited by propagation of flame kernels from the downstream side to the ORZ. Flame oscillation between two stable flame regions is also reported by Kim *et al.* (Kim *et al.*,

2017) during LBO characterization of a premixed bluff-body stabilized flame with PAC. DMD is also performed on the spark images acquired during this oscillation (Figure 9.2) and no coherent motion of the spark is found.

Table 9.2 Probability of flame blow out during the oscillating phase. $\hat{p}$ is given for each fuel with and without PAC (lower is better). At least ten experiments are performed for each case. The 95% statistical confidence interval, computed using the Clopper-Pearson method, is indicated in with + and – signs.

	$\hat{p}_{w/o\ NRP}$	$\hat{p}_{with\ NRP}$
CH_4	$0.13^{+0.26}_{-0.11}$	$0^{+0.26}$
C_7H_{16}	$1.00_{-0.21}$	$0.27^{+0.34}_{-0.21}$
$C_{12}H_{26}$	$1.00_{-0.28}$	$0.26^{+0.25}_{-0.17}$

As indicated previously, after the oscillations, the flame either suddenly blows out or continue to burn while the equivalence ratio decreases. Table 9.2 indicates the probability of flame blow out, $\hat{p}$, during the oscillations for each fuel with and without PAC. The 95% interval of confidence is also given. The complete dataset of extinction is shown in Figure 9.8 (histogram). A statistically significant improvement (lower $\hat{p}$) is observed when PAC is used for heptane and dodecane. For these fuels, the flame is systematically blown out during the oscillating phase without PAC, but is much more robust with NRP discharges, leading to a significant improvement of the LBO limit. The improvement is less significant for premixed methane which already features a good resistance to LBO without PAC.

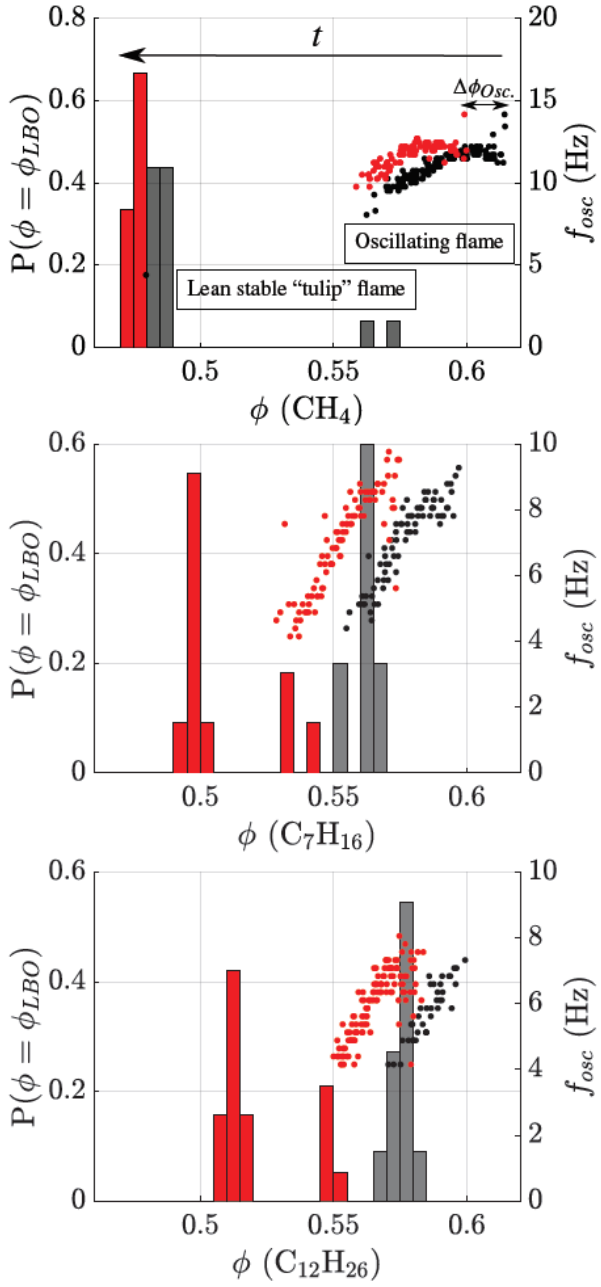

Figure 9.8 Probability of extinction (histogram, left axis) and frequency of oscillation (dots, right axis) with equivalence ratio. Experiments with and without plasma assistance are shown in red and black, respectively. This approach allows for a clear identification of the limits and frequency of the flame oscillations as a function of *Φ*.

Figure 9.8 also shows for each fuel the flame oscillation frequency, f_{osc}, as a function of Φ. For each experiment, a frequency spectrum of the OH PM signal is computed, and the dominant frequency of oscillation is reported in Figure 9.8. The periodogram is computed using short-time Fourier transform with a frequency resolution of 0.25 Hz and a temporal resolution of 0.5 s. This approach allows for a clear identification of the limits and frequency of the flame oscillations as a function of Φ. In each case, a set of several repeated experiments is presented, and a reproducibility better than 10% is obtained. For

all three fuels, the flame oscillation regime starts and ends at a leaner operating point with NRP discharges. Two main observations can be drawn from these results for all three fuels:

1. As Φ decreases, there is a decrease in the oscillation frequency.
2. The frequency trend is similar with and without PAC.

For methane, the end of the oscillating regime is nearly the same with and without plasma assistance. After the oscillation stage, the flame stabilizes as a "tulip" shape after the oscillation. For two of the tests without NRP discharges, LBO occurred during the oscillation phase.

For heptane and dodecane, without PAC, LBO always occurs during flame oscillations[1]. When NRP discharges are turned on, the flame is sustained after the oscillation and blows out under leaner conditions[2].

The increased LBO limit with PAC is quantified in Figure 9.9 for all three fuels. The LBO limit is extended in average by $\Delta\Phi = 0.05$ for both liquid fuels, and $\Delta\Phi = 0.019$ for methane. The beginning of the low frequency oscillation is also delayed by $\Delta\Phi \approx 0.02$ for all three fuels.

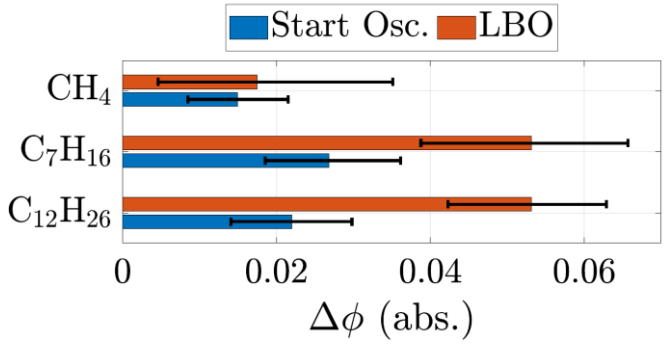

Figure 9.9 Reduction of the equivalence ratio, $\Delta\Phi$, at the start of the oscillations (in blue), and at the LBO (in red) by NRP discharges. Higher values indicate a stronger, more positive, effect of the plasma assistance. Uncertainty intervals are estimated from the repeatability of the mass flow controllers.

9.3.2 Impact of the electrode position

As already indicated in Section 9.1, it is not possible to operate the discharges at $r / r_{inj} < 1$, because the discharges would damage the liquid fuel atomizer head. Figure 9.10 shows the results obtained by varying the radial position of the electrode and measuring the LBO limit of a heptane flame from repeated

[1] If the NRP discharges are turned on immediately after the extinction, the flame does not reignite.

[2] If the NRP discharges are turned off once the flame stops oscillating and stabilizes in its "tulip" shape, the flame continues to burn until LBO at $\Phi \approx 0.52$, indicating that the "tulip" flame can exist without plasma, but that state cannot be reached without plasma assistance.

experiments. The position r / r_{inj} = 6 is optimal for this test rig in terms of efficiency and repeatability. This may be linked to the structure of the flame, associated flow and more specifically to the location of the ORZ.

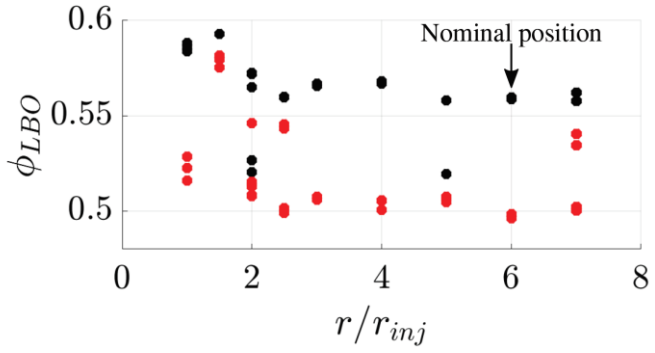

Figure 9.10 LBO of the SICCA burner in heptane for several electrode locations

The typical shape of a heptane flame at Φ = 0.63 is "M+ORZ" (see Figure 9.1). From this pattern and from previously measured velocity profiles (in nonreactive, unconfined conditions (Prieur *et al.*, 2017)), one may infer that near the combustor backplane the ORZ extends from r / r_{inj} = 3 to r / r_{inj} = 6. This region is filled with hot gases at relatively low velocity and turbulent intensity, with augmented residence time, and a longer convective delay to the base of the flame. In the outer region, beyond 6 r_{inj}, the flow is cooled down by the wall. Between the injector rim and r / r_{inj} = 2 the flow is relatively fast, cold and turbulent. It is suggested by Kong *et al.* (Kong *et al.*, 2019), that an electrode placement in a relatively slow recirculation zone will favor plasma-induced chemical effects. This is probably why the electrode location at r / r_{inj} = 6 provides the best performance in terms of LBO improvement.

9.3.3 Efficiency of NRP discharges in burst mode

As described in Section 9.1, the thermal power of the flame is equal to $P_{thermal}$ = 5 kW, and the electrical power of the plasma is 100 W, which represents 2% of $P_{thermal}$. This energy cost could be too high for practical application and it is already shown in the Mini-PAC burner (Section 8.3.1) that a power cost of 0.3% is enough for significant results. A possible way to reduce the power of the plasma assistance would be to reduce the frequency or the energy per pulse. We explore in this section another solution applied to the heptane flame, which consists in applying the NRP discharge with a burst sequence. The parameters used in the previous sections will be conserved (20 kHz and 5 mJ per discharge), but with periods without discharges. The duration of the NRP discharge burst divided by the duration without discharge is defined here as the burst duty cycle, Eq. 6.16.

$$D_{burst} = \frac{\Delta t_{ON}}{\Delta t_{OFF}} \qquad \text{Eq. 9.1}$$

Strictly speaking, NRP discharges are already in duty-cycle by themselves (*i.e.* 10 ns pulses applied at 20 kHz in continuous mode have a duty cycle of 0.2%). We use here this convention of language to simplify the discussion of this section.

For instance, in a burst duty cycle of D_{burst} = 80%, the flame will be assisted by NRP discharges during 10 ms (series of 200 pulses ON), a pause of 2.5 ms (50 pulses OFF), then re-assisted during 10 ms, a break of 2.5 ms, *etc*. This principle is illustrated in Figure 9.11.

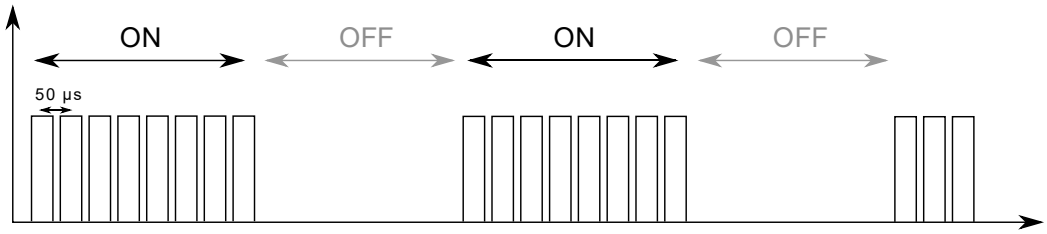

Figure 9.11 Principle of the NRP discharges in burst mode. The discharges are applied at 20 kHz during the ON period, which is repeated with a defined duty-cycle.

In the present case, the duration without the pulses is set constant to 2.5 ms (corresponding to 50 pulses OFF) for simplicity. The number of pulses ON in Figure 9.11 is varied from 50 (D_{burst} = 50%) to 200 (D_{burst} = 80%). In Figure 9.12, the LBO equivalence ratio of these experiments is reported. In Figure 9.12, the improvement of the LBO limit is visible above D_{burst} = 60% compared to the case without plasma-assistance. As the duty-cycle is increased, the oscillations limit decreases. For Φ > 0.77, the probability of LBO during the oscillation is equal to 63% (= 5/8). As shown in Section 9.3, the NRP discharges in continuous mode allow the heptane flame to pass the oscillation phase with a probability of 73%. More experiments are required to refine the statistics, but this result is an encouraging step toward further reduction of the electrical cost of plasma-assistance.

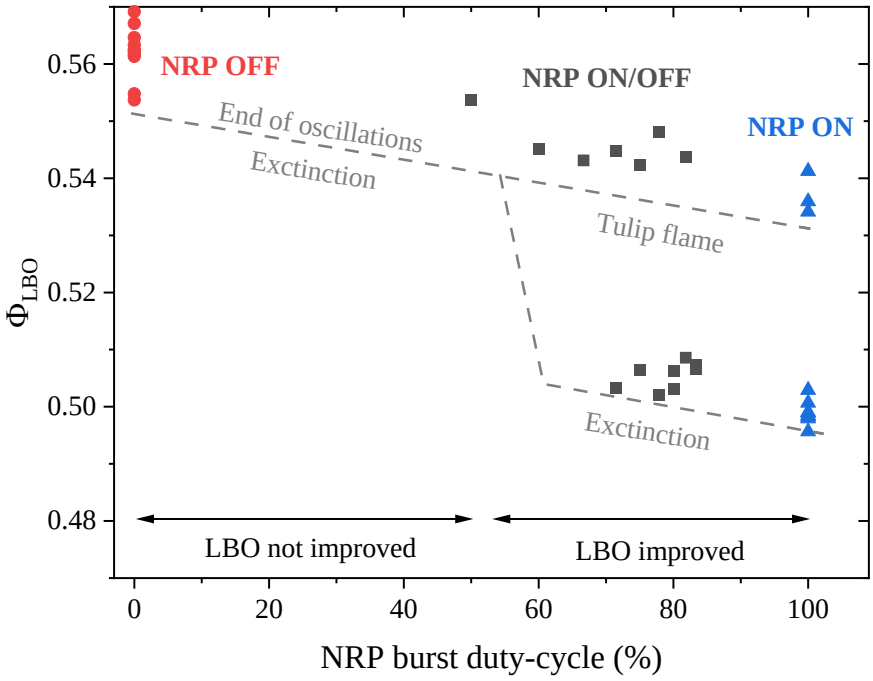

Figure 9.12 LBO limit of a liquid heptane flame at varying NRP duty-cycles. For comparison, the red circles correspond to the non-assisted flame (0% duty-cycle), while the blue triangles show the results obtained when the NRP discharges are consistently ON (100% duty-cycle).

Other strategies could be employed. The number of pulses off (50) could also be reduced: for instance, a duty cycle ON/OFF of 8/2 could be more efficient than 200/50. This effect could also be investigated at higher frequencies. A campaign of experiments with such a broad set of free parameters is left for future work.

9.4 Conclusions of the SICCA experiment

This chapter is focused on an extension of the lean blow out (LBO) limit of liquid (heptane and dodecane) and gaseous (methane) swirled flames by NRP discharges. For these experiments, the fuel flow rate is kept constant and the air flow rate is slowly increased until LBO occurs. The NRP discharges are applied at 20 kHz and the ratio of electrical and thermal power is equal to 2%. Three phases are identified in the blow out sequence: first, the flames present initially a “V” or “M” shape burning further in the outer recirculation zone (ORZ). In the second phase, the flames oscillate at frequencies below 13 Hz. For methane, the flame stabilizes in a “tulip” shape after the oscillations (third phase), until LBO occurs. An extension of the LBO is obtained with NRP discharges. For liquid fuels, the flame systematically blows out during the oscillations. In this case, the NRP discharges stabilize the flame during the oscillations, up to the “tulip” shape regime. The LBO limit is, thereby, greatly increased.

The position of the electrode is identified as a critical factor in the efficiency of the PAC system. An electrode positioned near the outer edge of the ORZ is found to be the most favorable position, both for LBO performance and ease of installation in most practical systems.

A practical way to further reduce the already low-power cost of NRP discharge has been explored. This study marks another step toward the application of NRP discharges to real applications.

Chapter 10

Conclusions

10.1 Principal contributions of this thesis

In this thesis, we investigated how Nanosecond Repetitively Pulsed (NRP) discharges impact lean flames. In parallel, we also described, both experimentally and numerically, the formation and decay of fully ionized plasma generated by nanosecond discharges.

The principal contributions of this thesis begin with, in Chapter 4, the experimental characterization of the thermal spark. The electron number density of the thermal spark is measured with high spatial and temporal resolution. These measurements show that the thermal spark formation occurs in five stages. From a general perspective, we showed that, for a given initial temperature, the increase of pressure favors the formation of thermal sparks. We demonstrated that the nature of the spark, thermal or not thermal, cannot be determined from the deposited energy. Finally, we showed that the nanosecond thermal spark is indeed equivalent to the 'breakdown phase' of the longer discharges used for flame ignition.

Also, in Chapter 4, we discriminated five stages in the formation of the thermal spark. These stages are found to apply to other independent works in the literature. In Chapter 6, the increase of the electron number density was measured using the Stark broadening of H_α, the calibrated continuum emission of electrons, the calibrated intensity of N^+ and O^+ lines, and the Stark broadening of N^+ and O^+ lines. We demonstrated that the electron number density near the electrodes increases from 10^{17} cm^{-3} to 10^{19} cm^{-3} in 0.5 ns. The plasma is in chemical and thermal equilibrium. The temperature ranges between 35,000 and 50,000 K. In the afterglow, the decay of the electron number density is explained by isentropic expansion alone. These conclusions are also found to apply to other independent measurements, and hence, can be considered as general.

Another contribution of this work is the development of a kinetic mechanism for the thermal spark formation. This reaction set can reproduce the 0.5-ns ionization phase of the thermal spark. The role of the N and O excited states was found to be dominant during the transition from a non-equilibrated to a thermal plasma. The increase in temperature, approximately 40,000 K in 0.5 ns is caused by electron-ion elastic collisions.

Finally, in Chapter 8, this thesis presents a new set of experimental results in Plasma-Assisted Combustion. In the Mini-PAC experiment, chemiluminescence, OES, and OH-LIF were performed with temporal and spatial resolution. With these diagnostics, we first determined the non-thermal nature of the NRP sparks. The general mechanisms of heating (during the energy deposition) and cooling (during the interpulse period) were described. From the non-assisted to the plasma-assisted flame, the NRP discharges induce a three-fold increase of the OH number density in the flame, thus significantly increasing the mixture reactivity. These measurements are validated by a PAC-LES model developed in parallel. In Chapter 9, experiments in the SICCA burner, which are close to realistic conditions, showed that NRP discharges can significantly extend the LBO limit of methane, n-heptane, and dodecane flames. The NRP discharges stabilize the flame during an oscillation phase, which leads to an LBO extension.

The next section provides further insight into our experimental and numerical findings.

10.2 Summary and insights gained

The first part of this thesis was dedicated to the theoretical and experimental grounds of our work. In Chapter 3, remaining close to textbook theories, we derived the internal properties of atoms and molecules, and a LIF model. Then, we described how to measure the gas temperature in nanosecond discharges. Finally, we simplified the theory of atomic line broadening developed by Griem *et al.* and provided original formulas for rapid linewidth determination. The Chapter 2 focuses on the practical use of nanosecond discharges and we carefully describe the measurement of electrical characteristics of nanosecond discharges. We demonstrated that valuable information is gained when probing the current and voltage in the middle of a coaxial cable.

In Part II of this thesis, we described the formation and decay of a fully ionized plasma by a single nanosecond pulse in air. We chose to name this state “the thermal spark” to highlight that the plasma is in thermal equilibrium (thermal) and that this phenomenon is transient (spark). This denomination is also compatible with the NRP corona/glow/spark nomenclature of Pai *et al.*, already widespread in the literature. Based on a literature review and our experimental results in air, the following stages of formation of the thermal spark were evidenced:

1. A partially ionized non-equilibrium plasma is first formed in the interelectrode gap. The typical plasma diameter at these early instants is 200 - 300 µm and the emission is dominated by the N2(C→B) radiative transition.
2. A filament is generated at the cathode on a timescale below 0.5 ns. Its emission is several orders of magnitude more intense than the rest of the plasma. Its spectrum is dominated by N+ and a broadband continuum. The filament's typical diameter is 10 – 100 µm, while its typical length is 0.1 – 1 mm. During this stage, the plasma reaches full ionization and thermal equilibrium.

3. In a nanosecond timescale, another filament is formed later at the anode, with similar properties.
4. The two filaments propagate toward each other in the interelectrode gap. The typical speed of propagation is pressure dependent and ranges from 10^4 to 10^5 m·s^{-1}.
5. The filaments merge: the thermal spark is formed.

Although the formation and propagation of a partially ionized plasma, stage 1, has been widely treated in the literature, a gap remained for the other stages. We addressed this gap using a numerical approach (Chapter 5), supplementing a baseline kinetic mechanism of low-temperature plasmas with reactions of ionization of O and N excited states. The 0-D model demonstrated that, to explain the 0.5-ns ionization phase from 10^{17} to 10^{19} cm^{-3}, it is necessary to introduce the ionization of the excited states of N and O. In our conditions, we demonstrated that at least six excited states of N and three excited states of O must be included in the kinetic mechanism. Our simulation results were compared to the measurement of the electron number density by Stark broadening of N^+ and H_α with excellent agreement. Additional confirmations were obtained using the calibrated measurement of the electron continuum radiation and N^+ and O^+ lines emission. The high gas temperatures, also reported in the experiments, are explained by the increase of the electron-ion collision frequency, otherwise negligible in non-thermal plasmas.

Concerning the recombination following the thermal spark, the decrease in electron number density in nanosecond discharges was measured by Stark broadening of H_α and N^+ lines. Synchronously, the electron temperature was measured by fitting the emission of excited electronic states of N^+. With these measurements, the three-body recombination of electrons with N^+ was found to be equilibrated by ionization. Therefore, the plasma is in equilibrium, even after the end of the voltage pulse. The decrease of temperature, and hence the decay of the electron number density, is explained by isentropic expansion alone up to t = 100 ns. Heat removal by conduction is negligible on this timescale, and heat removal by radiation remains secondary. Therefore, we demonstrated that the thermal spark afterglow can be simply described by a plasma in chemical equilibrium subject to volume expansion.

Finally, in Part III, NRP non-thermal sparks were applied in combustible mixtures. In the Mini-PAC burner, in Chapter 8, NRP spark discharges of 2 mJ were initiated at 20 kHz in the recirculation zone of a CH_4 premixed turbulent flame at $\Phi = 0.8$. Within the transition from a non-assisted to a plasma-assisted flame, OH* and CH* chemiluminescence measurements showed that the NRP discharges impact the flame topology after ~ 1 ms (~ 20 pulses), which corresponds to the flow recirculation time near the bluff-body. The plasma-assisted flame reaches steady state after approximately 200 pulses. OH-LIF measurements showed that the OH number density increases by a factor of 2 to 3 between the non-assisted and the plasma-assisted flame. The timescale of the increase of the OH profile is consistent with the chemiluminescence results.

A significant understanding of the plasma heating and cooling was gained in this thesis. In the near-electrode regions, during the period between two pulses, the hydrodynamic effects generated by the nanosecond sparks induce the entrance of fresh gas (at 2000 K). Then, in 10 ns, the temperature increases from 2000 K up to 3500 K at the cathode (up to 3000 K at the anode). This temperature increase is due to the heating of the ions by electron impact. In the middle of the gap, the interpulse cooling is weaker, and the temperature rise is comparatively lower, from 3000 K to 3500 K in 10 ns. Under these conditions, N_2 excited states are likely quenched by O_2, explaining the 500-K heating. We calculated that 53% of the deposited energy in the first pulse is spent in the temperature increase. Finally, the temperature, the spectrum composition, and the electron number density indicate that the plasma is non-thermal, although the cathode region is close to a thermal regime.

Chapter 9 focused on the extension of the Lean Blow Out (LBO) of the SICCA experiment. The NRP non-thermal discharges extend the LBO limit of swirled flames feed with liquid (heptane and dodecane) and gaseous (methane) fuels. Three phases are identified in the blow out sequence. First, the flames present initially a “V” or “M” shape burning further in the outer recirculation zone (ORZ). In the second phase, the flame oscillates and usually blows out. For methane, the flame can sometimes stabilize in a “tulip” shape after the oscillations (third phase), until LBO occurs. NRP discharges significantly reduce the probability of LBO during the second phase, with any fuel. The position of the electrode was identified as a critical factor in the effectiveness of the PAC system. An electrode positioned near the outer edge of the ORZ was found to be the most favorable position, both for LBO performance and ease of installation. Finally, the already low-power cost of NRP discharges can be further reduced by applying them in a duty-cycle.

10.3 Recommendations for future work

This section summarizes in which direction the author would have continued if more time could have been dedicated to this thesis.

10.3.1 Thermal spark

Four techniques were used to measure the electron number density (continuum radiation of the electrons, intensity of N^+ lines, and Stark broadening of N^+ and H_α). These measurements could be compared with other techniques such as laser interferometry and Thomson scattering. We showed that excited states of nitrogen play a significant role in forming the filament, which implies that the number density of these states should be measured by OES or absorption. The measurement of the electric field by the E-FISH method would also provide further validation of the model presented in this thesis. These measurements would be challenging, given the needed spatial and temporal resolution. More measurements in different mixtures, temperatures, and pressures conditions would also be valuable to validate the kinetic model.

Regarding the thermal spark simulations, the kinetic mechanism presented in this thesis was applied in a 0-D simulation. Although significant insight was gained on the filament formation and the role of atomic excited states, the construction of a 2-D simulation reproducing the streamer propagation, the filament propagation, and the plasma recombination would undoubtedly be worthwhile. Time should also be spent on including endothermic and exothermic reactions to reproduce the ultra-fast heating observed in non-thermal sparks.

10.3.2 Plasma-assisted combustion

The work performed in the Mini-PAC burner was essentially focused on the phenomena occurring in the discharge along the interelectrode axis. The radial distribution of the excited species would be a challenging but useful task to pursue. In parallel, the measurement of atomic oxygen formation by nanosecond discharge in the Mini-PAC experiment would allow gaining further information on plasma kinetics. Regarding PAC chemistry outside the discharge vicinity, quantitative OH LIF should be continued (in the saturated or predissociative regime), along with the determination of the temperature distribution by Rayleigh or Raman scattering. Finally, we should pursue the demonstration of NRP discharges in conditions closer to industrial applications with heavier fuels, higher pressures, and higher powers.

Appendix A

High-voltage generators for nanosecond discharges

Four generators of high-voltage pulses (abbreviated “pulser”) are available in the EM2C laboratory. Two of them have been used in this work. They are named here “pulser #2” and “pulser #4” and are both based on fast diodes developed by FID Technology. A short description can be found in the thesis of Pai (Pai, 2008). In the following, we will detail their specificities.

A.1 FID 10-30NM10 (pulser #4)

This generator can provide positive pulses of +12 kV to a load matching the pulser impedance (75 Ω), at a maximum repetition frequency of 30 kHz. However, we found experimentally that the pulse amplitude decreases above 27 kHz. The Full-Width Half Maximum (FWHM) of the pulses is approximately 10 ns. The pulser is air-cooled and does not require an external DC supply. We performed the plasma-assisted combustion experiments with pulser #4, which can run several hours in continuous mode without any particular precautions.

A.2 FID FPG 30-100MC4K (pulser #2)

The FID FPG 30-100MC4K generator has four output channels: two positives and two negatives. The duration of the high-voltage pulses (FWHM) is fixed to 10 ns. The frequency of the pulses can be adjusted from single shot to 100 kHz using an external trigger. The maximal amplitude that each channel can provide is equal to 7.5 kV in a 75 Ω load (impedance of each channel). The pulser can run one or all outputs simultaneously. It is possible to combine the four channels of the pulser to increase the voltage amplitude. Two configurations are possible. In the “+/- configuration”, the pulser has two outputs of +15 kV and -15 kV (see Figure A.1). If we number the primary outputs from one to four (1 and 2 are positive; 3 and 4 are negative) the following connections must be made:

- “Ground 1” to the earth
- “Core 1” to “Ground 2”
- “Ground 4” to the earth
- “Core 4” to “Ground 3”

If one output with the maximal voltage is desired, then the connection sketched in Figure A.2 must be made. This configuration is called "++/ground" or "--/ground":

- "Ground 1" to the earth
- "Core 1" to "Ground 2"
- "Core 2" to "Core 3"
- "Ground 3" to "Core 4"

If the generator had been delivering a DC current, these connections would lead to a short circuit because the "ground" of the cable is connected to the earth on the generator output. Considering a 10-ns pulse propagating at 20 $cm.ns^{-1}$ in the coaxial cable, we obtain a pulse length of 2 m comparable with the cable length. Therefore, the classical rules of DC electrokinetic are not applicable, and we instead use the laws of wave propagation in transmission lines (Martin and Martin, 2018).

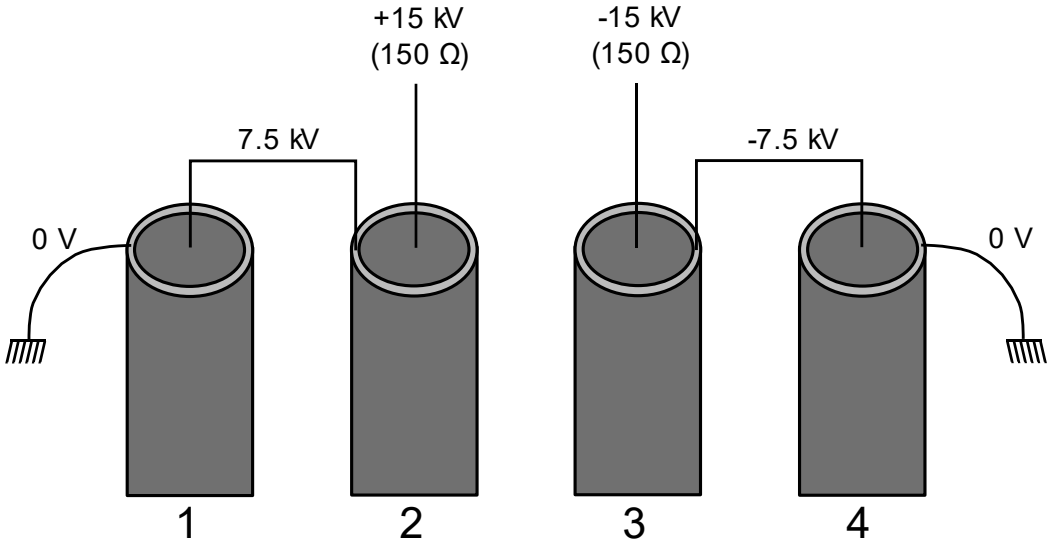

Figure A.1 Electrical configuration for a +/- output. Maximal potential (during the pulse) in the connection are showed. The impedance of the output is shown in brackets.

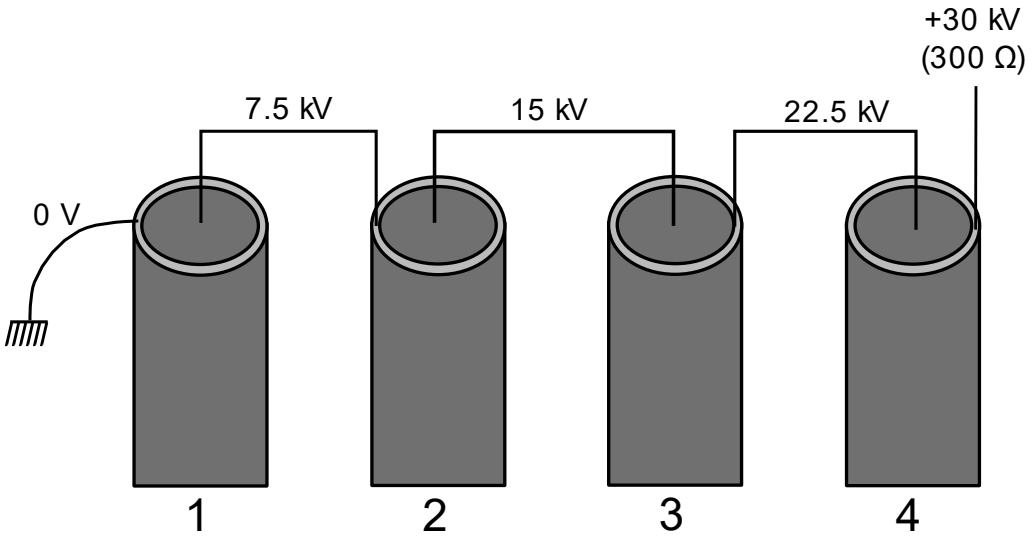

Figure A.2 Electrical configuration for a ++/ground output. For a negative output, the scheme is identical, exchanging the negative and positive primary channels. Maximal potentials in the connection are showed.

In the configuration +/-, two outputs with an impedance of 75 Ω are connected in series. Therefore, the impedance of the negative and positive outputs is equal to 150 Ω. In the configuration ++/ground (or --/ground), the output impedance is equal to 300 Ω.

Precautions have to be taken when the ground of one output is linked to the core of another one. In the +/- configuration, "Core 1" is connected to the "Ground 2". Therefore, high-voltage pulses can propagate to the pulser via "Ground 2" and damage the pulser. Ferrites are plugged around the cable 2 to prevent the pulses from propagating toward the pulser via the "Ground 2". Note that the ferrites dissipate the energy transported by the high-voltage pulses in heat. After running[1] the pulser #2 for 15 minutes at 30 kHz, the temperature of the ferrites can reach 120 °C. Temperature measurements are performed with a FLIR-i7 IR camera and are reported in Figure A.3. The emissivity of the ferrites being unknown, these temperature measurements are approximative. No heating of the ferrites is seen in the cables 1 and 4, because their grounds are not linked to any high-voltage source. It is therefore recommended to plug a maximum of ferrites on the cables 2 and 3 if the +/- configuration is used. If the ++/ground configuration is preferred, it is recommended to plug a number of ferrites proportional to the "ground voltage". See Table A.1 for the recommended repartition of ferrites.

[1] We do not recommend running pulser #2 at high frequencies for such a long time.

Table A.1 Recommended repartition of ferrites depending on the configuration used. The applied pulse voltage on the "ground" is given.

Cable / Conf.	1		2		3		4	
	U (kV)	Ferrites reparti-tion	U (kV)	Ferrites reparti-tion	U (kV)	Ferrites reparti-tion	U (kV)	Ferrites reparti-tion
+/-	0	0	7.5	50%	-7.5	50%	0	0
++/ground	0	0	7.5	16%	15	33%	22.5	50%
--/ground	-22.5	50%	-15	33%	-7.5	16%	0	0

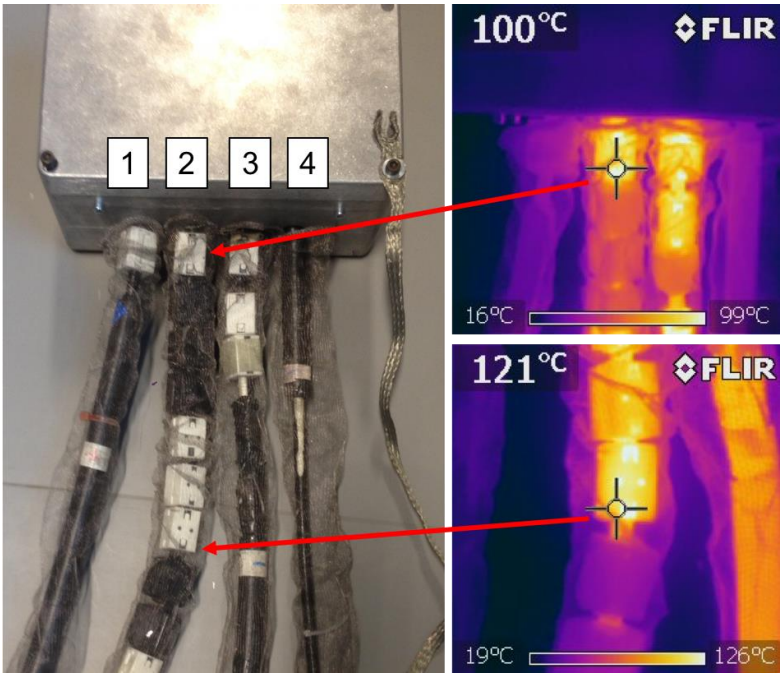

Figure A.3 (Left) Picture of the four output-cables of pulser #2. (Right) Ferrite temperature measured by a thermal camera. The maximal temperature reaches 121 °C after running the pulser in a configuration +/- at 30 kHz for 15 minutes.

For frequencies below 50 Hz, the internal supply of the pulser is enough to provide the maximum voltage in the four outputs. If higher frequencies are used, an external DC supply must be connected to the pulser #2 to sustain the voltage amplitude. Varying the voltage of the DC supply (from 0 to 220 V) allows controlling the amplitude of the nanosecond pulses (from 0 to 30 kV in a ++/ground configuration). The maximum repetition frequency is F_{REP} = 100 kHz. If the load impedance does not match the pulser impedance, reflected pulses will be sent back to the pulser through the core of the coaxial cable. We note that at high frequencies, the pulser cannot be operated continuously for more than one minute if the load impedance is equal 0 Ω (short circuit), or more than three minutes if the load impedance is more

than 600 Ω. The load being a plasma, it is difficult to estimate an equivalent load impedance. For example, in a pin-to-pin configuration, the impedance is infinite at the beginning of the pulse. Whereas, in the case of breakdown and plasma full ionization, the impedance falls to zero. The allowed continuous regimes are shown in Figure A.4 under the dashed area; outside of this area, it is recommended not to run the pulser for more than one minute. It should also be noted that the limit between safe and dangerous continuous operation is not utterly known. For example, we noted that one output of pulser #2 had broken during this thesis, despite the strict application of the previous rules.

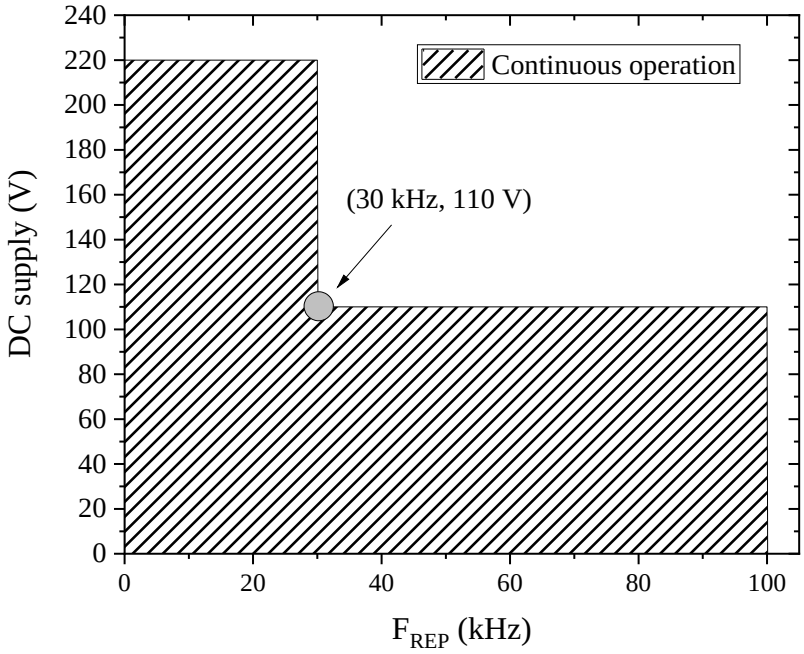

Figure A.4 Allowed regimes of continuous operation of the pulser #2. Outside of the dashed area, only one minute of continuous running is allowed.

Appendix B

Absolute calibration of OES

Optical Emission Spectroscopy (OES) is a standard tool to probe the plasma characteristics without perturbing the plasma environment. The experimental setup of Section 4.1, is used and reproduced in Figure A.5

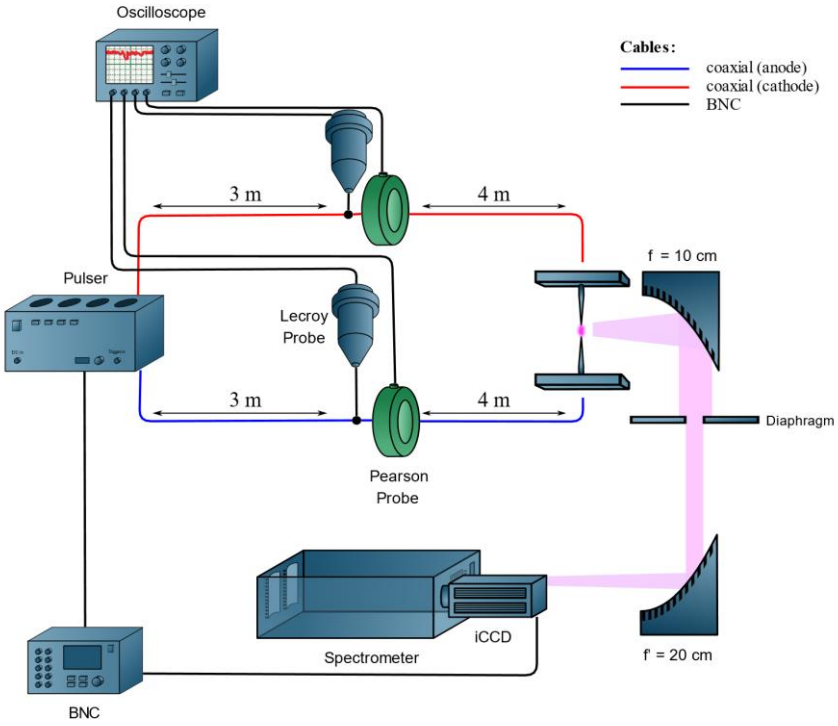

Figure A.5 Experimental setup.

As shown in Figure A.5, the discharge was placed at the focal point of an off-axis parabolic mirror (f = 10 cm). The collimated light from the plasma is then refocused by a second parabolic mirror (f = 20 cm) onto the entrance slit of the monochromator (Acton 500i). The pitch of the pixels on the ICCD is 13 μm, and the overall optical system has a spatial resolution of about 8 μm per pixel. The monochromator is equipped with three gratings of 300, 1800, and 2400 gr/mm, blazed at 500, 500, and 300 nm, respectively. An ICCD camera (Pi-MAX4) coupled to the monochromator is employed to record the spectra with a minimum gate of 450 ps. A HeNe laser (Thorlabs) is used to determine the instrumental broadening of the OES system. The variation of the instrumental broadening with wavelength is found to be negligible at the two ranges of interest, 656 ± 20 nm for H_α and 500 ± 20 nm for N^+ emission. The high

discharge reproducibility is sufficient to perform phase-locked acquisitions for imaging and OES experiments, the temporal jitter of the pulse being below 0.5 ns. The discharge imaging is performed using the zeroth diffraction order of the monochromator grating. The axis of the plasma channel shifts typically ±50 μm from shot-to-shot. A 150-μm slit, aligned with the interelectrode axis, is used to capture the entire emission of the discharge.

OES measurements on-CCD suffer background noise due to the dark-current (the electrical noise of the internal camera system) and other sources such as room light. Straylight pollution arises when unwanted light (such as grating 0^{th} order) reaches the CCD after multiple reflections inside the monochromator. This cannot be predicted and is strongly dependent on the grating position. Two background measurements can be performed to differentiate the straylight pollution from background. The first one consists of measuring without the plasma source (the discharge turned off). The second one, consists of turning the grating to 100 nm and record the signal with the plasma ON. This second option is, however, very sensitive to the grating position, and gives only an indication of the straylight. It is checked in this work that a similar level of background is obtained with both options.

B.1 Gate linearity

The PIMAX4 used in this work has “sub-nanosecond gates” available. The linearity of the signal intensity with the gate width, Δt, is checked with an integrating sphere (OL 455, Gooch and Housego), used as a stable source of light and is positioned at the discharge location in Figure A.5. After waiting one hour to stabilize the integrating sphere intensity, the averaged emission on the CCD is recorded for camera gates ranging from 0.45 ps to 10 ns. The intensity is relatively low, and the signal on-CCD is accumulated with 10 000 to 500 000 gates. The number of accumulations is taken into account when comparing the results in Figure A.5. For $\Delta t > 5$ ns, the total intensity recorded by the CCD is linear with the gate width, and a linear fit of the expected sensitivity is given. For 2.5 ns > $\Delta t > 5$ ns, the number of counts is below the linear response. At $\Delta t < 2.5$ ns, the “sub-nanosecond gates” mode is ON. The response of this mode is not linear. For a gate of 1.5 ns, the response of the camera is four times lower than the expected response from the long gate extrapolation (linear fit). This non-linearity with the gate width imposes to perform intensity calibration with identical gates for $\Delta t < 4$ ns. In addition, in Figure A.5, the linearity of the on-CCD accumulation is validated: the measurement with 500,000 on-CCD accumulations is five times more intense than the measurements with 100,000 on-CDD accumulations.

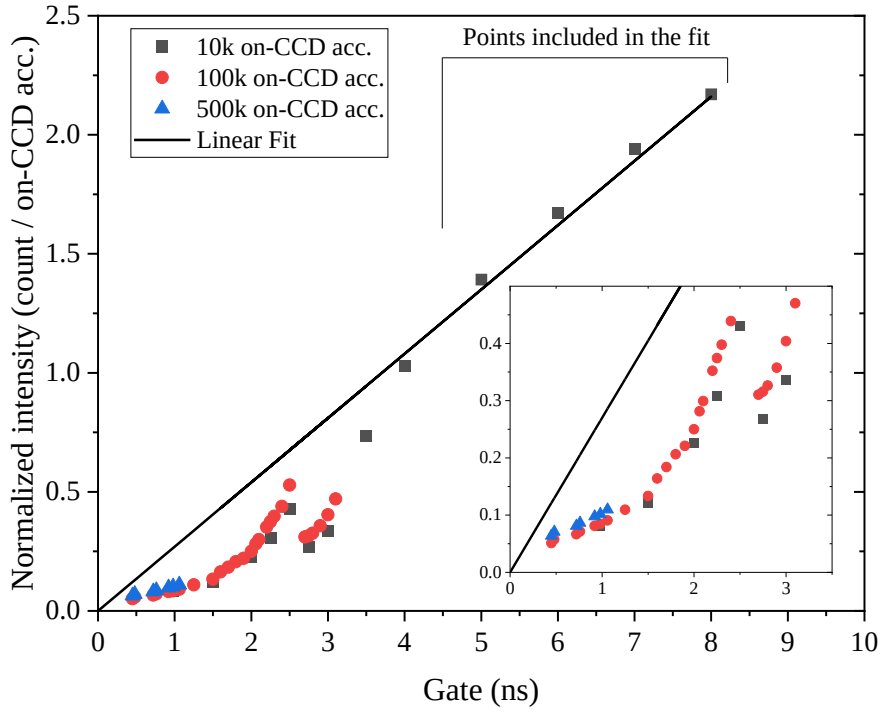

Figure A.6 Number of counts recorded on the CCD as a function of the camera gate. The number of counts is normalized by the number of on-CCD accumulations. A linear fit of the five last points is showed (solid line).

B.2 Comparison of the three calibration sources

Intensity calibration has to be performed to balance the wavelength sensitivity of the optical system. For this purpose, the EM2C laboratory uses three calibration sources:

1. An integrating sphere (OL455, Gooch and Housego), calibrated by NIST.
2. A tungsten lamp with a glass window. The black body theory is used to compute the intensity emitted by the lamps and assuming the glass transmissivity is equal to 1.
3. A tungsten lamp with a Sapphire window mounted for high transmissivity in the UV spectral domain. The lamp was calibrated by comparison with another calibrated source (Laux, 1993).

We describe here "absolute" calibration, the process of converting the on-CCD counts into spectral radiance (in $W.sr^{-1}.cm^{-2}.nm^{-1}$), according to Eq. A.1.

$$S(\lambda)\left[\mathrm{W.sr^{-1}.cm^{-2}.nm^{-1}.counts^{-1}}\right] = \frac{I_{lampe}\left[\mathrm{W.st^{-1}.cm^{-2}.nm^{-1}}\right]}{I_{lampe}[\mathrm{counts}]} \qquad \text{Eq. A.1}$$

In this following example, the camera gate ($\Delta t = 1 - 100$ µs) and the number of accumulations are varied depending on the calibration source to obtain the maximal signal-to-noise ratio. For each calibration,

the source is placed at the focal point of the optical system (discharge location in Figure A.5). Then the measured signal can be converted in absolute units using:

$$I_{meas}\left[\mathrm{W.st^{-1}.cm^{-2}.nm^{-1}}\right] = S(\lambda) \times I_{meas}[\mathrm{counts}] \qquad \text{Eq. A.2}$$

The grating used for this calibration has 300 gr/mm and is blazed at 500 nm. In Figure A.7, the spectrometer sensibility function is shown from 250 nm to 1200 nm. To avoid second (or higher) order of diffraction, we used optical high-pass filters:

- 250 – 430 nm: no filter
- 400 – 800 nm: filter with a cut-off at 400 nm (Melles Griot 03 FCG 055)
- 800 – 1250 nm: filter with a cut-off at 800 nm (43TAF20 0247 DTM)

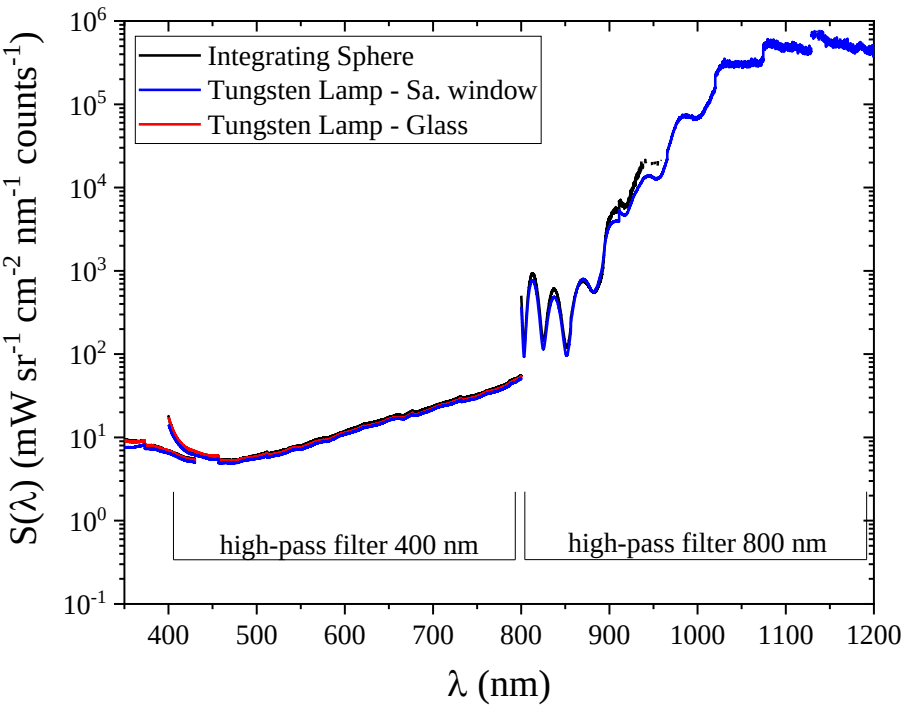

Figure A.7 Coefficient of absolute calibration for different calibration sources.

The spectrometer sensibility function does not depend on the calibration source. To check the calibration procedure, we plot in Figure A.8, the ratios of the tungsten lamps and the integrating sphere calibration coefficients. The coefficients agree within 10% in the 400-800 nm range. Below 350 nm, the signal of the calibration sources is too weak. In the infrared range, the signal of the integrating sphere is intense enough up to 950 nm but agrees within +20/-30% with the tungsten lamp mounted with a Sapphire window.

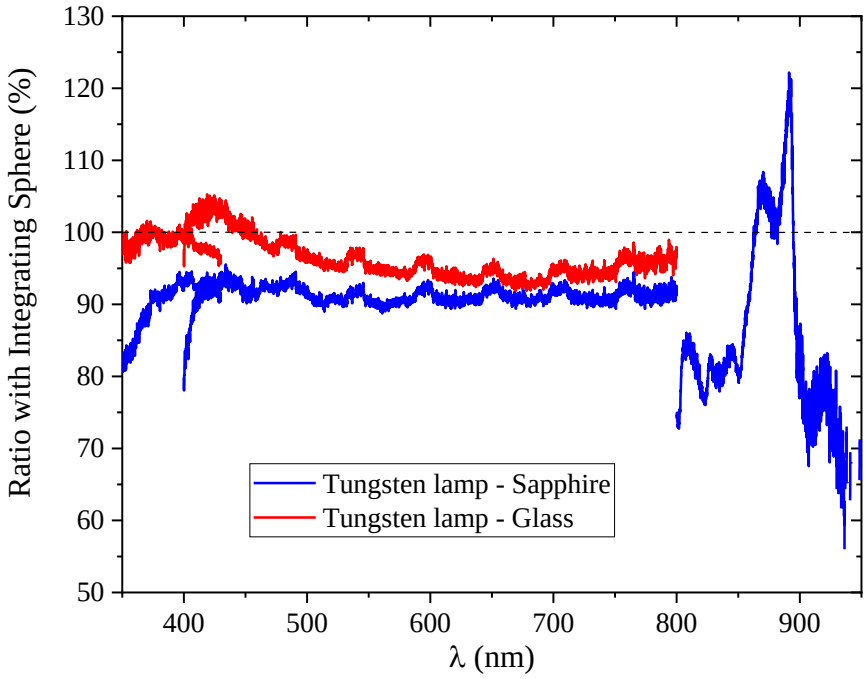

Figure A.8 Ratio of the spectrometer sensitivity function of the tungsten lamps and the integrating sphere.

In this work, if an absolute calibration is required, the integrating sphere will be used for the following reasons.

- The calibration of the integrating sphere is recent.
- The integrating sphere is equipped with a sensor indicating if steady-state radiance is reached (takes approximately one hour). The tungsten lamps are not equipped with such a device, and it is not possible to check the evolution of its characteristics or if the source was not damaged since last use.
- The integrating sphere is also more practical to place at the focal point of the optical system. Thus, the source of errors due to misalignment is reduced.

However, the intensity of the integrating sphere is weaker by one order of magnitude compared to the tungsten lamps, and the procedure requires more integration time or on-CCD accumulations.

Appendix C

Cross-sections for N_2 excitation, dissociation, and ionization

The simulations presented in Part II rely partially on the accuracy of the dissociation and ionization cross-sections calculated in (Bacri and Medani, 1982). In their paper, their results are compared with a few other values obtained in the literature of 1982, but the discussion could be extended with more recent measurements and calculations. **Our first aim is to compare N_2(X) dissociation, and ionization calculations of Bacri & Medani with the cross-sections included in the Phelps and Itikawa database of LXCat**, see Table C.1**.**

Table C.1 Available cross-sections of excitation and ionization of N_2 (Cartwright *et al.*, 1977; Bacri and Medani, 1982; Itikawa, 2006)

Reference	Bacri & Medani	Cartwright *et al.*	Itikawa
LXCat Database		• Phelps • IST-LISBON	Itikawa
$N_2(X) + e \rightarrow N_2(A, B, a', C) + e$	✓	✓	✓
$N_2(A) + e \rightarrow N_2(B, a', C) + e$	✓		
$N_2(B) + e \rightarrow N_2(a', C) + e$	✓		
$N_2(a') + e \rightarrow N_2(C) + e$	✓		
$N_2(X) + e \rightarrow N_2^+(X, B) + e$	✓	✓	✓
$N_2(X) + e \rightarrow N_2^+(A) + e$	✓		✓
$N_2(X) + e \rightarrow N_2^+(C) + e$	✓		

In Part II, we used the cross-sections of Cartwright *et al.* for the excitation of N_2(X) by electron impact. The data of Cartwright *et al.* are often the reference of calculation and appear in the IST-LISBON and Phelps databases of LXCat. Note that these data were renormalized by Trajmar *et al.* (Cartwright *et al.*, 1977; Trajmar, Register and Chutjian, 1983) and most of the papers refer to (Phelps and Pitchford, 1985) when using these renormalized values. However, new measurements and calculations of these cross-sections are now available. In his review, Itikawa used the cross-sections recommended by Brunger *et*

al. (Brunger, Buckman and Elford, 2005; Itikawa, 2006). Brunger *et al.* usually averaged the cross-sections of selected sources and provided error-bars to their recommendations. The cross-section recommended by Brunger *et al.* are also discussed and compared graphically in (Campbell *et al.*, 2001). In the following, they will be noted "Itikawa database", because they can be found in the Itikawa database. Hence, **our second aim is to compare the N_2(X) excitation cross-sections of Bacri and Medani with those of Itikawa.**

C.1 Electronic excitation of N2(X) by electron impact

More than twenty electronic states of N_2 are organized schematically in Figure C.1 (Laux, 1993). Some of these states can be grouped to simplify the plasma kinetics. In part II, we included in the simulation the excitation to N_2(A), N_2(B), N_2(C), and N_2(a'). The $N_2(B^3\Pi_g, B'\ ^3\Sigma_u^-, W^3\Delta_u)$ states are lumped together in the N_2(B) state, whereas $N_2(C^3\Pi_u, E^3\Sigma_g^+)$ states are lumped in N_2(C). Three singlet states $N_2(a'^1\Sigma_u^-, a^1\Pi_g, w^1\Delta_u)$ states are lumped together in the N_2(a') state.

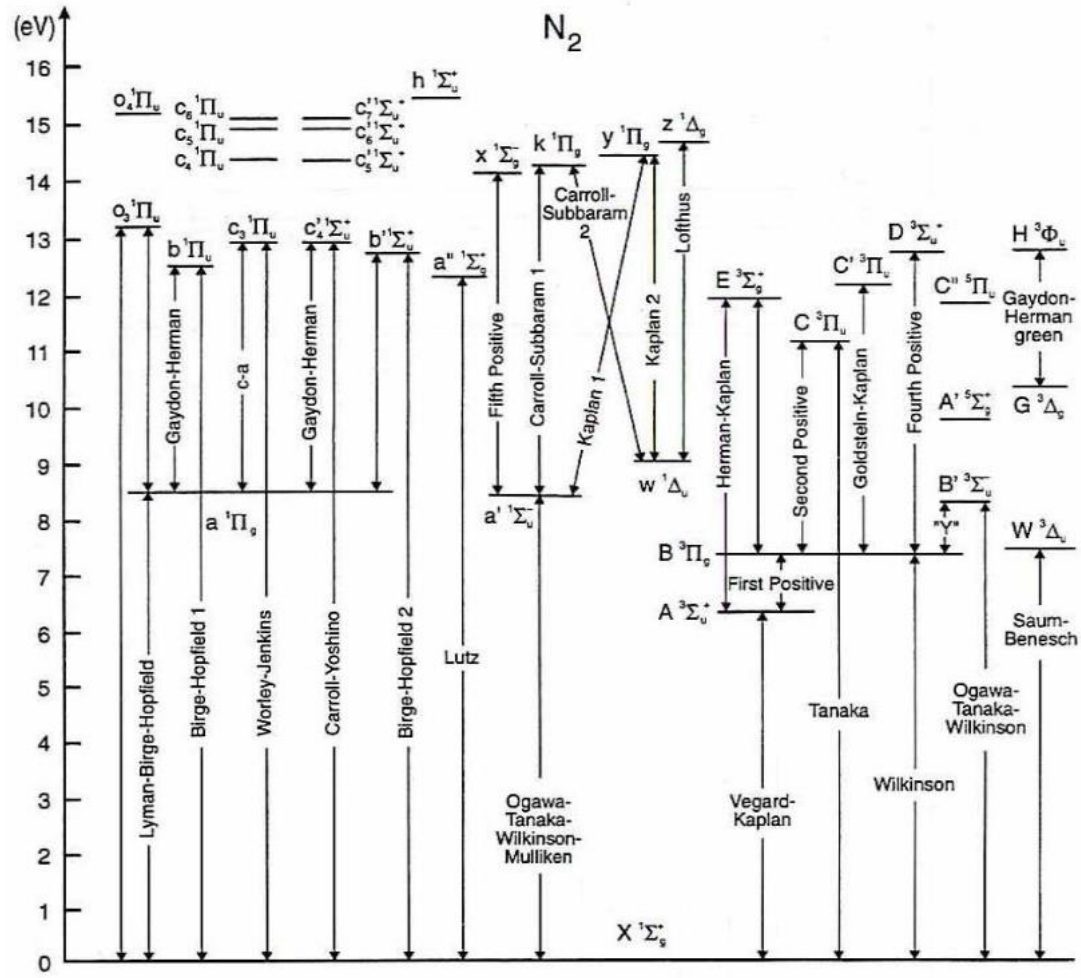

Figure C.1 Electronic states of N_2, reproduced from Figure F.2 of (Laux, 1993)

C.1.1 Electronic excitation to the $N_2(A)$ lumped state

In Figure C.2, we compare the electron impact excitation cross-sections to $N_2(A)$ measured and calculated by several references (Stanton and St. John, 1969; Cartwright *et al.*, 1977; Bacri and Medani, 1982; Trajmar, Register and Chutjian, 1983; Huo and Dateo, 1998; Campbell *et al.*, 2001; Itikawa, 2006). Most of these data are extracted from Figure 3 of (Campbell *et al.*, 2001) and served to build the recommended cross-section of Brunger *et al.* (Brunger, Buckman and Elford, 2005). According to Gillan *et al.*, the peak in the excitation cross-section at 12 eV is "associated with the $B^3\Pi_g$ threshold". This feature is also reproduced in the simulations of Huo and Dateo, taken from Figure 3 of (Campbell *et al.*, 2001), which justify why Brunger *et al.* did not discard it. In this case, the cross-section of Bacri and Medani is two to three-fold higher than the recommended cross-section of Itikawa, whereas that of Cartwright *et al.* that we used in Chapter 5 is twice lower.

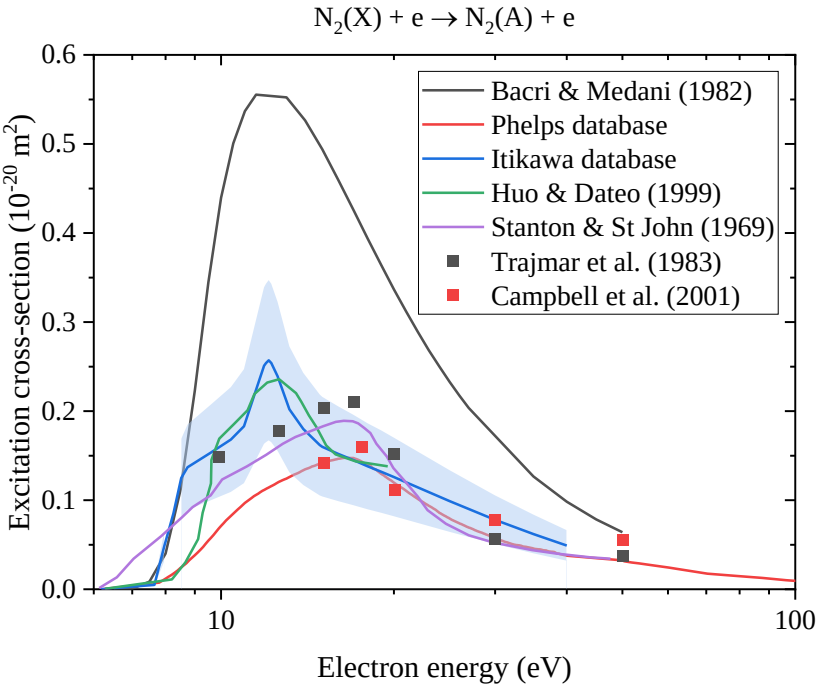

Figure C.2 Electronic excitation cross-section of $N_2(X)$ to $N_2(A)$. The uncertainty on the Itikawa cross-section is of ± 40% for $\varepsilon < 15$ eV and ± 35% for 15 eV $\leq \varepsilon \leq$ 50 eV (Brunger, Buckman and Elford, 2005).

C.1.2 Electronic excitation of $N_2(B)$ lumped state

In Figure A.2, in a similar fashion than for $N_2(A)$, we compare the electron impact excitation cross-sections of $N_2(B^3\Pi_g)$ measured or calculated by several works (Cartwright *et al.*, 1977; Bacri and Medani, 1982; Trajmar, Register and Chutjian, 1983; Campbell *et al.*, 2001; Itikawa, 2006). The cross-section of Bacri and Medani is close to the recommended cross-section by Itikawa, whereas that of Cartwright is below the others. Concerning the $N_2(B'^3\Sigma_u^-)$ and $N_2(W^3\Delta_u)$ states lumped in $N_2(B)$, the cross-sections calculated by Bacri and Medani are increasing too quickly compared to two others, but

their order of magnitude is correct. In Figure C.4, the cross-sections of Cartwright *et al.* is well below that of Itikawa, whereas the correspondence is good in Figure C.5.

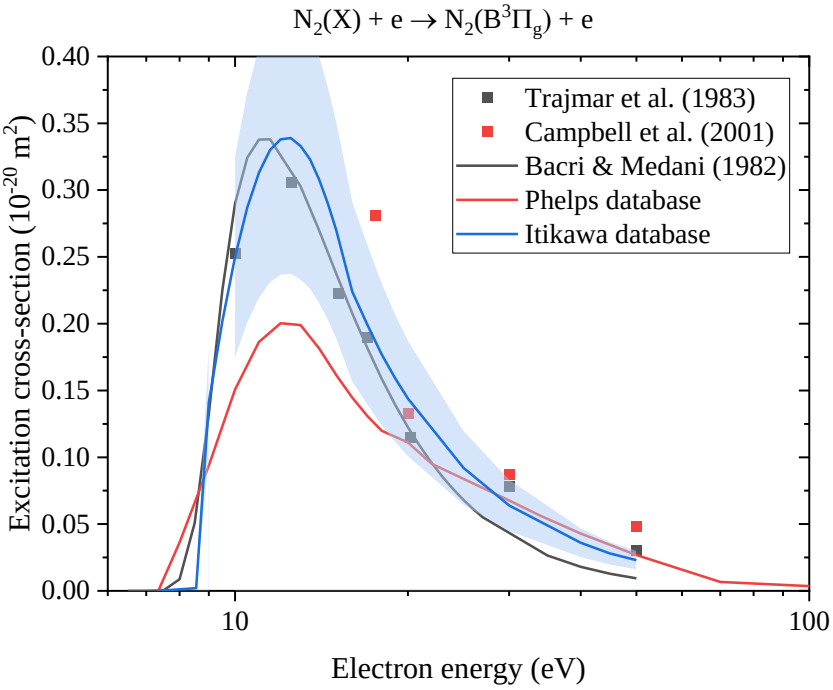

Figure C.3 Electronic excitation cross-section of $N_2(X)$ to $N_2(B^3\Pi_g)$. The Itikawa cross-section's uncertainty is of ± 35% (Brunger, Buckman and Elford, 2005).

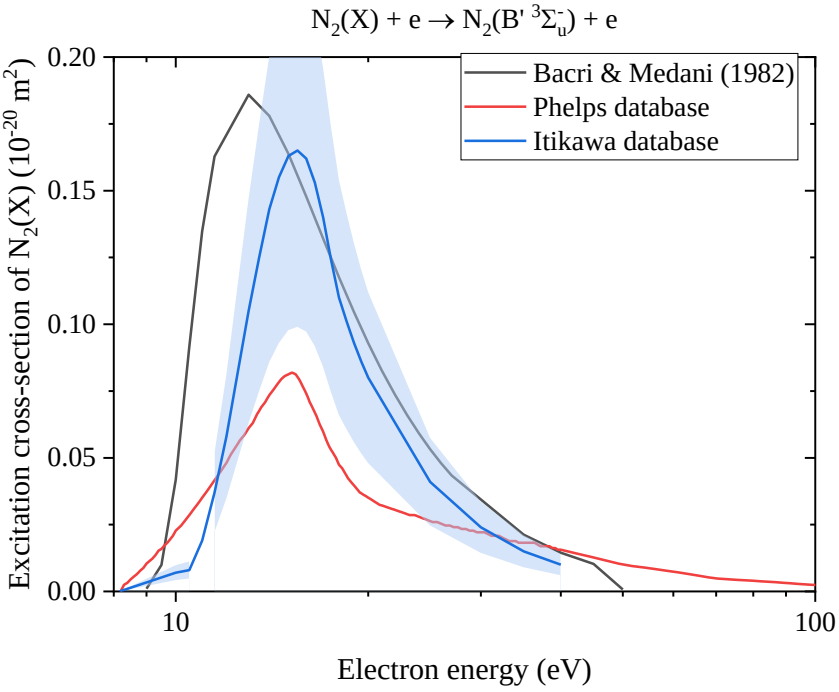

Figure C.4 Electronic excitation cross-section of $N_2(X)$ to $N_2(B' \, ^3\Sigma_u^-)$. The Itikawa cross-section's uncertainty is ± 40% (Brunger, Buckman and Elford, 2005).

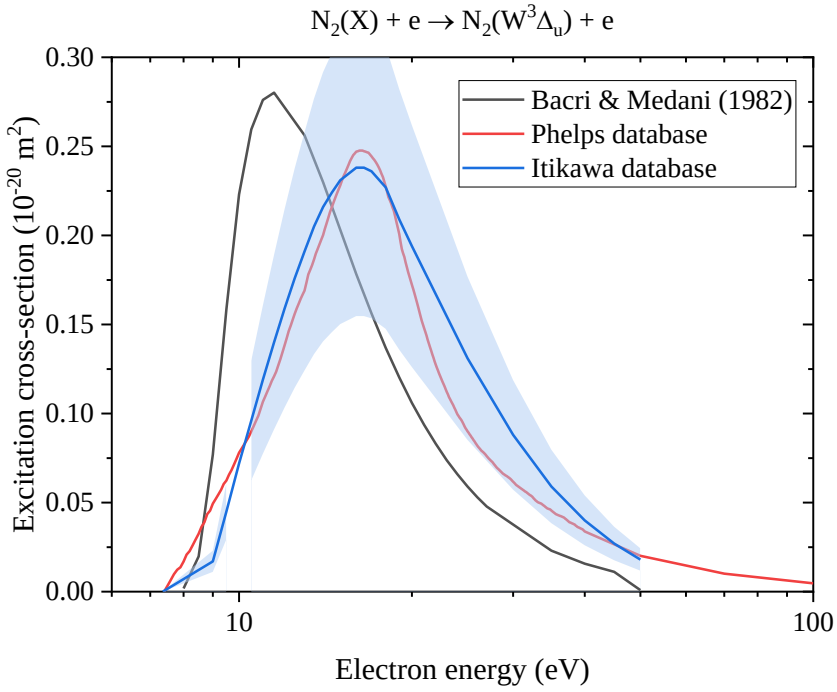

Figure C.5 Electronic excitation cross-section of $N_2(X)$ to $N_2(W^3\Delta_u)$. The Itikawa cross-section's uncertainty is ± 35% (Brunger, Buckman and Elford, 2005).

C.1.3 Electronic excitation to the $N_2(C)$ lumped state

In Figure C.6, the excitation cross-section to $N_2(C)$ shows a good agreement between the work of Cartwright *et al.* and Itikawa. The cross-section calculated by Bacri *et al.* has the right shape but should be multiplied by two to agree with Itikawa.

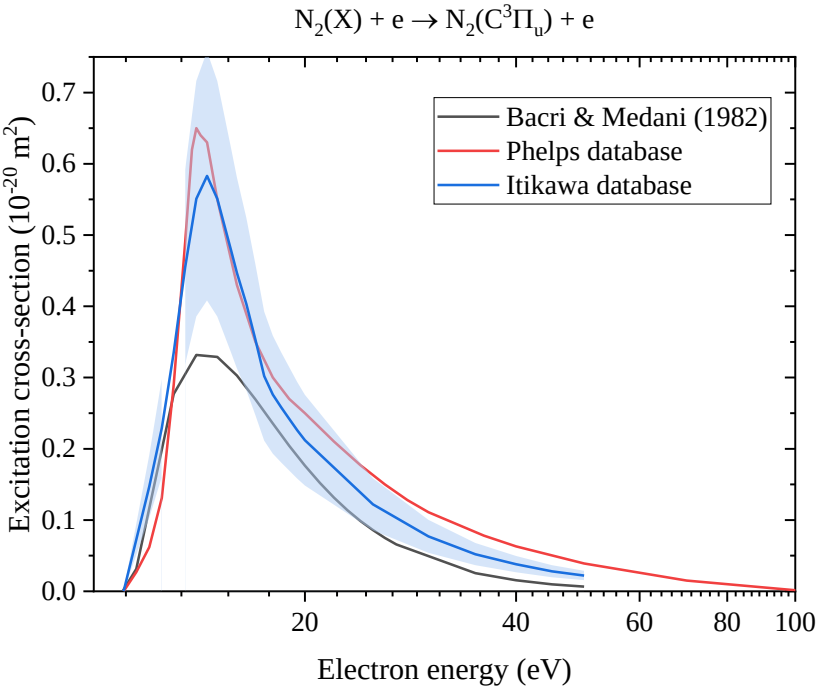

Figure C.6 Electronic excitation cross-section of $N_2(X)$ to $N_2(C^3\Pi_u)$. The Itikawa cross-section's uncertainty is ± 30% (Brunger, Buckman and Elford, 2005).

The excitation cross-sections to $N_2(E^3\Sigma_g^+)$ in Figure C.7 remains a source of uncertainty: none of the three literature references agree. The sharp peak at 11.9 eV in the Itikawa cross-section is due to a resonance whose amplitude was subject to several measurements reported by Brunger *et al.* (Brunger, Buckman and Elford, 2005). However, the uncertainty on the Itikawa cross-section remains relatively high (40%), which is not a problem given the low amplitude of this cross-section.

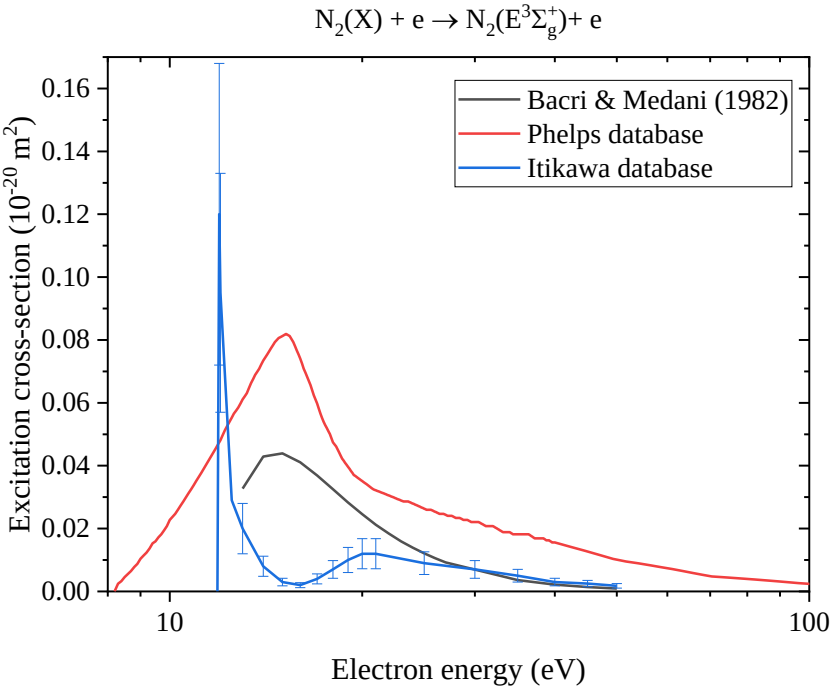

Figure C.7 Electronic excitation cross-section of $N_2(X)$ to $N_2(E^3\Sigma_g^+)$. The Itikawa cross-section's uncertainty is ± 40% (Brunger, Buckman and Elford, 2005).

C.1.4 Electronic excitation to the $N_2(a')$ lumped state

The excitation cross-sections to $N_2(a'^1\Sigma_u^-$, $a^1\Pi_g)$ is provided in Figure C.8, whereas that to $N_2(w^1\Delta_u)$ is given in Figure C.9. Most of the measurements agree[1] on the cross-section of $N_2(w^1\Delta_u)$ and $N_2(a^1\Pi_g)$. However, the cross-sections of Bacri and Medani are not in agreement with that of Itikawa.

The excitation cross-section to $N_2(a')$ is several times higher than that of $N_2(a)$ and $N_2(w)$, which justify why these states are lumped in $N_2(a')$. For excitation to $N_2(a')$, Figure C.8, the cross-section of Bacri and Medani is closer to Itikawa than Cartwright *et al.* Brunger *et al.* report "a very good level of agreement between all the reported integral cross-sections" (Brunger, Buckman and Elford, 2005).

[1] The interested reader can refer to the discussion in (Brunger, Buckman and Elford, 2005) and the Figure 4 of (Campbell *et al.*, 2001).

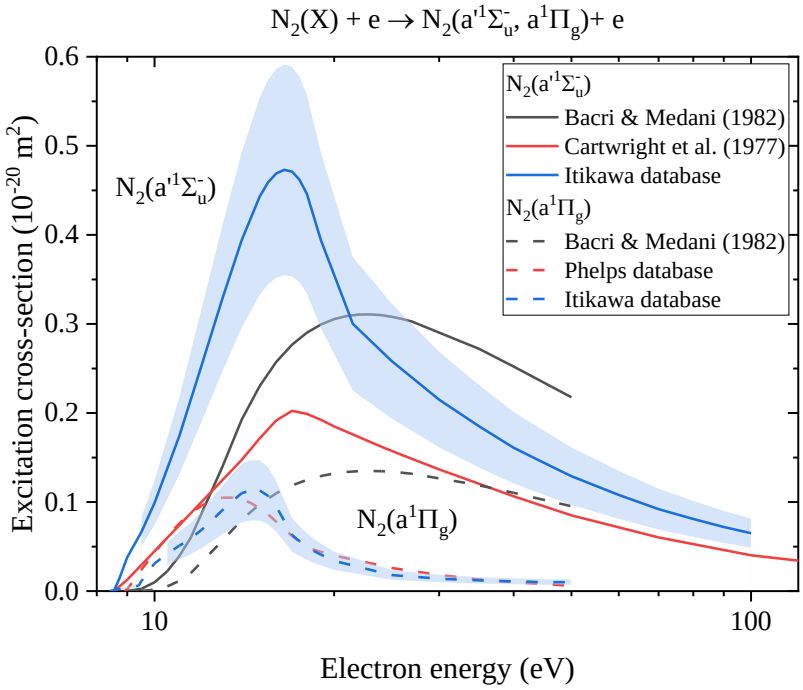

Figure C.8 Electronic excitation cross-section of $N_2(X)$ to $N_2(a^1\Sigma_u^-, a^1\Pi_g)$. The Itikawa cross-section's uncertainty is ± 25% and ± 30% for $N_2(a^1\Sigma_u^-)$ and $N_2(a^1\Pi_g)$, respectively (Brunger, Buckman and Elford, 2005).

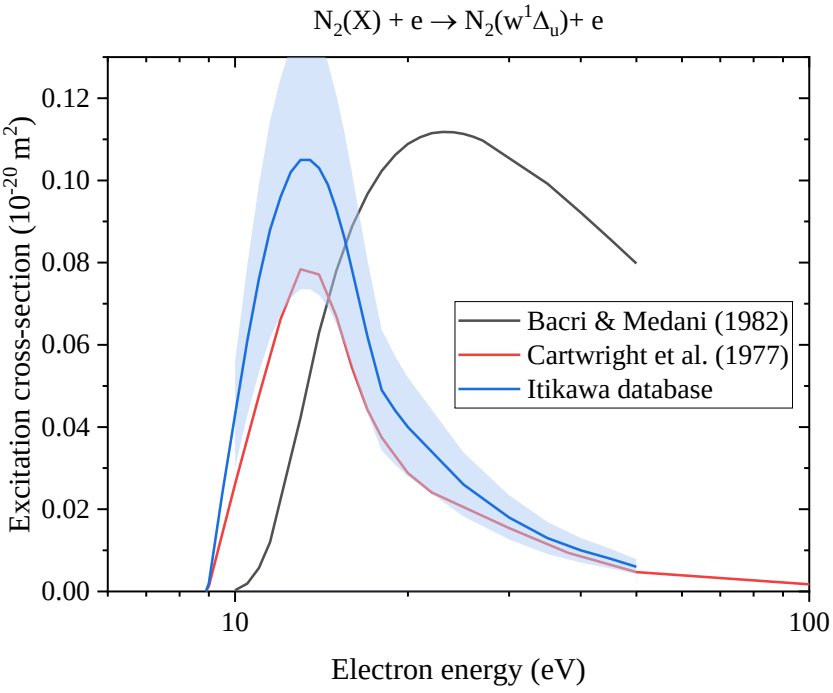

Figure C.9 Electronic excitation cross-section of $N_2(X)$ to $N_2(w^1\Delta_u)$. The Itikawa cross-section's uncertainty is ± 30% (Brunger, Buckman and Elford, 2005).

C.1.5 Partial conclusions

We showed that the Phelps and Itikawa databases do not agree with all excitations. Also, the cross-sections calculated by Bacri and Medani are sometimes outside the error-bars provided by Brunger *et al.* (Itikawa database). However, the cross-sections of $N_2(X)$ excitation calculated by Bacri & Medani's are, in overall, closer to Brunger *et al.* recommendations than that of Cartwright *et al.* Therefore, concerning excitation cross-section from $N_2(A)$, $N_2(B)$, and $N_2(a')$, which cannot be compared to experimental data, we can safely assume these are correct within the same accuracy.

C.2 Dissociation cross-sections of N_2 electronic states

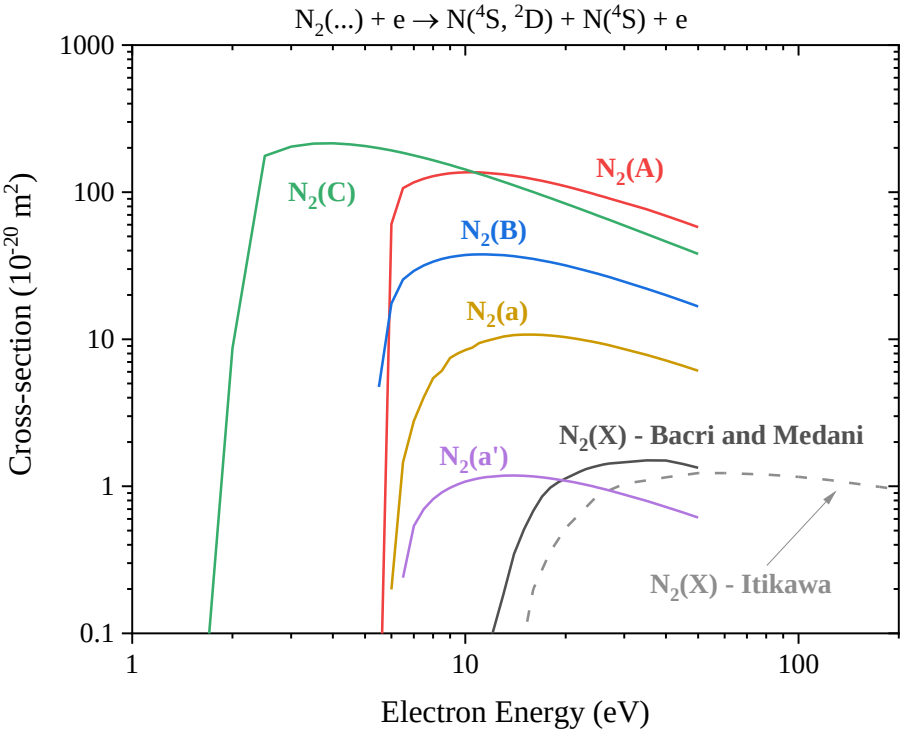

Figure C.10 Dissociation cross-section computed by Bacri and Medani (full lines). The cross-section of $N_2(X)$ recommended by Itikawa is also provided for reference (dashed lines).

In Figure C.10, we demonstrate that the dissociation cross-section of $N_2(X)$ calculated by Bacri and Medani is close to the one recommended by Itikawa. Teulet *et al.* later extended the Weighted Total Cross Section (WTCS) theory used by Bacri and Medani, including higher rovibrational states (Teulet, Sarrette and Gomes, 1999). They provided dissociation rate coefficients which are compared in Figure C.11 to the rates calculated by Bacri and Medani. For $N_2(X)$ dissociation cross-section, at $T_e > 10000$ K, the rate calculated by Teulet *et al.* is one order of magnitude higher than that of Bacri & Medani. The comparison in Figure C.11 shows that the dissociation cross-sections of $N_2(A)$ and $N_2(B)$ calculated by Bacri and Medani might be overestimated. However, it also confirms that the relative magnitude of these cross-sections is correct.

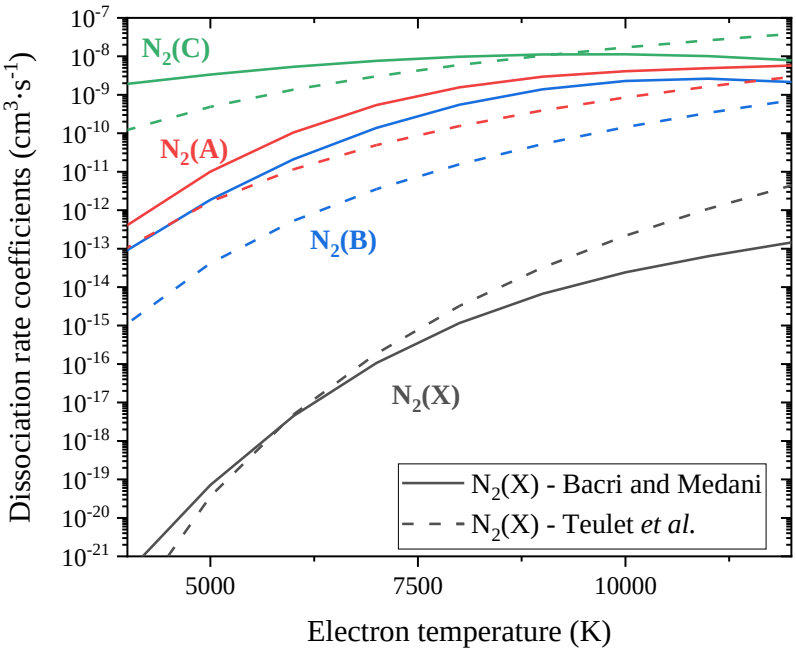

Figure C.11 Comparison of the dissociation rate coefficient of N_2(X, A, B, C) calculated by Bacri and Medani (full lines) and Teulet *et al.* (dashed lines) using the WTCS theory (Bacri and Medani, 1982; Teulet, Sarrette and Gomes, 1999)

It was shown that dissociation mainly occurs due to excitation to pre-dissociative singlet states (Zipf and McLaughlin, 1978; Cosby, 1993). These states are also found to produce principally N(^{4}S) and N(^{2}D) fragments (Cosby, 1993; Walter, Cosby and Helm, 1993). The absence of two N(^{4}S) fragments is explained by the absence of crossing of the singlet states and the N_2(A) and $N_2(^7\Sigma_u^+)$ states.

C.3 Ionization cross-sections of N_2 electronic states

C.3.1 Ionization cross-sections of N_2(X)

Usually, the total cross-sections of N_2 ionization are available, but partial cross-sections to N_2^+, N^+, and N^{++} are scarce. The differentiation of the final electronic states, N_2^+(X, A, B, C) in this case, is even more challenging to find. In his review, Itikawa provided ionization cross-sections for the ionization of N_2(X) to N_2^+, N^+, and N^{++} (Itikawa, 2006). Based on available cross-sections, he also recommended a normalization constant for each electronic state of N_2^+. These partial cross-sections are reproduced in Figure C.12 and compared to those calculated by Bacri and Medani. As noted by Bacri and Medani, their cross-section maxima are slightly shifted to lower energies (peak located at 60 – 70 eV instead of 100 eV), but their values correspond to those reviewed later by Itikawa. Partial ionization cross-sections to N_2^+(X) and N_2^+(B) are also available[1] in (Isola, Gómez and Guerra, 2010). However, Isola *et al.* used the total ionization cross-section measured by (Rapp and Englander-Golden, 1965), which includes the formation of N^+ and N^{++}. Also, they did not subtract the partial ionization to N_2^+(A), which is a dominant partial cross-section (Bacri and Medani, 1982; Itikawa, 2006). According to Itikawa, the ionization cross-section from N_2(X) to N_2^+(X) is equal to 7.03×10^{17} cm^{-2} at 100 eV, whereas the same cross-section is equal to 21.07×10^{17} cm^{-2} in the LXCat *LISBON database.* Therefore, the partial cross-sections of Isola *et al.* to N_2^+(X) is overestimated by a factor of two because it includes dissociative ionization and the partial cross-sections to N_2^+(A).

[1] Downloaded from the LXCat *LISBON database* (updated in 2012).

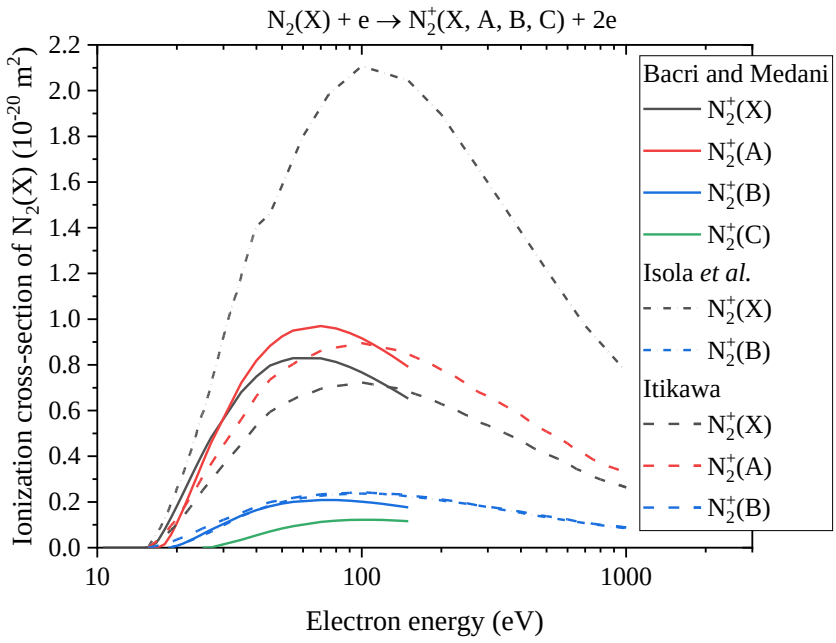

Figure C.12 Partial ionization cross-sections of $N_2(X)$. We emphasize the differences between the values recommended by Itikawa, those calculated by Bacri and Medani, and those estimated by Isola *et al.* (Bacri and Medani, 1982; Itikawa, 2006; Isola, Gómez and Guerra, 2010)

C.3.2 Ionization cross-sections of electronically excited states of N_2

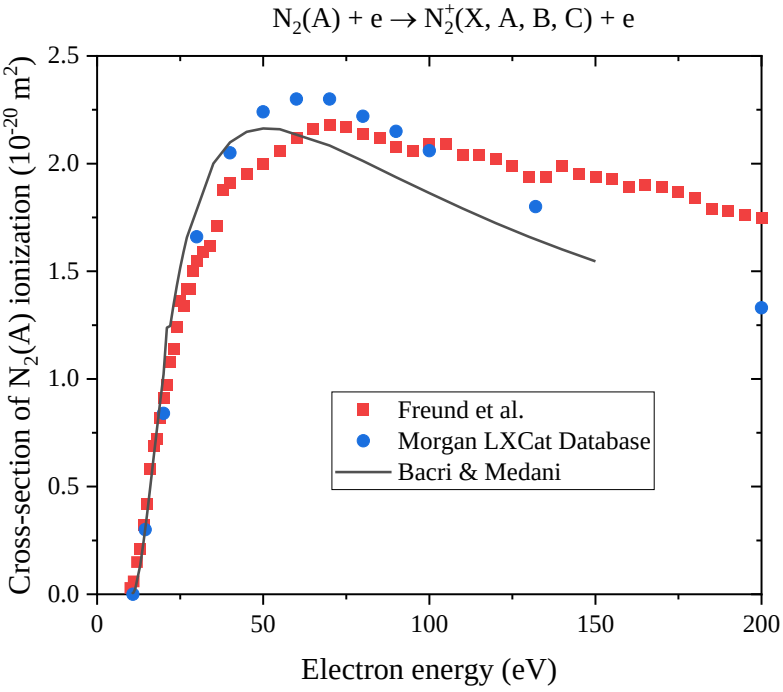

Figure C.13 Ionization cross-section of $N_2(A)$ calculated by Bacri & Medani compared with the indirect measurements of Freund *et al.* and the Morgan LXCat Database.

In Figure C.13, we compare the ionization cross-section of $N_2(A)$ calculated by (Bacri and Medani, 1982) and measured indirectly by (Freund, Wetzel and Shul, 1990). The agreement is relatively good with a maximum discrepancy of 22% at $\varepsilon = 150$ eV. As it was observed for the $N_2(X)$ cross-sections, the maximum in the calculation of Bacri & Medani is slightly shifted to the low energies compared to the experiments but the two cross-sections remain close. These two sets are also in agreement with the data available in the Morgan LXCat Database (Pancheshnyi *et al.*, 2012).

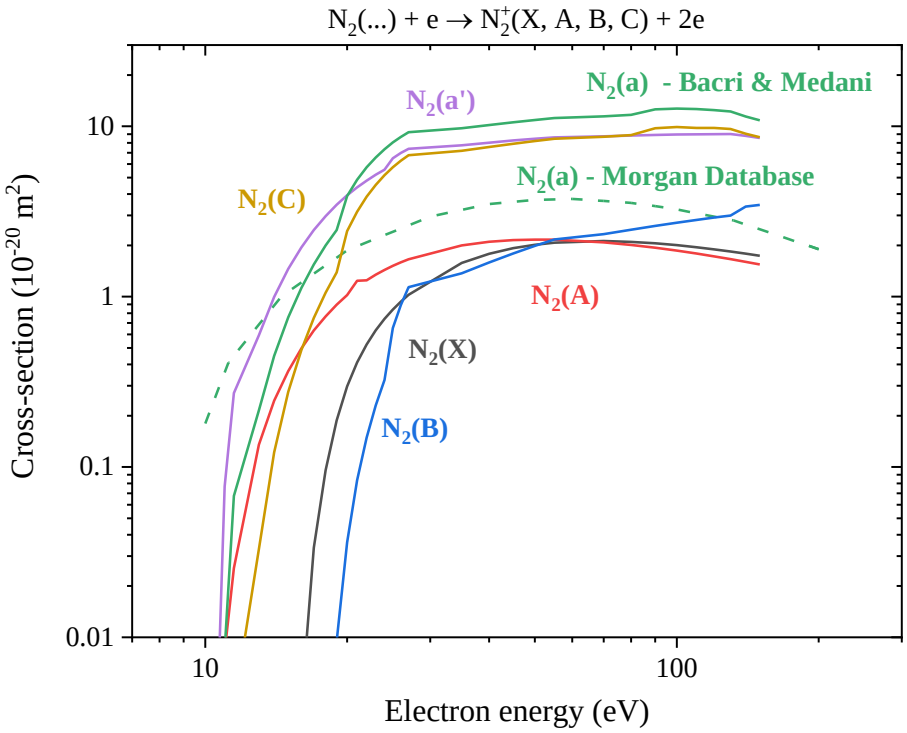

Figure C.14 Ionization cross-sections of $N_2(X)$, $N_2(A)$, $N_2(B)$, $N_2(C)$, $N_2(a)$, and $N_2(a')$ to the parent ion calculated by Bacri and Medani (full lines). The $N_2(a)$ ionization cross-section in the Morgan LXCat database is also shown for reference (dashed line).

In Figure C.14, the ionization cross-section of N_2 electronic states calculated by (Bacri and Medani, 1982) are provided. Two groups of cross-sections are formed:

- The states prompt to ionization: $N_2(C)$, $N_2(a')$, and $N_2(a)$.
- The states resistant to ionization: $N_2(X)$, $N_2(A)$, and $N_2(B)$.

The cross-section of $N_2(a)$ in the Morgan Database lies between these two groups. This difference is unexpected, given that the relative difference for $N_2(A)$ ionization cross-sections is small (Figure C.13). However, no other comparison is available to our knowledge.

C.4 Conclusions

Based on the comparisons developed in this appendix, we develop several conclusions and directions for future work. We used the Itikawa LXCat Database as a reference for comparisons (Itikawa, 2006). This database was built on the recommendations of (Brunger, Buckman and Elford, 2005). We first remark that the N_2 electronic excitation cross-sections in the Phelps LXCat Database, based on the historical measurements of (Cartwright *et al.*, 1977) and the normalization of (Trajmar, Register and Chutjian, 1983), are most of the time not in agreement with Itikawa's cross-section. Cartwright *et al.*'s measurements were the first of their kind and are still a reference in the community[1], which justify why they were chosen in the first place in our simulations. For future work, we recommend replacing these excitation cross-sections with those of Itikawa.

Concerning dissociation cross-sections of N_2 electronic states, we showed in Section C.2 that the calculations of (Bacri and Medani, 1982) could be improved. The relative amplitude of the cross-sections is however correct, compared to the calculations of (Teulet, Sarrette and Gomes, 1999).

Finally, the partial ionization cross-sections calculated by (Bacri and Medani, 1982) compare well with those recommended in (Itikawa, 2006). The partial ionization cross-section of (Isola, Gómez and Guerra, 2010) is overestimated because it includes the ionization cross-section to $N_2^+(A)$ and N^+.

[1] See for instance the IST-Lisbon database.

Appendix D

Synthèse

If the thesis is written in English, the French legislation imposes to produce an extended abstract of the thesis in French.

Cette thèse porte sur l'étude de la formation et de la recombinaison d'un plasma complétement ionisé généré par une impulsion électrique de quelques nanosecondes. Dans une première partie, les aspects théoriques et pratiques des diagnostics employés dans cette thèse sont décrits. Des rappels fondamentaux sur les fonctions de partitions sont employés pour ensuite décrire la détermination de la température des plasmas par spectroscopie d'émission. Une étude détaillée de l'élargissement de raies atomique est entreprise, afin de mesurée la densité des électrons par élargissement Stark. Elle est suivie par une description simplifiée de la fluorescence induite par laser en se servant d'un modèle à deux niveaux. Finalement, la mesure de tension et courant dans les décharges Nanosecondes Répétitives Pulsées (NRP) est décrite. L'interprétation des mesures d'énergie est aussi discutée.

Dans une deuxième partie, un état de l'art des observations de décharges complétement ionisées est entrepris. Un court résumé des simulations de décharges nanosecondes est donné. Cette étude bibliographique montre que des décharges nanosecondes peuvent générer des plasmas complétement ionisés mais qu'aucun modèle ne parvient à expliquer un tel état de la matière. Nous montrons ensuite que, dans nos expériences, la formation d'une décharge complétement ionisée se décompose en cinq étapes : (i) ionisation partielle de l'espace inter-électrode, (ii) formation d'un filament à la cathode, (iii) formation d'un filament à l'anode, (iv) propagation des filaments et (v) fusion des filaments. Ces derniers sont caractérisés par une émission intense de N^+ et d'un continuum des électrons. Cette chronologie en cinq étapes est applicable aux mesures de la littérature. La densité des électrons est mesurée par élargissement Stark de H_α et N^+, mais aussi en se servant de l'émission continue des électrons. La calibration absolue de la spectroscopie d'émission permet d'obtenir le rayon de la décharge, grâce aux raies de N^+ et O^+. Dans les filaments, nos mesures montrent que la densité d'électrons augmente de 10^{17} à 10^{19} cm^{-3} en moins de 0.5 ns. Cette augmentation abrupte est due à l'ionisation des états excités de N et O, comme le montre un mécanisme cinétique développé dans cette thèse. Le plasma complétement ionisé est à l'équilibre chimique et thermique. Après que l'ionisation complète est atteinte, la densité et la température des électrons décroissent en raison d'une expansion isentropique de la colonne de plasma.

Finalement, dans une troisième partie, les décharges NRP sont utilisées en régime hors-équilibre dans deux brûleurs afin de réaliser des études fondamentales et appliquées en combustion assistée par plasma.

Suite à une revue, nous montrons que les modèles de combustion assistée par plasma doivent encore être améliorés pour être plus prédictifs. Ensuite, nous décrivons le brûleur Mini-PAC, avec et sans assistance plasma. Les décharges NRP déposent 2 mJ par pulse à une fréquence de 20 kHz. La puissance théorique de la flamme de méthane est de 13.6 kW. Une imagerie des radicaux CH* et OH* pendant la transition entre la flamme « weak » et la flamme assistée par plasma montre que les zone de contact entre les gaz frais et la zone de recirculation devient très réactive. Cette mesure est confirmée par fluorescence induite par laser du radical OH. La mesure de la densité d'OH est comparée à un modèle simplifié de combustion assistée par plasma. L'accord montre que le modèle simplifié est à même de décrire le processus de stabilisation. Dans le brûleur Mini-PAC, près des électrodes, la spectroscopie d'émission montre que la température du plasma augmente de 1500 K en raison d'une "lente" formation d'un filament. Au centre de la décharge, l'augmentation de la température est plus modérée, environ 200 K. Cette augmentation est attendue si l'on considère le phénomène de chauffage ultrarapide par quenching des états excités de N_2 par O_2. Les décharges NRP accélèrent la réactivité de la flamme comme le montre l'augmentation de la densité des espèces excitées dans le plasma. Parmi ces espèces, les densités de $N_2(B)$, $N_2(C)$, OH(A), CN(B), NH(A) et $N_{2+}(B)$ sont mesurées par spectroscopie d'émission calibrée. Dans le brûleur SICCA, les décharges NRP sont aussi appliquées. Ces décharges sont plus énergétiques (5 mJ) mais toujours hors-équilibre. La puissance des flammes de méthane, n-heptane et dodécane est d'environ 5 kW. Lorsqu'elles sont appliquées, les décharges NRP réduisent l'instabilité des flammes oscillantes (à environ 10 Hz) et étendent ainsi leur limite d'extinction pauvre. Les flammes de spray sont particulièrement promptes à l'extinction lors de ces oscillations et une amélioration significative de la résistance à l'extinction est obtenue en utilisant des décharges NRP. Une modulation de trains de décharges NRP permet de réduire le coût énergétique de l'assistance plasma tout en améliorant significativement la limite d'extinction d'une flamme d'heptane.

References

Alberty, R. A. and Silbey, R. J. (1992) *Physical chemistry 1st Edition*. John Wiley & Sons, Inc.

Albrecht, H. *et al.* (1977) 'New Aspects on Spark Ignition', *SAE Technical Papers*. SAE International, p. 770853. doi: 10.4271/770853.

Albugues, F. *et al.* (1974) 'Destruction of the levels C3Πu (v′ = O, v′ = 1) of nitrogen by O2, CO2, CH4, and H2O', *The Journal of Chemical Physics*. American Institute of Physics, 61(7), pp. 2695–2699. doi: 10.1063/1.1682401.

Aleksandrov, N. L. *et al.* (2010) 'Mechanism of ultra-fast heating in a non-equilibrium weakly ionized air discharge plasma in high electric fields', *Journal of Physics D: Applied Physics*, 43(25), p. 255201. doi: 10.1088/0022-3727/43/25/255201.

Ali, A. W. and Griem, H. R. (1965a) '[Errata] Theory of resonance broadening of spectral lines by atom-atom impacts', *Physical Review*, 140(4A), p. 891. doi: 10.1103/PhysRev.140.A1044.

Ali, A. W. and Griem, H. R. (1965b) 'Theory of resonance broadening of spectral lines by atom-atom impacts', *Physical Review*, 140(4A), p. 891. doi: 10.1103/PhysRev.140.A1044.

Allard, N. F. *et al.* (2008) 'Self-broadening of the hydrogen Balmer α line', *Astronomy and Astrophysics*, 480, p. 581. doi: 10.1051/0004-6361:20078437.

Allard, N. and Kielkopf, J. (1982) 'The effect of neutral nonresonant collisions on atomic spectral lines', *Reviews of Modern Physics*, 54(4), pp. 1103–1182. doi: 10.1103/RevModPhys.54.1103.

Alves, L. L. (2014) 'The IST-LISBON database on LXCat', in *Journal of Physics: Conference Series*. doi: 10.1088/1742-6596/565/1/012007.

Annaloro, J. *et al.* (2017) 'Non-uniqueness of the multi-temperature law of mass action. Application to 2T plasma composition calculation by means of a collisional-radiative model', *European Physical Journal D*, 71(12). doi: 10.1140/epjd/e2017-80284-5.

Babický, V. *et al.* (2018) ' Spectroscopic characteristics of H α /O I atomic lines generated by nanosecond pulsed corona-like discharge in deionized water ', *Journal of Physics D: Applied Physics*, 51(12), p. 124001. doi: 10.1088/1361-6463/aaabb1.

Bacri, J. and Medani, A. (1982) 'Electron diatomic molecule weighted total cross section calculation. III. Main inelastic processes for N2 and N2+', *Physica B+C*, 112(1), pp. 101–118. doi: 10.1016/0378-4363(82)90136-X.

Bak, M. S. and Cappelli, M. A. (2015) ‘A reduced set of air plasma reactions for nanosecond pulsed plasmas’, *IEEE Transactions on Plasma Science*, 43(4), pp. 995–1001. doi: 10.1109/TPS.2015.2409300.

Balamuta, J. and Golde, M. F. (1982) ‘Formation of electronically excited oxygen atoms in the reactions of Ar(3P0,2) and Xe(3P2) atoms with O2’, *Journal of Physical Chemistry*. American Chemical Society, 86(14), pp. 2765–2769. doi: 10.1021/j100211a041.

Bane, S. P. M., Ziegler, J. L. and Shepherd, J. E. (2015) ‘Investigation of the effect of electrode geometry on spark ignition’, *Combustion and Flame*, 162(2), pp. 462–469. Available at: http://www.sciencedirect.com/science/article/pii/S0010218014002120.

Barbosa, S. *et al.* (2015) ‘Influence of nanosecond repetitively pulsed discharges on the stability of a swirled propane/air burner representative of an aeronautical combustor’, *Philosophical Transactions of the Royal Society A: Mathematical, Physical and Engineering Sciences*, 373(2048), p. 20140335. doi: 10.1098/rsta.2014.0335.

Barreto, E., Jurenka, H. and Reynolds, S. I. (1977) ‘The formation of small sparks’, *Journal of Applied Physics*. American Institute of Physics, 48(11), pp. 4510–4520. doi: 10.1063/1.323465.

Bastiaans, G. J. and Mangold, R. A. (1985) ‘The calculation of electron density and temperature in Ar spectroscopic plasmas from continuum and line spectra’, *Spectrochimica Acta Part B: Atomic Spectroscopy*, 40(7), pp. 885–892. doi: 10.1016/0584-8547(85)80059-8.

Bastien, F. and Marode, E. (1977) ‘Stark broadening of Hα and Hβ in ionized gases with space-charge field’, *Journal of Quantitative Spectroscopy and Radiative Transfer*, 17(4), pp. 453–469. doi: 10.1016/0022-4073(77)90093-0.

Bastien, F. and Marode, E. (1979) ‘The determination of basic quantities during glow-to-arc transition in a positive point-to-plane discharge’, *Journal of Physics D: Applied Physics*, 12(2), pp. 249–263. doi: 10.1088/0022-3727/12/2/010.

Bechane, Y. (2021) *Simulations numériques de la combustion assistée par plasma*. Université Paris-Saclay, PhD Thesis (in preparation).

Bechane, Y. and Fiorina, B. (2020) ‘Numerical investigations of turbulent premixed flame ignition by a series of Nanosecond Repetitively Pulsed discharges’, *Proceedings of the Combustion Institute*. Elsevier. doi: 10.1016/j.proci.2020.06.258.

Brau, C. A. and Jonkman, R. M. (1970) ‘Classical theory of rotational relaxation in diatomic gases’, *The Journal of Chemical Physics*. American Institute of Physics, 52(2), pp. 477–484. doi:

10.1063/1.1673010.

Bruggeman, P. J. *et al.* (2014) ‘Gas temperature determination from rotational lines in non-equilibrium plasmas: a review’, *Plasma Sources Science and Technology*, 23(2), p. 23001. doi: 10.1088/0963-0252/23/2/023001.

Brunger, M., Buckman, S. J. and Elford, M. T. (2005) ‘6.4 Excitation cross sections’, *Interactions of Photons and Electrons with Molecules*, pp. 6118–6201. doi: 10.1007/10874891_7.

Burnette, D. *et al.* (2014) ‘Nitric oxide kinetics in the afterglow of a diffuse plasma filament’, *Plasma Sources Science and Technology*, 23(4), p. 045007. doi: 10.1088/0963-0252/23/4/045007.

Campbell, I. M. and Thrush, B. A. (1966) ‘Behaviour of carbon dioxide and nitrous oxide in active nitrogen’, *Transactions of the Faraday Society*. Royal Society of Chemistry, 62(0), pp. 3366–3374. doi: 10.1039/tf9666203366.

Campbell, L. *et al.* (2001) ‘Integral cross sections for electron impact excitation of electronic states of N 2’, *Journal of Physics B: Atomic, Molecular and Optical Physics*, 34(7), pp. 1185–1199. doi: 10.1088/0953-4075/34/7/303.

Del Campo, F. G. *et al.* (2017) ‘Preliminary results from a plasma-assisted 7-point Lean Direct Injection (LDI) combustor and resulting impacts on combustor stability and combustion dynamics’, in *53rd AIAA/SAE/ASEE Joint Propulsion Conference, 2017*. Reston, Virginia: American Institute of Aeronautics and Astronautics. doi: 10.2514/6.2017-4778.

Capitelli, M. *et al.* (2000) *Plasma Kinetics in Atmospheric Gases*. Berlin, Heidelberg: Springer Berlin Heidelberg (Springer Series on Atomic, Optical, and Plasma Physics). doi: 10.1007/978-3-662-04158-1.

Capitelli, M. *et al.* (2017) ‘Self-consistent time dependent vibrational and free electron kinetics for CO2 dissociation and ionization in cold plasmas’, *Plasma Sources Science and Technology*. IOP Publishing, 26(5). doi: 10.1088/1361-6595/aa6427.

Cartwright, D. C. *et al.* (1977) ‘Electron impact excitation of the electronic states of N2. I. Differential cross sections at incident energies from 10 to 50 eV’, *Physical Review A*. American Physical Society, 16(3), pp. 1013–1040. doi: 10.1103/PhysRevA.16.1013.

Castela, M. *et al.* (2017) ‘A 3-D DNS and experimental study of the effect of the recirculating flow pattern inside a reactive kernel produced by nanosecond plasma discharges in a methane-air mixture’, *Proceedings of the Combustion Institute*. Elsevier Ltd, 36(3), pp. 4095–4103. doi: 10.1016/j.proci.2016.06.174.

Castera, P. (2015) *Energy coupling mechanisms in pulsed surface discharges for flow control*. Ecole Centrale Paris, PhD Thesis. Available at: http://www.theses.fr/2015ECAP0041.

Ciccarino, C. J. and Savin, D. W. (2019) 'Electron-impact ionization of atomic nitrogen', *Journal of Thermophysics and Heat Transfer*. American Institute of Aeronautics and Astronautics, 33(1), pp. 154–162. doi: 10.2514/1.T5463.

Colonna, G., D'Angola, A. and Capitelli, M. (2012) 'Electronic excitation and isentropic coefficients of high temperature planetary atmosphere plasmas', *Physics of Plasmas*. American Institute of Physics, 19(7), p. 072115. doi: 10.1063/1.4737190.

Cosby, P. C. (1993) 'Electron-impact dissociation of nitrogen', *The Journal of Chemical Physics*. American Institute of PhysicsAIP, 98(12), pp. 9544–9559. doi: 10.1063/1.464385.

Croonenbroek, T. (1996) *Diagnostics optiques appliques aux milieux reactifs. Application aux flammes laminaires etirees a contre-courant*. Paris 6, PhD Thesis, in French.

Demtröder, W. (2008) *Laser spectroscopy: Fourth edition*, *Laser Spectroscopy: Fourth Edition*. Springer Berlin Heidelberg. doi: 10.1007/978-3-540-73418-5.

Dere, K. P. *et al.* (1997) 'CHIANTI - an atomic database for emission lines', *Astronomy and Astrophysics Supplement Series*. EDP Sciences, 125(1), pp. 149–173. doi: 10.1051/aas:1997368.

Dere, K. P. *et al.* (2019) 'CHIANTI—An Atomic Database for Emission Lines. XV. Version 9, Improvements for the X-Ray Satellite Lines', *The Astrophysical Journal Supplement Series*. American Astronomical Society, 241(2), p. 22. doi: 10.3847/1538-4365/ab05cf.

Dilecce, G., Ambrico, P. F. and De Benedictis, S. (2007) 'On N2(C3Πu, v = 0) state lifetime and collisional deactivation rate by N2', *Chemical Physics Letters*. North-Holland, 444(1–3), pp. 39–43. doi: 10.1016/j.cplett.2007.07.004.

Ding, C. *et al.* (2019) 'Filamentary nanosecond surface dielectric barrier discharge. Experimental comparison of the streamer-to-filament transition for positive and negative polarities', *Plasma Sources Science and Technology*, 28(8), p. 085005. doi: 10.1088/1361-6595/ab2d7a.

Djurovi'c, S. and Konjevi'c, N. (2009) 'On the use of non-hydrogenic spectral lines for low electron density and high pressure plasma diagnostics', *Plasma Sources Science and Technology*, 18(3), pp. 1–8. doi: 10.1088/0963-0252/18/3/035011.

Drake, G. W. F. (2006) *Atomic, Molecular, and Optical Physics*. Springer, New York. Available at: http://www.springer.com/physics/atoms/book/978-0-387-20802-2.

Dresvin, S. V. (1977) *Physics and technology of low-temperature plasmas*. English Ed. Press, The Iowa State University.

Dumitrache, C. *et al.* (2019) 'Hydrodynamic regimes induced by nanosecond pulsed discharges in air: mechanism of vorticity generation', *Journal of Physics D: Applied Physics*, 52(36), p. 364001. doi: 10.1088/1361-6463/ab28f9.

Dutuit, O. *et al.* (2013) 'Critical review of N, N+, N+2, N ++, and N++2 main production processes and reactions of relevance to titan's atmosphere', *Astrophysical Journal, Supplement Series*, 204(2). doi: 10.1088/0067-0049/204/2/20.

Field, G. B., Somerville, W. B. and Dressler, K. (1966) 'Hydrogen Molecules in Astronomy', *Annual Review of Astronomy and Astrophysics*, 4(1), pp. 207–244. doi: 10.1146/annurev.aa.04.090166.001231.

Flitti, A. and Pancheshnyi, S. (2009) 'Gas heating in fast pulsed discharges in N 2 –O 2 mixtures', *The European Physical Journal Applied Physics*. EDP Sciences, 45(2), p. 21001. doi: 10.1051/epjap/2009011.

Flow and combustion in reciprocating engines (2009) *Experimental fluid mechanics*. Berlin: Springer.

Foucher, F. *et al.* (2013) 'Influence of ozone on the combustion of n-heptane in a HCCI engine', *Proceedings of the Combustion Institute*, 34(2), pp. 3005–3012. doi: 10.1016/j.proci.2012.05.042.

Freund, R. S., Wetzel, R. C. and Shul, R. J. (1990) 'Measurements of electron-impact-ionization cross sections of N2, CO, CO2, CS, S2, CS2, and metastable N2', *Physical Review A*. American Physical Society, 41(11), pp. 5861–5868. doi: 10.1103/PhysRevA.41.5861.

Galley, D. *et al.* (2005) 'Plasma-Enhanced Combustion of a Lean Premixed Air-Propane Turbulent Flame using a Nanosecond Repetitively Pulsed Plasma', in *43rd AIAA Aerospace Sciences Meeting and Exhibit*. Reston, Virigina: American Institute of Aeronautics and Astronautics. doi: 10.2514/6.2005-1193.

Gaydon, A. G. (1974) *The Spectroscopy of Flames*. Springer Netherlands.

De Giacomo, A. *et al.* (2010) 'The role of continuum radiation in laser induced plasma spectroscopy', *Spectrochimica Acta - Part B Atomic Spectroscopy*. Elsevier B.V., 65(5), pp. 385–394. doi: 10.1016/j.sab.2010.03.016.

Gigosos, M. A. *et al.* (1996) 'New plasma diagnosis tables of hydrogen Stark broadening including ion dynamics', *Journal of Physics B: Atomic, Molecular and Optical Physics*, 29(20), pp. 4795–4838. doi: 10.1088/0953-4075/29/20/029.

Gigosos, M. A., González, M. Á. and Cardeñoso, V. (2003) 'Computer simulated Balmer-alpha, -beta and -gamma Stark line profiles for non-equilibrium plasmas diagnostics', *Spectrochimica Acta - Part B Atomic Spectroscopy*. Elsevier, 58(8), pp. 1489–1504. doi: 10.1016/S0584-8547(03)00097-1.

Gilmore, F. R. (1965) 'Potential energy curves for N2, NO, O2 and corresponding ions', *Journal of Quantitative Spectroscopy and Radiative Transfer*, 5(2), pp. 369–389.

Gökçen, T. (2007) 'N2 - CH4 - Ar chemical kinetic model for simulations of titan atmospheric entry', *Journal of Thermophysics and Heat Transfer*, 21(1), pp. 9–18. doi: 10.2514/1.22095.

Griem, H. R. (1964) *Plasma spectroscopy*. Edited by McGraw-Hill. New York: McGraw-Hill Book Company.

Griem, H. R. (1974) *Spectral Line Broadening by Plasmas*. New York: ACADEMIC PRESS, INC.

Griem, H. R. (1997) *Principles of Plasma Spectroscopy, Principles of Plasma Spectroscopy*. Cambridge University Press. doi: 10.1017/cbo9780511524578.

Guerra, V. *et al.* (2019) 'Modelling N 2 –O 2 plasmas: volume and surface kinetics', *Plasma Sources Science and Technology*, 28(7), p. 073001. doi: 10.1088/1361-6595/ab252c.

Hagelaar, G. J. M. (2016) 'Coulomb collisions in the Boltzmann equation for electrons in low-temperature gas discharge plasmas', *Plasma Sources Science and Technology*. IOP Publishing, 25(1), p. 015015. doi: 10.1088/0963-0252/25/1/015015.

Hagelaar, G. J. M. and Pitchford, L. C. (2005) 'Solving the Boltzmann equation to obtain electron transport coefficients and rate coefficients for fluid models', *Plasma Sources Science and Technology*. IOP Publishing, 14(4), pp. 722–733. doi: 10.1088/0963-0252/14/4/011.

Heid, G. *et al.* (2009) 'Assisted combustion of an air-kerosene mixture by repetitive impulse nanoseconds plasma discharges', in *ISABE*, p. 474.

Herron, J. T. (1999) 'Evaluated chemical kinetics data for reactions of N(2D), N(2P), and N2(A3Σ+u) in the gas phase', *Journal of Physical and Chemical Reference Data*. American Institute of Physics Inc., 28(5), pp. 1453–1483. doi: 10.1063/1.556043.

Herron, J. T. and Green, D. S. (2001) 'Chemical kinetics database and predictive schemes for nonthermal humid air plasma chemistry. Part II. Neutral species reactions', *Plasma Chemistry and Plasma Processing*, 21(3), pp. 459–481. doi: 10.1023/A:1011082611822.

Hicks, Y. R. *et al.* (2012) 'Investigations of a Combustor Using a 9-Point Swirl-Venturi Fuel Injector: Recent Experimental Results', *Nasa*, (April).

van der Horst, R. M. *et al.* (2012) 'Time-resolved optical emission spectroscopy of nanosecond pulsed discharges in atmospheric-pressure N 2 and N 2 /H 2 O mixtures', *Journal of Physics D: Applied Physics*. IOP Publishing, 45(34), p. 345201. doi: 10.1088/0022-3727/45/34/345201.

Houpt, A. W. and Leonov, S. B. (2016) 'Charge Transfer in Constricted Form of Surface Barrier Discharge at Atmospheric Pressure', *Journal of Thermophysics and Heat Transfer*, 31, pp. 1–9. doi: 10.2514/1.T4970.

Huber, K. P. and Herzberg, G. (1979) *Molecular Spectra and Molecular Structure, Molecular Spectra and Molecular Structure*. Springer US. doi: 10.1007/978-1-4757-0961-2.

Hübner, M. *et al.* (2012) 'On time resolved gas temperature measurements in a pulsed dc plasma using quantum cascade laser absorption spectroscopy', *Measurement Science and Technology*, 23(11), pp. 115602–115609. doi: 10.1088/0957-0233/23/11/115602.

Huo, W. M. and Dateo, C. E. (1998) 'Electron-Impact Excitation of N2', *APS*, 27, p. LP.28.

Iordanova, E. *et al.* (2009) 'A novel method to determine the electron temperature and density from the absolute intensity of line and continuum emission: application to atmospheric microwave induced Ar plasmas', *Journal of Physics D: Applied Physics*. IOP Publishing, 42(15), p. 155208. doi: 10.1088/0022-3727/42/15/155208.

Isola, L. M., Gómez, B. J. and Guerra, V. (2010) 'Determination of the electron temperature and density in the negative glow of a nitrogen pulsed discharge using optical emission spectroscopy', *Journal of Physics D: Applied Physics*, 43(1), p. 015202. doi: 10.1088/0022-3727/43/1/015202.

Itikawa, Y. (2006) 'Cross sections for electron collisions with nitrogen molecules', *Journal of Physical and Chemical Reference Data*, 35(1), pp. 31–53. doi: 10.1063/1.1937426.

Itikawa, Y. (2009) 'Cross sections for electron collisions with oxygen molecules', *Journal of Physical and Chemical Reference Data*, 38(1), pp. 1–20. doi: 10.1063/1.3025886.

Itikawa, Y. (2016) 'Cross sections for electron collisions with nitric oxide', *Journal of Physical and Chemical Reference Data*, 45(3), p. 1464. doi: 10.1063/1.4961372.

Ju, Y. and Sun, W. (2015) 'Plasma assisted combustion: Dynamics and chemistry', *Progress in Energy and Combustion Science*, 48, pp. 21–83. doi: 10.1016/j.pecs.2014.12.002.

Karzas, W. J. and Latter, R. (1961) 'Electron Radiative Transitions in a Coulomb Field.', *The Astrophysical Journal Supplement Series*. IOP Publishing, 6, p. 167. doi: 10.1086/190063.

Kelleher, D. E. (1981) 'Stark broadening of visible neutral helium lines in a plasma', *Journal of*

Quantitative Spectroscopy and Radiative Transfer. Pergamon, 25(3), pp. 191–220. doi: 10.1016/0022-4073(81)90089-3.

Kienle, R., Jörg, A. and Kohse-Höinghaus, K. (1993) 'State-to-state rotational energy transfer in OH (A2Σ+, υ′=1)', *Applied Physics B Photophysics and Laser Chemistry*, 56(5), pp. 249–258. doi: 10.1007/BF00325212.

Kim, G. T. *et al.* (2017) 'Effects of applying non-thermal plasma on combustion stability and emissions of NOx and CO in a model gas turbine combustor', *Fuel*. Elsevier Ltd, 194, pp. 321–328. doi: 10.1016/j.fuel.2017.01.033.

Kim, W. *et al.* (2006a) 'Flame stabilization enhancement and NOx production using ultra short repetitively pulsed plasma discharges', *Collection of Technical Papers - 44th AIAA Aerospace Sciences Meeting*, 9(January), pp. 6770–6772.

Kim, W. *et al.* (2006b) 'Plasma-discharge stabilization of jet diffusion flames', *IEEE Transactions on Plasma Science*, 34(6), pp. 2545–2551. doi: 10.1109/TPS.2006.886084.

Kim, W. *et al.* (2007) 'Investigation of NO production and flame structure in plasma enhanced premixed combustion', *Proceedings of the Combustion Institute*, 31 II, pp. 3319–3326. doi: 10.1016/j.proci.2006.07.107.

Kliner, D. A. V. and Farrow, R. L. (1999) 'Measurements of ground-state OH rotational energy-transfer rates', *Journal of Chemical Physics*, 110(1), pp. 412–422. doi: 10.1063/1.478073.

Koch, A., Chryssostomou, A., *et al.* (1993) 'Multi-species detection in spray flames with tunable excimer lasers', *Applied Physics B Photophysics and Laser Chemistry*, 56(3), pp. 165–176. doi: 10.1007/BF00332196.

Koch, A., Voges, H., *et al.* (1993) 'Planar imaging of a laboratory flame and of internal combustion in an automobile engine using UV rayleigh and fluorescence light', *Applied Physics B Photophysics and Laser Chemistry*, 56(3), pp. 177–184. doi: 10.1007/BF00332197.

Kong, C. *et al.* (2019) 'Stabilization of a turbulent premixed flame by a plasma filament', *Combustion and Flame*, 208, pp. 79–85. doi: 10.1016/j.combustflame.2019.07.002.

Konjević, N. *et al.* (2002) 'Experimental Stark Widths and Shifts for Spectral Lines of Neutral and Ionized Atoms (A Critical Review of Selected Data for the Period 1989 Through 2000)', *Journal of Physical and Chemical Reference Data*, 31(3), pp. 819–927. doi: 10.1063/1.1486456.

Konjević, N., Ivković, M. and Sakan, N. (2012) 'Hydrogen Balmer lines for low electron number density plasma diagnostics', *Spectrochimica Acta Part B: Atomic Spectroscopy*. Elsevier, 76, pp. 16–26. doi:

10.1016/J.SAB.2012.06.026.

Kono, M. *et al.* (1989) ‘Mechanism of flame kernel formation produced by short duration sparks’, *Symposium (International) on Combustion*. Elsevier, 22(1), pp. 1643–1649. doi: 10.1016/S0082-0784(89)80176-6.

Kossyi, I. A. *et al.* (1992) ‘Kinetic scheme of the non-equilibrium discharge in nitrogen-oxygen mixtures’, *Plasma Sources Science and Technology*. IOP Publishing, 1(3), pp. 207–220. doi: 10.1088/0963-0252/1/3/011.

Kramida, A. *et al.* (2018) *NIST ASD, NIST Atomic Spectra Database (ver. 5.6.1)*. Available at: https://physics.nist.gov/asd.

Lacoste, D. A. *et al.* (2013) ‘Effect of Nanosecond Repetitively Pulsed Discharges on the Dynamics of a Swirl-Stabilized Lean Premixed Flame’, *Journal of Engineering for Gas Turbines and Power*. American Society of Mechanical Engineers, 135(10), p. 101501. doi: 10.1115/1.4024961.

Lacour, C. *et al.* (2016) ‘Characterisation of electric discharge in laminar flow with optical diagnostics’, *18th International Symposium on the Application of Laser and Imaging Techniques to Fluid Mechanics*, (July).

Laux, C. *et al.* (1999) ‘Ionization Mechanisms in Two-Temperature Air Plasmas’, *30th Plasmadynamic and Lasers Conference*. Reston, Virigina: American Institute of Aeronautics and Astronautics, (99–3476). doi: 10.2514/6.1999-3476.

Laux, C. O. (1993) *Optical Diagnostics and Radiative Emission of Air Plasmas*. Stanford University, PhD Thesis. Available at: http://adsabs.harvard.edu/abs/1993PhDT.....206L (Accessed: 10 October 2019).

Laux, C. O. (2002) ‘Radiation and nonequilibrium collisional-radiative models’, *VKI Special course on Physico-chemical models for high enthalpy and plasma flow modelling*, pp. 1–55.

Laux, C. O. *et al.* (2003) ‘Optical diagnostics of atmospheric pressure air plasmas’, *Plasma Sources Science and Technology*, 12, pp. 125–138. doi: 10.1088/0963-0252/12/2/301.

Laux, C. O. (2017) ‘Plasma-assisted stabilization: fundamental mechanisms and applications’, *Colloque de l’INitiative en Combustion Avancée (INCA)*, (CentraleSupélec).

Lepikhin, N. D. *et al.* (2016) ‘Long-lived plasma and fast quenching of N2(C3Π u) by electrons in the afterglow of a nanosecond capillary discharge in nitrogen’, *Plasma Sources Science and Technology*. Institute of Physics Publishing, 25(4), p. 045003. doi: 10.1088/0963-0252/25/4/045003.

Lo, A. *et al.* (2014) 'Space and time analysis of the nanosecond scale discharges in atmospheric pressure air: I. Gas temperature and vibrational distribution function of N_2 and O_2', *Journal of Physics D: Applied Physics*, 47(11), p. 115201. doi: 10.1088/0022-3727/47/11/115201.

Lo, A. *et al.* (2017) 'Streamer-to-spark transition initiated by a nanosecond overvoltage pulsed discharge in air', *Plasma Sources Science and Technology*, 26(4), p. 45012. doi: 10.1088/1361-6595/aa5c78.

Lo, A., Cessou, A. and Vervisch, P. (2014) 'Space and time analysis of the nanosecond scale discharges in atmospheric pressure air: II. Energy transfers during the post-discharge', *Journal of Physics D: Applied Physics*, 47(11), p. 115202. doi: 10.1088/0022-3727/47/11/115202.

Luque, J. and Crosley, D. R. (1998) 'Transition probabilities in the A2Σ+-X2Πi electronic system of OH', *Journal of Chemical Physics*, 109(2), pp. 439–448. doi: 10.1063/1.476582.

Magin, T. E. *et al.* (2006) 'Nonequilibrium radiative heat flux modeling for the Huygens entry probe', *Journal of Geophysical Research*, 111(E7), p. E07S12. doi: 10.1029/2005JE002616.

Mar, S. *et al.* (2000) 'Measurement of Stark broadening and shift of visible N II lines', *Journal of Physics B: Atomic, Molecular and Optical Physics*. IOP Publishing, 33(6), pp. 1169–1184. doi: 10.1088/0953-4075/33/6/304.

Martin, A. *et al.* (2010) 'Chemistry model for ablating carbon-phenolic material during atmospheric re-entry', *48th AIAA Aerospace Sciences Meeting Including the New Horizons Forum and Aerospace Exposition*, (January). doi: 10.2514/6.2010-1175.

Martin, S. and Martin, S. (2018) 'Transmission and Propagation of Electromagnetic Waves', in *Modern Telecommunications*. Cambridge University Press, pp. 103–130. doi: 10.1201/b22525-5.

McBride, B. J. and Gordon, S. (1992) 'Computer program for calculating and fitting thermodynamic functions'.

McGuire, S. D. *et al.* (2020) 'Measurements and modeling of CO 4th positive (A–X) radiation', *Journal of Quantitative Spectroscopy and Radiative Transfer*, 245. doi: 10.1016/j.jqsrt.2020.106855.

McQuarrie, D. A. and Simon, J. D. (2014) *Physical Chemistry : A molecular approach*. University Science Books, Sausalito. doi: 10.1039/c1cs15191f.

Minesi, N. *et al.* (2019) 'On the arc transition mechanism in nanosecond air discharges', *AIAA Scitech 2019 Forum*. San Diego, Cal.: American Institute of Aeronautics and Astronautics, 2019-0463, 2019, p. 0463. doi: 10.2514/6.2019-0463.

Minesi, N., Stepanyan, S., *et al.* (2020) 'Fully ionized nanosecond discharges in air: the thermal spark',

Plasma Sources Science and Technology, 29, p. 85003. doi: 10.1088/1361-6595/ab94d3.

Minesi, N., Mariotto, P., *et al.* (2020) 'Role of the excited electronic states in the ionization of ambient air by a nanosecond discharge', *AIAA Scitech 2020 Forum*. Reston, Virginia: American Institute of Aeronautics and Astronautics, 2020, p. 0437. doi: 10.2514/6.2020-0437.

Morozov, A. *et al.* (2005) 'Gas kinetic studies using a table-top set-up with electron beam excitation: Quenching of molecular nitrogen emission by water vapour', *European Physical Journal D*, 33(2), pp. 207–211. doi: 10.1140/epjd/e2005-00051-7.

Neame, G. R. *et al.* (1995) 'Improving the fuel economy of stoichiometrically fuelled S.I. engines by means of EGR and enhanced ignition - A comparison of gasoline, methanol and natural gas', *SAE Technical Papers*, (412). doi: 10.4271/952376.

Olsen, H. L., Edmonson, R. B. and Gayhart, E. L. (1952) 'Microchronometric Schlieren Study of Gaseous Expansion from an Electric Spark', *Journal of Applied Physics*. American Institute of Physics, 23(10), pp. 1157–1162. doi: 10.1063/1.1702001.

Ombrello, T., Ju, Y. and Fridman, A. (2008) 'Kinetic ignition enhancement of diffusion flames by nonequilibrium magnetic gliding arc plasma', in *AIAA Journal*, pp. 2424–2433. doi: 10.2514/1.33005.

Ono, R. and Oda, T. (2008) 'Measurement of OH density and gas temperature in incipient spark-ignited hydrogen-air flame', *Combustion and Flame*. Elsevier, 152(1–2), pp. 69–79. doi: 10.1016/j.combustflame.2007.07.022.

Orriere, T. (2018) *Confinement micrométrique des décharges pulsées nanosecondes dans l'air à pression atmosphérique et effets électro-aérodynamiques*. Université de Poitiers, PhD Thesis, in French.

Orriere, T., Moreau, E. and Pai, D. Z. (2018) 'Ionization and recombination in nanosecond repetitively pulsed microplasmas in air at atmospheric pressure', *Journal of Physics D: Applied Physics*, 51(49), p. 494002. doi: 10.1088/1361-6463/aae134.

Packan, D. (2004) *Repetitive nanosecond glow discharge in atmospheric pressure air*. Stanford University, PhD Thesis.

Pai, D., Lacoste, D. A. and Laux, C. O. (2008) 'Images of Nanosecond Repetitively Pulsed Plasmas in Preheated Air at Atmospheric Pressure', *IEEE Transactions on Plasma Science*, 36(4), pp. 974–975. doi: 10.1109/TPS.2008.924484.

Pai, D. Z. (2008) *Nanosecond Repetitively Pulsed Plasmas in Preheated Air at Atmospheric Pressure*. Ecole Centrale Paris, PhD Thesis.

Pai, D. Z. *et al.* (2009) ‘Nanosecond repetitively pulsed discharges in air at atmospheric pressure - The glow regime’, *Plasma Sources Science and Technology*, 18(4), p. 045030. doi: 10.1088/0963-0252/18/4/045030.

Pai, D. Z., Lacoste, D. A. and Laux, C. O. (2010a) ‘Nanosecond repetitively pulsed discharges in air at atmospheric pressure-the spark regime’, *Plasma Sources Science and Technology*, 19(6), p. 065015. doi: 10.1088/0963-0252/19/6/065015.

Pai, D. Z., Lacoste, D. A. and Laux, C. O. (2010b) ‘Transitions between corona, glow, and spark regimes of nanosecond repetitively pulsed discharges in air at atmospheric pressure’, *Journal of Applied Physics*. American Institute of Physics, 107(9), p. 093303. doi: 10.1063/1.3309758.

Pancheshnyi, S. (2006) ‘Comments on “Intensity ratio of spectral bands of nitrogen as a measure of electric field strength in plasmas”’, *Journal of Physics D: Applied Physics*, 39(8), pp. 1708–1710. doi: 10.1088/0022-3727/39/8/N01.

Pancheshnyi, S. *et al.* (2012) ‘The LXCat project: Electron scattering cross sections and swarm parameters for low temperature plasma modeling’, *Chemical Physics*. Elsevier B.V., 398(1), pp. 148–153. doi: 10.1016/j.chemphys.2011.04.020.

Pancheshnyi, S. V., Starikovskaia, S. M. and Starikovskii, A. Y. (1998) ‘Measurements of rate constants of the N2(C3Πu, v′ =0) and N2+(B2Σ+u, v′ =0) deactivation by N 2 , O 2 , H 2 , CO and H 2 O molecules in afterglow of the nanosecond discharge’, *Chemical Physics Letters*, 294(6), pp. 523–527. doi: 10.1016/S0009-2614(98)00879-3.

Pancheshnyi, S. V., Starikovskaia, S. M. and Starikovskii, A. Y. (2000) ‘Collisional deactivation of N2(C3Π(u), v = 0, 1, 2, 3) states by N2, O2, H2 and H2O molecules’, *Chemical Physics*, 262(2–3), pp. 349–357. doi: 10.1016/S0301-0104(00)00338-4.

Pancheshnyi, S. V *et al.* (2008) ‘Computer code ZDPlasKin’. University of Toulouse, LAPLACE, CNRS-UPS-INP. Available at: http://www.zdplaskin.laplace.univ-tlse.fr.

Panesi, M. *et al.* (2013) ‘Rovibrational internal energy transfer and dissociation of N 2(1Σg+)-N(4S u) system in hypersonic flows’, *Journal of Chemical Physics*, 138(4). doi: 10.1063/1.4774412.

Pannier, E. (2019) *Conversion of carbon dioxyde with nanosecond repetitive discharges*. CentraleSupélec, PhD Thesis.

Pannier, E. and Laux, C. O. (2019) ‘RADIS: A nonequilibrium line-by-line radiative code for CO2 and HITRAN-like database species’, *Journal of Quantitative Spectroscopy and Radiative Transfer*, 222–223, pp. 12–25. doi: 10.1016/j.jqsrt.2018.09.027.

Panteleev, E. V., Panteleeva, G. V. and Panteleev, P. E. (2013) 'Biofuel composition'. Available at: https://patents.google.com/patent/DE112013000510T5/en (Accessed: 4 September 2020).

Paris, P. *et al.* (2005) 'Intensity ratio of spectral bands of nitrogen as a measure of electric field strength in plasmas', *Journal of Physics D: Applied Physics*, 38(21), pp. 3894–3899. doi: 10.1088/0022-3727/38/21/010.

Paris, P. *et al.* (2006) 'Reply to comments on "Intensity ratio of spectral bands of nitrogen as a measure of electric field strength in plasmas"', *Journal of Physics D: Applied Physics*, 39(12), pp. 2636–2639. doi: 10.1088/0022-3727/39/12/N01.

Park, C. (1989) 'A review of reaction rates in high temperature air', in *AIAA 24th Thermophysics Conference, 1989*. American Institute of Aeronautics and Astronautics Inc, AIAA. doi: 10.2514/6.1989-1740.

Park, C. (1990) *Nonequilibrium Hypersonic Aerothermodynamics*. Wiley, New York.

Park, C. (1993) 'Review of chemical-kinetic problems of future NASA missions, I: Earth entries', *Journal of Thermophysics and Heat Transfer*, 7(3), pp. 385–398. doi: 10.2514/3.431.

Parker, J. G. (1959) 'Rotational and Vibrational Relaxation in Diatomic Gases', 449. doi: 10.1063/1.1724417.

Parkevich, E. V., Khirianova, A. I., *et al.* (2018) 'Anode Plasma Formation at the Initial Stage of a Nanosecond Air Discharge', *Journal of Experimental and Theoretical Physics*. Pleiades Publishing, 126(3), pp. 422–429. doi: 10.1134/S1063776118030160.

Parkevich, E. V., Medvedev, M. A., *et al.* (2018) 'The peculiarities of near-cathode processes in air discharge at atmospheric pressure', p. 1804.01336. Available at: http://arxiv.org/abs/1804.01336.

Parkevich, E. V. *et al.* (2019) 'Fast fine-scale spark filamentation and its effect on the spark resistance', *Plasma Sources Science and Technology*. Institute of Physics Publishing, 28(09), p. 095003. doi: 10.1088/1361-6595/ab3768.

Perrin-Terrin, J. (2020) *Rapport 'Parcours recherche' - 2ème année (in French)*.

Peterson, J. R. *et al.* (1998) 'Dissociative recombination and excitation of N+2: Cross sections and product branching ratios', *Journal of Chemical Physics*, 108(5), pp. 1978–1988. doi: 10.1063/1.475577.

Pham, Q. L. L., Lacoste, D. A. and Laux, C. O. (2011) 'Stabilization of a premixed methane-air flame using nanosecond repetitively pulsed discharges', *IEEE Transactions on Plasma Science*, 39(11 PART 1), pp. 2264–2265. doi: 10.1109/TPS.2011.2163806.

Phelps, A. V. (1985) ‘Report 28 JILA Information Center’, *University of Colorado, Boulder*.

Phelps, A. V and Pitchford, L. C. (1985) ‘Anisotropic scattering of electrons by N2 and its effect on electron transport’, *Physical Review A*, 31(5), pp. 2932–2949. doi: 10.1103/PhysRevA.31.2932.

Phuoc, T. X. (2005) ‘An experimental and numerical study of laser-induced spark in air’, *Optics and Lasers in Engineering*, 43(2), pp. 113–129. doi: 10.1016/j.optlaseng.2004.07.003.

Pilla, G. *et al.* (2006) ‘Stabilization of a Turbulent Premixed Flame Using a Nanosecond Repetitively Pulsed Plasma’, *IEEE Transactions on Plasma Science*, 34(6), pp. 2471–2477. doi: 10.1109/TPS.2006.886081.

Pilla, G. (2008) *Etude Expérimentale de la Stabilisation de Flammes Propane-Air de Prémélange par Décharges Nanosecondes Impulsionnelles Répétitives*. Ecole Centrale Paris, PhD Thesis (in French).

Piper, L. G. (1982) ‘The excitation of O(1S) in the reaction between N2(A 3∑u+) and O(3P)’, *The Journal of Chemical Physics*. American Institute of PhysicsAIP, 77(5), pp. 2373–2377. doi: 10.1063/1.444158.

Piper, L. G. (1987) ‘Quenching rate coefficients for N2(a′ 1Σ u-)’, *The Journal of Chemical Physics*, 87(3), pp. 1625–1629. doi: 10.1063/1.453223.

Piper, L. G. (1992) ‘Energy transfer studies on N2(X 1Σg+,V) and N2(B 3πg)’, *The Journal of Chemical Physics*. American Institute of Physics, 97(1), pp. 270–275. doi: 10.1063/1.463625.

Pitchford, L. C. and Phelps, A. V. (1982) ‘Comparative calculations of electron-swarm properties in N2 at moderate en values’, *Physical Review A*. American Physical Society, 25(1), pp. 540–554. doi: 10.1103/PhysRevA.25.540.

Popov, N. A. (2001) ‘Investigation of the mechanism for rapid heating of nitrogen and air in gas discharges’, *Plasma Physics Reports*, 27(10), pp. 886–896. doi: 10.1134/1.1409722.

Popov, N. A. (2008) ‘Effect of a pulsed high-current discharge on hydrogen-air mixtures’, *Plasma Physics Reports*, 34(5), pp. 376–391. doi: 10.1134/S1063780X08050048.

Popov, N. A. (2009a) ‘Associative ionization reactions involving excited atoms in nitrogen plasma’, *Plasma Physics Reports*. SP MAIK Nauka/Interperiodica, 35(5), pp. 436–449. doi: 10.1134/S1063780X09050092.

Popov, N. A. (2009b) ‘Erratum to: “Associative ionization reactions involving excited atoms in nitrogen plasma”’, *Plasma Physics Reports*. SP MAIK Nauka/Interperiodica, 35(6), pp. 528–528. doi: 10.1134/S1063780X09060117.

Popov, N. A. (2011a) ‘Fast gas heating in a nitrogen–oxygen discharge plasma: I. Kinetic mechanism’, *Journal of Physics D: Applied Physics*, 44(28), p. 285201. doi: 10.1088/0022-3727/44/28/285201.

Popov, N. A. (2011b) ‘Kinetic processes initiated by a nanosecond high-current discharge in hot air’, *Plasma Physics Reports*. SP MAIK Nauka/Interperiodica, 37(9), pp. 807–815. doi: 10.1134/s1063780x1108006x.

Popov, N. A. (2013) ‘Fast Gas Heating Initiated by Pulsed Nanosecond Discharge in Atmospheric Pressure Air’, *51st AIAA Aerospace Sciences Meeting including the New Horizons Forum and Aerospace Exposition 2013*, (January), pp. 1–20. doi: 10.2514/6.2013-1052.

Popov, N. A. (2016a) ‘Kinetics of plasma-assisted combustion: effect of non-equilibrium excitation on the ignition and oxidation of combustible mixtures’, *Plasma Sources Science and Technology*, 25(4), p. 043002. doi: 10.1088/0963-0252/25/4/043002.

Popov, N. A. (2016b) ‘Pulsed nanosecond discharge in air at high specific deposited energy: Fast gas heating and active particle production’, *Plasma Sources Science and Technology*. IOP Publishing, 25(4), p. 44003. doi: 10.1088/0963-0252/25/4/044003.

Popov, N. A., Babaeva, N. and Naidis, G. (2019) ‘Recent advances in the chemical kinetics of non-equilibrium plasmas’, *Journal of Physics D: Applied Physics*. Institute of Physics Publishing, p. 6. doi: 10.1088/1361-6463/aaff46.

Prieur, K. *et al.* (2017) ‘Ignition dynamics in an annular combustor for liquid spray and premixed gaseous injection’, *Proceedings of the Combustion Institute*, 36(3), pp. 3717–3724. doi: 10.1016/j.proci.2016.08.008.

Radzig, A. A. and Smirnov, B. M. (1985) *Reference Data on Atoms, Molecules, and Ions*. Berlin, Heidelberg: Springer Berlin Heidelberg (Springer Series in Chemical Physics). doi: 10.1007/978-3-642-82048-9.

Raizer, Y. P. (1991) *Gas Discharge Physics*. Corr. prin. Edited by J. E. Allen. Springer Verlag. Berlin.

Rapp, D. and Englander-Golden, P. (1965) ‘Total cross sections for lonization and attachment in gases by electron impact. I. Positive ionization’, *The Journal of Chemical Physics*, 43(5), pp. 1464–1479. doi: 10.1063/1.1696957.

Rivière, P. (2002) ‘Systematic semi-classical calculations of Stark broadening parameters of NI, OI, NII, OII multiplets for modelling the radiative transfer in atmospheric air mixture plasmas’, *Journal of Quantitative Spectroscopy and Radiative Transfer*. Pergamon, 73(1), pp. 91–110. doi: 10.1016/S0022-4073(01)00173-X.

Rusterholtz, D. (2012) *Nanosecond Repetitively Pulsed Discharges in Atmospheric Pressure Air*. Ecole Centrale Paris, PhD Thesis.

Rusterholtz, D. L. *et al.* (2013) 'Ultrafast heating and oxygen dissociation in atmospheric pressure air by nanosecond repetitively pulsed discharges', *Journal of Physics D: Applied Physics*, 46(46), p. 464010. doi: 10.1088/0022-3727/46/46/464010.

Sainct, F. (2014) *Etude de la réactivité de décharges électriques nanoseconde à la pression atmosphérique dans la vapeur d'eau*. Ecole Centrale Paris, PhD Thesis (in French). Available at: https://hal.archives-ouvertes.fr/tel-01020267/.

Sainct, F. P. *et al.* (2014) 'Temporal evolution of temperature and OH density produced by nanosecond repetitively pulsed discharges in water vapour at atmospheric pressure', *Journal of Physics D: Applied Physics*, 47(7), p. 75204. doi: 10.1088/0022-3727/47/7/075204.

Sainct, F. P. *et al.* (2020) 'Electron number density measurements in nanosecond repetitively pulsed discharges in water vapor at atmospheric pressure', *Plasma Sources Science and Technology*. IOP Publishing, 29, p. 025017. doi: 10.1088/1361-6595/ab681b.

Salmon, A. *et al.* (2018) 'Quenching rate of N(2P) atoms in a nitrogen afterglow at atmospheric pressure', *Journal of Physics D: Applied Physics*. IOP Publishing, 51(31). doi: 10.1088/1361-6463/aace71.

Salmon, J. T. and Laurendeau, N. M. (1985) 'Calibration of laser-saturated fluorescence measurements using Rayleigh scattering', *Applied Optics*, 24(1), p. 65. doi: 10.1364/ao.24.000065.

Schmid, P. J. (2010) 'Dynamic mode decomposition of numerical and experimental data', *Journal of Fluid Mechanics*. doi: 10.1017/S0022112010001217.

Shao, T. *et al.* (2011) 'Runaway electron preionized diffuse discharges in atmospheric pressure air with a point-to-plane gap in repetitive pulsed mode', *Journal of Applied Physics*, 109(08), p. 083306. doi: 10.1063/1.3581066.

Shao, T. *et al.* (2012) 'Spark discharge formation in an inhomogeneous electric field under conditions of runaway electron generation', *Journal of Applied Physics*, 111(2), p. 023304. doi: 10.1063/1.3677951.

Shcherbanev, S. A. *et al.* (2016) 'Optical emission spectrum of filamentary nanosecond surface dielectric barrier discharge', *Plasma Sources Science and Technology*, 26(2), p. 02LT01. doi: 10.1088/1361-6595/26/2/02LT01.

Shcherbanev, S. A. *et al.* (2019) 'Filamentary nanosecond surface dielectric barrier discharge. Plasma

properties in the filaments', *Plasma Sources Science and Technology*. IOP Publishing, 28(6), p. 065013. doi: 10.1088/1361-6595/ab2230.

Sher, E., Ben-Ya'ish, J. and Kravchik, T. (1992) 'On the birth of spark channels', *Combustion and flame*, 89(2), pp. 186–194. doi: 10.1016/S0304-419X(01)00029-4.

Shkurenkov, I. *et al.* (2014) 'Kinetics of excited states and radicals in a nanosecond pulse discharge and afterglow in nitrogen and air', *Plasma Sources Science and Technology*, 23(6), p. 065003. doi: 10.1088/0963-0252/23/6/065003.

Shneider, M. N. (2006) 'Turbulent decay of after-spark channels', *Physics of Plasmas*, 13(7), pp. 1–11. doi: 10.1063/1.2218492.

Smith, G. P. *et al.* (2000) *GRI-Mech 3.0, http://www.me.berkeley.edu/gri_mech/*.

Stancu, G. D., Kaddouri, F., *et al.* (2010) 'Atmospheric pressure plasma diagnostics by OES, CRDS and TALIF', *Journal of Physics D: Applied Physics*, 43(12), p. 124002. doi: 10.1088/0022-3727/43/12/124002.

Stancu, G. D., Janda, M., *et al.* (2010) 'Time-resolved CRDS measurements of the N2(A3Σ u+) density produced by nanosecond discharges in atmospheric pressure nitrogen and air', *Journal of Physical Chemistry A*. American Chemical Society, 114(1), pp. 201–208. doi: 10.1021/jp9075383.

Stanton, P. N. and St. John, R. M. (1969) 'Electron Excitation of the First Positive Bands of N_2 and of the First Negative and Meinel Bands of N_2^+*', *Journal of the Optical Society of America*. The Optical Society, 59(3), p. 252. doi: 10.1364/josa.59.000252.

Starikovskaia, S. M. (2014) 'Plasma-assisted ignition and combustion: Nanosecond discharges and development of kinetic mechanisms', *Journal of Physics D: Applied Physics*, 47(35). doi: 10.1088/0022-3727/47/35/353001.

Stepanyan, S. *et al.* (2017) 'Large-volume excitation of air, argon, nitrogen and combustible mixtures by thermal jets produced by nanosecond spark discharges', *Plasma Sources Science and Technology*, 26(4), pp. 22–24. doi: 10.1088/1361-6595/aa5a2b.

Stepanyan, S. *et al.* (2019) 'Spatial evolution of the plasma kernel produced by nanosecond discharges in air', *Journal of Physics D: Applied Physics*, 52(29), p. 295203. doi: 10.1088/1361-6463/ab1ba4.

Stepanyan, S. A. *et al.* (2014) 'A nanosecond surface dielectric barrier discharge in air at high pressures and different polarities of applied pulses: transition to filamentary mode', *Plasma Sources Science and Technology*. IOP Publishing, 23(4), p. 045003. doi: 10.1088/0963-0252/23/4/045003.

Stöhr, M. *et al.* (2011) 'Dynamics of lean blowout of a swirl-stabilized flame in a gas turbine model combustor', *Proceedings of the Combustion Institute*, 33(2), pp. 2953–2960. doi: 10.1016/j.proci.2010.06.103.

Stritzke, P., Sander, I. and Raether, H. (1977) 'Spatial and temporal spectroscopy of a streamer discharge in nitrogen', *Journal of Physics D: Applied Physics*, 10(16), pp. 2285–2300. doi: 10.1088/0022-3727/10/16/019.

Sun, W. *et al.* (2013) 'Direct ignition and S-curve transition by in situ nano-second pulsed discharge in methane/oxygen/helium counterflow flame', *Proceedings of the Combustion Institute*. Elsevier Ltd, 34(1), pp. 847–855. doi: 10.1016/j.proci.2012.06.104.

Sun, W. *et al.* (2019) 'The effect of ozone addition on combustion: Kinetics and dynamics', *Progress in Energy and Combustion Science*. Elsevier Ltd, 73, pp. 1–25. doi: 10.1016/j.pecs.2019.02.002.

Sutherland, R. S. (1998) 'Accurate free-free Gaunt factors for astrophysical plasmas', *Monthly Notices of the Royal Astronomical Society*. Blackwell Publishing Ltd, 300(2), pp. 321–330. doi: 10.1046/j.1365-8711.1998.01687.x.

Sutton, J. A. and Driscoll, J. F. (2004) 'Rayleigh scattering cross sections of combustion species at 266, 355, and 532 nm for thermometry applications', *Optics Letters*. Optical Society of America, 29(22), p. 2620. doi: 10.1364/ol.29.002620.

Tawara, H. and Kato, T. (1987) 'Total and partial ionization cross sections of atoms and ions by electron impact', *Atomic Data and Nuclear Data Tables*. Academic Press, pp. 167–353. doi: 10.1016/0092-640X(87)90014-3.

Tayal, S. S. and Zatsarinny, O. (2016) 'B -spline R -matrix-with-pseudostates approach for excitation and ionization of atomic oxygen by electron collisions', *Physical Review A*, 94(4), pp. 1–15. doi: 10.1103/PhysRevA.94.042707.

Teulet, P., Sarrette, J. P. and Gomes, A. M. (1999) 'Calculation of electron impact inelastic cross sections and rate coefficients for diatomic molecules. Application to air molecules', *Journal of Quantitative Spectroscopy and Radiative Transfer*, 62(5), pp. 549–569. doi: 10.1016/S0022-4073(98)00129-0.

Thomas, J. M. and Kaufman, F. (1996) 'An upper limit on the formation of NO(X2Pi) in the reactions N2(A3Sig) + O(3P) and N2(A) + O2(X3SIg) at 298 K', *Journal of Physical Chemistry*, 100(21), pp. 8901–8906. doi: 10.1021/jp960164v.

Tibère-inglesse, A. (2019) *Radiation of nonequilibrium recombining plasma flows*. Université Paris-

Saclay, PhD Thesis. Available at: https://tel.archives-ouvertes.fr/tel-02454286.

Töpperwien, K. (2021) *Numerical simulation of combustion instabilities and ignition in annular combustion chambers.* Université Paris-Saclay, PhD Thesis (in preparation).

Trajmar, S., Register, D. F. and Chutjian, A. (1983) 'Electron scattering by molecules II. Experimental methods and data', *Physics Reports*. North-Holland, 97(5), pp. 219–356. doi: 10.1016/0370-1573(83)90071-6.

U.S. Energy Information Administration (2020) *Energy Review*. Available at: https://www.eia.gov/totalenergy/.

Valentini, P. *et al.* (2014) 'Rovibrational coupling in molecular nitrogen at high temperature: An atomic-level study', *Physics of Fluids*, 26(5). doi: 10.1063/1.4875279.

Valk, F. *et al.* (2010) 'Measurement of collisional quenching rate of nitrogen states N 2 (C 3 Π u , v = 0) and {\rm N}_2^+ (B\,^{\rm 2}\Sigma_{\rm g}^+,v=0)', *Journal of Physics D: Applied Physics*, 43(38), p. 385202. doi: 10.1088/0022-3727/43/38/385202.

Verner, D. A. *et al.* (1996) 'Atomic Data for Astrophysics. II. New Analytic FITS for Photoionization Cross Sections of Atoms and Ions', *The Astrophysical Journal*, 465, p. 487. doi: 10.1086/177435.

Verreycken, T. *et al.* (2011) 'Validation of gas temperature measurements by OES in an atmospheric air glow discharge with water electrode using Rayleigh scattering', *Plasma Sources Science and Technology*, 20(2), p. 024002. doi: 10.1088/0963-0252/20/2/024002.

Verreycken, T. *et al.* (2012) 'Time and spatially resolved LIF of OH in a plasma filament in atmospheric pressure HeH 2O', *Journal of Physics D: Applied Physics*, 45(4). doi: 10.1088/0022-3727/45/4/045205.

Verreycken, T. *et al.* (2013) 'Absolute calibration of OH density in a nanosecond pulsed plasma filament in atmospheric pressure He–H 2 O: comparison of independent calibration methods', *Journal of Physics D: Applied Physics*, 46(46), p. 464004. doi: 10.1088/0022-3727/46/46/464004.

Vignat, G. *et al.* (2020) 'Improvement of lean blow out performance of spray and premixed swirled flames using nanosecond repetitively pulsed discharges', *Proceedings of the Combustion Institute*. Elsevier. doi: 10.1016/j.proci.2020.06.136.

Vincent-Randonnier, A. *et al.* (2019) 'An experimental and computational study of hydrogen-air combustion in the LAPCAT II supersonic combustor', *Proceedings of the Combustion Institute*. Elsevier Inc., 37(3), pp. 3703–3711. doi: 10.1016/j.proci.2018.05.127.

Vincenti, W. G. and Kruger, C. H. (1965) *Introduction to Physical Gas Dynamics*. Wiley, New York.

Walpot, L. M. *et al.* (2006) ‘Convective and radiative heat flux prediction of Huygens entry on Titan’, *Journal of Thermophysics and Heat Transfer*. American Institute of Aeronautics and Astronautics Inc., 20(4), pp. 663–671. doi: 10.2514/1.20901.

Walter, C. W., Cosby, P. C. and Helm, H. (1993) ‘N(4S0), N(2D0), and N(2P0) yields in predissociation of excited singlet states of N2’, *The Journal of Chemical Physics*, 99(5), pp. 3553–3561. doi: 10.1063/1.466152.

Wang, H. (2015) ‘Combustion Chemistry’, *Princeton-CEFRC Summer School On Combustion*.

Wang, Y., Zatsarinny, O. and Bartschat, K. (2014) ‘B-spline R-matrix-with-pseudostates calculations for electron-impact excitation and ionization of nitrogen’, *Physical Review A*, 89(6), p. 062714. doi: 10.1103/PhysRevA.89.062714.

Wilbers, A. T. M. *et al.* (1991) ‘The continuum emission of an arc plasma’, *Journal of Quantitative Spectroscopy and Radiative Transfer*. Pergamon, 45(1), pp. 1–10. doi: 10.1016/0022-4073(91)90076-3.

Xu, D. (2013) *Thermal and hydrodynamic effects of nanosecond discharges in air and application to plasma-assisted combustion*. Ecole Centrale Paris, PhD Thesis. Available at: https://hal.archives-ouvertes.fr/tel-00978527/.

Xu, D. A. *et al.* (2011) ‘Experimental study of the hydrodynamic expansion following a nanosecond repetitively pulsed discharge in air’, *Citation: Appl. Phys. Lett*, 99. doi: 10.1063/1.3641413.

Young, R. A., Black, G. and Slanger, T. G. (1969) ‘Vacuum-Ultraviolet Photolysis of N 2 O. II. Deactivation of N2(A 3Σu+) and N2(B 3Πg)’, *The Journal of Chemical Physics*. AIP Publishing, 50(1), pp. 303–308. doi: 10.1063/1.1670792.

Yu, L. *et al.* (2001) ‘Effects of vibrational nonequilibrium on the chemistry of two-temperature nitrogen plasmas’, *Plasma Chemistry and Plasma Processing*, 21(4), pp. 483–503. doi: 10.1023/A:1012073800284.

Zare, R. N. (1964) ‘Calculation of Intensity Distribution in the Vibrational Structure of Electronic Transitions: The $B^3\Pi_{0^+u} - X^1\Sigma_{0^+g}$ Resonance Series of Molecular Iodine’, *The Journal of Chemical Physics*. American Institute of Physics, 40(7), pp. 1934–1944. doi: 10.1063/1.1725425.

Zipf, E. C. and McLaughlin, R. W. (1978) ‘On the dissociation of nitrogen by electron impact and by E.U.V. photo-absorption’, *Planetary and Space Science*. Pergamon, 26(5), pp. 449–462. doi: 10.1016/0032-0633(78)90066-1.

Almazova, K. I. *et al.* (2020) ‘Investigation of plasma properties in the phase of the radial expansion of

spark channel in the pin-to-plate geometry', *Plasma Sources Science and Technology*. IOP Publishing. doi: 10.1088/1361-6595/aba8cc.